The fine structure of the sunspot penumbra

Dissertation
zur Erlangung des Doktorgrades
der Mathematisch–Naturwissenschaftlichen Fakultäten
der Georg–August–Universität zu Göttingen

vorgelegt von
Juan Manuel Borrero Santiago
aus Algeciras / Cádiz / España

Göttingen 2004

Bibliografische Information Der Deutschen Bibliothek
Die Deutsche Bibliothek verzeichnet diese Publikation in der Deutschen Nationalbibliografie; detaillierte bibliografischen Daten sind im Internet über http://dnb.ddb.de abrufbar.

D7
Referent: Prof. Dr. Franz Kneer
Korreferent: Prof. Dr. Sami K. Solanki
Tag der mündlichen Prüfung: 31 August 2004

Copyright © Copernicus GmbH 2004

ISBN 3-936586-33-0

Copernicus GmbH, Katlenburg-Lindau
Satz & Coverdesign: Juan Manuel Borrero
Front picture edit: Johann Hirzberger & Franz Kneer
Druck: Schaltungsdients Lange, Berlin

Printed in Germany

Nunca perseguí la gloria.
Caminante son tus huellas el camino y nada más;
Caminante no hay camino
Se hace camino al Andar. Al andar se hace camino
Y al volver la vista atrás
Se ve la senda que nunca se ha de volver a Pisar.
Caminante no hay camino sino estelas en la Mar.

Antonio Machado (Poet)

Dedicated to Rubén, to Anna
and to my parents

Contents

Introduction **5**

1 Spectropolarimetry **9**
1.1 Stokes parameters . . . 9
1.1.1 Definition . . . 9
1.1.2 Measuring the Stokes parameters . . . 10
1.2 Zeeman effect . . . 12
1.2.1 Molecular Zeeman effect . . . 16
1.3 Radiative Transfer Equation . . . 16
1.4 Formal solution of the RTE . . . 19
1.4.1 Symmetries . . . 19
1.4.2 Evolution Operator . . . 20
1.4.3 Milne-Eddington approximation . . . 22
1.4.4 General case . . . 25
1.5 Inversion of Stokes profiles . . . 26
1.5.1 Iterative and non-iterative methods . . . 27
1.5.2 The merit χ^2 function . . . 28
1.5.3 Linearization of the RTE and Response functions . . . 29
1.5.4 Derivatives of χ^2 . . . 30
1.5.5 Inversion procedure . . . 32
1.5.6 SPINOR . . . 35
1.5.7 Should we believe inversions ? . . . 37

2 Sunspot Penumbra **45**
2.1 Sunspots . . . 45
2.1.1 Umbra . . . 46
2.1.2 Penumbra . . . 47
2.1.3 The Evershed effect . . . 48
2.2 Penumbral structure . . . 49
2.2.1 Penumbral horizontal structure . . . 51
2.2.2 Penumbral vertical structure . . . 56
2.3 Theoretical understanding of the Evershed flow . . . 66

3 Comparison of two semiempirical models **69**
3.1 Introduction . . . 69
3.2 Observations . . . 71
3.3 Inversion procedure . . . 71
3.4 Geometrical models adopted for the inversion . . . 73
3.5 Results . . . 74
3.6 Stokes V area asymmetry . . . 82
3.7 Magnetic flux tubes and the Evershed flow . . . 83
3.8 A picture of the penumbral fine structure . . . 86
3.9 Summary . . . 87

4 The nature of the Evershed flow **91**
4.1 Introduction . . . 91
4.2 Description of the employed model and inversion process . . . 92
4.3 Observations and data reduction . . . 95
4.4 Results and discussion . . . 98
4.4.1 Example . . . 98
4.4.2 General properties . . . 98
4.5 Size of the penumbral filaments and area asymmetry . . . 101
4.6 Nature of the Evershed Flow . . . 105
4.6.1 General considerations . . . 105
4.6.2 Gas pressure gradient . . . 107
4.6.3 Cooling flux tubes . . . 108
4.6.4 Shock front . . . 110
4.7 Summary and conclusions . . . 113

5 Size of the penumbral filaments **117**
5.1 Introduction . . . 117
5.2 Observations . . . 118
5.3 Inversion results . . . 120
5.3.1 Fitting examples . . . 120
5.3.2 Radial dependences . . . 120
5.4 Size of the Penumbral Flux tubes . . . 122
5.5 Discussion . . . 127
5.6 Conclusions . . . 128

6 MHS equilibrium of thick penumbral filaments **129**
6.1 Introduction . . . 129
6.2 Basic equations and boundary conditions . . . 129
6.3 Pressure and density balance . . . 131
6.4 Potential external field . . . 132
6.5 Non-uniform flux tube field . . . 133

Conclusions **137**

Acknowledgements **145**

Scientific contributions **147**

Lebenslauf **149**

Introduction

Sunspots are the most readily manifestation of the solar magnetism. The main constituents of a sunspot, as seen in continuum images (see e.g. Fig. 1) are a central dark core: *umbra*, which is surrounded by a brighter region characterized by a well organized filamentary structure: *the penumbra* or *penumbrae*. As the spatial resolution of the observations increases, more details about the sunspot fine structure are revealed. The umbra possesses bright points called *umbral dots* and the penumbral filaments can have very bright tails: *penumbral grains*. Sometimes the penumbral structure seems to pour into the umbra forming *light bridges* that eventually can split the umbral region into two parts.

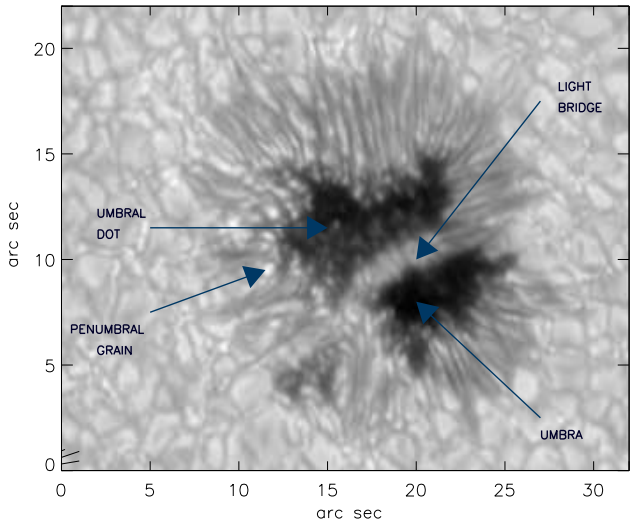

FIGURE 1: Speckle reconstructed broad band continuum image of NOAA 9145 at 7090 Å taken with the Göttingen Fabry Perot Interferometer attached at the German telescope VTT (Izaña observatory). The achieved spatial resolution is about 0.3 arc sec. Many of the different constituents of the umbral and penumbral fine structure can be distinguished: umbral dots, penumbral grains, filamentary penumbral structure and light bridge. *Courtesy of J. Hirzberger & F. Kneer*.

Understanding the formation, evolution, dynamics and magnetic structure of sunspots is key to disentangle the basic physical processes taking place in the solar photosphere. The intense magnetic field in the umbra of sunspots inhibits convection, making it much cooler than the surrounding granulation, and therefore appearing darker. The umbra is believed to be formed when emerging magnetic flux tubes that, stored below the convective region of the Sun, rise until the reach the solar surface. The magnetic field in the penumbra is less than a factor of two smaller than in the umbra, however its brightness is at least four times larger. The physical magnetoconvective mechanism that leads to its formation and explains its enhanced brightness, despite its strong magnetic field, is still unknown. The origin of its filamentary structure and nature of the ubiquitous outflow present in the penumbra (see below) are nowadays, after almost a century since it was discovered, a matter of intense debate and study.

This thesis deals with the study of the fine structure of sunspot penumbrae and their relation with its well known dynamical behaviour: the Evershed effect. It is observed as a shift and asymmetry in spectral lines. The underlying flow is characterized by a blueshift or velocities towards the observer when one looks at the center side of the penumbra (penumbral region closer to the Sun's disk center), but redshift or velocities away from the observer if we observe the limb side (region closer to the solar limb; see Fig. 2).

The Evershed effect is believed to be produced by a plasma flow that is directed from the inner penumbra towards the outer boundary with the quiet Sun. This flow is often explained as siphon flow. If the gas pressure at the outer boundary is smaller than in the inner penumbra, a flow is initiated from the point with larger gas pressure towards the outer penumbra, where the gas pressure is smaller. According to this the flow will be directed outwards as it is observed. However, from spectropolarimetric observations is also well known that the sunspots' magnetic field strength decreases rapidly from the umbra towards the quiet Sun (see Fig. 3). This induces an inwards flow, in contradiction to observations.

In order to try to solve this controversy we shall study the magnetic structure of sunspot penumbrae, taking into account its fine structure, to investigate whether the magnetic field really decreases with radial distance or, as required by the siphon flow mechanism to work, increases. This study has been carried out using spectropolarimetric observations (i.e the full Stokes vector) that, together with inversion techniques, allow the vertical stratification of the temperature, velocity and magnetic field vector to be inferred with great accuracy.

Inversion of Stokes profiles is a powerful tool to investigate solar magnetism and the structure of the solar atmosphere. The basic underlying idea is to produce synthetic profiles using an atmospheric model (which is characterised by the stratifications with optical depth of temperature, strength and direction of the magnetic field vector as well as line-of-sight velocity) by solving the Radiative Transfer Equation. The synthetic profiles are then compared with the observed ones and the original atmosphere is iteratively modified by means of a χ^2 minimization algorithm until a best fit to the observation is achieved. The retrieved atmosphere is then used as the basis of further analyses and interpretations. The concepts and mathematical formulation of the forward problem (synthesis) and the inverse one (inversion) are reviewed in Chapter 1.

The largest uncertainty in this form of analysis is introduced by the fact that the obtained results must be interpreted in terms of the adopted geometrical model for the inversion. In practice the use of different models leads to different inferred properties for the atmosphere whose polarized radiation we measure. This is particularly true for sunspot penumbrae. An exhaustive

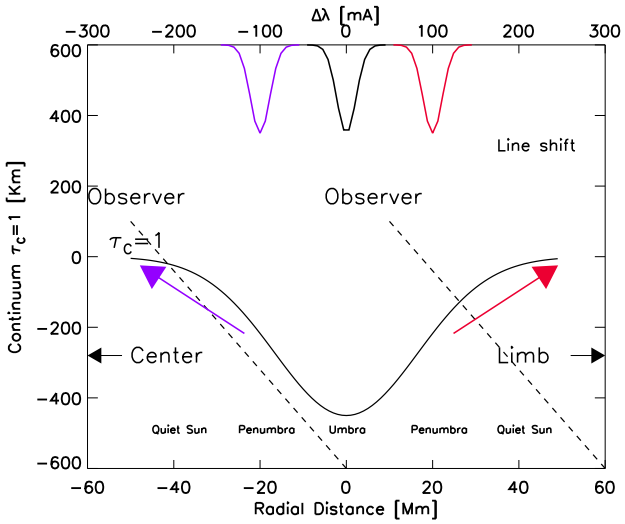

FIGURE 2: Cartoon representing the basic observational feature of the Evershed effect. The Wilson depression of a sunspot is shown in the solid black line as the geometrical height where the continuum $\tau_c = 1$ is formed. The depression achieves the largest values, ~ -400 km in the umbra, where the magnetic field is stronger and more vertical. At the center side of the penumbra the spectral lines are shifted towards shorter wavelengths (blue profile on the top) indicating that there is a flow (blue arrow) towards the observer (inclined dashed lines). At the limb side of the penumbra the shift is towards larger wavelengths (red profile at the top) and therefore the flow (red arrow) is directed away from the observer. This indicates that the Evershed flow is directed radially outwards, from the umbra (where no wavelength shift is observed; see black profile on the top) towards the quiet Sun.

description about the different, often contradictory, results of previous investigations of penumbral structure and dynamics is given in Chapter 2.

Therefore, one of the main aims of this thesis is to investigate sunspot penumbrae using different geometrical models to describe its fine structure. Beyond testing the ability of these models to reproduce the observed polarization signals, we carry out a thorough comparative study of their physical properties and make use of other tools in order to decide which model comes closest to reality. This is the main objective of Chapter 3. There, we conclude that the results arising from different models could in fact be compatible with each other if we assume that the structure of penumbrae is *uncombed* (i.e. two different magnetic structures with different inclinations, along the vertical and horizontal directions, coexist in the resolution element, where the most inclined one carries the Evershed flow). The term *uncombed* is chosen following a similar model already proposed by Solanki & Montavon in the early nineties in order to explain the asymmetry of the observed circular polarization signals (i.e. Stokes V) emerging from sunspot penumbrae.

Chapters 4 and 5 are entirely devoted to presenting the first results from the inversion of spectropolarimetric data using the uncombed model, including force balance. In Chapter 4 the uncombed model is applied to the widely used infrared neutral iron lines located at 1.56 μm,

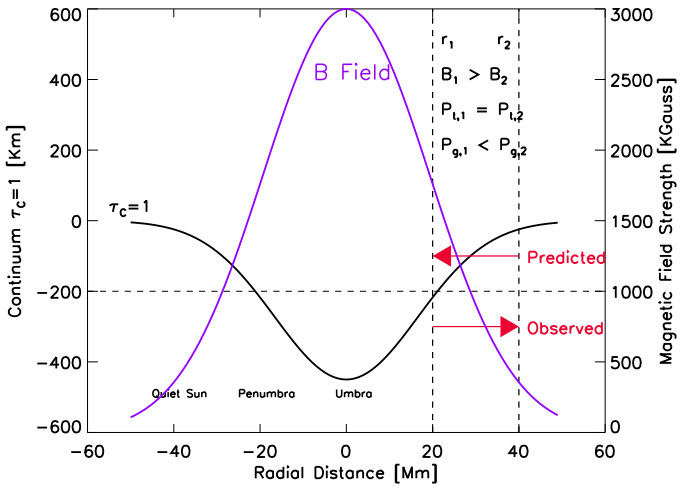

FIGURE 3: Cartoon representing the Wilson depression of a sunspot (black solid line) together with the radial variation of the magnetic field strength (blue solid line). The two vertical dashed lines show the position of two different radial positions on the limb side of the penumbra, r_1 and r_2, with $r_2 > r_1$. The Evershed flow goes from the inner selected point r_1 towards the outer one, r_2. The horizontal dashed line indicates a selected geometrical height z_0, where the gas and magnetic pressure are evaluated. If the magnetic field strength decreases towards the quiet Sun and the total pressure (gas plus magnetic) is equal at all radial distances for a given height, then the gas pressure at the outer point $P_g(r_2)$ is larger than at the inner point $P_g(r_1)$. According to the siphon flow mechanism this initiates an inwards flow, in disagreement with observations.

whereas in Chapter 5 we apply it to commonly used neutral iron spectral lines in the visible spectral range. These two different and complementary studies have revealed the existence of a radial gas pressure gradient along the magnetic structure with a nearly horizontal magnetic field. This result provides the greatest piece of evidence ever reported, supporting the siphon flow models as the physical mechanism that drives the Evershed flow. In particular, it removes a major hurdle facing this otherwise promising model. Furthermore, we have been able, by means of a careful interpretation of the observed polarization signals, to infer typical vertical sizes of the horizontal magnetic structure of about 100-200 km, in close agreement with the horizontal widths of penumbral fibrils deduced from observations with high angular resolution.

The presence of 100 km thick penumbral fibrils has important consequences, in particular those associated with theoretical models and MHD simulations aiming to explain the Evershed effect, since they have always considered fibrils whose diameter is much smaller than the pressure scale height, in direct contradiction to our findings. To overcome the lack of theoretical work in this issue, we have developed in Chapter 6 a simple magnetohydrostatic equilibrium for thick penumbral fibrils that might help as a starting point for further and more complex theoretical work.

Chapter 1

Spectropolarimetry

In this chapter we sketch the theory of spectral line formation in magnetized stellar atmospheres, starting from the definition of the Stokes parameters and the Zeeman effect. We will then write the Radiative Transfer Equation in the presence of a magnetic field, describing its mains constituents. Finally we will introduce the reader to the concepts of inversion of spectral lines/Stokes profiles, describing the common methods employed. In this chapter we will closely follow the approach (as well as the notation) from Wittmann (1974), Rees et al. (1989), Landi Degl'Innocenti (1992) and more recently, del Toro Iniesta (2003a).

1.1 Stokes parameters

1.1.1 Definition

Let us consider a quasi-monochromatic electromagnetic plane wave[1] propagating along the Z-axis. The electric field vector, E, rotates in the plane perpendicular to the direction of propagation. The projections on the X and Y axis are:

$$E_{\rm x}(t) = a_{\rm x}(t)\exp i[\phi_{\rm x}(t) - 2\pi\nu t + 2\pi z/\lambda] \quad (1.1)$$

$$E_{\rm y}(t) = a_{\rm y}(t)\exp i[\phi_{\rm y}(t) - 2\pi\nu t + 2\pi z/\lambda] \quad (1.2)$$

Defining $\delta = \phi_{\rm x} - \phi_{\rm y}$, the rotation of the electric field in the plane XY is said to be counterclockwise if $\sin\delta < 0$ and clockwise if $\sin\delta > 0$. The Stokes parameters are defined as time averages over an entire period:

[1] quasi-monochromatic wave is defined as a superposition of monochromatic waves with different amplitudes distributed over a frequency range $\Delta\nu$ centered at ν_0, where $\nu_0 \gg \Delta\nu$

$$I = < a_{\rm x}^2 > + < a_{\rm y}^2 > \quad (1.3)$$

$$Q = < a_{\rm x}^2 > - < a_{\rm y}^2 > \quad (1.4)$$

$$U = 2 < a_{\rm x} a_{\rm y} \cos\delta > \quad (1.5)$$

$$V = 2 < a_{\rm x} a_{\rm y} \sin\delta > \quad (1.6)$$

These four parameters are often expressed in vectorial form as: $\mathrm{S} = (I,Q,U,V)^T$, where superindex T means transposition. This is the so-called *Stokes vector*. An obvious condition is that the amount of polarized light can not be larger than the total amount of light:

$$I^2 \geqslant Q^2 + U^2 + V^2 \quad (1.7)$$

where the equality is achieved only for a perfect monochromatic wave.

1.1.2 Measuring the Stokes parameters

Measuring the polarization state of the light means to measure the direction of motion of the electric field vector ($a_{\rm x}$ and $a_{\rm y}$), as well as the phase difference between the two Cartesian components of the field. This can be successfully done by means of optical devices. The most widely used components are the *linear polarizer* and *linear retarder*.

- The linear polarizer is an optical system that transmits all the light along a given direction (i.e. optical axis), but reflects or absorbs all the light along its perpendicular direction. Let us, for example assume that the incoming light beam has an electric field $\mathrm{E} = E_{\rm x}\hat{e_{\rm x}} + E_{\rm y}\hat{e_{\rm y}}$. If the optical axis of the linear polarizer is inclined by an angle θ with respect to the X-axis, the outgoing electric field, after passing such a device would be (see Fig 1.1; top panel):

$$\mathrm{E}^{'} = [\mathrm{E}\hat{e_\theta}]\hat{e_\theta} = [E_{\rm x}\cos\theta + E_{\rm y}\sin\theta]\hat{e_\theta} \quad (1.8)$$

- The linear retarder induces a retardance (i.e. a phase lag) δ to one of the Cartesian components of the incoming light beam. In this case the outgoing electric field components are: $E_{\rm x}^{'} = E_{\rm x}$ and $E_{\rm y}^{'} = E_{\rm y}e^{i\delta}$ (see Fig 1.1; bottom panel). The axis where no modification is applied is said to be the *fast axis*, while the axis along which the retardance is imparted is called the *slow axis*.

Let us now assume that we have an incoming light beam, characterized by $E_{\rm x}$ and $E_{\rm y}$. We make it pass through a linear retarder and afterwards through a linear polarizer (both working as previously described). The beam properties after passing through these two optical devices can be described as:

$$\mathrm{E}^{'} = E_\theta\hat{e_\theta} = [E_{\rm x}\cos\theta + E_{\rm y}\sin\theta e^{i\delta}]\hat{e_\theta} \quad (1.9)$$

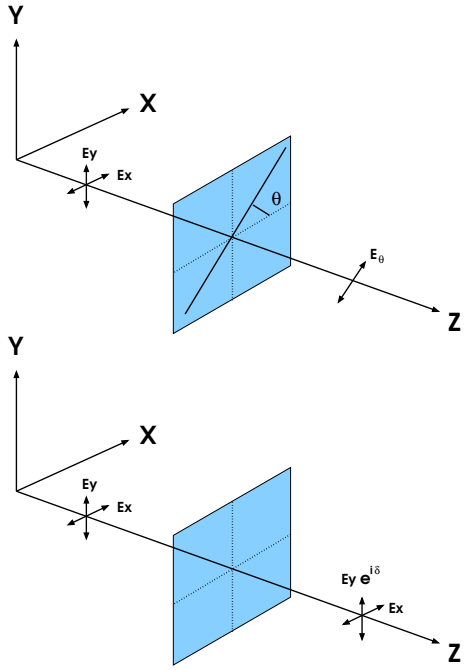

FIGURE 1.1: Top panel: linear polarizer with optical axis at angle θ. Bottom panel: linear retarder with fast axis along the X-coordinate and slow axis along the Y-coordinate.

The intensity we measure in the output beam is

$$I_{\rm mes}(\theta,\delta) = \quad < E_\theta(\theta,\delta)E^*_\theta(\theta,\delta) > \tag{1.10}$$

$$\begin{aligned} I_{\rm mes}(\theta,\delta) = \quad & < E_{\rm x}E^*_{\rm x}\cos^2\theta + E_{\rm y}E^*_{\rm y}\sin^2\theta \\ & + \tfrac{1}{2}E_{\rm x}E^*_{\rm y}\sin 2\theta e^{-i\delta} + \tfrac{1}{2}E^*_{\rm x}E_{\rm y}\sin 2\theta e^{i\delta} > \end{aligned} \tag{1.11}$$

Employing Eq. 1.3-1.6 we can write:

$$< E_{\rm x}E^*_{\rm x} > \;=\; \frac{1}{2}(I+Q) \tag{1.12}$$

$$< E_{\rm y}E^*_{\rm y} > \;=\; \frac{1}{2}(I-Q) \tag{1.13}$$

$$< E_{\rm x}E^*_{\rm y} > \;=\; \frac{1}{2}(U+iV) \tag{1.14}$$

$$< E^*_{\rm x}E_{\rm y} > \;=\; \frac{1}{2}(U-iV) \tag{1.15}$$

This allows us to rewrite Eq. 1.11 in the form:

$$I_{\mathrm{mes}}(\theta,\delta) = \frac{1}{2}(I + Q\cos 2\theta + U\cos\delta\sin 2\theta + V\sin\delta\sin 2\theta) \tag{1.16}$$

The output intensity is a linear combination of the four Stokes parameters. Hence, by changing δ and θ we can determine I,Q,U and V in the following way:

$$\begin{aligned} I &= I_{\mathrm{mes}}(0,0) + I_{\mathrm{mes}}(\pi/2,0) && (1.17)\\ Q &= I_{\mathrm{mes}}(0,0) - I_{\mathrm{mes}}(\pi/2,0) && (1.18)\\ U &= I_{\mathrm{mes}}(\pi/4,0) - I_{\mathrm{mes}}(3\pi/4,0) && (1.19)\\ V &= I_{\mathrm{mes}}(\pi/4,\pi/2) - I_{\mathrm{mes}}(3\pi/4,\pi/2) && (1.20) \end{aligned}$$

- I represents the sum of the measured intensities transmitted through 2 linear polarizers whose transmission axes are mutually orthogonal: $\theta = 0^\circ$ and $\theta = 90^\circ$.
- Q is the difference between the measured intensities transmitted through two linear polarizers at $\theta = 0^\circ$ and $\theta = 90^\circ$.
- U represents the difference between the measured intensities transmitted through two linear polarizers at $\theta = 45^\circ$ and $\theta = 135^\circ$.
- V is the difference between the measured intensities transmitted through a quarter-wave linear retarder, followed by two linear polarizers at $\theta = 45^\circ$ and $\theta = 135^\circ$, respectively.

1.2 Zeeman effect

The Hamiltonian of an electron in a atom is characterized by the kinetic and electrostatic interaction with the nuclear charge. If the atom is multi-electronic the Coulomb interactions with the rest of the electronic cloud must be also considered. A general approach is to consider that the electron is subject to an averaged electrostatic interaction (sum of the attraction with the nuclear charge and the repulsions from the other electrons) that possesses spherical symmetry.

There are more interactions that must be taken into account. In particular the spin-orbit interaction, which couples the spin angular momentum of the electron *S* with the orbital angular momentum *L* into the total angular momentum of the electron *J*.

The application of an external agent along a given direction introduces a preferred direction that breaks the spherical symmetry. If this external agent is the magnetic field, the new Hamiltonian of the system should include a new term to account for the interaction of the magnetic moment of the electron with the magnetic field, $\mathrm{H} = \mathrm{H_C} + \mathrm{H_{LS}} + \mathrm{H_B}$, where $\mathrm{H_C}$ represents the Hamiltonian of the electron only affected by the Coulomb interaction and $\mathrm{H_{LS}}$ represents the coupling between the spin angular momentum and the orbital angular momentum. The interaction between the external magnetic field and the magnetic moment of the electron is denoted by $\mathrm{H_B}$

$$\begin{aligned} \mathrm{H_B} &= \mu B && (1.21)\\ \mu &= \mu_0(J+S) && (1.22)\\ \mu_0 &= \frac{e\hbar}{2m_e c} && (1.23) \end{aligned}$$

The terms $\mathrm{H_{LS}}$ and $\mathrm{H_B}$ are much smaller in magnitude than $\mathrm{H_C}$. Therefore a simple perturbation analysis yields the new energy levels. Three possibilities can be distinguished:

1. $\mathrm{H_{LS}} \gg \mathrm{H_B}$ (weak magnetic field): the energy associated with the spin-orbit interaction is much greater. Therefore, the energy levels should be calculated, first, considering $\mathrm{H_{LS}}$ as a perturbation to $\mathrm{H_C}$, and later $\mathrm{H_B}$ to $\mathrm{H_C} + \mathrm{H_{LS}}$. This is the *Zeeman regime*.

2. $\mathrm{H_B} \gg \mathrm{H_{LS}}$ (strong magnetic field): the energy associated with the interaction with the external magnetic field is much greater that the spin-orbit interaction. In this case we must first consider $\mathrm{H_B}$ as a perturbation to $\mathrm{H_C}$ and later $\mathrm{H_{LS}}$ to $\mathrm{H_C} + \mathrm{H_B}$. This is the so-called *Paschen-Back regime*.

3. $\mathrm{H_B} \sim \mathrm{H_{LS}}$ leads to consider directly $\mathrm{H_{LS}} + \mathrm{H_B}$ as a perturbation to $\mathrm{H_C}$. This is the intermediate regime.

For intermediate/large nuclear charges, the spin-orbit interaction is dominant over the interaction with the external magnetic field. In this situation, the base $\{L^2, S^2, J^2, J_\mathrm{k}\}$, with J_k being the projection of the total angular momentum along the direction of the magnetic field, forms a complete set of observable quantities. The energy corrections, due to the interaction with the magnetic field, can be written as:

$$\mathrm{H_B}|\mathrm{nlsjm}\rangle = Mg\frac{e\hbar B}{2m_e c}|\mathrm{nlsjm}\rangle \qquad (1.24)$$

Where e represent the electron charge and $\mathrm{m_e}$ its mass. B is the magnetic field strength, $\hbar$ is the Planck's constant divided by 2π and c is the speed of light. The quantum number M represents the possible values for J_k. Finally, g is the so-called Landé factor, which in LS coupling has the form,

$$g = \begin{cases} \frac{3}{2} + \frac{S(S+1)-L(L+1)}{2J(J+1)} & : \text{ if J} \neq 0 \\ 0 & : \text{ Otherwise} \end{cases} \qquad (1.25)$$

This energy correction turns out to depend on the quantum number M, which indicates the projection of the total angular momentum on the direction where the magnetic field is applied. The dependence of the energy on this quantum number degenerates the energy levels, which in the unperturbed case depended only on J, into $2J+1$ sublevels with possible values for $M = -J, ..., +J$. This phenomenon is known as the *Zeeman effect*. Classical electrodynamics considerations (i.e. Lorentz's theory of the electron) can account for the case of the *normal Zeeman effect*, that is produced in a transition $J_\mathrm{u} = 0 \rightarrow J_\mathrm{l} = 1$ or vice versa. For other quantum numbers, *anomalous Zeeman effect*, the quantum mechanical approach is mandatory.

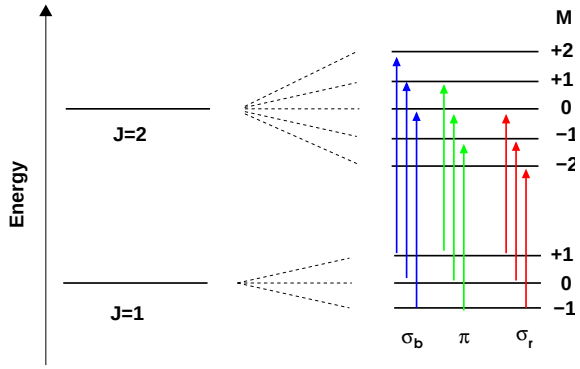

FIGURE 1.2: Allowed transitions between the Zeeman split levels of two energy levels with $J_u = 2$ and $J_l = 1$. σ_b components ($\Delta M = 1$) are indicated with blue colour. σ_r components ($\Delta M = -1$) are indicated with red colour. π components ($\Delta M = 0$) are in green colour.

New transitions can appear between these new energy levels. For electric dipole transitions the selection rules $\Delta J = J_u - J_l = 0, \pm 1$ and $\Delta M = M_u - M_l = 0, \pm 1$ apply. Transitions having $\Delta M = 0$ are called π-components, while $\Delta M = \pm 1$ transitions give rise to the σ_b and σ_r components, respectively. The index *r* and *b* are used to indicate that the wavelength corresponding to the transition is shifted towards longer or shorter values with respect to the unperturbed central π transition (i.e. it has the same wavelength as the original one). This shift can be written as:

$$\Delta\lambda = \frac{e\lambda_0^2 B}{4\pi m_e c}(g_l M_l - g_u M_u) \tag{1.26}$$

where indexes u and l stand for the upper and lower energy levels. Note that the classification in σ_r and σ_b is done in the sense that, according to Eq. 1.26, the σ_r ($M_u - M_l = -1$)) is shifted to the red (neglecting the Landé factors), while σ_b ($M_u - M_l = +1$) is shifted to the blue. In general we have:

- $N_p = 2J_{min} + 1$ π-transitions: $\Delta M = 0$
- $N_b = J_u + J_l$ σ_b-transitions: $\Delta M = +1$
- $N_r = J_u + J_l$ σ_r-transitions: $\Delta M = -1$

Fig. 1.2 shows an example of the allowed transitions for an original transition $J = 1 \rightarrow J = 2$. Each possible transition corresponds to one component of the Zeeman pattern.

Let $N_{p,b,r}$ denote the number of Zeeman components of each type according to the ΔM value of the transition. The strength of the various Zeeman components are normalized individually for each kind of transition, according to their ΔM. The normalized strengths can be written as:

$$s_{i_j} = S_{i_j}\left(\sum_{i_j=1}^{N_j} S_{i_j}\right)^{-1} \tag{1.27}$$

TABLE 1.1: Unnormalized strengths S_{ij} for the different Zeeman components

	$\Delta M=+1$ (σ_b)	$\Delta M=0$ (π)	$\Delta M=-1$ (σ_b)
$\Delta J=+1$	$(J_u+M_u)(J_l+M_u)$	$2(J_u^2-M_u^2)$	$(J_u-M_u)(J_l-M_u)$
$\Delta J=0$	$(J_u+M_u)(J_u-M_u+1)$	$2M_u^2$	$(J_u-M_u)(J_u+M_u+1)$
$\Delta J=-1$	$(J_l-M_u)(J_u-M_u+2)$	$2(J_l^2-M_u^2)$	$(J_l+M_u)(J_u+M_u+2)$

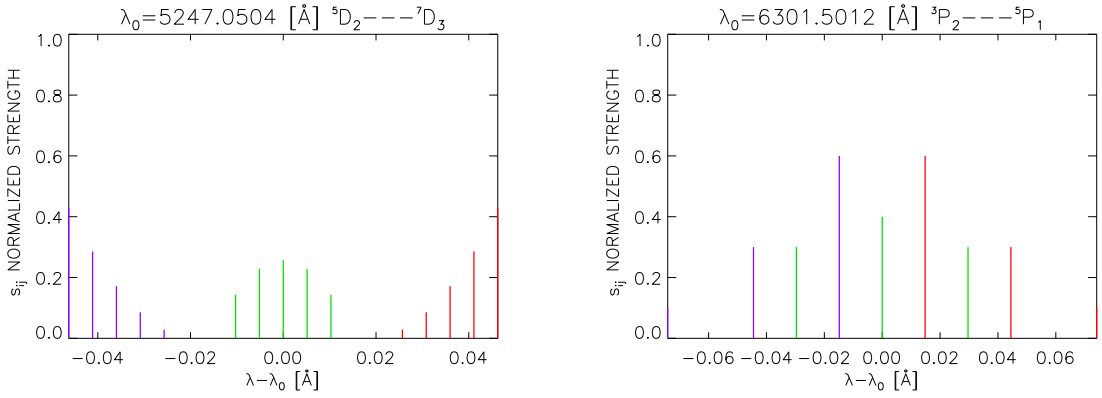

FIGURE 1.3: Zeeman patterns for the neutral iron lines (Fe I) at 5247.05 Å (left panel) and 6301.50 Å (right panel). The atomic configurations are ${}^5D_2-{}^7D_3$ (g_{eff}=2) and ${}^3P_2-{}^5P_1$ ($g_{eff}=1.67$) respectively. Both patterns were calculated for a field strength of 1500 gauss. Colours are as in Fig. 1.2

where $j=p,b,r$; $i_p=1,...,N_p$; $i_b=1,...,N_b$ and $i_r=1,...,N_r$. The unnormalized strengths S_{ij} are given in Table 1.1.

The simplest Zeeman pattern occurs when either $J_u=0$, $J_l=0$ or both Landé factors are equal. In this case only one σ_r, one σ_b and one π component is present (i.e. a normal Zeeman triplet). In general, the fine structure of the Zeeman pattern cannot be resolved. Therefore, in some cases it is useful to treat them as *effectives normal Zeeman triplets* having an unshifted π component and two symmetrical σ components shifted by

$$\Delta\lambda=\frac{e\lambda_0}{4\pi m_e c}g_{eff}B \tag{1.28}$$

where the effective Landé factor g_{eff} is independent of the coupling scheme used, and can be written as follows:

$$g_{eff}=\frac{1}{2}(g_l+g_u)+\frac{1}{4}(g_l-g_u)[J_l(J_l+1)-J_u(J_u+1)] \tag{1.29}$$

This approach is very useful whenever the Russell-Saunders coupling scheme (LS coupling) is not valid. This is the case for heavy atoms (i.e. with very large nuclear charge) or transitions

between highly excited levels, where the spin-orbit interactions become as strong as the interactions between individual spins or orbital angular momenta. In these situations, intermediate or JJ coupling should be used instead. Unfortunately there are no explicit derivations of the interaction energy H_B (Eq. 1.24) or the Landé factors for the upper and lower levels (Eq. 1.25) in these cases. Then it is convenient to treat these cases as effective normal Zeeman triplets.

1.2.1 Molecular Zeeman effect

The Zeeman effect in molecular lines has been less investigated than its atomic counterparts (Kroning 1928; Hill 1929; Crawford 1934; Schadee 1978). However, its great applicability to the study of the solar surface, as well as cool stars, is beyond any question. Berdyugina & Solanki (2002), Berdyugina et al. (2003) have offered a comprehensible compilation of the molecular Zeeman effect for astrophysical purposes, improving and removing some errors in previous calculations.

The basic idea is to consider the interaction of the total angular momentum **J** (composition of the total electronic angular momentum and the nucleus rotational momentum) with the external magnetic field. Depending whether the spin angular momentum of the electron, **S**, is coupled strongly or not with the nuclear axis two cases (Hund's cases *a* and *b*) can be distinguished. Analogues formulas for the energy splitting (Eq. 1.26)), Landé factors (Eq. 1.25) and the strength of the Zeeman components (Table 1.1) can be found for Hund's pure cases *a* and *b* as well as intermediate coupling cases in Berdyugina & Solanki (2002).

1.3 Radiative Transfer Equation

The Radiative Transfer Equation (RTE) in the presence of a magnetic field was first derived by Unno (1956) using classical electrodynamics arguments. It was later extended by Rachkovsky (1962a,1962b) to include magneto-optical effects and by Beckers (1969a,1969b) to treat arbitrary Zeeman patterns. The first derivation using more general quantum mechanical principles is due to Landi Degl'Innocenti (1983). The RTE describes how energy (i.e. a polarized light beam) is transmitted through a medium where a magnetic field is present, taking into account how the magnetic field modifies the polarization state of the light. A widely used expression for the RTE is[2]

$$\frac{\mathrm{d}\mathbf{I}(\mathrm{z})}{\mathrm{dz}} = -\hat{\mathcal{K}}\left[\mathbf{I}(\mathrm{z}) - \mathbf{S}(\mathrm{z})\right] \tag{1.30}$$

where **I** is the Stokes vector $\mathbf{I} = (I,Q,U,V)$ emerging from the solar or stellar. The source function vector $\mathbf{S}(\mathrm{z})$ is, under LTE, the Planck function with a temperature corresponding to a local height *z* in the atmosphere, $\mathbf{B}(\mathrm{T}(\mathrm{z}))$. Its radiation field is unpolarized: $\mathbf{S}(\mathrm{z}) = (\mathrm{B}(\mathrm{z}),0,0,0)$. The matrix $\hat{\mathcal{K}}$, the so-called *absorption matrix*, can be decomposed into continuum and line contributions

[2]We consider here the Z-axis, the direction of propagation of the light, to be perpendicular to the solar-stellar surface.

$$\hat{\mathcal{K}} = \chi_c \mathbb{1} + \hat{\chi}_{lin} \tag{1.31}$$

where χ_c is the *continuum absorption coefficient*, $\mathbb{1}$ is the 4×4 unity matrix and $\hat{\chi}_{lin}$ is the *line absorption matrix*. The last matrix can be redefined as:

$$\hat{\chi}_{lin} = \chi_{lin}\hat{\phi} = \frac{h\nu}{4\pi}(n_l B_{lu} - n_u B_{ul})\hat{\phi} \tag{1.32}$$

where n_l and n_u denote the total populations of the lower and upper levels of the transition respectively. h is Planck's constant. B_{ij} stands for the Einstein coefficient of the transition $i \rightarrow j$ and $h\nu$ is its associated energy. With these definitions the RTE adopts a new form:

$$\frac{d\mathbf{I}(z)}{dz} = -\chi_c \left[\mathbb{1} + \frac{\chi_{lin}}{\chi_c}\hat{\phi}\right][\mathbf{I}(z) - \mathbf{S}(z)] \tag{1.33}$$

Introducing the *optical depth scale*: $d\tau_c = -\chi_c dz$, and defining the *line to continuum absorption coefficient*: $\eta_0 = \frac{\chi_{lin}}{\chi_c}$, we can write:

$$\frac{d\mathbf{I}(\tau_c)}{d\tau_c} = \left[\mathbb{1} + \eta_0\hat{\phi}\right][\mathbf{I}(\tau_c) - \mathbf{S}(\tau_c)] \tag{1.34}$$

To obtain the final form of the RTE, we will finally redefine the *propagation matrix* as:

$$\hat{\mathcal{K}} = \mathbb{1} + \eta_0\hat{\phi} \tag{1.35}$$

This gives us

$$\frac{d\mathbf{I}(z)}{d\tau_c} = \hat{\mathcal{K}}[\mathbf{I}(\tau_c) - \mathbf{S}(\tau_c)] \tag{1.36}$$

In vectorial form the RTE would be:

$$\frac{d}{d\tau_c}\begin{pmatrix} I \\ Q \\ U \\ V \end{pmatrix} = \begin{pmatrix} \eta_I & \eta_Q & \eta_U & \eta_V \\ \eta_Q & \eta_I & \rho_V & -\rho_U \\ \eta_U & -\rho_V & \eta_I & \rho_Q \\ \eta_V & \rho_U & -\rho_Q & \eta_I \end{pmatrix}\begin{pmatrix} I-B \\ Q \\ U \\ V \end{pmatrix} \tag{1.37}$$

The elements of the propagation matrix are expressed as:

$$\eta_{\rm I} = 1+\frac{\eta_0}{2}\left(\phi_p\sin^2\gamma+\frac{1}{2}[\phi_b+\phi_r](1+\cos^2\gamma)\right) \quad (1.38)$$

$$\eta_{\rm Q} = \frac{\eta_0}{2}\left(\phi_p-\frac{1}{2}[\phi_b+\phi_r]\right)\sin^2\gamma\cos 2\varphi \quad (1.39)$$

$$\eta_{\rm U} = \frac{\eta_0}{2}\left(\phi_p-\frac{1}{2}[\phi_b+\phi_r]\right)\sin^2\gamma\sin 2\varphi \quad (1.40)$$

$$\eta_{\rm V} = \frac{\eta_0}{2}[\phi_r-\phi_b]\cos\gamma \quad (1.41)$$

$$\rho_{\rm Q} = \eta_0\left(\psi_p-\frac{1}{2}[\psi_b+\psi_r]\right)\sin^2\gamma\cos 2\varphi \quad (1.42)$$

$$\rho_{\rm U} = \eta_0\left(\psi_p-\frac{1}{2}[\psi_b+\psi_r]\right)\sin^2\gamma\sin 2\varphi \quad (1.43)$$

$$\rho_{\rm V} = \frac{\eta_0}{2}[\psi_r-\psi_b]\cos\gamma \quad (1.44)$$

The absorption and anomalous dispersion profiles are given by:

$$\phi_j = \sum_{i_j=1}^{N_j} s_{i_j}H(a,\nu+\nu_D+\nu_{i_j}) \quad (1.45)$$

$$\psi_j = 2\sum_{i_j=1}^{N_j} s_{i_j}F(a,\nu+\nu_D+\nu_{i_j}) \quad (1.46)$$

In these two last equations the index j runs for r,p,b as in equations 1.38-1.44. The summation over $i_j = 1,...,{\rm N}_j$ indicates that the absorption/profiles are calculated taking into account all the the $\sigma_{\rm r}$, π and $\sigma_{\rm b}$ components of the Zeeman pattern (Sect. 1.2). s_{i_j} are the normalized strength for each component as given by Eq. 1.27. H and F functions are the Voigt and Faraday functions evaluated for a given damping a and at a given distance from line center, λ_0, in units of Doppler width, $\nu = \frac{\lambda-\lambda_0}{\Delta\lambda_D}$. However it has to be taken into account that for each component of the Zeeman pattern, the central position is shifted by two quantities: ν_D and ν_{i_j}. The first quantity affects all the Zeeman components equally and it denotes the wavelength shift produced by a net macroscopic velocity along the vertical axis (i.e. Doppler effect).

$$\nu_{\rm D} = \frac{{\rm v_z}\lambda_0}{{\rm c}\Delta\lambda_{\rm D}} \quad (1.47)$$

The second quantity, ν_{i_j} takes into account that for each component of the Zeeman pattern, its absorption/dispersion profile is shifted, due to the Zeeman splitting by an amount: $\nu_{i_j} = \frac{\Delta\lambda_{i_j}}{\Delta\lambda_D}$, where $\Delta\lambda_{i_j}$ is given by Eq. 1.26.

$$\Delta\lambda_{i_j} = \frac{e\lambda_0^2 B}{4\pi m_{\rm e}c}(g_{\rm l}M_{\rm l}-g_{\rm u}M_{\rm u})_{i_j} \quad (1.48)$$

The damping a and the Doppler width $\Delta\lambda_D$ are expressed as follows:

$$a = \frac{\lambda_0^2}{4\pi c\Delta\lambda_D}(\Gamma_{\rm rad}+\Gamma_{\rm col}) \tag{1.49}$$

$$\Delta\lambda_D = \frac{\lambda_0}{c}\left(\frac{2KT}{M}+v_{\rm mic}^2\right)^{1/2} \tag{1.50}$$

where $\Gamma_{\rm rad}$ and $\Gamma_{\rm col}$ describe the line broadening parameters due to the radiative lifetime of the energy levels and due to collisions with external perturbers. The Doppler width is evaluated for a given temperature T and microturbulent velocity $v_{\rm mic}$.

The Voigt, H,and Faraday, F, functions are:

$$H(a,\nu') = \frac{a}{\pi}\int_{-\infty}^{\infty}\frac{e^{-y^2}}{(\nu'-y)^2+a^2}{\rm dy} \tag{1.51}$$

$$F(a,\nu') = \frac{1}{2\pi}\int_{-\infty}^{\infty}\frac{(\nu'-y)e^{-y^2}}{(\nu'-y)^2+a^2}{\rm d}y \tag{1.52}$$

Finally, the angles γ and φ appearing in Eq. 1.38-1.44 indicate the orientation of the magnetic field vector, with γ, the angle between the magnetic field vector and the observer, and φ the angle of the projection the magnetic field vector onto the plane perpendicular to the observer (see Fig 1.4). Note that when the observer's viewing angle is not aligned with the vertical axis on the surface (Z-axis; see footnote in page 10), the RTE has the form:

$$\mu\frac{{\rm d}\mathbf{I}({\rm z})}{{\rm dz}} = -\hat{\mathcal{K}}\left[\mathbf{I}({\rm z})-\mathbf{S}({\rm z})\right] \tag{1.53}$$

where $\mu=\cos\theta$, being θ the angle between the observer's line of sight and the Z-axis (e.g. heliocentric angle). In this case the RTE as presented in Eq. 1.36 keeps the same form by just defining the optical depth scale along the line of sight as: ${\rm d}\tau_{\rm c}^{\rm los}=-(\chi_{\rm c}/\mu){\rm dz}$. In addition, Eq. 1.47 must be also modified as ${\rm v_z}\rightarrow{\rm v_{los}}$.

1.4 Formal solution of the RTE

1.4.1 Symmetries

In the absence of gradients in the kinematic and magnetic properties of the atmosphere (namely the propagation matrix $\hat{\mathcal{K}}$ in Eq. 1.30), i.e. in the line of sight velocities (Eq. 1.47), magnetic field strength (Eq. 1.48) and orientation (Eq. 1.38-1.44), the solution of the RTE possesses the following symmetries:

$$I(\lambda-\lambda_0) = I(\lambda_0-\lambda) \tag{1.54}$$

$$Q(\lambda-\lambda_0) = Q(\lambda_0-\lambda) \tag{1.55}$$

$$U(\lambda-\lambda_0) = U(\lambda_0-\lambda) \tag{1.56}$$

$$V(\lambda-\lambda_0) = -V(\lambda_0-\lambda) \tag{1.57}$$

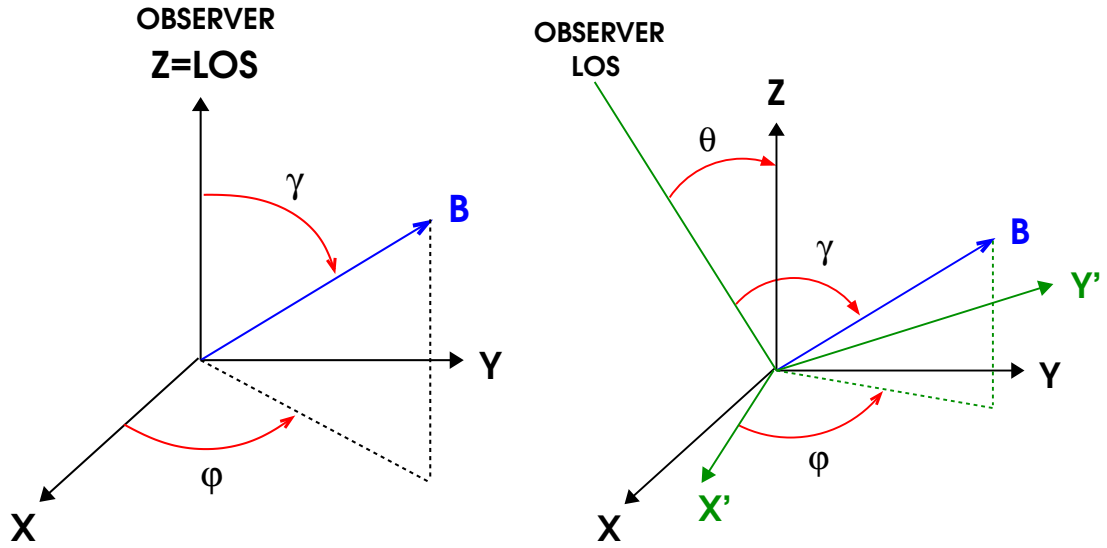

FIGURE 1.4: Schematic representation of the angles that define the magnetic field vector orientation in the observer's reference frame. *Left panel*: case when the observer is aligned with the vertical to the solar surface (i.e. observations on the disk center). *Right panel*: case when the observer is inclined an angle θ with respect to the vertical (i.e observations out of the disk center).

This means that the net circular polarization (NCP) is zero if no gradients are present:

$$\int_{-\infty}^{\infty} V(\lambda-\lambda_0)\mathrm{d}\lambda = 0 \tag{1.58}$$

As soon as the NCP is found not to be zero, gradients in the mentioned physical quantities are known to be present in the atmosphere. This is a potentially powerful diagnostic tool (see Sect. 2.2.2)

1.4.2 Evolution Operator

Let us introduce the *evolution operator* $\hat{O}(\tau_c,\tau_c')$. This operator has the ability to transform the Stokes vector as seen at a given optical depth τ_c to another optical depth location τ_c' in the absence of emission processes along the path between these two points.

$$\mathbf{I}^*(\tau_c) = \hat{O}(\tau_c,\tau_c')\mathbf{I}^*(\tau_c') \tag{1.59}$$

where the index * denotes the solution for the homogeneous equation (i.e. the source function in Eq. 1.36 is neglected and the differential equation becomes homogeneous). The evolution operator fullfills the two following properties:

$$\hat{O}(\tau_c,\tau_c) = \mathbb{1} \tag{1.60}$$
$$\hat{O}(\tau_c,\tau_c'') = \hat{O}(\tau_c,\tau_c')\hat{O}(\tau_c',\tau_c'') \tag{1.61}$$

$\hat{O}(\tau_c, \tau_c')$ can be used as an integration factor of the non-homogeneous differential equation 1.36 to obtain:

$$\mathbf{I}(\tau_1) = \hat{O}(\tau_1, \tau_0)\mathbf{I}(\tau_0) - \int_{\tau_0}^{\tau_1} \hat{O}(\tau_1, \tau_c)\hat{\mathcal{K}}(\tau_c)\mathbf{S}(\tau_c)d\tau_c \tag{1.62}$$

where τ_0 and τ_1 are two optical depth points, indicating the bottom and top of the considered medium. The observer is located at $\tau_1 = 0$. The first term in Eq. 1.62 indicates the radiation entering the medium at the inner boundary τ_0 *evolves* until it is observed in τ_1. If this inner point is chosen to be deep enough ($\tau_0 \to \infty$), then the atmosphere is so optically thick that no photons emitted at τ_0 are able to reach the top of the medium:

$$\lim_{\tau_0 \to \infty} \hat{O}(0, \tau_0)\mathbf{I}(\tau_0) = 0 \tag{1.63}$$

The second term in Eq. 1.62 takes into account all possible emissions at each infinitesimally thin layer between the inner and outermost boundaries, and how they evolve to the next one until the observation point is reached. Applying Eq. 1.62 into 1.61 we obtain the final formal solution of the RTE:

$$\mathbf{I}(0) = \int_0^{\infty} \hat{O}(0, \tau_c)\hat{\mathcal{K}}(\tau_c)\mathbf{S}(\tau_c)d\tau_c \tag{1.64}$$

The solution of the RTE as presented in Eq. 1.64 may look easy to evaluate, but in practice is plagued with difficulties. First of all, for the evaluation of the absorption matrix $\hat{\mathcal{K}}(\tau_c)$, we must know the populations of the atomic levels participating in the transition (Eq. 1.32). These populations depend, in the general case of Non Local Thermodynamic equilibrium (NLTE), on the radiation field itself, because the atomic transitions are induced partially by the incident photons. This self dependence implies that Eq. 1.64 needs to be solved iteratively. When the collisions in the plasma are strong enough, the atomic populations are no longer coupled with the radiation field, but with the local temperature (LTE). In this case Eq. 1.32 can be solved using the Boltzmann equation, thus simplifying the problem to a large extend. Even now, there are no analytical means to know the evolution operator $\hat{O}(0, \tau_c)$, and therefore it must be evaluated numerically. From its properties (Eq. 1.59-1.61) the following differential equation for $\hat{O}(\tau_c, \tau_c')$ can be derived:

$$\frac{d\hat{O}(\tau_c, \tau_c')}{d\tau_c} = \hat{\mathcal{K}}(\tau_c)\hat{O}(\tau_c', \tau_c) \tag{1.65}$$

Eq. 1.65 can not be readily integrated to obtain the evolution operator, namely because the exponential of a matrix is given by its Taylor expansion and matrixes do not necessarily commute (see del Toro Iniesta 2003a). Thus, in general we **can not** write

$$\hat{O}(0, \tau_c) = e^{-\int_0^{\tau_c} \hat{\mathcal{K}}(t)dt} \tag{1.66}$$

Therefore, numerical approaches are needed. Numerical integrations of the RTE have been carried out in the past using the fourth-order Runge-Kutta algorithm (Wittmann 1974). Other strategies apply Feautrier's method (1964). One of the most widely used algorithms is the Diagonal Element Lambda Operator (DELO: Rees et al. 1989) that has the advantage to provide an approximation to the evolution operator with no extra cost when the RTE is solved. Improvements, based on larger order Taylor expansions of the Stokes vector have been carried out by Auer (1976) and Bellot Rubio et al. (1998).

1.4.3 Milne-Eddington approximation

There are few exceptions when the solution of Eq. 1.65 is given by Eq. 1.66. A well known one is the unidimensional case when no polarization is considered ($Q = U = V = 0$). As soon as a magnetic field is present, things become more complicated. However, if the absorption matrix can be written as:

$$\hat{\mathcal{K}}(\tau_c) = \hat{\mathcal{K}}_0 f(\tau_c) \tag{1.67}$$

Eq. 1.66 holds and Eq. 1.65 can be integrated to obtain.

$$\hat{O}(0,\tau_c) = e^{-\int_0^{\tau_c} \hat{\mathcal{K}}(t)dt} \tag{1.68}$$

The simplest case when this can be done is when:

$$\hat{\mathcal{K}}(\tau_c) = \hat{\mathcal{K}}_0 \tag{1.69}$$

This is the so-called *Milne-Eddington approximation*. It requires the absorption matrix to be constant throughout the atmosphere. In other words: inclination angles of the magnetic field vector (γ and φ) that enter into Eq. 1.38-1.44, as well as damping parameter a, line of sight velocity $V_{\rm los}$, and magnetic field strength B, that enter into Eq. 1.45-1.46, must be constant with optical depth. In addition, the line-to-continuum absorption coefficient η_0 must be also constant with optical depth.

A further assumption is to consider that the source function varies linearly with optical depth:[3]

$$\mathbf{S}(\tau_c) = (S_0 + S_1\tau_c, 0, 0, 0)^T \tag{1.70}$$

With this, Eq. 1.64 is reduced to:

$$\mathbf{I}(0) = \int_0^\infty e^{-\hat{\mathcal{K}}_0\tau_c} \hat{\mathcal{K}}_0 (S_0 + S_1\tau_c) d\tau_c \tag{1.71}$$

[3] As pointed out in Sec. 1.3, the source function in LTE approximation is the Planck function with a local temperature T, $\mathbf{S}(\tau_c) = (\mathrm{B}(\tau_c), 0, 0, 0)$.

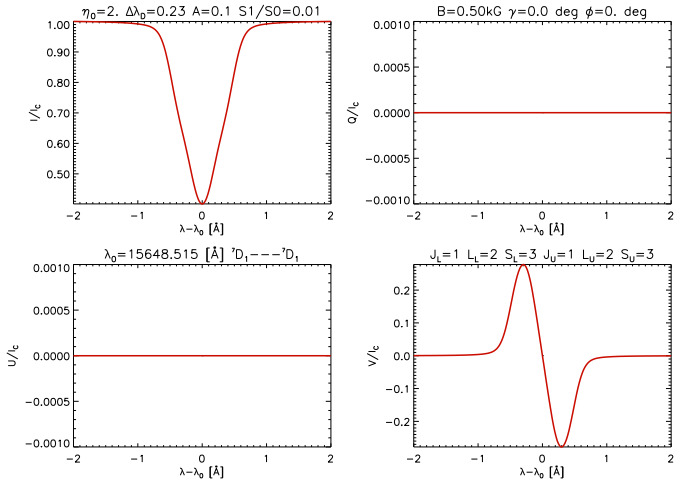

FIGURE 1.5: Milne-Eddington synthesis of the Fe I 15648.5 Å line. The employed parameters are: $\eta_0 = 2$, $\Delta\lambda_D = 0.23$, $a = 0.1$ and $S_1/S_0 = 0.01$, $\gamma = 0$, $\varphi = 0$, $B = 500$ G. Stokes Q and U are zero because the magnetic field is parallel to the observer. The magnetic field is not strong enough to make the σ and σ_b components to be fully split: there is only a broadening of the line.

This last form of the RTE in the Milne-Eddington approximation has the advantage that can be solved by parts analytically (Landi Degl'Innocenti 1992), finally yielding:

$$I(0) = S_0 + \frac{\eta_I}{\Delta}[\eta_I^2 + \rho_Q^2 + \rho_U^2 + \rho_V^2]S_1 \tag{1.72}$$

$$Q(0) = -\frac{S_1}{\Delta}[\eta_I^2\eta_Q + \eta_I(\eta_V\rho_U - \eta_U\rho_V) + \rho_Q\Pi] \tag{1.73}$$

$$U(0) = -\frac{S_1}{\Delta}[\eta_I^2\eta_U + \eta_I(\eta_Q\rho_V - \eta_V\rho_Q) + \rho_U\Pi] \tag{1.74}$$

$$V(0) = -\frac{S_1}{\Delta}[\eta_I^2\eta_V + \eta_I(\eta_U\rho_Q - \eta_Q\rho_U) + \rho_V\Pi] \tag{1.75}$$

where

$$\Delta = \eta_I^2(\eta_I^2 - \eta_Q^2 - \eta_U^2 - \eta_V^2 + \rho_Q^2 + \rho_U^2 + \rho_V^2) - \Pi^2 \tag{1.76}$$

$$\Pi = \eta_Q\rho_Q + \eta_U\rho_U + \eta_V\rho_V \tag{1.77}$$

For visualization purposes we have synthetized the Fe I line at 15648.5 Å ($^7D_1 - ^7D_1$; $g_{\rm eff} = 3$) with different values of the magnetic field strength and inclination angles (see Fig. 1.5,1.6,1.7 and 1.8). The very different polarization profiles obtained should be understood as a powerful tool, to unequivocally determine the magnetic field vector from the observation of the Stokes parameters (see Sect. 1.5).

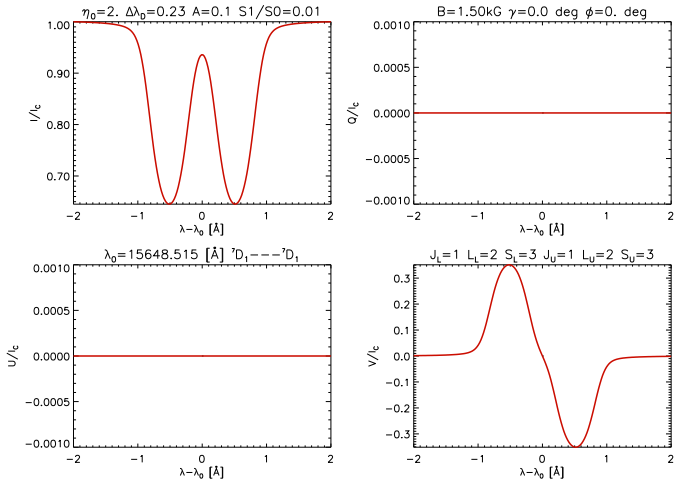

FIGURE 1.6: Milne-Eddington synthesis of the Fe I 15648.5 Å line. The employed parameters are: $\eta_0 = 2$, $\Delta\lambda_D = 0.23$, $a = 0.1$ and $S_1/S_0 = 0.01$, $\gamma = 0$, $\varphi = 0$, $B = 1500$ G. Stokes Q and U are zero because the magnetic field is parallel to the observer. The magnetic field is now strong enough to make the σ_r and σ_b components to be completely split in Stokes I. Note that in Stokes I the central π component does not appear because $\gamma = 0$, hence, in Eq. 1.38, $\phi_p \sin^2\gamma = 0$ and therefore it does not contribute in η_I or Stokes I (Eq. 1.72; compare with Fig. 1.5).

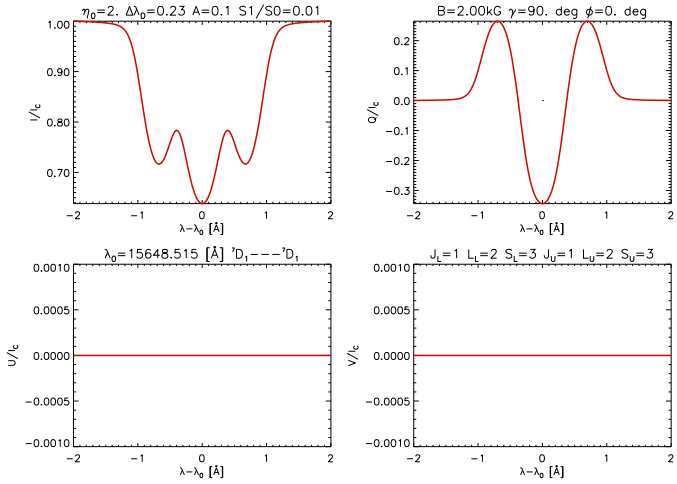

FIGURE 1.7: Milne-Eddington synthesis of the Fe I 15648.5 Å line. The employed parameters are: $\eta_0 = 2$, $\Delta\lambda_D = 0.23$, $a = 0.1$ and $S_1/S_0 = 0.01$, $\gamma = 90$, $\varphi = 0$, $B = 2000$ G. Stokes V is zero because the magnetic field is perpendicular to the observer. In addition, Stokes U is zero because $\varphi = 0$ and thus, η_U also vanishes (see Eq. 1.40). The magnetic field is strong enough to make the σ_r and σ_b components to be completely split from the central π component in Stokes I, which now appears because in Eq. 1.38, $\phi_p \sin^2\gamma \neq 0$ and therefore having a net contribution in Stokes I (see Eq. 1.72; compare with Fig. 1.6).

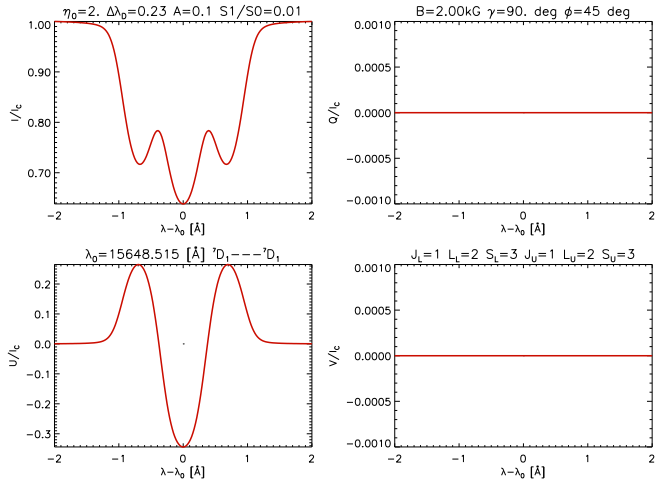

FIGURE 1.8: Milne-Eddington synthesis of the Fe I 15648.5 Å line. The employed parameters are: $\eta_0 = 2$, $\Delta\lambda_D = 0.23$, $a = 0.1$ and $S_1/S_0 = 0.01$, $\gamma = 90$, $\varphi = 45$, $B = 2000$ G. Stokes V is zero because the magnetic field is perpendicular to the observer. In addition, Stokes Q is zero because $\varphi = 45$ and thus, η_Q also vanishes (see Eq. 1.39). The magnetic field is strong enough to make the σ_r and σ_b components to be completely split from the central π component in Stokes I, which now appears because in Eq. 1.38, $\phi_p \sin^2\gamma \neq 0$ and therefore having a net contribution in Stokes I (see Eq. 1.72; compare with Fig. 1.6 and Fig. 1.7).

1.4.4 General case

It is important to notice that the Milne-Eddington approximation is reliable as long as no net circular polarizaton is observed (see Sect. 1.4.1), since this is an indicator that no gradients along the line of sight are present (condition for the absorption matrix to be constant along the ray path). Another important point is that the Milne-Eddington approximation neglects much of the thermodynamics of the atmosphere: first assuming that the level populations and continuum opacity are such that η_0 is constant, and constraining the real temperature stratification of the atmosphere assuming that the source function changes linearly with optical depth.

In the general case, the RTE has to be solved numerically because the absorption matrix is no longer constant. The continuum absorption coefficient (Eq. 1.31) has to be calculated for each wavelength taking into account contributions from the bound-free and free-free transitions: mainly the opacity due to the negative hydrogen ion H^- and Thompson scattering by free electrons. The electron pressure and partial pressures of the different elements needed for this purpose are derived using the Saha equation (LTE approximation), partition functions, element abundances and the hydrostatic equilibrium equation. The line absorption coefficient (Eq. 1.32) is calculated by means of the Boltzmann equation. This has to be done for each atmospheric layer since the temperature changes continously from the $\tau_c = 1$ level (not necessarily following a linear trend).

In addition the damping parameter (Eq. 1.49) changes with depth in the atmosphere. This is produced by changes in the temperature itself and by changes in the collisional damping, which

depends on the density (or partial pressures) of neutral species such as hydrogen and helium [4]. A possible strategy can be simplified as:

1. The physical quantities $T(\tau)$, $B(\tau)$, $\gamma(\tau)$, $\phi(\tau)$, $V_{los}(\tau)$, $V_{mic}(\tau)$ as well as an estimate of the gas pressure (boundary condition) on top of the atmosphere, $P_{gas}(\tau_{max})$, must be known.

2. $T(\tau)$ and $P_{gas}(\tau_{max})$ can provide us with $P_{gas}(\tau)$, $P_{elec}(\tau)$, $\rho(\tau)$, $\chi_c(\tau)$. This is done by means of iterative strategies (as in Wittmann 1974; Mihalas 1978; Gray 1992; solving the Saha equation for a number of important electron donors and a given set of element abundances), integrating the hydrostatic equilibrium equation and calculating the continuum opacity at each atmospheric layer: $\chi_c(T(\tau), P_{elec}(\tau))$ (Gustaffson 1973; Wittman 1974). In general χ_c (exceptions: i.e. Balmer jumps) does not change much in small wavelengths rages, therefore it is sufficient to evaluate it for a single wavelength near each transition considered.

3. The level populations (Eq. 1.32) are calculated in LTE with the Boltzmann equation, and correcting the line absorption coefficient by the oscillator strength of the considered transition.

4. The components of the Zeeman pattern must be calculated for each layer knowing the electronic configuration of the transition and the magnetic field strength (Eq. 1.25-1.26-1.27 and Table 1.1).

5. The damping parameter (Eq. 1.49) is calculated by knowing the radiative lifetime of the atomic transition Γ_{rad} (e.g. damped harmonic oscillator; Mihalas 1978) and the broadening by collisions with neutral perturbers Γ_{col} (e.g. by van der Waals interaction potential; Unsöld 1955)

6. We have now all the required elements to evaluate the absorption matrix for each atmospheric layer. And therefore the RTE (Eq. 1.64) is now integrated using any appropriate method that yields a good approximation for the evolution operator (Eq. 1.65) (e.g. DELO)

1.5 Inversion of Stokes profiles

The term *Inversion of Stokes profiles* applies to any method used to, by knowing the emergent radiation field (i.e. Stokes vector $\mathbf{I}(\lambda)$) or any other quantity related (e.g. net circular polarization) from a given source, derive the physical parameters: temperature stratification, magnetic field strength and orientation and line-of-sight velocity (in the the general case, also stratifications with optical depth) of the source (star, sun etc.).

Many methods rely on some kind of approximation that helps to derive analytical solutions of the RTE (e.g. weak field approximation, longitudinal field approximation etc.). Others are more phenomenological and directly ignore the radiative transfer to calculate a particular quantity of interest: measurements of the velocity by calculating the central position in Stokes *I* or velocity

[4] In the photosphere of the sun and of cool stars the main contribution to the collisional broadening are neutral species. Other contributions, such as linear or quadratic Stark effect can be neglected

stratifications using bisector analysis, measurements of the field strength from the separation of the blue and red peaks in Stokes V etc. Although these methods provide a good first look into the data and are reliable as long as the assumptions on which they rely are fulfilled, they are not to be trusted in general cases because they do not solve the full radiative transfer problem (see del Toro Iniesta & Ruiz Cobo 1996;1997).

1.5.1 Iterative and non-iterative methods

In the following we shall assume that we address the full problem of the line formation in presence of a magnetic field by self-consistently solving the RTE (Eq. 1.64) by means of some numerical approach (as sketched in Sect. 1.4.4 for instance). The question is now how the synthetic profiles are compared to observed ones in order to obtain reliable values for the physical parameters: temperature, magnetic field vector and line-of-sight velocity and its stratifications with optical depth. According to del Toro Iniesta (2003b) we will classify these methods into iterative and non-iterative algorithms.

Iterative algorithms modify an initial guess atmosphere, characterized by a given set of parameters defining the relevant physical quantities, by means of a least-squares minimization algorithm, until the synthetic profiles match the observed ones. The atmosphere retrieved is assumed to be the real one. Among the advantages of the iterative algorithms we shall highlight the possibility to deal (in principle) with any possible stratification with optical depth in the physical parameters. Non-linear iteration algorithms can make use of the derivatives of the merit function with respect to the free parameters (Steepest descent, Levenberg-Marquardt etc.; Press et al. 1986; Ruiz Cobo & del Toro Iniesta 1992) or use more complex and reliable (at cost of speed) genetic algorithms (e.g. Pikaia; Lagg et al. 2004).

Non-iterative algorithms are basically based on the idea of building a huge database, where synthetic profiles along with the physical quantities that produce them are stored. The observed Stokes vector is compared with the profiles in the data base and by just finding the closest one, the parameters defining the atmosphere are recovered. In order to get a reliable inversion the database must be as complete as possible.

Non-iterative algorithms are orders of magnitude faster than iterative ones. The most time consuming process is to build up a sufficiently large database, but once it is available, the inversion process takes just some few seconds. In principle it is also possible to create a huge database where all possible stratifications are contained, but in reality this is unachievable. Just building a database for a Milne-Eddington model (which uses only 10 free parameters) needs up to 10^{10} profiles (see Socas-Navarro et al. 2001). If the Milne-Eddington approximation is relaxed and one tries to use a model containing more generic stratifications, the number of needed profiles becomes virtually unpractical. Some methods are used to reduce the dimension of the problem in non-iterative algorithms, like the Principal Component Analysis method (PCA; Rees et al. 2000), which tries to classify the profiles in terms of a smaller set of eigenprofiles (coefficients of an expansion of the profiles in a given orthogonal base) and therefore requiring less amount of parameters in the database. Skumanich & López Ariste (2002) has investigated this issue and they have found that almost all coefficients of the expansion posses a physical counterpart (velocity, magnetic field strength etc.). Socas-Navarro & Sánchez Almeida (2002) have used the PCA technique to build a database with profiles rising from MISMA (Sánchez Almeida &

Degl'Innocenti 1996) atmospheres. Artificial Neural Networks have been also used for inversion purposes (Carroll & Staude 2001). Like the PCA strategy, it is very time consuming to train the network for a given model atmosphere and for a given spectral line, but once this is done the inversion is performed even faster than with PCA.

Each method has its advantages and shortcomings. In particular, iterative methods suffer from the all the problems associated with least squares fitting: the possibility that the minimization stops at a local minimum, thus retrieving an incorrect atmosphere. Of course several ways can be worked out to avoid this problem: e.g. using very different initial guess models and check whether the retrieved atmosphere is the same for all cases (unique). Non-iterative methods always find a global minimum within the database but of course this is no proof that the atmosphere is unique, since the database can be incomplete. Furthermore, all inversion techniques, iterative and non-iterative, are ill-posed in the sense that two different set of parameters (atmospheres) can yield identical observed polarization signal. This is a mayor problem in all inversion issues and the user has to learn how to live with this. In general, once two different models are proved to be able to reproduce the observed profiles, one must rely on theoretical considerations or other kinds of observations in order to decide which model comes closer to reality.

In general, it is accepted that, for large amounts of data and to get a first idea of the spatial distribution of the magnetic field, velocities etc. non-iterative algorithms are preferred due to its much larger speed. However, for a more thorough extraction of information from the observed profiles iterative methods, which can very easy handle general stratifications with optical depth, are more suitable. In the following we shall study in more detail the latter strategy.

1.5.2 The merit χ^2 function

Least squares fitting algorithms are based on the minimization of the so-called *merit function*, defined as:

$$\chi^2 = \frac{1}{\mathrm{L}} \sum_{k=1}^{4} \sum_{i=1}^{M} [I_k^{\mathrm{obs}}(\lambda_i) - I_k^{\mathrm{syn}}(\mathbf{x}, \lambda_i)]^2 \frac{w_k^2}{\sigma_k^2} \tag{1.78}$$

where L is the total number of free parameters, the index $k = 1,2,3,4$ refers to the 4 components of the Stokes vector: $I_1 = I$, $I_2 = Q$ etc. Index $i = 1,...,M$ samples the full wavelength range of the observations. $I_k^{\mathrm{obs}}(\lambda_i)$ are the observed profiles, while: $I_k^{\mathrm{syn}}(\mathbf{x}, \lambda_i)$ are the synthetic profiles produced by an atmosphere which is characterized by the set of L free parameters $\mathbf{x} = [x_1, ..., x_{\mathrm{L}}]$. The noise in the observations (different for each Stokes profile) comes into the equation through σ_k^2. Finally each component of the Stokes vector is weighted with w_k^2 in order to ensure that each of them has the same relative weight on χ^2 independent of their amplitudes.

Note that the parameters defining the atmosphere are, in the case of the Milne-Eddington approximation: $\mathbf{x} = [S_0, S_1, \eta_0, a, \Delta\lambda_D, V_{\mathrm{los}}, B, \gamma, \varphi]$, with a total number of free parameters $L = 9$. However in the general case, where quantities are functions of the optical depth τ_{c} we would have:

$$\mathbf{x} = [T(\tau_1), ..., T(\tau_{\mathrm{F}}), V_{\mathrm{los}}(\tau_1), ..., V_{\mathrm{los}}(\tau_{\mathrm{F}}), B(\tau_1), ..., B(\tau_{\mathrm{F}}), ...] \tag{1.79}$$

where F is the total number of points in which the atmosphere is discretized. If we have Q depth-dependent variables and R depth independent, the total amount of free parameters would then be: $L = Q \times F + R$. In this general case, if the temperature $T(\tau)$ is known, the Doppler width and damping parameters can be derived by thermodynamics means (see Sect. 1.4.4), and therefore they are no longer free parameters as in the case of the Milne-Eddington approximation.

1.5.3 Linearization of the RTE and Response functions

Let us now consider the case when we apply small perturbations to all the atmospheric parameters in the form:

$$\delta x_p(\tau_c) = \delta x_p \delta(\tau_c - \tau^*) \tag{1.80}$$

where $\delta(\tau_c - \tau^*)$ denotes the delta Dirac function centered at an optical depth point τ^*. Index $p = 1, ..., F+R$, that is, we perturb both height dependent and independent quantities at a single optical depth point. These small perturbations will induce small changes in the absorption matrix as well as the source function:

$$\delta\hat{\mathcal{K}}(\tau_c) = \sum_{p=1}^{F+R} \frac{\delta\hat{\mathcal{K}}}{\delta x_p} \delta x_p \delta(\tau_c - \tau^*) \tag{1.81}$$

$$\delta\mathbf{S}(\tau_c) = \sum_{p=1}^{F+R} \frac{\delta\mathbf{S}}{\delta x_p} \delta x_p \delta(\tau_c - \tau^*) \tag{1.82}$$

When these perturbations are introduced into the RTE (Eq. 1.36) we obtain:

$$\frac{d(\mathbf{I}+\delta\mathbf{I})}{d\tau_c} = (\hat{\mathcal{K}} + \delta\hat{\mathcal{K}})[\mathbf{I} + \delta\mathbf{I} - \mathbf{S} - \delta\mathbf{S}] \tag{1.83}$$

By expanding these terms, taking into account that some terms cancel out because they form the RTE itself and neglecting terms in second order of perturbations (linearization), we obtain:

$$\frac{d(\delta\mathbf{I})}{d\tau_c} = \hat{\mathcal{K}}[\delta\mathbf{I} - \delta\mathbf{S}] + \delta\hat{\mathcal{K}}[\mathbf{I} - \mathbf{S}] \tag{1.84}$$

Assuming that the inverse of the absorption matrix exists (its determinant is different from zero) we can now define a new source function,

$$\tilde{\mathbf{S}} = \delta\mathbf{S} - \hat{\mathcal{K}}^{-1}\delta\hat{\mathcal{K}}[\mathbf{I} - \mathbf{S}] \tag{1.85}$$

With this definition Eq. 1.84 can be expressed as

$$\frac{d(\delta\mathbf{I})}{d\tau_c} = \hat{\mathcal{K}}[\delta\mathbf{I} - \tilde{\mathbf{S}}] \tag{1.86}$$

which is formally the same as the general RTE (Eq.1.36) but for the perturbations in the radiation field instead of the radiation field itself. Therefore the solution can be written also as in Eq. 1.64 as follows:

$$\delta\mathbf{I}(0) = \int_0^\infty \hat{O}(0,\tau_c)\hat{\mathcal{K}}(\tau_c)\tilde{\mathbf{S}}(\tau_c)d\tau_c \tag{1.87}$$

with the definition of $\tilde{\mathbf{S}}$, we can insert the perturbations as in Eq. 1.81 and 1.82. Taking into account the properties of the Dirac function, Eq. 1.87 can be integrated directly by just evaluating the integrand at the optical depth point where the perturbation was performed, τ^*,

$$\delta\mathbf{I}(0) = \hat{O}(0,\tau^*)\hat{\mathcal{K}}(\tau^*)\left[\sum_{p=1}^{F+R}\frac{\delta\mathbf{S}}{\delta x_p}\delta x_p - [\mathbf{I}(\tau^*)-\mathbf{S}(\tau^*)]\hat{\mathcal{K}}^{-1}(\tau^*)\sum_{p=1}^{F+R}\frac{\delta\hat{\mathcal{K}}}{\delta x_p}\delta x_p\right] \tag{1.88}$$

or in a more compact form,

$$\delta\mathbf{I}(0) = \sum_{p=1}^{F+R}\underbrace{\hat{O}(0,\tau^*)\left[\hat{\mathcal{K}}(\tau^*)\frac{\delta\mathbf{S}}{\delta x_p} - [\mathbf{I}(\tau^*)-\mathbf{S}(\tau^*)]\frac{\delta\hat{\mathcal{K}}}{\delta x_p}\right]}_{\mathbf{R}_p(\tau^*)}\delta x_p \tag{1.89}$$

where $\mathbf{R}_p(\tau^*)$ is called the *response function* vector to perturbations in the parameter x_p at τ^*. It is a four component vector, where each component refers to one of the Stokes parameters,

$$\mathbf{R}_p(\tau_c) = (\mathcal{R}_p^I, \mathcal{R}_p^Q, \mathcal{R}_p^U, \mathcal{R}_p^V) \tag{1.90}$$

With this definition, the perturbation in the emergent spectrum (Eq. 1.86) can be written as

$$\delta\mathbf{I}(0) = \sum_{p=1}^{F+R}\mathbf{R}_p(\tau^*)\delta x_p \tag{1.91}$$

1.5.4 Derivatives of χ^2

Let us now consider the merit function (Eq. 1.78) and study how it changes when a parameter x_p is slightly changed at a single optical depth point.

$$\frac{\partial\chi^2}{\partial x_p} = -\frac{2}{L}\sum_{k=1}^{4}\sum_{i=1}^{M}[I_k^{obs}(\lambda_i) - I_k^{syn}(\mathbf{x},\lambda_i)]\frac{w_k^2}{\sigma_k^2}\frac{\partial I_k^{syn}(\mathbf{x},\lambda_i)}{\partial x_p} \tag{1.92}$$

Considering now another perturbation in another parameter x_q we have

$$\frac{\partial^2\chi^2}{\partial x_p \partial x_q} = -\frac{2}{\mathrm{L}}\sum_{k=1}^{4}\sum_{i=1}^{M}\left[\frac{\partial I_k^{\mathrm{syn}}(\mathbf{x},\lambda_i)}{\partial x_p}\frac{\partial I_k^{\mathrm{syn}}(\mathbf{x},\lambda_i)}{\partial x_q} - I_k^{\mathrm{syn}}(\mathbf{x},\lambda_i)\frac{\partial^2 I_k^{\mathrm{syn}}(\mathbf{x},\lambda_i)}{\partial x_p \partial x_q}\right]\frac{w_k^2}{\sigma_k^2} \tag{1.93}$$

Ignoring second derivatives of the synthetic profiles, we realize that the derivatives of the merit function with respect to the atmospheric parameters can be written in terms of the response functions as follows:

$$\frac{\partial\chi^2}{\partial x_p} = -\frac{2}{\mathrm{L}}\sum_{k=1}^{4}\sum_{i=1}^{M}[I_k^{\mathrm{obs}}(\lambda_i) - I_k^{\mathrm{syn}}(\mathbf{x},\lambda_i)]\frac{w_k^2}{\sigma_k^2}\mathcal{R}_p{}^k(\lambda_i) \tag{1.94}$$

$$\frac{\partial^2\chi^2}{\partial x_p \partial x_q} \simeq -\frac{2}{\mathrm{L}}\sum_{k=1}^{4}\sum_{i=1}^{M}\mathcal{R}_p{}^k(\lambda_i)\mathcal{R}_q{}^k(\lambda_i)\frac{w_k^2}{\sigma_k^2} \tag{1.95}$$

Therefore, the derivatives of the merit function can be written as combinations of the response functions. An important advantage of this approach is that all response functions can be evaluated analytically at the same time that the RTE is solved (Eq. 1.89), therefore significantly reducing the computing time. A clear example is found if we again consider the Milne-Eddington approximation, where the integration of the RTE does not even need to be performed. In this case, the free parameters to be determined from the inversion are:

$$\mathbf{x} = [S_0, S_1, \eta_0, a, \Delta\lambda_D, \mathrm{v}_{\mathrm{los}}, B, \gamma, \varphi] \tag{1.96}$$

As can be seen in Eq. 1.72-1.77, the emergent spectrum can be easily derived with respect to S_0 and S_1. Derivatives with respect to the rest of the parameters are to be evaluated through the derivatives of the elements of the absorption matrix. Among them, response functions to perturbations in η_0, γ and φ are easy to calculate, as they can be obtained through Eq. 1.38-1.44. Perturbations in a, $\Delta\lambda_D$, $\mathrm{v}_{\mathrm{los}}$ and B imply the derivation of the Voigt and Faraday functions (Eq. 1.45 and 1.46). This is somewhat more complicated, but can be worked out by applying the chain rule:

$$\frac{\partial H(a,\nu')}{\partial \mathrm{v}_{\mathrm{los}}} = \frac{\partial H(a,\nu')}{\partial \nu'}\frac{\partial \nu'}{\partial \mathrm{v}_{\mathrm{los}}} \tag{1.97}$$

$$\frac{\partial H(a,\nu')}{\partial \Delta\lambda_D} = \frac{\partial H(a,\nu')}{\partial \nu'}\frac{\partial \nu'}{\partial \Delta\lambda_D} \tag{1.98}$$

$$\frac{\partial H(a,\nu')}{\partial B} = \frac{\partial H(a,\nu')}{\partial \nu'}\frac{\partial \nu'}{\partial B} \tag{1.99}$$

and the same for the Faraday function $F(a,\nu')$. Here we just need to take into account that $\nu' = \nu + \nu_D(\Delta\lambda_D, \mathrm{v}_{\mathrm{los}}) + \nu_{i_j}(B)$. In addition,

$$\frac{\partial H(a,\nu')}{\partial \nu'} = 2aF(a,\nu') - 2\nu' H(a,\nu') \tag{1.100}$$

$$\frac{\partial F(a,\nu')}{\partial \nu'} = \sqrt{\frac{4}{\pi}} - 2aH(a,\nu') - 2\nu' F(a,\nu') \tag{1.101}$$

$$\frac{\partial H(a,\nu')}{\partial a} = -\frac{\partial F(a,\nu')}{\partial \nu'} \tag{1.102}$$

$$\frac{\partial F(a,\nu')}{\partial a} = \frac{\partial H(a,\nu')}{\partial \nu'} \tag{1.103}$$

In a more general case, the derivatives with respect to S_0, S_1, a, η_0 and $\Delta\lambda_D$ are to be substituted by derivatives with respect to the temperature T. This introduces new complications, since the derivative with respect to the temperature of the line-to-continuum absorption coefficient radio, η_0, implies the derivation of the Boltzmann equation and partition functions. Furthermore, derivatives of the damping parameter a, and in particular of the collisional damping $\Gamma_{\rm col}$ are not easy to handle. In addition, in this case we do not have an analytical expression for the emergent spectrum, as happens in the Milne-Eddington atmosphere. Therefore the response functions must be evaluated through Eq. 1.89. There we notice that $\mathbf{I}(\tau^*)$ must be known, and therefore we must integrate the RTE in order to evaluate the response function. Fortunately, these two processes can be carried out simultaneously, and as already mentioned, a single integration of the RTE provides us with all the needed response functions.

1.5.5 Inversion procedure

We now have all the tools available to introduce the analytical derivatives of the merit function into a minimization algorithm, that will iteratively look for the optimum values in the atmospheric parameters that fit the observed profiles. Classical methods are, for instance, the steepest descent method and the Hessian method.

The *steepest descent method* is reliable when the initial guess parameters are far from the final solution. In this case a first order Taylor expansion of $\mathbf{I^{syn}}(\lambda_i,\mathbf{x})$ suffices when a δx_p perturbation is performed. According to Eq. 1.91 we have

$$\mathbf{I^{syn}}(\mathbf{x}+\delta x_p,\lambda_i) \simeq \mathbf{I^{syn}}(\mathbf{x},\lambda_i) + \mathbf{R_p}(\lambda_i)\delta x_p \tag{1.104}$$

The new merit function is then given by

$$\begin{aligned}\chi^2(\mathbf{x}+\delta x_p) &\simeq \frac{1}{\mathrm{L}}\sum_{k=1}^{4}\sum_{i=1}^{M}[I_k^{\rm obs}(\lambda_i) - I_k^{\rm syn}(\mathbf{x}+\delta x_p,\lambda_i)]^2\frac{w_k^2}{\sigma_k^2} \\ &= \frac{1}{\mathrm{L}}\sum_{k=1}^{4}\sum_{i=1}^{M}[I_k^{\rm obs}(\lambda_i) - I_k^{\rm syn}(\mathbf{x},\lambda_i) - \mathcal{R}_p^{\,k}(\lambda_i)\delta x_p]^2\frac{w_k^2}{\sigma_k^2}\end{aligned} \tag{1.105}$$

Looking for a minimum it must be verified that the first derivative of $\chi^2(\mathbf{x}+\delta x_p)$ with respect to δx_p vanishes.

$$\begin{aligned}\frac{\partial\chi^2(\mathbf{x}+\delta x_p)}{\partial x_p} &\simeq -\frac{2}{L}\sum_{k=1}^{4}\sum_{i=1}^{M}[I_k^{\rm obs}(\lambda_i)-I_k^{\rm syn}(\mathbf{x},\lambda_i)-\mathcal{R}_p{}^k(\lambda_i)\delta x_p]\mathcal{R}_p{}^k(\lambda_i)\frac{w_k^2}{\sigma_k^2}\\ &= \underbrace{-\frac{2}{L}\sum_{k=1}^{4}\sum_{i=1}^{M}[I_k^{\rm obs}(\lambda_i)-I_k^{\rm syn}(\mathbf{x},\lambda_i)]\mathcal{R}_p{}^k(\lambda_i)\frac{w_k^2}{\sigma_k^2}}_{=\frac{\partial\chi^2}{\partial x_p}\text{ (Eq. 1.94)}}+\\ &+\frac{2}{L}\sum_{k=1}^{4}\sum_{i=1}^{M}\mathcal{R}_{p,k}^{2}(\lambda_i)\delta x_p\frac{w_k^2}{\sigma_k^2}=\frac{\partial\chi^2}{\partial x_p}+\frac{2}{L}\sum_{k=1}^{4}\sum_{i=1}^{M}\mathcal{R}_{p,k}^{2}(\lambda_i)\delta x_p\frac{w_k^2}{\sigma_k^2}=0\end{aligned} \tag{1.106}$$

This expression provides us with the needed perturbation in the atmospheric parameters that decreases χ^2.

$$\delta x_p = -\frac{L}{2}\frac{\partial\chi^2}{\partial x_p}\left[\sum_{k=1}^{4}\sum_{i=1}^{M}\mathcal{R}_{p,k}^{2}(\lambda_i)\frac{w_k^2}{\sigma_k^2}\right]^{-1} \tag{1.107}$$

Near the minimum $\frac{\partial\chi^2}{\partial x_p}$ rapidly vanishes, and therefore the perturbations δx_p produced by the steepest descent method are far too small. Here a new method, that considers second derivatives of the merit function is preferred. A common one is the *Hessian method*, that considers a second order Taylor expansion of the merit function after a perturbation $\delta\mathbf{x}$ has been introduced.

$$\chi^2(\mathbf{x}+\delta\mathbf{x}) \simeq \chi^2(\mathbf{x})+\nabla\chi^2(\mathbf{x})\delta\mathbf{x}+\frac{1}{2}\delta\mathbf{x}^T\hat{\mathcal{H}}\,\delta\mathbf{x} \tag{1.108}$$

where $\hat{\mathcal{H}}$ is the Hessian matrix, whose elements contain the second derivatives of the merit function with respect to the free parameters, or according to Eq. 1.95

$$\mathcal{H}_{ij}=\frac{\partial^2\chi^2}{\partial x_i\partial x_j}\simeq-\frac{2}{\rm L}\sum_{k=1}^{4}\sum_{i=1}^{M}\mathcal{R}_p{}^k(\lambda_i)\mathcal{R}_q{}^k(\lambda_i)\frac{w_k^2}{\sigma_k^2} \tag{1.109}$$

Here $\delta\mathbf{x}$ minimizes the merit function if the partial derivatives of $\chi^2(\mathbf{x}+\delta\mathbf{x})$ with respect to $\delta\mathbf{x}$ are zero. This leads to the expression

$$\nabla\chi^2(\mathbf{x})+\hat{\mathcal{H}}\,\delta\mathbf{x}=0 \tag{1.110}$$

$$\delta\mathbf{x}=-\hat{\mathcal{H}}^{-1}\nabla\chi^2(\mathbf{x}) \tag{1.111}$$

The technique that combines both methods, in order to deal with situations both far away and near the minimum, is the so-called *Levenberg-Marquardt algorithm*. The idea is to use the same formalism as in the Hessian method, but using a modified Hessian matrix, $\hat{\mathcal{H}}'$, whose elements are:

$$\mathcal{H}_{ij}^{'} = \begin{cases} \mathcal{H}_{ij}(1+\varepsilon) & \text{if } i=j \\ \mathcal{H}_{ij} & \text{Otherwise} \end{cases} \tag{1.112}$$

being the required perturbations to produce a minimization in the merit function, in the form

$$\nabla\chi^2(\mathbf{x}) + \hat{\mathcal{H}}'\delta\mathbf{x} = 0 \tag{1.113}$$

$$\delta\mathbf{x} = -\hat{\mathcal{H}}'^{-1}\nabla\chi^2(\mathbf{x}) \tag{1.114}$$

Note that when the parameter $\varepsilon \gg 1$ the modified Hessian matrix is quasi-diagonal and the perturbations can be expressed as in Eq. 1.107. We are therefore in the limit where the steepest descent method is recovered. On the other hand, when $\varepsilon = 0$ the Hessian method is obtained. By varying the weight of ε we can switch from one method to the other according to the our requirements. For instance:

1. Try with an initial guess atmosphere characterized by $\mathbf{x}$ with $\varepsilon \ll 1$.
2. Calculate the perturbations $\delta\mathbf{x}$ by solving the set of linear equations Eq. 1.112.
3. Check whether $\chi^2(\mathbf{x}+\delta\mathbf{x}) < \chi^2(\mathbf{x})$. If so, update the new atmosphere to $\mathbf{x}^{'} = \mathbf{x}+\delta\mathbf{x}$ and repeat step 2 decreasing ε by an order of magnitude. If not, we are far from the minimum, therefore we keep the original trial atmosphere $\mathbf{x}$ and repeat step 2 increasing ε by an order of magnitude in order to approach the steepest descent method.
4. The procedure is stopped if $\chi^2 \simeq 1$ or χ^2 does not decrease significantly after 3-4 iterations.

The calculation of the inverse of the modified Hessian matrix in order to solve the system of equations that yield the needed perturbations to minimize the merit function (Eq. 1.110) is noteworthy. For the inverse matrix to exist, its determinant must be different from zero. The fact that the Stokes vector is much more sensitive to some parameters (e.g. temperature) than to other can make one or several response functions, and hence some matrix elements of the modified Hessian, to be much larger than the rest. This implies that $\hat{\mathcal{H}}^{'}$ is usually numerically quasi-singular. A classical way to work out the problem is the use of the Singular Value Decomposition (SVD). The basic idea would then be to factorize the modified Hessian as:

$$\hat{\mathcal{H}}' = \hat{\mathcal{U}}\,\hat{\mathcal{W}}\,\hat{\mathcal{V}}^T \tag{1.115}$$

where $\hat{\mathcal{W}}$ is a diagonal matrix with elements $\mathcal{W}_{jj}$, and where the vectors $\hat{\mathcal{U}}$ and $\hat{\mathcal{V}}$ are orthogonal

$$\hat{\mathcal{U}}^T\hat{\mathcal{U}} = \hat{\mathcal{V}}^T\hat{\mathcal{V}} = \mathbb{1} \tag{1.116}$$

Note that $\hat{\mathcal{H}}^{'}$ is an $L \times L$ matrix, being $L = Q \times F + R$ the total amount of free parameters, where R are height independent, Q height dependent and F the total amount of optical depth

points in the atmosphere (see Sect. 1.5.2). Note that according to the SVD formulation, $\hat{\mathcal{U}}$, $\hat{\mathcal{V}}$ and $\hat{\mathcal{W}}$ are also $L \times L$ matrices. The inverse of the matrix $\hat{\mathcal{H}'}$ can be written as:

$$\hat{\mathcal{H}'}^{-1} = \hat{\mathcal{V}}\,[\mathrm{diag}(\frac{1}{\mathcal{W}_{jj}})]\,\hat{\mathcal{U}}^T \tag{1.117}$$

If $\hat{\mathcal{H}'}$ is singular or numerically singular, some of the $\mathcal{W}_{jj}$ elements are zero and the inverse matrix is no longer defined. SVD method makes $1/\mathcal{W}_{jj} = 0$ whenever the diagonal element is below a given threshold $\mathcal{W}_{jj} \leq \xi$, with typically $\xi \simeq 10^{-3} - 10^{-5}$. Making this, implies that the linear system of equations 1.113 will not be verified. However the SVD technique provides an optimum solution to the problem in the sense that it minimizes the quantity $||\nabla\chi^2(\mathbf{x}) + \hat{\mathcal{H}'}\delta\mathbf{x}||$.

As already mentioned above, the response functions to some perturbations can be very small as compared to others. If SVD is applied to avoid singularities, very small response functions will be ignored, and thus the associated free parameter will not be taken into account in the inversion. To avoid this, Ruiz Cobo & del Toro Iniesta (1992) have proposed a clever modification of the SVD method in which the matrix $\hat{\mathcal{W}}$ is decomposed in a sum of $Q+R$ matrices, where each of them contains information about one single physical parameter. SVD is then applied separately to each of those matrices. Therefore at least one diagonal element of each matrix is preserved, and the solution accounts for all physical quantities at each iteration step.

1.5.6 SPINOR

SPINOR (Stokes-Profiles-INversion-O-Routines; Frutiger et al. 1999) is an inversion code (IC) developed at the ETH Zürich and Max Planck Institut für Aeronomie by Cristoph Frutiger, Sami K. Solanki and Svetlana Berdyugina, with important contributions from Jo Bruls and Marcel Fligge. It is based on a synthesis code (STOPRO) previously written by Sami Solanki.

SPINOR's synthesis package (STOPRO) perform spectral line (atomic and molecular) synthesis under local thermodynamic equilibrium (LTE). The radiative transfer equation can be solved, either using the Hermitian approach by Bellot Rubio et al. (1998) or DELO (Rees et al. 1989), although the former is normally used due to its more rapid convergence. Unlike the original Hermitian method, modifications have been introduced to perform such integration in the optical depth scale. The Hermitian strategy is based in a fourth order Taylor expansion of the Stokes vector in order to evaluate the spectrum at each atmospheric layer as a function of the previous one. An advantage is that it yields an approximation of the evolution operator at each atmospheric layer at the same time that the RTE is solved.

The continuum absorption coefficient is calculated for a given wavelength, temperature and electron pressure using the MULTI opacity package by Mats Carlson (based on the previous Uppsala opacity package by Gustaffson 1973), which takes into account contributions from H, He, H^-, He^-, H_2^+, H_2^- and other electron donor species, as well as Rayleigh scattering by H and H_2 and Thompson scattering by free electrons.

Several broadening mechanisms are considered: microturbulent and macroturbulent velocities are used to account for velocity fields below the resolution element. In addition, radiative broadening (in the classical damped oscillator approximation) and broadening by collisions with

neutral perturbers (for which the ABO theory is employed in substitution of the van der Waals interaction potential; see Barklem & O'Mara 1997 and Barklem et al. 1998) are considered.

SPINOR is able to deal with any number of atmospheric components. In the synthesis mode the RTE must be solved for each of them, being the final emergent polarized spectrum a linear combination of the individual rays as follows

$$\mathbf{I}(\lambda) = \sum_{k=1}^{N} \alpha_k \mathbf{I}_k(\lambda) \tag{1.118}$$

where N is the total number of components. An obvious normalization condition that must be verified is

$$\sum_{k=1}^{N} \alpha_k = 1 \tag{1.119}$$

defining thus α_k as the area of the resolution element covered by the atmospheric component k. This feature is important when modelling structures smaller than the resolution element of the observations: granulation (downflows and upflows present in the same resolution element), scattered light in observations with a spectrograph, etc.

SPINOR's inversion routines (INVERT) perform the inversion of the RTE using the modified singular value decomposition scheme described in Sect. 1.5.5, although for testing purposes other methods are implemented. In the inversion, a number of optical depth points, called *nodes*, are specified. At these points analytical equivalent Response Functions are calculated by linear combination of the response functions at each atmospheric layer of the discretized atmosphere. In this way, the number of free parameters is significantly reduced, since the calculated perturbations, that improve the fit on the observed data, are evaluated in a coarser grid, rather than the whole atmospheric grid. After each iteration step the new atmospheric parameters at the nodes are updated. The new full stratification is obtained through a smooth spline interpolation through the nodes. Therefore the free parameters shown in Eq. 1.79 are to be changed to:

$$\mathbf{x} = [\mathrm{T}(\tau_1), ..., \mathrm{T}(\tau_\mathrm{H}), \mathrm{V}_\mathrm{los}(\tau_1), ..., \mathrm{V}_\mathrm{los}(\tau_\mathrm{H}), ...] \tag{1.120}$$

where H represents the number of nodes. The total number of free parameters is now: $L = Q \times H + R$, with Q and R being the depth-dependent and depth independent physical quantities respectively.

Unlike other inversion codes (e.g. SIR; see Ruiz Cobo & del Toro Iniesta 1992), where the nodes are placed equally-spaced along the atmospheric grid, SPINOR allows for the possibility to choose the location of the nodes. This feature is very useful in practice, since it permits to concentrate the nodes on those layers where the observed spectral lines are more sensitive.

Another important feature of SPINOR is the possibility to switch the calculation of the response functions to numerical means

$$\mathbf{R}_\mathrm{p}(\tau_\mathrm{m}) = \frac{1}{2\delta \mathrm{x}_\mathrm{p}(\tau_\mathrm{m})} [\mathbf{I}(\mathbf{x} + \delta \mathrm{x}_\mathrm{p}(\tau_\mathrm{m})) - \mathbf{I}(\mathbf{x} - \delta \mathrm{x}_\mathrm{p}(\tau_\mathrm{m}))] \tag{1.121}$$

where $\mathbf{R}_{\rm p}(\tau_{\rm m})$ is the response function to perturbations of the free parameter x_p ($p = 1,...,L$) at a given node τ_m ($m = 1,...,H$). This results in a significant increase of the computing time since the RTE must be solved twice for each free parameter (one with $+\delta x_p$ and another for $-\delta x_p$). Nevertheless, it is convenient when complex geometrical models, for which analytical response functions do not exist, are to be implemented.

1.5.7 Should we believe inversions ?

Let us now address the question of whether spectropolarimetric inversion techniques, as described in previous sections, retrieve results that can be considered unique (i.e. global minimum of the merit function in the space spanned by the free parameters). In this section, we propose a test on the numerical performance of the inversion code SPINOR (Sect. 1.5.6) that will allow us to introduce the reader on the practical problems one faces when using ICs.

Fig.1.9 (top panel) shows a two-dimensional continuum intensity image (at a reference wavelength of 5000 Å) taken from a radiative MHD simulation of the solar granulation (Shelyag & Vögler, private communication) at $\mu = 1$ (i.e. center of the Solar disk) with a pixel size of 20 Km. These simulations solve self-consistently the MHD equations coupled with the radiative transfer equation, which is the dominant energy transfer mechanism in the solar photosphere.

In this way, they provide the full thermal, magnetic, kinematics and dynamics properties at each point of the simulation box (X,Y,Z). Let us now take a point in this two-dimensional map at a given position $\rm X_0 = 84$ and $\rm Y_0 = 242$ (marked with the red circle in Fig. 1.9) and extract the depth dependence of the physical parameters: T(z), $\rm v_{los}$(z), B(z), γ(z), ϕ(z) etc. With these we are ready to produce synthetic Stokes profiles for any spectral line of our choice. Our aim is to invert these synthetic lines and compare the retrieved stratifications with the original ones.

Selection of lines

We have selected the widely used neutral iron lines Fe I 6302.5 Å and 15648.5 Å. The first of these lines is formed in the mid-high photosphere, $\log\tau_5 = [-1,-4]$, and is one of the most magnetic sensitive spectral lines in the visible range ($\rm g_{eff}$=2.5). In addition it is also reasonably sensitive to variations in the temperature due to its small excitation energy of the lower level of the transition $\chi_l = 3.68$ eV. The second line is formed in deeper layers, $\log\tau_5 = [0,-2]$, partly due to the fact that the continuum opacity of the negative hydrogen ion presents a minimum around 16400 Å (thus allowing to sample deeper layers near this wavelength) and because of its large excitation potential, $\chi_l = 5.25$ eV (which at the same time makes it be somewhat insensitive to the temperature). However this is perhaps one of the most magnetic sensitive spectral lines in the whole solar spectrum, because of the joint effect that the Zeeman splitting scales as $\sim \lambda_0^2$ and because of its high Landé factor of $\rm g_{eff}$=3. Note that the Doppler width, Eq. 1.50, scales as $\sim \lambda_0$. But the net effect still makes this line roughly 3 times more sensitive to the magnetic field than Fe I 6302.5 Å. The synthetic lines produced by the atmosphere corresponding to the selected pixel in the simulation are shown with filled circles in Fig. 1.9 (bottom panels).

Selection of model for the inversion and nodes

We must now select a proper model to describe the stratifications: T(z), v_{los}(z), etc. In this case, we know that all physical quantities depend only on the vertical coordinate Z, therefore we should use a model where this feature is included. Attending to Sect. 1.5.6 (Eq. 1.118 and 1.119) the most obvious one is a *1-Component* model, where no horizonal inhomogeneities are allowed, because only one atmosphere is present in the resolution element ($N = 1$ and $\alpha = 1$ in Eq. 1.118-1.119).

Once this is done we must specify some optical depth points where response functions will be calculated (i.e nodes or free parameters) and hence where the different physical quantities (temperature, velocity, magnetic field etc) will be inferred. This step must be done carefully because a large number of nodes will certainly improve the quality of the fits to the observed profiles but it can also yield unrealistic stratifications. The common procedure is to start test inversions with a small number of nodes per physical quantity and increase them only if the profiles can not be fitted. For our test we have chosen 3 nodes (i.e. geometrical height or Z coordinate) at the following optical depth locations: $\log\tau_5 = [0, -1.75, -3.5]$. Since we are interested to infer the temperature, line-of-sight velocity, magnetic field strength, inclination and azimuth, this results in a total of 15 free parameters.

The initial guess model also deserves some attention. In order to prevent us from falling into a local minima in the χ^2 surface we will employ a total of 12 different initial guess models. For each of them we carry out 50 iterations steps and compare the achieve χ^2. Eight out of 12 of these initial guess models provide a final $\chi^2 \sim 9$, whereas the rest retrieve much larger values: $\chi^2 \sim 250$ (clear signature that they stopped at a local minimum) and therefore we will not consider them for the final solution. In Fig. 1.9 (bottom panels) we plot in solid red lines the best fit profiles obtained from all the initial guess models.

Inversion results

Prior to comparing the retrieved atmospheres to the original ones it is a good exercise to make a more detailed study of the observed profiles and see what kind of atmosphere can be expected from the inversion. With a first glance on the Stokes profiles we realize that Stokes I shows the σ_r and σ_b but no central π component, indicating thus that the magnetic field is mainly aligned, towards or way from, with the observer. This conclusion is confirmed when one realizes that $V \gg Q, U$ and therefore the projection of the magnetic field vector in the plane perpendicular to the observer is very small. In addition, it can be seen that the profiles are highly shifted towards larger wavelengths (e.g. center of gravity in Stokes *I*, Stokes *V* zero-crossing etc.) indicating that the plasma is essentially moving away from the observer.

Fig. 1.10 shows the original atmosphere coming from the MHD simulation in black solid lines, together with the average atmosphere retrieved by the inversion with the initial models whose χ^2 value was sufficiently small (red dashed lines). The node positions are indicated with vertical dotted lines. As can be seen the retrieved values at the nodes for the temperature, line-of-sight velocity and magnetic field matches almost perfectly the original values, except perhaps at the highest node in the atmosphere, where the sensitivity of the spectral lines is far too small. For the inclination of the magnetic field the inferred stratifications might look much worse. However

we must take into account that the real error is of the order of 1 deg when compared with the original atmosphere (whose values are very close to zero). Indeed, the inversion is even able to retrieve the real trend, that is, a magnetic field inclination that increases at the beginning and decreasing later on. Also for the azimuthal angle it seems that the code retrieves a wrong solution. This can be understood if we take into account that the magnetic field inclination is very close to zero and therefore the azimuthal angle is not really defined, since, as already mentioned, the projection of the magnetic field vector on the plane perpendicular to the observer is far too small: $V \gg Q,U$. Nonetheless, although with larger uncertainties than in the case of the magnetic field inclination, the correct trend (increasing azimuthal angle with increasing depth in the photosphere) is obtained. Logically, in order to be able to reproduce the original discontinuity in the azimuthal angle in the MHD simulation, the number of nodes should have been increased, but this is something that a priori was unknown.

Problems in practice

The example shown in this section illustrates some of the problems that one can find when using iterative inversion codes to retrieve the original physical properties of the atmosphere. We shall mention here the most important ones:

- **Noise in the observations**: here we have carried out an inversion of synthetic spectral lines coming from a MHD simulation. In real observing conditions, the Stokes vector is always affected, to some extend, by noise. One must always handle it carefully. Playing around with the different weights for the components of the Stokes vector in the merit function is often a good idea. This is done in order to find a good balance between the information we are really interested in and the information that the profiles really contain. A clear example can be given if we introduce a noise level of $5 \times 10^{-4} I_{\rm C}$ (common one in solar polarimetry) in the synthetic profiles in Fig. 1.9. Under these conditions, the linear polarization profiles, Stokes Q and U, would be heavily affected by it, and therefore we should try to decrease their weights in the χ^2 function. Fortunately, in this case, this is not critical, because the result from the inversion would then be a magnetic field inclination of 0 deg, which is still not too far from reality.

- **Height coverage**: very important to increase the reliability of the inferred atmospheres, is to include lines which are formed at different atmospheric layers. In addition, data redundancy (i.e. lines whose forming regions are partially overlapped) is highly desirable in order to obtain more accurate values at the nodes. If for example, in addition to the Fe I lines 6302.5 and 15648.5 Å we would have included the Fe I lines 6301.5 and 15652.8 Å, it is very likely that all 12 initial guess models would have resulted in an equally small χ^2 value.

- **Atomic data**: the availability of accurate atomic parameters for the line transitions is, beyond any question, a very important point, not only the quantum numbers of the transitions (that define the Zeeman pattern) but also transition probabilities and excitation potentials (that change the height of formation of the spectral lines) as well as laboratory wavelength positions. In our example, we can rule out any uncertainty arising from them as we have used the same atomic parameters to produce the synthetic profiles as for the inversion.

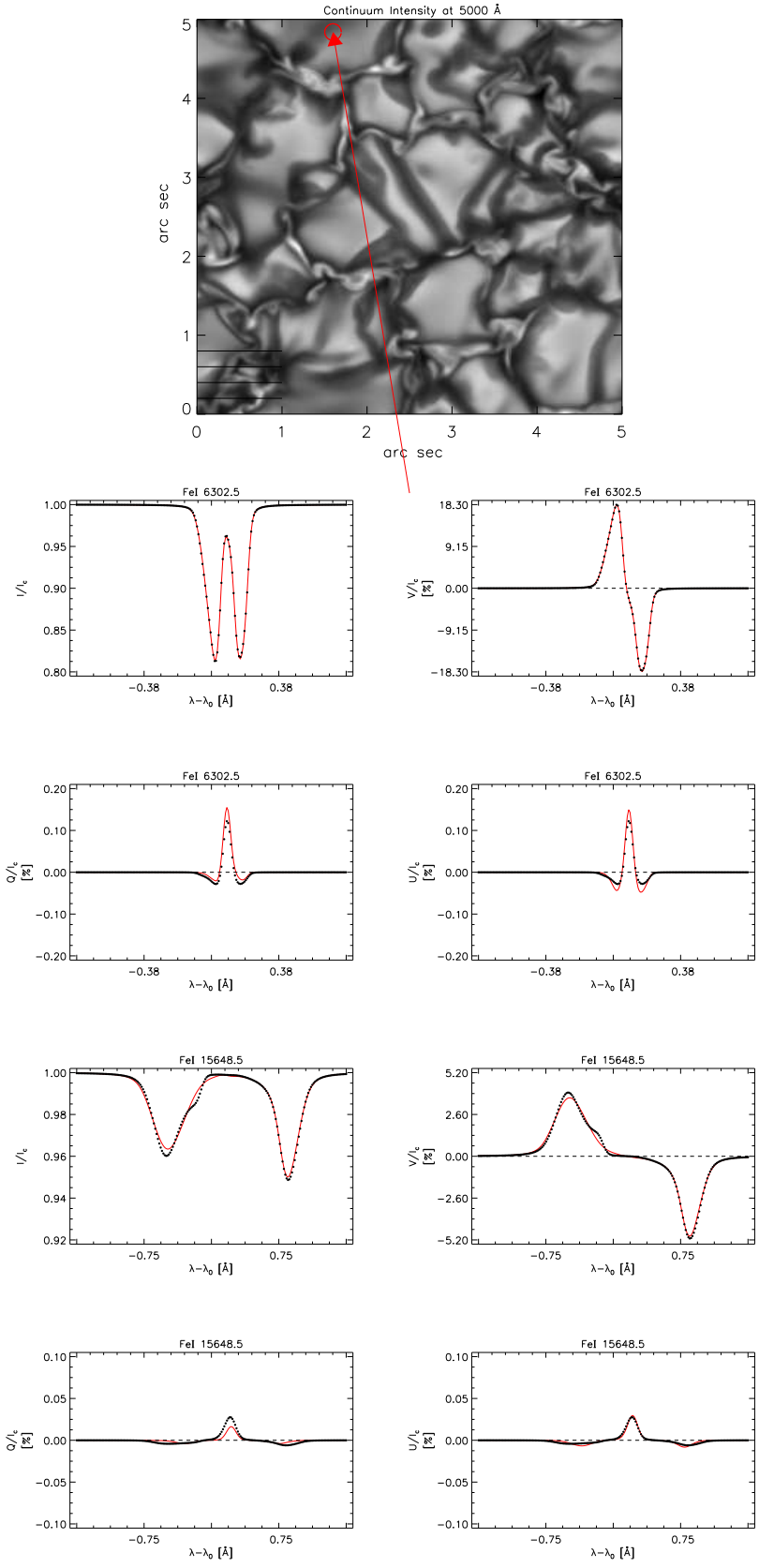

FIGURE 1.9: *Top panel*: continuum intensity image for a radiative MHD simulation (*Courtesy of Shelyag & Vögler*). Red circles indicates the point in the simulation box whose profiles are analyzed. *Bottom panel:* Observed (filled circles) and best-fit profiles from the inversion (solid red lines) Stokes profiles for the Fe I lines at 6302.5 and 15648.5 Å.

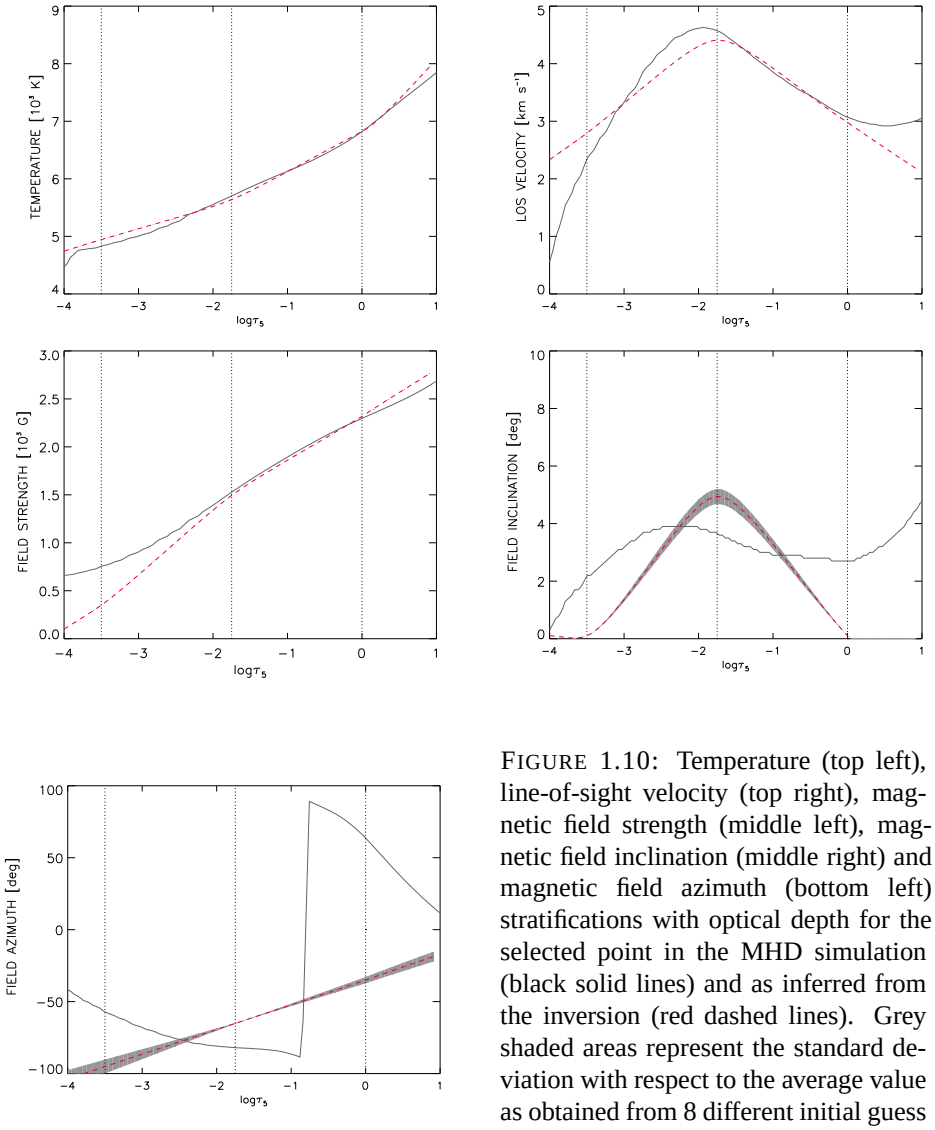

FIGURE 1.10: Temperature (top left), line-of-sight velocity (top right), magnetic field strength (middle left), magnetic field inclination (middle right) and magnetic field azimuth (bottom left) stratifications with optical depth for the selected point in the MHD simulation (black solid lines) and as inferred from the inversion (red dashed lines). Grey shaded areas represent the standard deviation with respect to the average value as obtained from 8 different initial guess models.

- **Discontinuities in the physical parameters**: discontinuities along the line of sight in the physical parameters should be understood as strong variations over a small optical depth range. These are easy to detect if enough node points are given to inversion, so that jumps are allowed to be present. However we must keep in mind that large number of free parameters should be avoided unless the observed profiles can not be successfully fitted with simpler models.

- **Unresolved structure**: the effect of the unresolved structure is perhaps the main reason why the scientific community, and among them, Solar physicist are still dubious about the potential of inversion techniques. The problem of the unresolved structure appears due to the limited spatial resolution that real observations can achieve. Let us for a moment consider the MHD simulation box used in this section as the 'real' Sun. If we were able to observe it with a 20 Km resolution it would be clear that all physical quantities could be considered as dependent only of the vertical coordinate (i.e. optical or geometrical depth). Since real spectropolarimetric observations rarely achieve resolutions better than 1 arc sec (about 700 Kilometres on the solar surface) many different features (granules, intergranules, bright points etc.) can be simultaneously present in the resolution element, each of them having different properties and hence, producing different observed profiles, from which we can only see an average. In almost all real situations we can be sure that, to some degree, we are dealing with unresolved structures. The key point here is to evaluate whether the vertical or horizontal variations play a major role in the observed spectral lines.

  Although plagued with problems, the Net Circular Polarization (see Sect. 1.4.1) is a widely used tool to check if vertical gradients, or on the other hand, horizontal inhomogeneities should be included ($N > 1$ in Eq. 1.118, 1.119). There are many situations when it is desirable to include both features (i.e. several components present in the resolution element together with gradients along the line-of-sight). Needless to say, including several components in the inversion can be only carried out in very favourable circumstances because the separate inference of the properties of each atmosphere is a very difficult task. This is due to the fact that spatially averaged profiles tend to lose the information of the individual components. Some examples can be given: granules produce a blueshift on the observed spectral line but the opposite occurs for intergranules. If we take an observation that contains both of structures, the averaged profile would show, either little or no net wavelength shift at all, and therefore we would not be able to infer any velocity, although we know it is present. The same happens for example when there are mixed polarities in the same resolution element ($\gamma_1 < 90^\circ$ and $\gamma_2 > 90^\circ$). The first one produces Stokes V profiles that have a positive blue lobe but negative red lobe, while the opposite happens for the γ_2. Therefore in the averaged profile we would observed no signal and hence no magnetic field would be inferred. This loss of information is basically the reason why the solar community believes that inversion codes are not robust and depend strongly on the initial guess model. As shown in this section, as well as demonstrated many times in the past (Ruiz Cobo & del Toro Iniesta 1994; Sánchez Almeida et al. 1996; del Toro Iniesta & Ruiz Cobo 1996,1997; Westendorp Plaza et al. 1998) this is not the case. As soon as one geometrical scheme (one component with gradients, two components without gradients, etc.) is chosen, IC's are extremely robust and retrieve the same atmosphere independently of the initial guess.

The real question is how to interpret the different results when different geometries are assumed. This will be one of the main subjects of this thesis, in particular the use of different models to study the fine structure of the sunspot penumbra.

Chapter 2

Sunspot Penumbra

In this chapter we introduce the reader to the most prominent photospheric manifestation of the solar magnetic field: sunspots. We briefly describe the main aspects of its magnetic and thermal structure as well as its best known dynamical aspect: the Evershed effect. For an exhaustive, detailed and up-to-date description of the current level of knowledge about Sunspots the reader is prompted to read the excellent review by Solanki 2003 and references therein.

2.1 Sunspots

Sunspots are the most readily observable manifestation of solar magnetism. Their existence was known already in ancient China . However, for Western culture they were discovered by Fabricus, Harriot, Galilei, Scheiner and others around 1610, when their newly-invented telescopes were turned to the Sun. At those times their main constituents were already distinguished: a dark core called *umbra*, surrounded by a brighter halo, the *penumbra*. The newest generation of solar telescopes, post focus instruments , image reconstruction techniques such as phase diversity or speckle reconstruction and the use of adaptive optics to get rid of the blurring effect introduced by the Earth's atmosphere, allow us to observe sunspots with an angular resolution of 0.12-0.20 arc sec (about 90-150 kilometres). At this level sunspots appear as an almost living entity, with prominent and highly dynamical fine structure (both in the umbra and in the penumbra; see Fig. 2.1).

Sunspots were the first astronomical objects to be known to harbour a magnetic field (Hale 1908). Nowadays it is accepted that they are formed after magnetic flux tubes (stored in the so-called *overshoot region* [1]) rise through the *convective zone* until they appear at the solar surface (i.e. *photosphere*). The intersection of such flux tubes and the solar surface constitutes the sunspot (see Schüssler 2002 for a review).

[1] i.e. transition layer located between the Solar radiative core and the convective zone

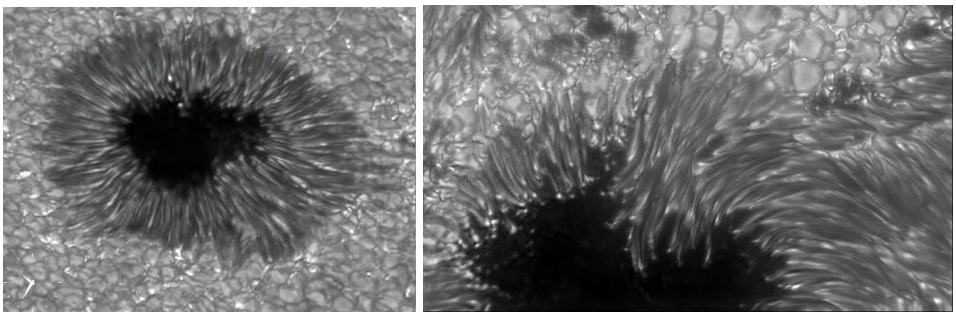

FIGURE 2.1: Left panel: Continuum image of NOAA AR 8704 taken with the Dutch Open Telescope (DOT) operating at the Spanish observatory of Roque de los Muchachos (La Palma, Teneriffe). The image was taken in the G-band (around 4305 Å). It was reconstructed using speckle technique developed at Göttingen Sternwarte. The achieved angular resolution is about 0.2 arc sec. *Courtesy of P. Sütterlin*. Right panel: G-Band continuum image of NOAA AR 10030. It was recorded using the adaptive optics system at the 1 meter Swedish Solar Telescope (SST) at the Spanish observatory of Roque de los Muchachos (La Palma, Teneriffe). Post image reconstruction was performed using the phase diversity technique. Spatial resolution is about 0.12 arc sec. *Courtesy of G. Scharmer*.

2.1.1 Umbra

In the umbra, the large magnetic field and its almost vertical inclination inhibits the convective energy transport, lowering its temperature to $T_{\rm umb}(\tau = 1) = 3500 - 5000$ K and making it appear darker than the quiet photosphere, where $T_{\rm pho}(\tau = 1) = 6000 - 6500$ K. In the umbra the average magnetic field is orientated vertically with respect to the solar surface, becoming slightly inclined as we approach the umbral-penumbral boundary ($\zeta_{\rm umb} = 20 - 40^{\circ}$)[2]. The magnetic field strength ranges from $B_{\rm umb} = 2000 - 3500$ Gauss, achieving the largest values for big sunspots. Except for some oscillatory phenomena, the umbra is commonly found to be at rest (no red-blue shift is found in spectral lines measured in the umbra). Fig. 2.3 shows the magnetic and kinematic structure of a regular sunspot obtained through the analysis of infrared spectropolarimetric data (Mathew et al. 2003).

The umbral fine structure is mainly composed of the so-called *umbral dots*, that appear as rounded bright features with typical sizes between 0.2-0.5 arc sec. They are believed to be hotter than the average umbral background, but the exact amount is still unknown. In general they are considered as being some sort of convective phenomena and many attempts, with controversial results, have been made to establish whether they carry any kind of flow or not. According to their relative position in the umbra, umbral dots are usually classified into central and peripheral. It is known that central dots remain stationary whereas peripheral ones seem to migrate from the outer towards the inner umbra. Their relation with the penumbra grains (see Sect. 2.1.2) is not yet clear.

[2]In the following we will distinguish between the magnetic field inclinations with respect to the solar surface or zenith angle (i.e. local reference frame where the vertical axis is perpendicular to the surface) ζ, and inclinations with respect to the observer or LOS angle (i.e. reference frame where the vertical axis is defined as the line connecting the observed point and the observer) γ. See also Sect 1.3 and Fig. 1.4 for further details.

2.1.2 Penumbra

If many phenomena observed in the umbra remain unknown, the penumbra overtakes its darker brother by a large amount. Even the question of why sunspots have a penumbra and how does it form remains unanswered. Our ability to offer a plausible explanation for its structure, brightness and dynamics is continuously being challenged by new features and fine structure revealed by the improvements in spatial resolution of the observations.

The penumbral fine structure, as seen in the continuum images (Fig. 2.1) is mainly characterized by a well organized radial distribution of, somewhat randomly alternating, bright and dark filaments. When their horizontal extension is under study one faces the difficulty of whether filaments are to be considered as bright features on a dark background or the other way around. In Fig. 2.2 we can see three examples of penumbral filaments taken at extremely high spatial resolution (0.12 arc sec; van der Voort et al. 2004). From these images it looks as if what we consider a filament is composed by a dark core escorted by a bright halo on both sides. At the birth of the filament the dark core is not present and the lateral brightening merge into a larger and brighter structure. If only the dark core is considered to be a penumbral filament then its horizontal extension is below 100 kilometres. According to van der Voort et al. (2004) it is likely that there is more unseen fine structure inside it. However the temporal evolution of these filaments seem to show that the whole structure (including the lateral brightening) move together, indicating that perhaps they are one single entity (Scharmer et al. 2002). These examples were taken near the umbra, where the density of filaments is small enough to distinguish individual filaments. Some of them can be traced to be as long as 5-9 arc sec (3600-6600 km; van der Voort et al. 2004). In the middle penumbra there are already so many of them that they become difficult to follow due to their fading and reappearing. Their vertical extension can not be derived from continuum images, but rather from methods involving the area asymmetry or Stokes profile inversions (see Sect. 3.2.3).

The initial, comet-shaped bright structure corresponds to the so-called *penumbral grains*. They are seen to move radially in the penumbra. A number of studies have tried to quantify their proper motions, finding basically that those in the inner penumbra move radially inwards (towards the umbra), whereas those located at large radial distances move predominantly outwards (Sobotka et al. 1999; Sobotka & Sütterlin 2001). Typical speeds for such motions are found to be of the order of 0.5-1 km s^{-1}.

It is important to remark that the information we can extract from continuum images is very limited, as they provide only partial information about the temperature. Nevertheless, the penumbral brightness (even neglecting its small scale variations) already arises a fundamental question. According to the penumbral magnetic field, convection should be heavily inhibited. However it is seen that its brightness is very much enhanced with respect to the umbra (where the magnetic field is only slightly stronger), being as much as 75 % of the quiet sun brightness. This is still one of the major unsolved problems (Schlichenmaier & Solanki 2003).

The definition of penumbral filament is more consistent when related to the magnetic field configuration of the penumbra and in particular its relation to the Evershed effect (Sect. 2.2.1). To investigate these issues a different kind of observations are required. Namely the most suitable ones are those where the full Stokes vector (I,Q,U,V) was measured in one/several magnetic sensitive lines ($g_{\rm eff} \neq 0$). Unfortunately these kind of observations lack from the high spatial

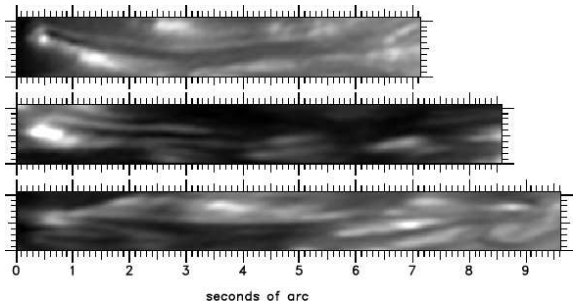

FIGURE 2.2: Three examples of penumbral filaments harbouring dark cores taken with the SST. Vertical and horizontal tickmarks are separated by 0.1 arc sec. *Courtesy of L. Rouppe van der Voort.*

resolution of the continuum images shown in Fig. 2.1 and 2.2. Typically, spectropolarimetric observations with 1 arc sec resolution are already catalogued as high resolution. This is an important point to be borne in mind when trying to extrapolate and compare the magnetic and kinematic structure with the brightness distribution.

In its simplest description (i.e. ignoring its fine structure) the penumbra appears as a smooth radially structured region where the magnetic field is smaller than in the umbra and more inclined (see Fig. 2.3): the magnetic field strength decreases radially from $B_{\rm pen} = 2000 - 2500$ gauss in the umbral-penumbral boundary, up to $B_{\rm pen} = 500 - 1000$ at the penumbral-quiet sun boundary; inclinations angles from $\zeta_{\rm pen} = 40^\circ$ to $\zeta_{\rm pen} = 70 - 80^\circ$. The temperature is close to that of the quiet sun: $T_{\rm pen} = 5800 - 6200$ K. The vertical and horizontal magnetic structure of the penumbra will be discussed in detail in Sect. 2.2.

2.1.3 The Evershed effect

In 1909, Evershed observed several spectral lines for a wide sample of sunspots at different positions on the solar disk (i.e. different heliocentric angles). From the observed Doppler shift he was able to establish that there is an outwards flow in the sunspot penumbra: producing red shifts in the spectral lines when looking in the limbward side of the penumbra, and a blue shift when looking at the diskward side. He also detected that the absolute magnitude of the shift was larger for sunspots located neat the limb, concluding that the outflow has primally parallel to the solar surface (see Fig. 2.3; bottom panel).

One year before this discovery, Hale (1908) detected the presence of a magnetic field in the sunspots and had ascribed it to vortex motions within the spot. Because of this, Evershed's first thought was to interpret such wavelengths shifts to azimuthal flows rather than radial. However, he finally abandoned this idea as he detected that the magnitude of the wavelength shift was maximum when the slit of his spectrograph lay along the line connecting the spot with the center of the solar disk (line of symmetry), but disappears when the slit his perpendicular to this line.

Moreover, Evershed already realized that the magnitude of the velocity related to the Evershed effect increases radially in the penumbra, achieving its largest values just at the outer boundary and suddenly disappearing after it. In his words: *This seems to imply an accelerating movement from the center of the spot outwards; yet at the limits of the penumbra the motion*

apparently ceases abruptly.

Although the radial dependence of the magnetic field strength and inclination seems to be well established, in the case of the Evershed effect the situation is very different. In particular whether the velocity continues beyond the visible limit of the penumbra or, as initially proposed by Evershed, disappears. A large number of studies have tried to settle the problem by means of different observations and analysis techniques: measuring the core/wing wavelength shifts in the intensity profiles in non-magnetic lines ($g_{\rm eff} = 0$), zero crossing in Stokes V, using lines formed at different heights etc. The literature is crowded with results favouring both pictures. Examples of works favouring the abrupt disappearance we shall cite: Maltby 1964; Beckers 1969a; Wiehr et al. 1986; Wiehr & Degenhardt 1992). Others, like Küveler & Wiehr 1985, Dialetis et al. 1985, Alissandrakis et al. 1988, Dere et al. 1990 found a continuity of the Evershed flow. A major contribution came in 1994, when Solanki and coworkers, analyzing the full Stokes vector of two neutral iron lines at 1.56 μm, were able to follow the Evershed effect well beyond the outer limit of the penumbra. However, through mass conservation considerations they argued that the flow they detected as a continuation of the Evershed flow beyond the penumbra, carries only a small fraction of the original mass flux. They therefore concluded that most of the flow had already disappeared within the penumbra.

Here we have explicitly mentioned that the Evershed effect implies a net mass transport (it is due to a plasma flow). However, it is important to recall that some attempts were made to explain the Evershed effect in terms of waves, that would not imply any net mass transport. This mechanism was first introduced by Maltby & Eriksen (1967). They considered isothermal sound waves propagating radially outwards where the density, pressure and velocity were oscillating in phase. In this case the opacity increases with increasing density and as a result there is a greater contribution to the average absorption coefficient when the particle velocity is directed toward the observer than when it is away from the observer, thus producing a net shift on the spectral lines and a line asymmetry. A difficulty with the sound-wave mechanism was noticed by Bünte et al. (1993). They pointed out that the propagation of such waves would have no preferred direction. Thus, this mechanism should produce an Evershed effect along the line of sight, including one perpendicular to the solar surface with the sunspot at disk center, contradicting observations. This problem with the sound wave mechanism led Bünte et al. (1993) to consider another kind of wave which would have a preferred horizonal direction of propagation: magneto acoustic surface gravity waves. Surprisingly they found that these surface waves should propagate radially inwards (towards the umbra) in order to reproduce the correct line asymmetry and shifts. This study was carried out for Fe I lines. Bünte & Solanki (1995) realized that the very same waves would produce the opposite shifts and line asymmetries for Fe II lines. Therefore, the wave mechanism seemed untenable and nowadays it is accepted that the Evershed effect is produced by flows, although very important questions related to the flow mechanism are still unanswered (see Sect 2.3).

2.2 Penumbral structure

In this section we will look at the penumbral structure by separating its vertical and horizontal features. Although this approach have several disadvantages, we deem it necessary in order to

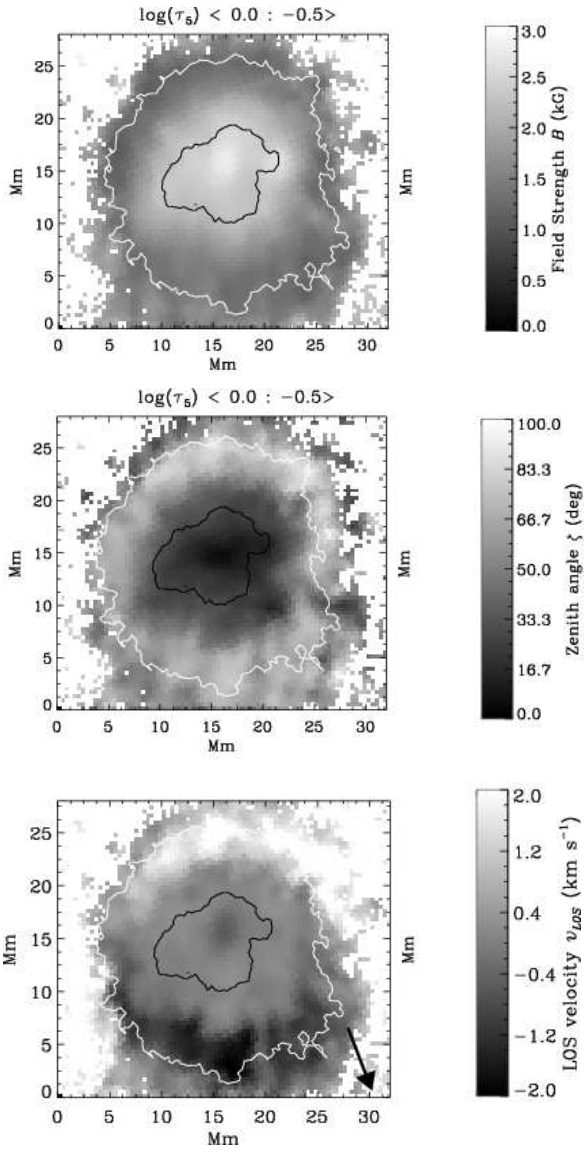

FIGURE 2.3: Two-dimensional map of the magnetic field strength B (top panel), magnetic field zenith angle ζ (middle panel) and line-of-sight-velocity $V_{\rm LOS}$ (bottom panel). Physical quantities correspond to the layers between optical depth: $\log\tau_5 = [0, -0.5]$. The black arrow in bottom panel indicates the direction of the center of the solar disk (i.e., direction of the observer). $V_{\rm LOS}$ shows a clear asymmetry between the limbward penumbra (redshifted velocities: $V_{\rm LOS} > 0$) and the diskward side (blue shifted velocities: $V_{\rm LOS} > 0$). The velocity goes away from the observer at the limb side but towards him at the center side, indicating therefore that the flow is directed radially outwards. These maps were obtained using a 1-component model applied to the pair of magnetic sensitive neutral iron lines at 1.56 μm (from Mathew et al. 2003).

clarify several aspects that will be the main topics of this thesis. In contrast to the previous section, where a more historical approach was followed, here we will mainly focus on those results that seem robust enough to be accepted, yet challenging to draw serious shortcomings to the theoretical models aiming to explain the nature of the Evershed flow (discussed in Sect. 2.3). Reviews about the penumbral structure are available in the literature, in particular we benefit from the excellent works by Martínez Pillet (1997) and Bellot Rubio (2003).

2.2.1 Penumbral horizontal structure

The penumbral horizonal structure is better seen when inversion methods that assume that all quantities are constant with depth are used (e.g. Milne-Eddington-like inversions, Sect. 1.4.3). Of course, when this is done the obtained results will be biased due to the fact that the vertical structure is not being taken into account, and therefore they should be considered as an average over the height range of formation of the studied lines. Nonetheless we will take this approach assuming that, if some correlations between the different physical parameters appear when this kind of inversion is carried out, they will be also clearly discernible at some optical depth when an inversion, that takes into account the depth dependence of the physical quantities, is used.

We shall therefore refer in this section mainly to those studies that consider all quantities depth independent. Hence, not only Milne-Eddington inversion applies, but also any other method that retrieves one single value of the magnetic field (peak-to-peak separation in Stokes V), velocity (line core shift) etc. at each pixel.

Azimuthal fluctuations in the magnetic field

During the early and mid 90's there was an intense debate over whether the magnetic field strength and/or inclination fluctuate azimuthally in the penumbra[3]. Schmidt et al. (1992) and Rimmele (1995) argued, from the investigation of Stokes I and V of Fe I lines at 6302.5 Å ($g_{\rm eff} = 2.5$) and 5250 Å ($g_{\rm eff} = 3$) respectively, that only the magnetic field inclination changes azimuthally by an rms fluctuation of $\Delta\gamma = 10 - 15^{\circ}$. The investigation of these authors is, however, subject to several drawbacks. First of all, the lack of knowledge of the other Stokes parameters (linear polarization: Q,U) prevent them from applying a reliable instrumental cross-talk correction. Secondly their values of the total magnetic field strength were obtained through the separation between the two σ components in the total intensity profiles. For typical penumbral field strengths, these two components almost overlap with the central π component in the lines they used, making their inference difficult.

Stronger support was given by Title et al. (1993) who found that the signal in their longitudinal magnetogram showed rapid azimuthal fluctuations. By using a simple geometrical model they conclude that fluctuations in the magnetic field strength could not explain such a behaviour. Thus, they ascribed such fluctuations to the magnetic field inclination (see Fig. 2.4; top panel). However, Lites et al. (1993) deduced, by means of a Milne-Eddington inversion of the full Stokes vector, that both the magnetic field strength and inclination were changing by rms values as large as $\Delta\gamma = 10^{\circ}$ and $\Delta B = 100$ G (see Fig. 2.4; bottom panel). The controversy was finally resolved

[3] Azimuthal fluctuation indicates its variation with the position angle along an azimuthal cut of a constant radius in the penumbra

by Martínez Pillet (1997) who noticed that, although ΔB was not able to produce the observed fluctuations in the circular polarization (a fact that led Title and co-workers to ascribe it to $\Delta\gamma$), it was able to change the linear polarization, explaining therefore why Lites et al. (1993), who measured the full Stokes vector, obtained fluctuations both in B and γ (see Fig. 2.5).

These fluctuations found by Lites et al. (1993) and later by Stanchfield et al. (1997), Westendorp Plaza et al. (2001b) and Mathew et al. (2003) were anticorrelated in the sense that stronger magnetic fields correspond to more vertical ones, the more inclined (with respect to the vertical) being weaker. This gave rise to what is known as the *fluted penumbra*.

Magnetic field-Evershed flow correlation

More clear seems to be the correlation between the magnetic field vector and the Evershed flow. Almost all authors have found that the Evershed flow is seen better at those locations where the magnetic field is stronger and more vertical (i.e. *spines*), being mainly concentrated in the regions where the magnetic field is weaker and more inclined (i.e. *intraspines*). Among others: Rimmele 1995, Stanchfield et al. 1997, Westendorp Plaza et al. 2001b, Mathew et al. 2003. See for example Fig. 2.6. Note that what it is measured are line-of-sight velocities, therefore this difference in the velocities cannot be explained in terms of projection effects. In particular, if $\mathbf{v} \parallel \mathbf{B}$ is assumed and it is measure that $v_{los,spines} < v_{los,intra}$ and $\gamma_{spines} < \gamma_{intra}$, then this means that in fact the absolute magnitude of the Evershed flow in the intraspines is much larger that in the spines: $v_{intra} \gg v_{spines}$.

The assumption of parallelism between the velocity and the magnetic field vector has been repeatedly tested in the past (Kinman 1952, Maltby 1964, Schröter 1965, Title 1993, Rimmele 1995, Schlichenmaier & Schmidt 2000) with the surprising result that the magnetic field vector seemed to be less inclined (with respect to the vertical) than the velocity vector by roughly 10°. Only very recently Bellot Rubio et al. (2003) have demonstrated that in fact $\mathbf{v} \parallel \mathbf{B}$.

Penumbral brightness-Evershed flow correlation

The relation between the penumbral brightness and the Evershed flow (and hence with the magnetic field) is one of the most elusive features of the sunspot penumbra. Most investigations conclude that the Evershed flow is mainly located along the dark radial structures: Wiehr & Degenhardt (1992), Lites et al. (1993), Rimmele (1995), Stanchfield et al. (1997), Tritschler et al. (2004). However, others find small correlation or no correlation at all: Wiehr & Stellmacher (1989), Lites et al. (1990), Schlichenmaier & Schmidt (2000), Hirzberger & Kneer (2001). In general it is accepted that the correlation increases with increasing spatial resolution (Wiehr & Degenhardt 1992) or when brightness and velocity are measured roughly at the same depths in the photosphere (Rimmele 1995; Fig. 2.7). However, as pointed out by Bellot Rubio et al. (2004a) the line asymmetries, and consequently the intensities in a spectral line, are dominated by the Evershed flow. Therefore, in this particular case intensity or brightness are to be associated more with the velocity field rather than with temperatures, explaining thus the very good correlation found by Rimmele (1995; see Fig. 2.7).

Spectropolarimetric observations achieve rarely resolutions better than 1 arc sec. Despite this, some authors have found a correlation between the penumbral brightness and the Evershed

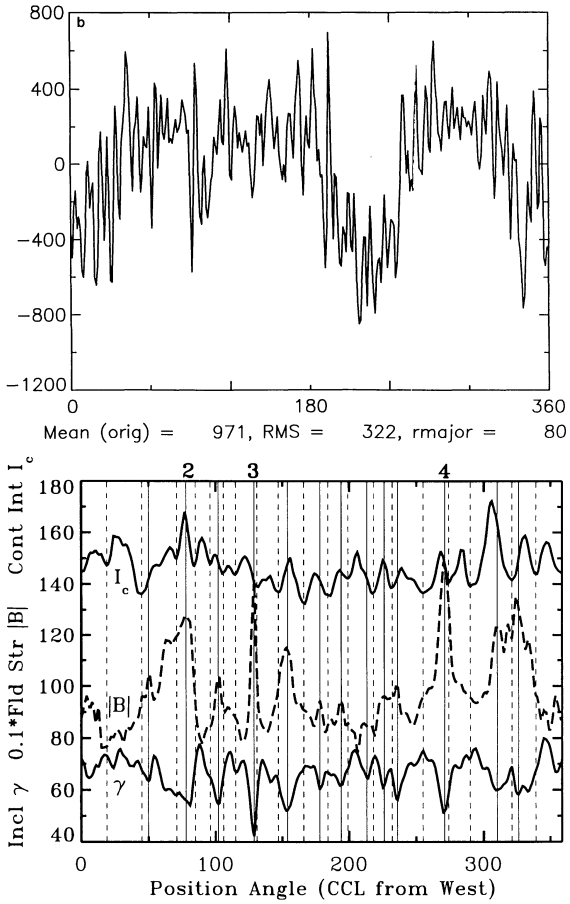

FIGURE 2.4: *Top panel*: azimuthal fluctuations in the longitudinal signal of the magnetic field (Stokes *V*) found by Title et al. 1993. They concluded that the quantity that undergoes these fluctuations is the magnetic field inclination. Bottom panels: azimuthal fluctuation of the continuum intensity (top solid line), magnetic field strength (dashed line) and magnetic field inclination (bottom solid line) found by Lites et al. (1993). Note that $\Delta\gamma$ and ΔB are anticorrelated.

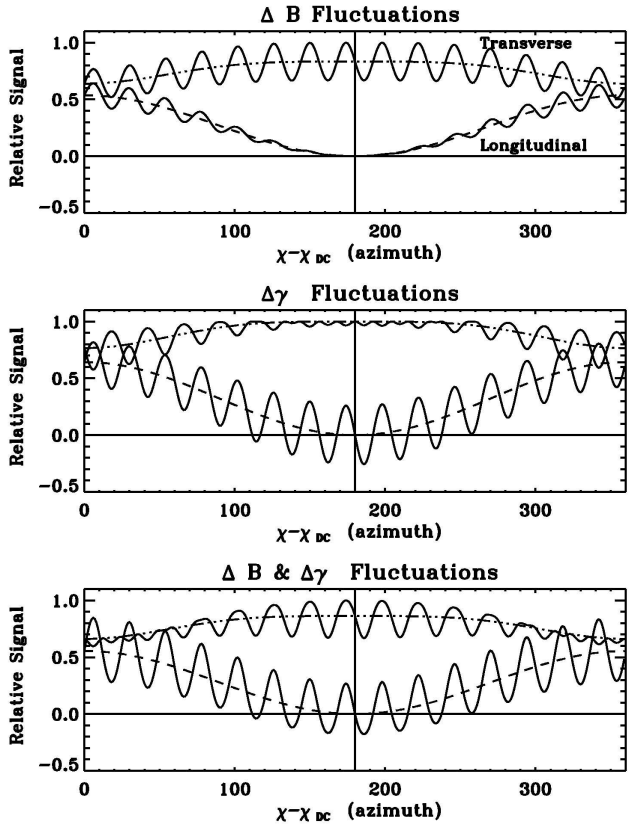

FIGURE 2.5: *Top panel*: azimuthal fluctuations in the longitudinal and transversal magnetogram signals (Stokes V and $\sqrt{Q^2+U^2}$ respectively) induced by ΔB. Only the transverse signal shows a variation. *Middle panel*: the same but for $\Delta\gamma$. Now only the longitudinal signal fluctuates. Note that Title et al. (1993; Fig. 2.4 top panel) only measured the longitudinal component of the magnetic field (Stokes V), hence deducing that the fluctuations are due to $\Delta\gamma$ rather than ΔB. *Bottom panel*: the same but for joint and anticorrelated fluctuations in $\Delta\gamma$ and ΔB. Now both signals undergo rapid azimuthal variations. Note that in order to be able to distinguish between variations in the magnetic field strength and/or inclination the linear polarization (Stokes Q and U) must be also measured as done by Lites et al. (1993; see Fig. 2.4 bottom panel). *From Martínez Pillet (1997)*.

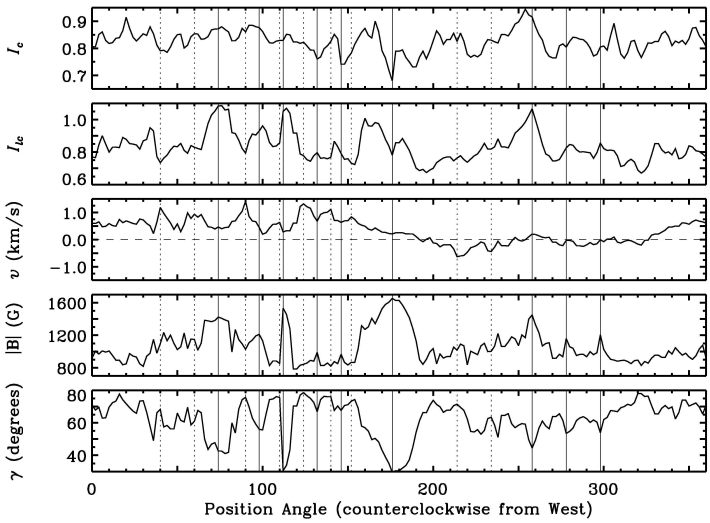

FIGURE 2.6: Azimuthal variations in the different physical quantities (from top to bottom: continuum intensity, core intensity, line of sight velocity, magnetic field strength and inclination) obtained from a Milne-Eddington inversion of the visible Fe I lines at 6300 Å . Note that in the limb side penumbra (position angles between 0 and 180 deg) there is a clear correlation between the line of sight velocity and magnetic field strength and inclination. Larger red shift velocities are located at the same places where the magnetic field is weak and more inclined. *From Stanchfield et al. 1997.*

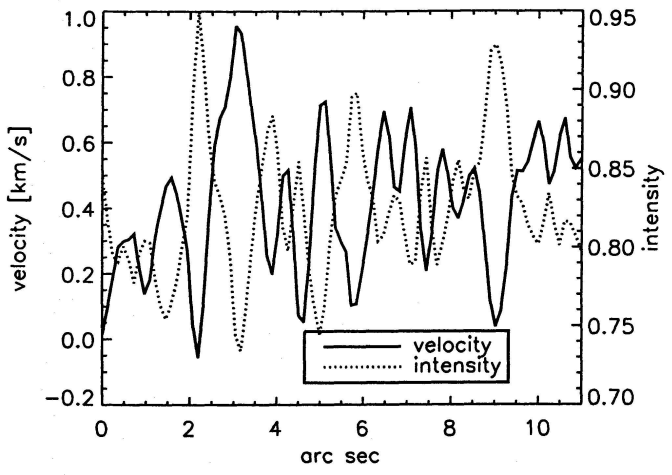

FIGURE 2.7: Intensity (dotted line) and line-of-sight velocity (solid) measured in the wings of the non-magnetic Fe I 5576 Å line. There is a clear anticorrelation: the larger the speed, the darker the structure. The spatial resolution of this observation is about 0.5 arc sec. *From Rimmele 1995.* Intensities are correlated with the measured line-of-sight velocities because the line asymmetries are induced by the Evershed flow.

flow (e.g. Stanchfield et al. 1997; Westendorp Plaza et al. 2001a) with such observations. Two-dimensional spectroscopy, in particular when combined with image reconstruction techniques, seem to yield better correlations between dark filaments and the Evershed flow (van der Oort 2002; Tritschler et al. 2004). Most of these studies have been carried out for non-magnetic spectral lines ($g_{\rm eff} = 0$), in order to avoid influences from the magnetic field. Nevertheless it is important to recall that those studies lack, in most cases, a very important source of information for the velocity field, such as Stokes V shift and asymmetry.

In this sense the visible Fe II 6149 Å line represents a step towards the resolution of the dilemma. Its Zeeman pattern does not produce linear polarization, making the cross talk correction between the components of the Stokes vector very reliable. Measurements of this line in Stokes I and V, combined with speckle reconstruction (Bello González & Kneer, private communication) and adaptive optics (Bellot Rubio, L.R., private communication) have already been carried out by the Göttingen and Freiburg groups, and very likely their results will throw some light on this question.

Last but not least, when we observe the penumbra at extremely high spatial resolution (Fig. 2.1 and 2.2) we do realize that the intensity fluctuations occur at scales (0.1 arc sec) much smaller than our ability to measure velocities (0.5 arc sec at best). Obviously a reliable determination of the relation between the azimuthal intensity fluctuations and the Evershed flow will be only achieved when high spatial resolution spectropolarimetric observations will become available.

2.2.2 Penumbral vertical structure

The vertical structure of the penumbra is far less understood. Traditionally, employed methods have been restricted to study Stokes I only, and therefore limited to investigate the depth dependence of the Evershed flow (measuring line core shifts of lines formed at different heights, Doppler shifts in the bisectors at different intensity levels, etc.). With this, it has been quite well established that the magnitude of the Evershed flow increases with increasing depth in the photosphere (Börner & Kneer 1992; Wiehr & Degenhardt 1992; cf. Rimmele 1995). At the temperature minimum (around 500 km above the continuum level) the signature of the flow disappears and becomes opposite further up (*inverse chromospheric Evershed flow*, which is characterized by blue shifts in the limb side penumbra and red shifted velocities in the center side; compare with Fig. 2.3).

To study the depth dependence of the magnetic field vector, it is not trivial (as in the case of Stokes I) to ascribe different heights to different wavelength positions (deep layers-wings, high layers-core etc.). In addition, Milne-Eddington inversions are not suitable to study the vertical stratification, as they neglect the dependence of the physical magnitudes with height. Therefore, only when the RTE is solved self-consistently (i.e. taking into account the different range of formation of the spectral lines, the different atmospheric layers which contribute to the polarization signals at each wavelength position etc.) this problem can be addressed (Ruiz Cobo & del Toro Iniesta 1992,1994; Collados et al. 1994, Sánchez Almeida et al. 1996).

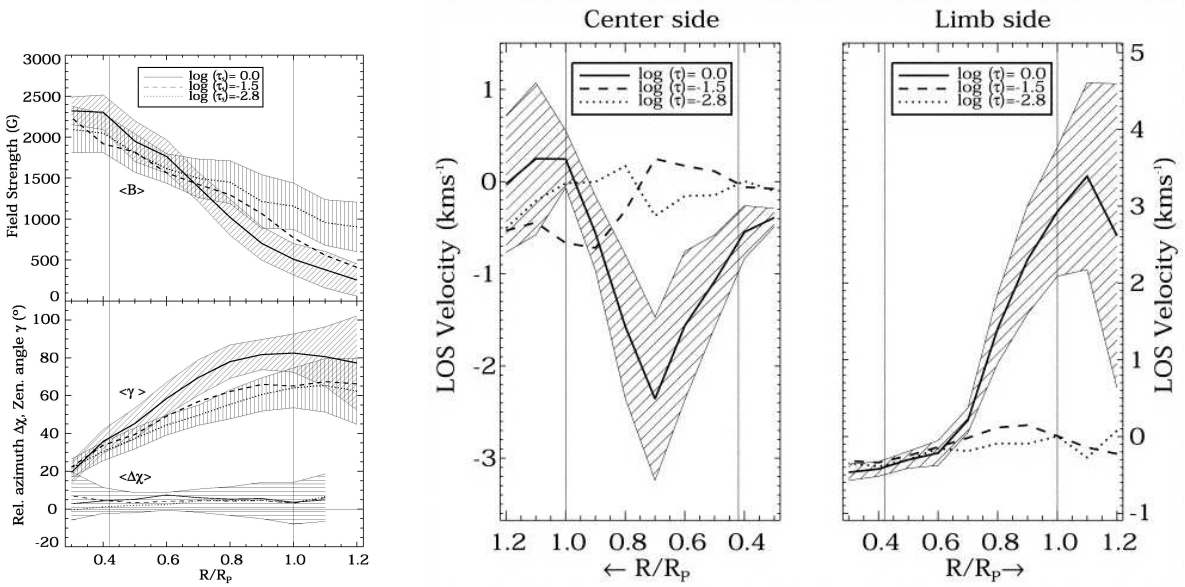

FIGURE 2.8: Radial variations of the magnetic field strength and inclination (left panels) and line of sight velocity (right panels) for three different optical depths: $\log\tau_5 = [0, -1.5, -2.8]$. The magnetic field strength increases with increasing height, whereas the opposite happens for the magnetic field inclination and the line-of-sight velocity. *From Westendorp Plaza et al. 2001a,2001b.*

Visible Stokes profle inversion

Westendorp Plaza and co-workers (1997; 2001a,2001b) have presented the first tomography of a sunspot penumbra with the pair of visible Fe I lines at 6300 Å recorded with the Advance Stokes Polarimeter (ASP, Elmore et al. 1992). They used a Stokes inversion technique based on Response functions (SIR; Ruiz Cobo & del Toro Iniesta 1992) to characterize for the first time the magnetic field strength and orientation as well as the line-of-sight velocity at different layers in the photosphere. Their study was based on a 1 magnetic component inversion, where physical magnitudes where allowed to change in the vertical direction, but not in the horizontal (e.g. Sect. 1.5.7).

Their results show (see Fig. 2.8) that, in most of the outer penumbra, the magnetic field strength increases towards higher layers, but the opposite occurs for the line of sight velocity and magnetic field inclination (they increase towards deeper layers). In terms of derivatives with respect to geometrical height we can therefore write that:

$$\frac{dB}{dz} > 0 \quad , \quad \frac{d\gamma}{dz} < 0 \quad , \quad \frac{dv_{los}}{dz} < 0 \tag{2.1}$$

Perhaps, their most striking result concerns the finding that in the deep layers of the outer penumbra (around $\log\tau = 0$) the magnetic field inclination (with respect to the vertical on the solar surface) reaches values larger than 90°, thus indicating that the magnetic field lines return

into the solar surface (see solid lines in right bottom panels in Fig. 2.8). The importance of this result lies in that fact that it solves the problem about the sudden disappearance of the Evershed flow at the outer penumbral edge (see Sect. 2.1.3) and offers a plausible explanation for the lack of mass conservation (Solanki et al. 1994).

Infrared Stokes profile inversion

Inversions in the infrared band, mainly for the pair of Fe I lines at 1.56 μm have been presented by Bellot Rubio et al. (2002) and, in a more detailed work, by Mathew et al. (2003). Using a very similar model to that used by Westendorp Plaza et al. they found that, although the same azimuthal correlations (Sect. 2.2.1) are detected, the stratifications with optical depth of the kinematic and magnetic properties of the sunspot penumbra differ significantly from those obtained with visible data (see Fig. 2.9). In particular a decreasing magnetic field, but increasing line-of-sight velocity and field inclination, with increasing height are found throughout almost the whole penumbra. As a function of the derivatives with respect to the geometrical height it can be written as:

$$\frac{\mathrm{dB}}{\mathrm{dz}} < 0 \quad , \quad \frac{\mathrm{d}\gamma}{\mathrm{dz}} > 0 \quad , \quad \frac{\mathrm{dv_{los}}}{\mathrm{dz}} > 0 \tag{2.2}$$

Note that these are exactly the opposite behaviours than those obtained through the inversion of the pair of Fe I lines at 6300 Å (Eq. 2.1). This apparent contradiction between the results from the inversion (1-component including gradients) of visible and infrared lines provides, as already pointed out by Mathew et al. (2003), a possible explanation if we assume that the penumbral structure is composed by horizontal flux tubes (that carry the Evershed flow) that are embedded in more vertical magnetic surroundings (i.e. *uncombed penumbral model* proposed by Solanki & Montavon 1993; see Fig. 2.10).

Fig. 2.11 shows an example of the inferred stratifications when profiles, that have been synthesized using an atmosphere whose stratifications are based on the uncombed model (dot-dashed line), are inverted with a 1 component model (such as those use by Westendorp et al. and Mathew et al.) separately for the visible Fe I lines at 6300 Å (dashed lines) and the infrared Fe I lines at 1.56 μm (solid lines). The synthetic profiles are shown with solid lines in the bottom panels, while the fits achieved by the inversion are represented by filled circles. This test was carried out, as in Sect. 1.5.7, using several different initial guess models. The retrieved stratifications show the opposite gradients for the visible and infrared lines (cf. Eqs. 2.1-2.2). This can be interpreted as if the visible lines were formed at a height were they are mainly affected by the upper discontinuity produced by the presence of a horizontal flux tube, whereas the infrared lines would be affected mainly by the lower discontinuity (see Fig. 2.10; right panel).

Stokes V area asymmetry

Stokes V area asymmetry, denoted as

$$\delta A = \frac{\int V(\lambda)\mathrm{d}\lambda}{\int |V(\lambda)|\mathrm{d}\lambda} \tag{2.3}$$

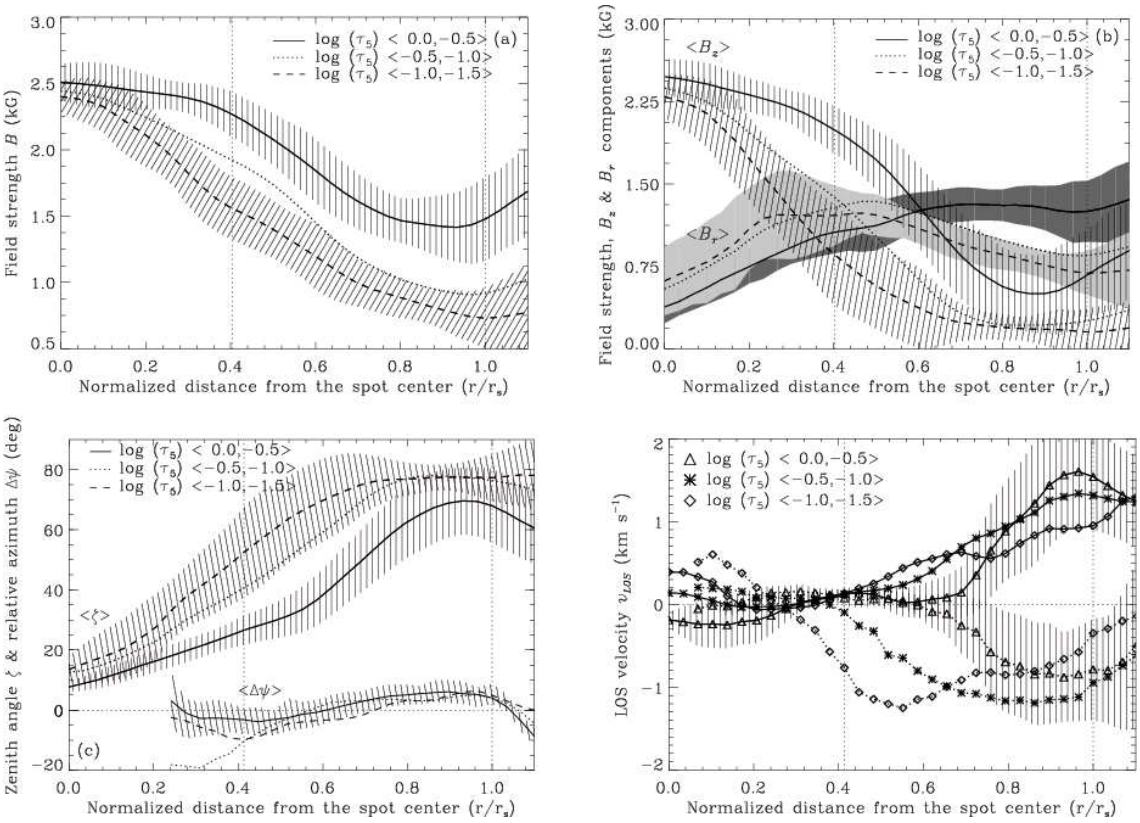

FIGURE 2.9: Radial variations of the magnetic field strength (top left panel) , magnetic field zenith angle (bottom left panel) and line of sight velocity (bottom right panels) for three different optical depths: $\log\tau_5 \simeq [0, -0.75, -1.25]$. The magnetic field strength decreases with increasing height, whereas the opposite happens for the magnetic field inclination and the line-of-sight velocity (i.e. the increase towards high layers). *From Mathew et al. 2003.*

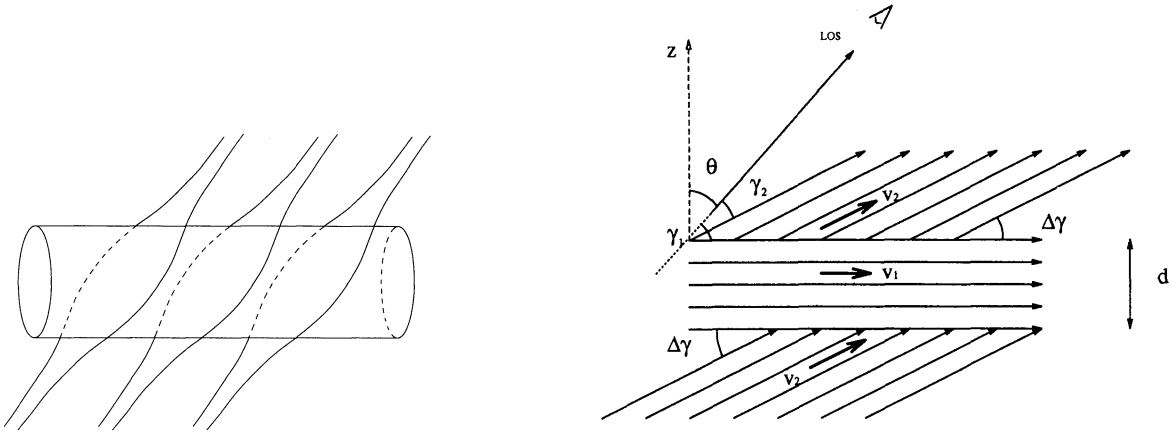

FIGURE 2.10: Left panel: Sketch of the *uncombed penumbral model*. The penumbral structure is assumed to be composed by horizontal flux tubes carrying the Evershed flow embedded in a magnetic surrounding, where the magnetic field is more vertical. Right panel: scheme of an observer whose line of sight crosses the surrounding atmosphere, pierces through a flux tube (with a diameter *d*) and sees again the surrounding atmosphere beneath it. *From Solanki & Montavon (1993).*

was first observed in sunspots by Illing et al. (1974a,1975b) and later by Kemp & Henson (1983), Henson & Kemp (1984), Makita (1986), Makita & Ohki (1986)[4]. These works established a number of empirical rules for the magnitude of the area asymmetry, as well as its spatial distribution in the sunspot (e.g. Fig. 2.12), that have long remained without explanation. Solar physicists were well aware that, in order to produce a net area asymmetry in the circular polarization, gradients along the line of sight in the magnetic field vector and line-of-sight velocity were needed [5] (e.g. Landolfi & Landi Degl'Innocenti 1982,1996; Landolfi 1987), but it was not until the remarkable paper by Sáchez Almeida & Lites (1992) that the magnitude of these gradients was evaluated. These authors found that, in order to reproduce the huge amount of area asymmetry observed in the penumbra of Sunspots in the Fe I lines at 6300 Å , gradients as large as $\frac{\mathrm{d}v_{\mathrm{los}}}{\mathrm{d}\tau} \sim 1.5$ km s^{-1} and $\frac{\mathrm{d}\gamma}{\mathrm{d}\tau} \sim 45^{\circ}$ for the line-of-sight velocity and magnetic field inclination respectively, were needed. Soon it was realized that such large variations over a small vertical extension would, very likely produce far too large curvature forces for a Sunspot to stay in mechanical equilibrium (see Solanki et al. 1993).

A major step towards the understanding of the NCP, was made by Solanki & Montavon (1993) when they proposed their *uncombed penumbral model*: a three layered model consisting of a central layer of horizonal field sandwiched between two layers of inclined field (Fig. 2.10). With the help of the following relation for the area of the blue, A_b, and red, A_r, lobes in Stokes V

[4] In fact, all these authors refer to the Net Circular Polarization (NCP; see Sect. 1.4.1). The area asymmetry is the NCP normalized to the total area of Stokes V.

[5] If gradients in these quantitates are not present the area of the blue lobe of Stokes V is equal and with opposite sign than that of the red lobe (see e.g. Fig. 1.6) and therefore $\delta A = 0$.

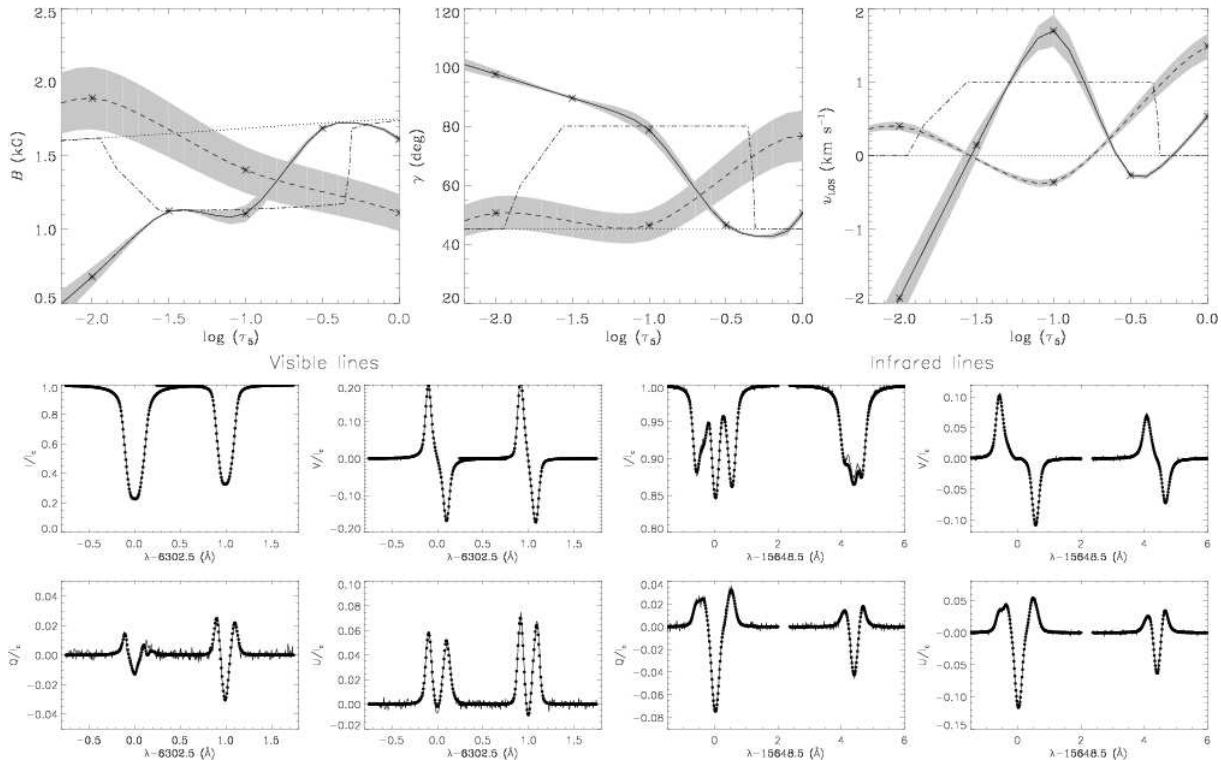

FIGURE 2.11: Top panels (from left to right): magnetic field strength, magnetic field inclination and line-of sight velocity. Original stratifications used to produce the synthetic profiles according to the uncombed model (dot-dashed lines), stratifications obtained after inverting the visible lines only (dashed lines) and the infrared lines alone (solid lines). Bottom panels: synthetic (solid lines) and best-fit profiles (filled circles) with the individual 1 component inversions. The stratifications used to simulate an uncombed penumbra can be understood in terms of Fig. 2.10, where we have made: $B_2 = 1750$ G, $\gamma_2 = 45^\circ$, $v_{\rm los,2} = 0$, $B_1 = 1250$ G, $\gamma_1 = 80^\circ$, $v_{\rm los,1} = 0$. The flux tube is located at a central position $z_0 = 150$ km above the continuum level and its radius was taken to be $d = 100$ km. *From Mathew et al. 2003.*

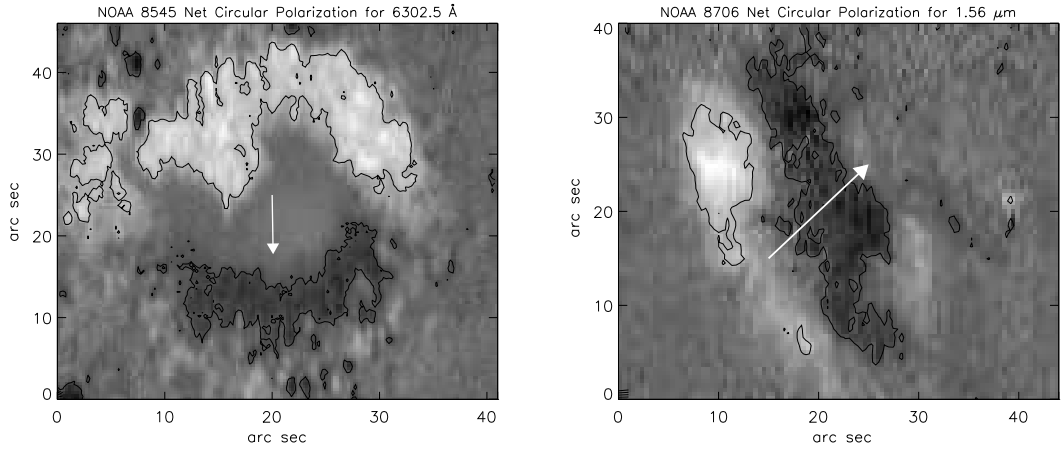

FIGURE 2.12: Left Panel: Net Circular Polarization (NCP) for the Fe I 6302.5 Å line in a sunspot, NOAA 8545, at an heliocentric angle $\mu = \cos\theta = 0.79$. The arrow points towards the Sun's disk center (this arrow also defines the line of symmetry of the spot). The sign of the NCP on the limb-side penumbra is positive, but negative for the center side. Right panel: NCP for the Fe I 15648.5 Å line in a sunspot, NOAA 8706, at an heliocentric angle $\mu = \cos\theta = 0.59$. The arrow points towards the Sun's disk center. Here, the azimuthal distribution of the NCP follows a different behaviour, with respect to the line of symmetry, than in the case of the visible Fe I line (left panel).

(see e.g. Solanki & Pahlke 1988; Sánchez Almeida et al. 1989),

$$\mathrm{sign}(|A_b| - |A_r|) = -\mathrm{sign}\left(\frac{\mathrm{d}v_{\mathrm{los}}}{\mathrm{d}\tau}\frac{\mathrm{d}|\cos\gamma|}{\mathrm{d}\tau}\right) \tag{2.4}$$

they were able to prove that this three layered model reproduces always Stokes V profiles such that the total area of the red lobe was larger than of the blue lobe: $|A_r| > |A_b|$ (see Fig. 2.13 and Table 2.1). Now, in the center-side penumbra, the average magnetic field is pointing towards the observer, so that $\gamma < 90^\circ$ and therefore: $A_r < 0$, while $A_b > 0$ (and the opposite happens in the limb-side penumbra since the average magnetic field is larger than 90 deg, so that the corresponding Stokes V profiles show the opposite polarity). This implies that the Net Circular Polarization, defined as $\int V(\lambda)\mathrm{d}\lambda$, changes it sign from the center-side, where it is negative, to the limb-side, where it becomes positive. This quantitatively reproduces the observed behaviour observer in the Fe I lines at 6300 Å (see Fig. 2.12; left panel). Note that the same behaviour would have been obtained by including only a two layers atmosphere: **a** or **c** for the limb-side and **b** or **d** for the center side. Indeed, the amount of NCP generated by a single boundary (i.e. jump in the physical quantities) is not sufficient to explain the observed one (e.g. considering only case **a**). However, in three layers atmosphere, that includes two of such jumps, the NCP generated at each discontinuity is not cancelled out but added (even though the sign of the jumps are opposite; see Table 2.1). We also note that, in the three layered model, there is no net jump in the physical parameters. In particular, for the magnetic field inclination ($\gamma_2 \rightarrow \gamma_1 \rightarrow \gamma_2$) this has the advantage that the equilibrium configuration of the penumbra is not affected. Last but not

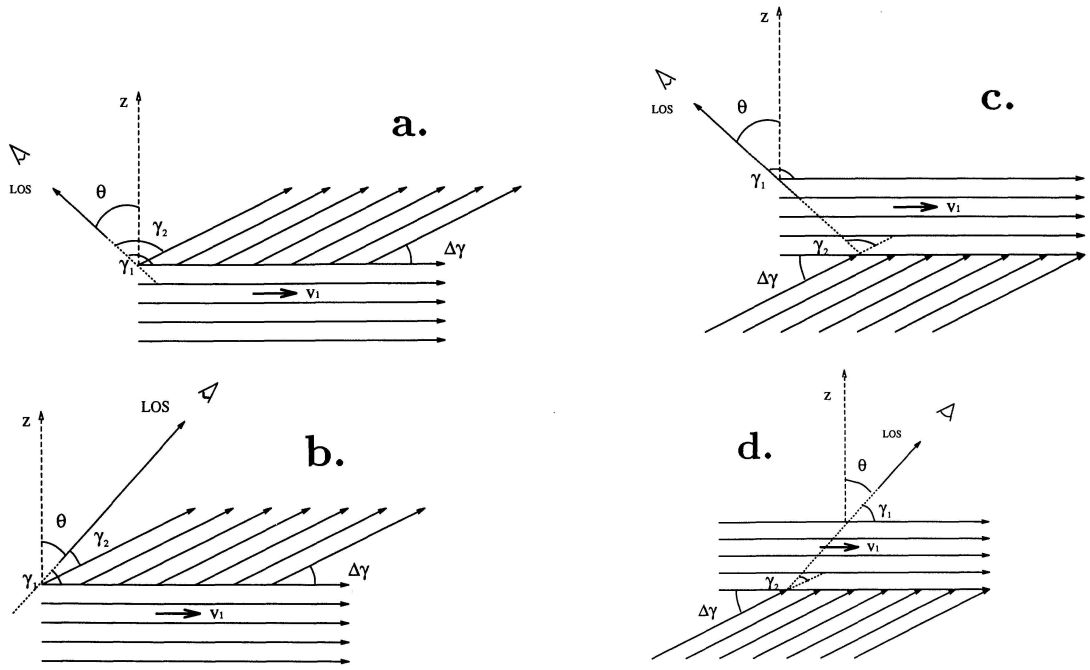

FIGURE 2.13: Geometrical scheme for the uncombed model. As the line-of-sight crosses the atmosphere, it finds first a magnetic field with an inclination γ_2 and velocity v_2 (**a** or **b** depending whether we look in the limb -side or center-side penumbra respectively). At a given position the properties of the atmosphere suffer a jump as the line-of-sight penetrates into the central layer, which is characterized by a field inclination γ_1 and a velocity v_1. Further down, another jump occurs from the horizontal field layer to the initial inclined field layer (**c** and **d** for the limb and center-side of the penumbra respectively). According to Eq. 2.4 one can work out the sign of the difference between the area harboured by the blue and red lobes in the circular polarization profiles (see Table 2.1). *From Solanki & Montavon (1993)*.

least it is important to remark that in order to reproduce the correct center-to-limb variation of the NCP[6], Solanki & Montavon deduced that most of the plasma velocity should be concentrated in the intermediate layer where the field is essentially horizontal, that is, $|v_1| \gg |v_2|$[7]. Note that this is exactly what was later obtained from more complex Stokes profiles inversions (see Fig. 2.11), and at the same time, it is consistent with the correlation between the Evershed flow and the magnetic field inclination found by other authors (see Sect. 2.2.1).

So far, we have discussed only the case of the visible Fe I lines at 6300 Å . For other wavelengths, the situation might significantly differ from what has been presented here. When infrared measurements became available, in particular for the Fe I lines at 1.56 μm (see Schlichenmaier & Collados 2002), different NCP azimuthal distributions appeared (see Fig. 2.12; right panel).

[6]The center-to-limb variation refers to the different viewing angles on the solar disk, that is, $\mu = \cos\theta$ ranging from 0 (Solar disk center) to 1 (Solar Limb).

[7]We use the absolute values in order to make this relation valid for the center-side penumbra, where velocities are negative (i.e. blue shift) and for the limb-side, where velocities are positive (i.e. red shift)

TABLE 2.1: Signs for the variations with optical depth in the line-of-sight velocity and magnetic field inclination, as well as the sign of $|A_b| - |A_r|$ (given by Eq. 2.4) corresponding to the geometries **a**-**d** in Fig. 2.13.

	$\frac{dv_{los}}{d\tau}$	$\frac{d\lvert\cos\gamma\rvert}{d\tau}$	$\mathrm{sign}(\lvert A_b\rvert - \lvert A_r\rvert)$
a	>0	>0	<0
b	<0	<0	<0
c	<0	<0	<0
d	>0	>0	<0

The mechanism invoked in the uncombed model, in order to reproduce the azimuthal behaviour of the NCP (jump in the line-of-sight velocity and magnetic field inclination), does not provide a satisfactory explanation for the observed NCP in the 1.56 μm lines. However, another very important contribution towards the understanding of the penumbral fine structure was made by Schlichenmaier et al. (2002) and Müller et al. (2002). They realized that, in the uncombed model, although the penumbral flux tubes and the magnetic surrounding have the same azimuthal angle in the local reference frame (l.r.f.), this is not the case for the observer's reference frame (o.r.f.). Let us, for example, consider a magnetic field vector such as that plotted in Fig. 1.4 (left panel). Let us also assume that the Y-axis in that plot corresponds to the line of symmetry of the spot in the limb-side penumbra (i.e. $-$Y points towards the direction of the Solar disk center). This defines the l.r.f., where of course the Z-axis is perpendicular to the solar surface. In this frame, the magnetic field vector **B** can be written as

$$\mathbf{B} = B\sin\gamma\cos\varphi\mathbf{e_x} + B\sin\gamma\sin\varphi\mathbf{e_y} + B\cos\gamma\mathbf{e_z} \tag{2.5}$$

Now we carry out a rotation of angle θ along the X-axis. Such a rotation yields the magnetic field vector in the o.r.f.,

$$\mathbf{B} = B\left(\sin\gamma\cos\varphi\mathbf{e}_\mathbf{x}^{'} + [\sin\gamma\sin\varphi\cos\theta + \cos\gamma\sin\theta]\mathbf{e}_\mathbf{y}^{'} + [\cos\gamma\cos\theta - \sin\gamma\sin\varphi\sin\theta]\mathbf{e}_\mathbf{z}^{'}\right) \tag{2.6}$$

Note that these would be the components of the vector magnetic field as seeing in Fig. 1.4 (right panel) with $X = X'$. We have added the superindex $'$ to the angles γ and φ from Fig.1.4 (right panel) in order to distinguish from the l.r.f. (same figure; left panel). Finally, $\gamma^{'}$ and $\varphi^{'}$ have the form

$$\cos\gamma^{'} = \frac{B_z^{'}}{B} = \cos\gamma\cos\theta - \sin\gamma\sin\varphi\sin\theta \tag{2.7}$$

$$\tan\varphi^{'} = \frac{B_y^{'}}{B_x^{'}} = \frac{\sin\gamma\sin\varphi + \cos\gamma\sin\theta}{\sin\gamma\cos\varphi} = \cos\theta\tan\varphi + \frac{\sin\theta}{\cos\varphi\tan\gamma} \tag{2.8}$$

Consider now, in the l.r.f., a radial penumbral fibril, whose inclination is γ_t at an azimuthal position on the penumbra φ_l. The magnetic atmosphere, surrouding the penumbral flux tube,

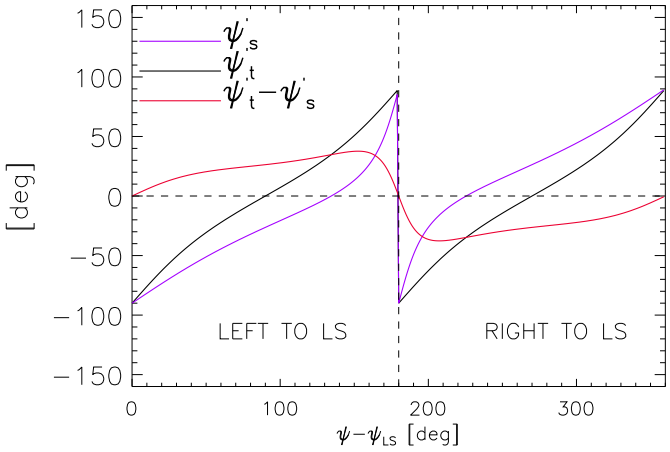

FIGURE 2.14: Variation, with respect to the line of symmetry, around a sunspot of the azimuhtal angle (in the observer's reference frame) for the penumbral flux tubes (black solid line), its magnetic surrounding (purple solid line) and difference between them (red solid line). For this example we have taken horizontal (in the local frame) flux tubes, $\gamma_t = 90^\circ$, and somewhat more vertical magnetic background, $\gamma_s = 55^\circ$. The obsever's viewing angle was taken to be $\theta = 45^\circ$. Note that the sign of $\varphi'_t - \varphi'_s$ changes from the left to the right side of the line of symmetry (denoted as LS).

possesses a more vertical magnetic field $\gamma_s < \gamma_t$ but the same azimuthal angle $\varphi_s = \varphi_t$ (i.e. it is also radially orientated). From the observer's point of view (o.r.f.), the azimuthal angle of the flux tube and its surroundings would be, however, different: $\varphi'_t \neq \varphi'_s$. This introduces a new discontinuity along the line of sight: $\Delta\varphi$ that must be taken into account, in addition to $\Delta\gamma$ and Δv_{los} in order to compute the NCP. Müller et al. (2002) have thoroughly investigated this issue, and realized that, according to the theoretical work of Landolfi & Landi Degl'Innocenti (1996), the NCP of visible Fe I lines at 6300 Å is mainly affected by the $\Delta\gamma$ mechanism (in agreement with Sánchez Almeida & Lites 1992). Interestingly, for the infrared Fe I lines at 1.56 μm the discontinuity that plays the more important role in the generation of the NCP turns out to be $\Delta\varphi$. With this finding, and taking into account the distribution around the penumbra of $\Delta\varphi$ (see Fig. 2.14), Müller et al. (2002) and Schlichenmaier et al. (2002) have been able to succesfully reproduce the NCP maps in the infrared (e.g. Fig. 2.12; right panel) with a model based on the uncombed penumbra. Note that $\Delta\varphi = \varphi'_t - \varphi'_s$ is positive in the region of the sunspot located to the left side of the line of symmetry, whereas it becomes negative of the region located on the right side (red solid line in Fig. 2.14).

Therefore we must conclude that the uncombed model provides a very satisfactory description of the penumbral vertical stratification in terms of horizontal flux tubes carrying the Evershed flow, embedded in a surrouding atmosphere with a more vertical magnetic field. It allows to understand, by means of discontinuities along the line of sight in the velocity and magnetic field vector, the NCP maps observed with very different spectral lines (i.e. different temperature and magnetic sesitivity, saturation etc.). Indeed it is also capable of reproducing NCP distributions for other lines, not mentioned here, such as the Fe I and Si I lines located at 1.07 μm (Schlichenmaier

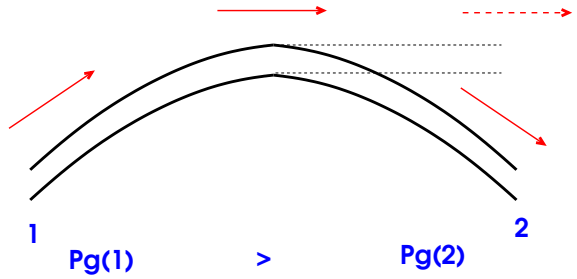

FIGURE 2.15: Cartoon representing a penumbral flux tube carrying the Evershed flow as in siphon flow models. The plasma will flow from the point where the gas pressure, P_g,is larger towards the point where the gas pressure is smaller. Arrows indicate the direction of the flow (radially outwards). Dashed lines corresponds to the case when the flux tube does not be back into the solar interior.

& Balthasar, *private communication*). Note that the aforementioned discontinuities are also seen from the inversion of Stokes profiles (Fig. 2.8,2.9,2.11).

2.3 Theoretical understanding of the Evershed flow

The theoretical understanding for the Evershed flow has evolved as our knowledge about the magnetic configuration of the penumbra has increased. The most successful models are those that explain the ubiquitous outwards flow found in the penumbra in terms of a gas pressure difference between the two footpoints of an arched loop that crosses it in the radial direction (see Fig. 2.15).

This is the basic idea of the so-called siphon flow models, as initially proposed by Meyer & Schmidt (1968). For the plasma to flow radially outwards in the penumbra, the gas pressure in the inner footpoint (referred to as 1 in Fig. 2.15) must be larger than at the outer footpoint (labelled as 2 in Fig. 2.15): $P_{g,1} > P_{g,2}$. If both footpoints are at the same geometrical height they must be in total pressure balance:

$$P_{g,1} + \frac{B_1^2}{8\pi} = P_{g,1} + \frac{B_2^2}{8\pi} \tag{2.9}$$

which basically means that for the plasma to flow outwards, as required from the observations, the magnetic field strength must be larger in the outer footpoint than in the inner one: $B_2 > B_1$.

Siphon flows have been modelled with increasing complexity and realism (Degenhardt 1989, 1991; Thomas 1988, Thomas & Montesinos 1990, 1993; Montesinos & Thomas 1989, 1997) including the effects of the flux tube geometry, radiative exchange with the surrounding atmosphere, etc. According to them, the outer footpoint would be situated outside the sunspot, in magnetic elements where the magnetic field is enhanced to values around 1500 Gauss (i.e. magnetic knots). This leaves some freedom to chose any inner footpoints within the penumbra (2) such that the magnetic field strength was smaller than in the external magnetic element. Siphon flow make use of the stationary MHD equations, in the thin flux tube approximation, to solve the equilibrium equations, deriving with this a flow speed that increases from the inner footpoint (1)

to the highest level of the arch and decreasing afterwards towards the outer footpoint. Note that if the top of the arch is located near the outer penumbral edged this can easily explain the sudden disappearance of the Evershed flow (see Sect. 2.1.3). According to the values of the magnetic field at the footpoints, different kinds of siphon flows can develop along the tube: subcritical ($v < v_t$), supercritical ($v > v_t$) and critical, where v_t is the characteristic tube's velocity:

$$v_t = \frac{v_s v_a}{\sqrt{v_s^2 + v_a^2}} \tag{2.10}$$

$$v_a = \frac{B}{\sqrt{4\pi\rho}} \rightarrow \text{Alven speed} \tag{2.11}$$

$$v_s = \sqrt{\gamma RT} \rightarrow \text{Adiabatic sound speed} \tag{2.12}$$

The critical flow occurs whenever the flow speed becomes larger than the tube's velocity $v > v_t$, and a standing shock front is formed at the downstream loop. This shock front dissipates the kinetic energy of the flow by transforming it into thermal energy. Hence, after the shock the plasma speed becomes subcritical again $v < v_t$.

Improvements, including the time dependent behaviour of the penumbral flux tubes, on the classical siphon flow model have been carried out by Schlichenmaier et al. (1998a, 1998b). Their simulations start with a thin flux tube which lies along the magnetopause (i.e. current sheet separating the penumbra and the quiet sun). After a perturbation the flux tube tube rises through the convectively unstable subsurface layers. Due to the superadiabatic stratification a hot plasma upflow develops along the tube. When the tube reaches the $\tau = 1$ level the atmosphere is transparent to radiation and therefore the hot plasma gradually cools down (Schlichenmaier et al. 1999). This is the ingredient that produces the gas pressure gradient along the tube and sustains it in time. In addition, the flux tube does not bend back into the solar photosphere but rather continues horizontally along the canopy. This is sketched with dashed lines in Fig. 2.15. In this case, since the two footpoints are not located at the same geometrical height the magnetic field in the outer footpoint (2) does not necessarily need to be stronger than at the inner footpoint (1).

Siphon flow models, including the moving flux tube simulations from Schlichenmaier et al, had to be revised after the investigations from Solanki et al. (1994) and in particular, from Westendorp Plaza et al. (1997; see also Sect. 2.2.2), who demonstrated that the magnetic field lines return to the solar surface still within the penumbra, meaning that the outer footpoint of the loop, as described by the siphon flow mechanism, should be located inside the penumbra (see Fig. 2.15). If we now take into account that the strength of the penumbral magnetic field decreases with radial distance (see Sect. 2.1.2 and Fig. 2.3) this means that $B_2 < B_1$, and therefore the plasma should flow inwards: $(1) \leftarrow (2)$, in clear disagreement with observations.

Montesinos & Thomas (1997) revised their calculations to account for penumbral flux tubes that lie completely within the penumbra. They argued that the Wilson depression of the sunspot penumbra makes the observations refer to different heights when the inner and outer penumbra are compared, thus making the the magnetic field in the outer penumbra appear smaller than in the inner penumbra, while in fact it is larger. This hypothesis, although physically valid must still be able to explain how a Wilson depression of about 100 Km can explain a drop in the observed magnetic field strength of about 1000 Gauss from the inner to the outer boundary of the

penumbra. In parallel, Schlichenmaier (2002) have presented new simulations of the moving flux tube where the flux tube is allowed to bend back into the photosphere while it is still within the penumbra. In this case, a quasi-stationary situation is reached in which, as in stationary siphon flows, the magnetic field strength is larger in the outer footpoint than in the inner one whenever both are taken at the same geometrical height.

Chapter 3

Comparison of two semiempirical models

Different interpretations of spectropolarimetric observations suggest different, sometimes contradictory, properties of the penumbral fine structure. In this chapter we show that the results of inversions of penumbral infrared profiles based on one-component models with gradients of the atmospheric parameters and two-component models without gradients are compatible with each other. Our analysis reconciles the results of previous investigations and provides further support for the picture that sunspot penumbrae are composed of penumbral flux tubes embedded in a magnetic background. The magnetic field in the tubes is more horizontal and weaker than that of the background atmosphere. While the tubes carry most of the Evershed flow, the background is essentially at rest. We notice also that the magnetic field strength in the flux tubes drops much more slowly with radial distance than the background field. This finding is discussed as a possible driver for the Evershed flow.[†]

3.1 Introduction

The fine structure of the penumbra has been the subject of many investigations (see Solanki 2003, Bellot Rubio 2003 for recent reviews) . Most of these involve high resolution imaging, allowing the horizontal distribution of brightness (and partly of the magnetic field if magnetograms were obtained), and its evolution to be deduced. Spectra and in particular spectropolarimetric measurements, i.e. the full polarization profiles of spectral lines, provide additional, largely complementary information. The full potential of spectropolarimetry is realized when combined with non–linear inversion techniques. This combination allows the line of sight velocity, magnetic field vector and temperature to be determined with high precision and in three dimensions, at the cost of temporal and spatial resolution.

[†]This chapter has been submitted for publication to Astronomy & Astrophysics: Borrero, J.M., Solanki, S.K., Bellot Rubio, L.R., Lagg, A. & Mathew, S.K. A&A (in press)

Inversion techniques have played a key role in the interpretation of observations. The first inversion of a complete sunspot was presented by Lites & Skumanich (1990) based on polarization profiles of the Fe I 630.25 nm line obtained with the Stokes II instrument. Subsequently, further inversions of sunspots have been carried out, mostly using the pair of Fe I lines at 630 nm observed by the Advanced Stokes Polarimeter (ASP, Elmore et al. 1992). The degree of sophistication of the physical models used in the inversions has increased with time. Until 1997, most inversions of penumbral profiles relied on one-component Milne-Eddington (ME) atmospheres. The ME inversion code of the High Altitude Observatory (Skumanich & Lites 1987) has been successfully used to study the structure of sunspot penumbrae by, among others, Lites & Skumanich (1990), Lites et al. (1993), Stanchfield et al. (1997), and Lites et al. (2002). The first inversion of a penumbra in terms of one-component models with gradients of the atmospheric parameters was carried out by Westendorp Plaza et al. (1997) using the SIR code (Stokes Inversion based on Response functions, Ruiz Cobo & del Toro Iniesta 1992). This code made it possible to investigate the structure of the penumbra in different layers of the photosphere (Westendorp Plaza et al. 2001a, 2001b).

The availability of infrared measurements, mainly the Fe I lines at 1565 nm recorded with the Tenerife Infrared Polarimeter (TIP, Martínez Pillet et al. 1999), made the deeper layers of the sunspot atmosphere accessible. Solanki et al. (1992a; 1994) presented the first inversions in this spectral window using numerical solutions of the Radiative Transfer Equation, which allowed the characterization of the magnetic canopy and the Evershed effect. This work was followed by one-component inversions allowing for gradients in the physical parameters (Bellot Rubio et al. 2002; Mathew et al. 2003). Finally, more complex inversions based on two–component models have been carried out (del Toro Iniesta et al. 2001; Bellot Rubio 2003; Bellot Rubio et al. 2003) which have the potential to partly overcome the problem of the limited spatial resolution.

The results of these investigations of the visible and infrared data support the idea that sunspot penumbrae consist of penumbral flux tubes embedded in a magnetic background (see Bellot Rubio 2003), as proposed by Solanki & Montavon (1993) in their uncombed penumbral model. However, inversions based on visible and infrared lines do not always agree on the properties of the fine structure, and the same is true for inversions based on one-component and two-component models (see Sect. 2.2.2). In extreme cases, opposite tendencies are deduced from visible and infrared lines. The one-component inversions of visible lines performed by Westendorp Plaza et al. (2001a), for example, revealed magnetic field strengths increasing with height in most of the outer penumbra, whereas a similar one-component model applied to infrared measurements results in field strengths decreasing with height (Mathew et al. 2003).

Here we show that the results of one component models with gradients of the atmospheric parameters and of two-component models without gradients are compatible with each other, and that differences between them are more apparent than real. The results of both models provide a possible explanation why the Evershed flow is directed outward in spite of the rapidly decreasing penumbral magnetic field strength. We also offer an explanation for the different behaviors inferred from visible and infrared lines based on the different sensitivity of these lines to the various atmospheric layers. To this end, we invert the same infrared observations (described in Sect. 3.2) with the same code (described in Sect. 3.3) in terms of one and two-component models (Sect. 3.4). The results of these inversions are compared in Sect. 3.5. A discussion of the reliability of the different physical models is presented in Sect. 3.6. We address the implications of our

results in Sect. 3.7 and offer a picture for the penumbral fine structure in Sect. 3.8 that attempts to reconcile the various observations. Finally, Sect. 3.9 summarizes our findings.

3.2 Observations

On 27th September 1999, a rather symmetric spot, NOAA 8706, was observed with the Tenerife Infrared Polarimeter (Martínez Pillet et al. 1999) attached to the 70cm German VTT of Teide Observatory. The spot was located at a heliocentric angle of 24° ($\mu = 0.91$). The recorded spectral region contained the line pair Fe I 15648 Å and Fe I 15652 Å, with effective Landé factors of $g_{eff} = 3$ and $g_{eff} = 1.53$, respectively. The seeing conditions were rather good during the observations, with the granulation being clearly discernible in the reconstructed continuum image (Figure 3.1). The spatial resolution can be estimated to be about 1 arcsec by calculating the power spectrum of the continuum intensity in the neighbouring granulation. The absolute wavelength scale of the observations was determined using the line core position of the average quiet sun intensity profile of Fe I 15648 Å and shifting it by 400 m s^{-1}. This value corresponds to the convective blueshift of the line as deduced from the two-component model of Borrero & Bellot Rubio (2002). The telluric blend affecting the red wing of Fe I 15648 Å was removed by inverting the quiet sun profile of the line and using the fit to determine its shape, which is subsequently extracted from the remaining profiles. The atomic parameters of the observed lines, taken from Borrero et al. (2003a), are summarized in Table 3.1. Recently, Mathew et al. (2003,2004) have used the same data set to study the global structure of this sunspot.

3.3 Inversion procedure

The inversions presented in this work were carried out with the code SPINOR (Frutiger et al. 1999; Frutiger 2000). SPINOR iteratively modifies an initial guess model atmosphere by means of response functions (Ruiz Cobo & del Toro Iniesta 1992) until the synthetic spectrum matches the observed one. The radiative transfer equation is solved in local thermodynamic equilibrium using the Hermitian algorithm of Bellot Rubio et al. (1998). The continuum absorption coefficient is calculated for a given wavelength, temperature, and electron pressure using the code of Gustaffson (1973) which takes into account contributions from H, He, H^-, He^-, H_2^+, H_2^- and other electron donor species, as well as Rayleigh scattering by H and H_2, and Thompson scattering by free electrons. Several broadening mechanisms are considered: microturbulence, radiative broadening (in the classical damped oscillator approximation), and collisions with neutral hydrogen atoms (for which the ABO theory is employed; see Barklem & O'Mara 1997 and Barklem et al. 1998).

Once the emergent spectrum has been computed for a given set of parameters which define the atmosphere, analytical equivalent Response Functions (RFs) are evaluated for the physical stratifications of the model (temperature, line-of-sight velocity, strength, inclination, and azimuth of the magnetic field vector, etc) at a number of optical depth points called *nodes*. These RFs enter into a Levenberg-Marquardt nonlinear least-squares algorithm (Press et al. 1986) and a new set of parameters at the nodes, able to provide a better fit to the observed profiles, is obtained. New stratifications of the physical parameters along the whole atmosphere are obtained by inter-

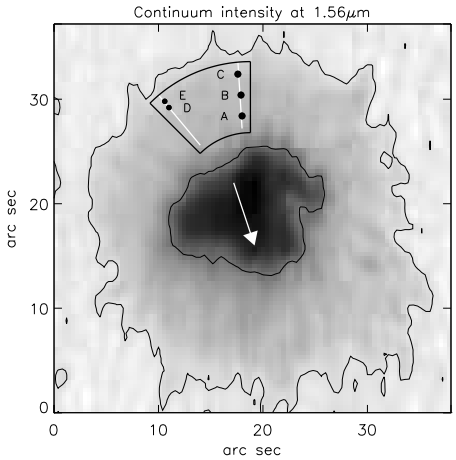

FIGURE 3.1: Continuum intensity image of NOAA 8706 at 1.56 μm. The black box indicates the region in the limb side of the penumbra considered in this work. It is centered on the line connecting the center of the solar disk and of the sunspot (line of symmetry) and spans an interval of 45° in azimuth. Inside it, examples of two radial cuts are plotted in white. The points labeled A, B, and C are three pixels at different radial positions in the penumbra. Points E and D are two consecutive pixels on a different radial cut. The white arrow in the umbra marks the direction to disk center. The two contours indicate the umbra–penumbra and quiet sun–penumbra boundaries. The reference value taken for the sunspot's radius, $r = R$, corresponds to the outer contour at each position angle.

TABLE 3.1: Atomic parameters of the observed lines. λ_0 represents the laboratory central wavelength, χ_l the excitation potential of the lower energy level, and $\log gf$ the logarithm of the oscillator strength times the multiplicity of the level. The parameters α and σ (in units of Bohr's radius, a_0) are used to calculate the broadening of the lines by collisions with neutral hydrogen atoms as resulting from the ABO theory. The last column gives the effective Landé factor of the transition, g_{eff}.

Species	λ_0 (Å)	χ_l (eV)	log gf (dex)	α	σ (a_0^2)	g_{eff}
Fe I	15648.515	5.426	−0.675	0.229	977	3.00
Fe I	15652.874	6.246	−0.043	0.330	1444	1.53

polating the perturbations at the nodes using splines under tension. These steps are repeated until the best fit is achieved. The synthesis and inversion are performed in an optical depth scale, but during each iteration step, the atmospheres are put in hydrostatic equilibrium using the ideal gas law as equation of state. More details on the code are given in Sect. 1.5.6.

Inversion techniques (ITs) have been used to investigate many structures of the solar photosphere and chromosphere (for recent reviews see Ruiz Cobo 1998; Socas-Navarro 2001; del Toro Iniesta 2003b). The reliability of inversion techniques has been repeatedly demonstrated in the past and we will not discuss this point further (e.g. Westendorp Plaza et al. 1998). However, some words about uniqueness are appropriate at this point. The retrieved results are unique only for the particular geometrical model adopted for the inversion. As long as this model is not changed and is appropriate to the data being inverted (e.g. one could not expect to obtain unique results for the magnetic field vector if only Stokes *I* is inverted), ITs have proven to be extremely robust and to retrieve the same stratifications of the atmospheric quantities independently of the initial guess. However, the question remains how to understand the results of ITs when different models are adopted to interpret the polarization profiles emerging from sunspot penumbrae. Bellot Rubio (2003) and Leka & Socas-Navarro (2000) have investigated this issue by concentrating on the global properties of the penumbra from the inversion of infrared and visible data respectively. Here we extend this work by focusing our attention on the properties of the penumbral fine structure that result when different geometries are adopted.

3.4 Geometrical models adopted for the inversion

We have selected two different models for the analysis of the observed penumbral profiles. The first model assumes that in each pixel the fine structure is spatially resolved, so that the shape of the line profiles are due to the height dependence of the thermal, magnetic and kinematic properties of the atmosphere, i.e. temperature T, magnetic field strength B, magnetic field inclination γ and azimuth ϕ (relative to the observer's reference frame) as well as line of sight velocity v_{LOS}. In addition, height independent macro- and microturbulent velocities are also obtained through the inversion in order to model those velocities which occur at scales smaller than the resolution element. For each height-dependent physical quantity we have selected four nodes at the following optical depths: $\log\tau_5 = [1, 0, -1, -2]$[1] . This results in a total of 23 free parameters. Hereafter, this model will be referred to as the *one-component (1C) model*. Similar models have been used to study the structure of sunspots by inverting the polarization signals of Zeeman sensitive spectral lines in the visible (e.g., Westendorp Plaza et al. 1997; 2001a; 2001b) and the infrared (e.g., Bellot Rubio et al. 2002; Mathew et al. 2003).

The second model considers two independent atmospheric components for each spatial pixel, thereby allowing for the possibility that there are horizontal inhomogeneities at scales below the spatial resolution. In order to keep the number of free parameters within reasonable limits, the physical quantities describing each component are assumed to be height independent, except for the temperature. In addition to the kinematic and magnetic parameters mentioned above, a filling

[1]The assignment of the number and position of the nodes was done by concentrating on those layers to which these lines are sensitive (i.e. calculating the Response Functions). Examples of RF's for these lines can be found in Mathew et al. 2003.

factor α_t (fractional area of the resolution element covered by the second component) is obtained from the inversion. Here we have a total number of 18 free parameters. In the following this model will be referred to as the *two-component (2C) model*. Bellot Rubio et al. (2003) have used the same physical description of the penumbra to confirm that the Evershed flow is aligned with the magnetic field vector in deep photospheric layers.

In all inversions we use a stray light correction. The stray light intensity profile, $I_{\rm q}$, is taken to be that emerging from the quiet sun according to the two-component model of Borrero & Bellot Rubio (2002). A stray light factor $\alpha_{\rm q}$ is used to combine the stray light profile with the polarization profiles emerging from the 1C and 2C models. $\alpha_{\rm q}$ is a free parameter of the inversion and is included in the total number of free parameters given above. In this way, the synthetic profiles used to fit the observations can be expressed as

$$\begin{aligned} \vec{S}_{\rm 1C}(\lambda) &= \alpha_{\rm q}\vec{S}_{\rm q}(\lambda)+(1-\alpha_{\rm q})\vec{S}_{\rm p}(\lambda) \\ \vec{S}_{\rm 2C}(\lambda) &= \alpha_{\rm q}\vec{S}_{\rm q}(\lambda)+(1-\alpha_{\rm q})[(1-\alpha_{\rm t})\vec{S}_{\rm p1}(\lambda)+\alpha_{\rm t}\vec{S}_{\rm p2}(\lambda)] \end{aligned} \tag{3.1}$$

where the Stokes vector is defined as $\vec{S}=(I,Q,U,V)$. $\vec{S}_{\rm p}$ stands for the synthetic profiles emerging from the penumbral atmosphere of the 1C model, $\vec{S}_{\rm p1}$ and $\vec{S}_{\rm p2}$ refer to the two magnetic components of the 2C model. The quiet sun contribution (stray light) is assumed to be unpolarized: $\vec{S}_{\rm q}=(I_{\rm q},0,0,0)$.

3.5 Results

We have inverted all 750 pixels in the region bounded by the thick black lines in Figure 3.1, covering r/R values roughly between 0.4 and 0.8, where R denotes the radius of the sunspot in the continuum map. The inverted pixels lie on the limbside penumbra close to the line of symmetry of the spot, i.e., the line connecting the sunspot center with the center of the solar disk. In Figure 3.2 we plot three examples of observed Stokes V profiles along with the best-fit profiles resulting from the 1C and 2C inversions. These examples correspond to points A, B, and C in Figure 3.1. Near the magnetic neutral line, the observed circular polarization profiles show three or more lobes. The fits, although not perfect, are reasonably successful given the simplicity of the two models. Residuals are always below 0.5 % (compared to an approximate noise level of 0.05 %). Although in general the 1C model leads to slightly better fits in terms of the final χ^2 values, the difference is not sufficiently large to declare this model more realistic, in particular since the 2C model uses fewer free parameters. The fits to the other Stokes parameters are equally good (not shown).

In Figure 3.3 we present the kinematic and magnetic stratifications as a function of the optical depth (for a wavelength reference of 5000 Å : τ_5) of the atmospheres inferred from the inversion of the profiles shown in Fig. 3.2. The atmospheres corresponding to the 1C model (dashed lines) consistently show large red shifted velocities in high layers (around $\log\tau_5\simeq-1$), while in deep layers velocities are negligible or even directed towards the observer, although comparatively weak in magnitude. Both, the magnetic field strength and its vertical gradient decrease from the inner to the outer penumbra. Large values ($\gamma\sim110^\circ$) of the magnetic field inclination in high layers along with smaller ones ($\gamma\sim60-80^\circ$) in deep layers are inferred. The parameters of the two penumbral components returned by the 2C inversion are also indicated in Fig. 3.3 by

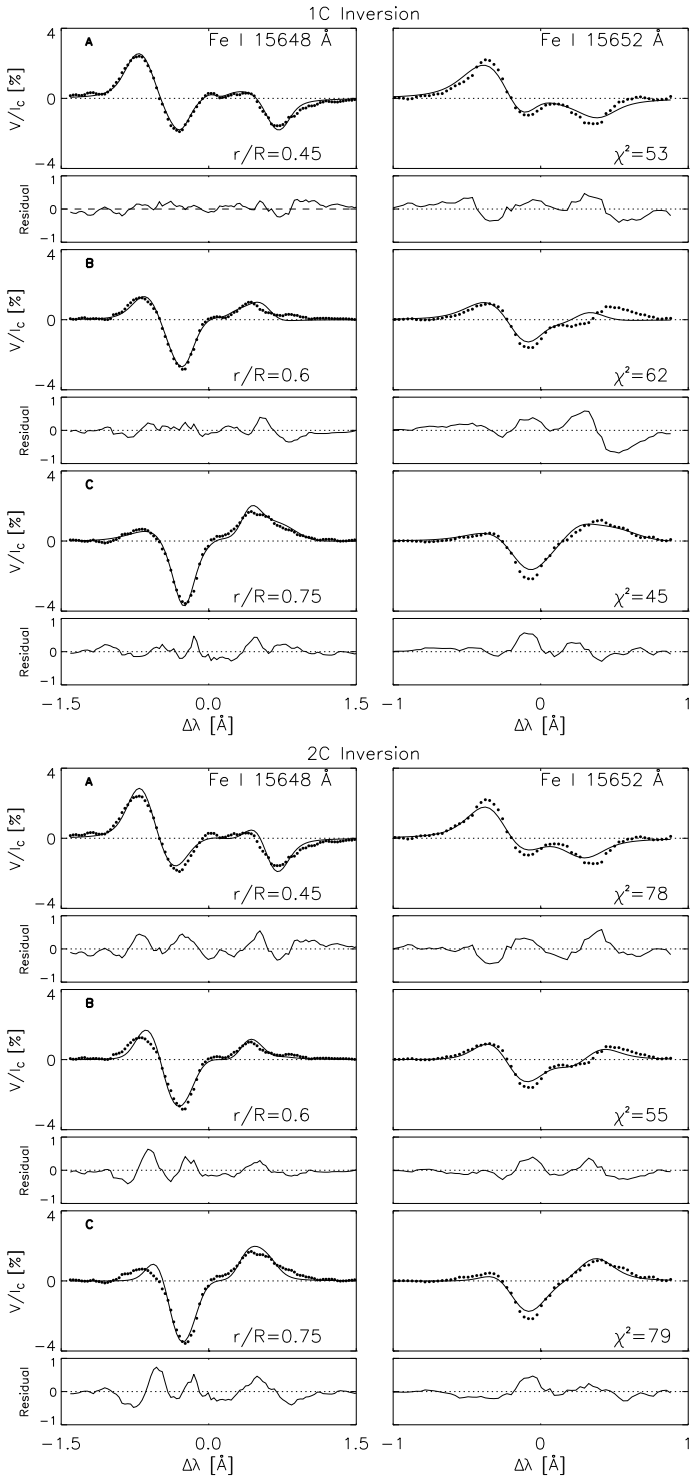

FIGURE 3.2: Top six panels: results from the inversions based on the 1C model. Bottom six panels: as before but for the 2C model. We each separate model we plot, from top to bottom: observed Stokes V profiles (filled circles) corresponding to the points marked as A, B and C in Fig. 1. The best-fit profiles resulting from the inversions are represented by the solid lines. Beneath each panel showing the V/I_C profile is plotted the difference between observed and best fit profiles (residuals). The χ^2 value is given for each fit. More weight was given during the inversion to the circular polarization than to the total intensity and linear polarizaion. Relative weights were the same in the 1C and 2C inversion.

horizontal solid lines. It can be seen that one of these atmospheres (#2) has moderate magnetic fields ($B \sim 1200$ G), high inclination angles ($\gamma \sim 100-110^{\circ}$) and large redshifted velocities ($v_{LOS} \sim 1.5-2$ km s^{-1}), while the other component (#1) is characterized by stronger ($B \sim 1500-2000$ G) and less inclined ($\gamma \sim 60-70^{\circ}$) magnetic fields. In component #1, the line-of-sight velocity is nearly zero. This figure also indicates a similarity between the values returned by the 1C inversion at $\log\tau_5 = -1$ and 0 and the 2C inversion results for component #2 and #1, respectively.

Next we test these hints in a statistically more robust fashion. For all the pixels we have selected the optical depths marked in Fig. 3.3 with vertical dotted lines ($\log\tau_5 = 0$ and $\log\tau_5 = -1$), extracted the values of the atmospheric parameters from the 1C inversion there and plotted them as a function of radial distance in the penumbra in Figure 3.4 (left panels) . The corresponding values for the two atmospheres of the 2C inversions are shown as well (right panels). In this figure, the magnetic field inclination is expressed in the local reference frame. Thus, instead of γ we plot the zenith angle ζ. A zenith angle of zero indicates fields pointing outwards perpendicularly to the solar surface.

At $\log\tau_5 = -1$ the magnetic field returned by the 1C model becomes more horizontal in the middle penumbra and eventually reaches values slightly larger than 90°, implying that the magnetic field returns to the solar surface. The field strength decreases only slowly with radial distance, whereas the LOS velocities are redshifted and increase radially. At $\log\tau_5 = 0$ we see a rather vertical magnetic field in the inner penumbra which gradually becomes more inclined, although it is never completely horizontal. In this layer, the magnetic field is stronger than at $\log\tau_5 = -1$ in the inner penumbra, but rapidly decreases to similar values at the outer part of the penumbra. The velocity here is almost zero, indicating that the Evershed flow is mostly concentrated in the upper part of the atmosphere.

The 2C inversions show a strikingly similar overall picture. In particular, one of the components (#2) possesses more horizontal, weaker fields whose strength remains more or less constant with radial distance. This component also carries a large flow, whose magnitude increases radially, although by only a small amount. Component #1 is characterized by more vertical and stronger magnetic fields and small LOS velocities. The field strength in this atmospheric component decreases quickly with radial distance.

These two components or layers can be identified with horizontal magnetic flux tubes (carrying the Evershed flow) embedded in a more vertical background (e.g., Solanki & Montavon 1993, Schlichenmaier et al. 1998a,1998b; Martínez Pillet 2000; Bellot Rubio et al. 2002, 2003; Mathew et al. 2003). Thus, the atmosphere represented by dashed lines in Fig. 3.4 corresponds to the flux tubes and the atmosphere indicated by solid lines to the background. The correspondence between 1C and 2C inversions is not always perfect. For example, the inclination of the background in the 1C model increases by roughly 20–30° as r/R increases, while it remains unchanged in the 2C inversions. However, these differences do not detract from the remarkable similarity of the behaviors deduced from both models.

One peculiarity of the 1C inversions is a sudden change of the sign of the gradients of LOS velocity and magnetic field inclination at a given radial position. In Figure 3.5 this behavior is illustrated for the two consecutive points along the same radial cut marked D and E in Fig. 3.1. Whereas in point D the flux tube is better identified with $\log\tau_5 = -1$ this is no longer the case in point E, where it seems appropriate to identify the background with this optical depth position

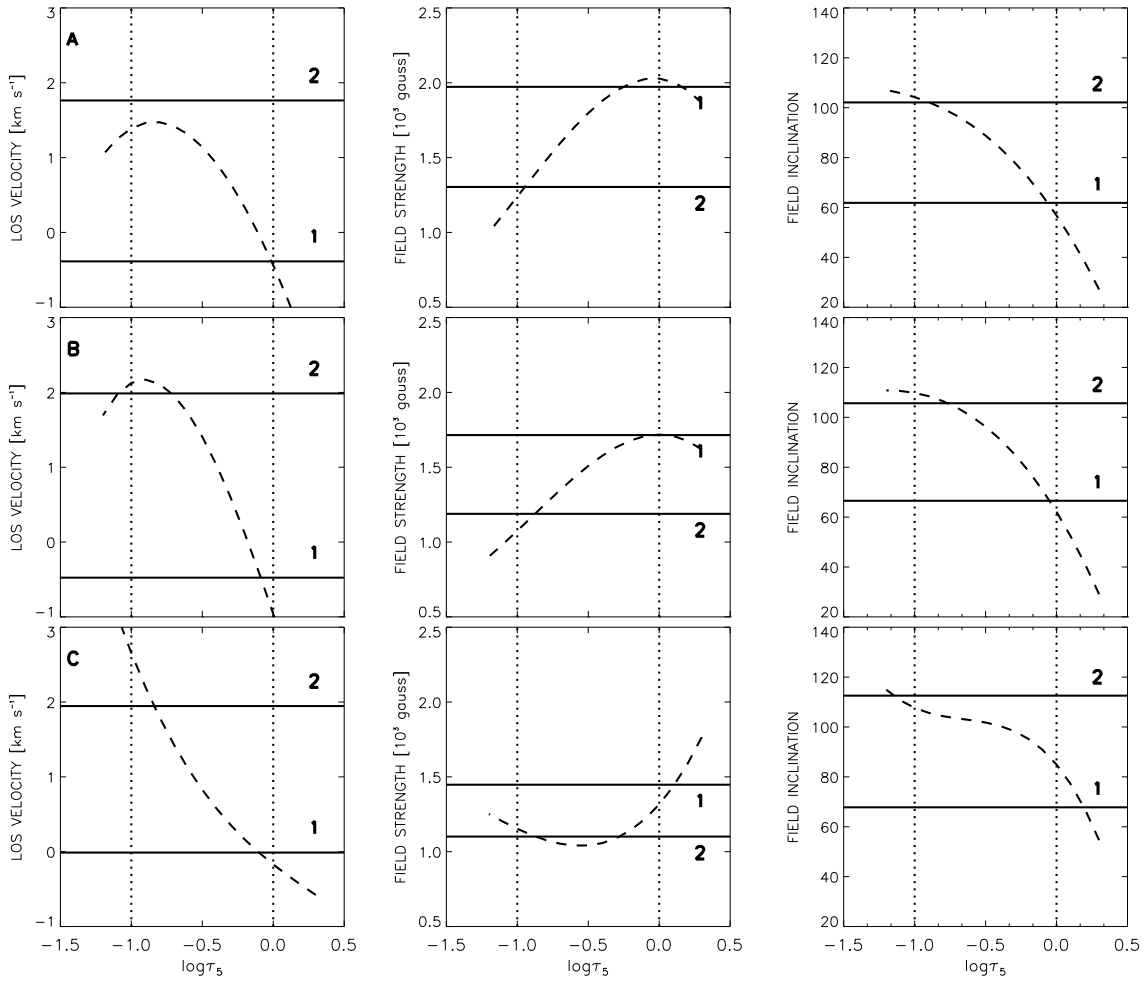

FIGURE 3.3: Examples of atmospheric stratifications resulting from the 1C and 2C inversions (dashed and solid lines, respectively). The numbers next to the solid lines indicate the corresponding magnetic component. From top to bottom: results for pixels A, B, and C (see text and caption of Fig. 3.1 for details). From left to right: line-of-sight velocity, magnetic field strength, and magnetic field inclination. The two vertical dotted lines mark the optical depth points selected for further analysis ($\log\tau_5 = 0$ and $\log\tau_5 = -1$). Positive velocities indicate redshifts.

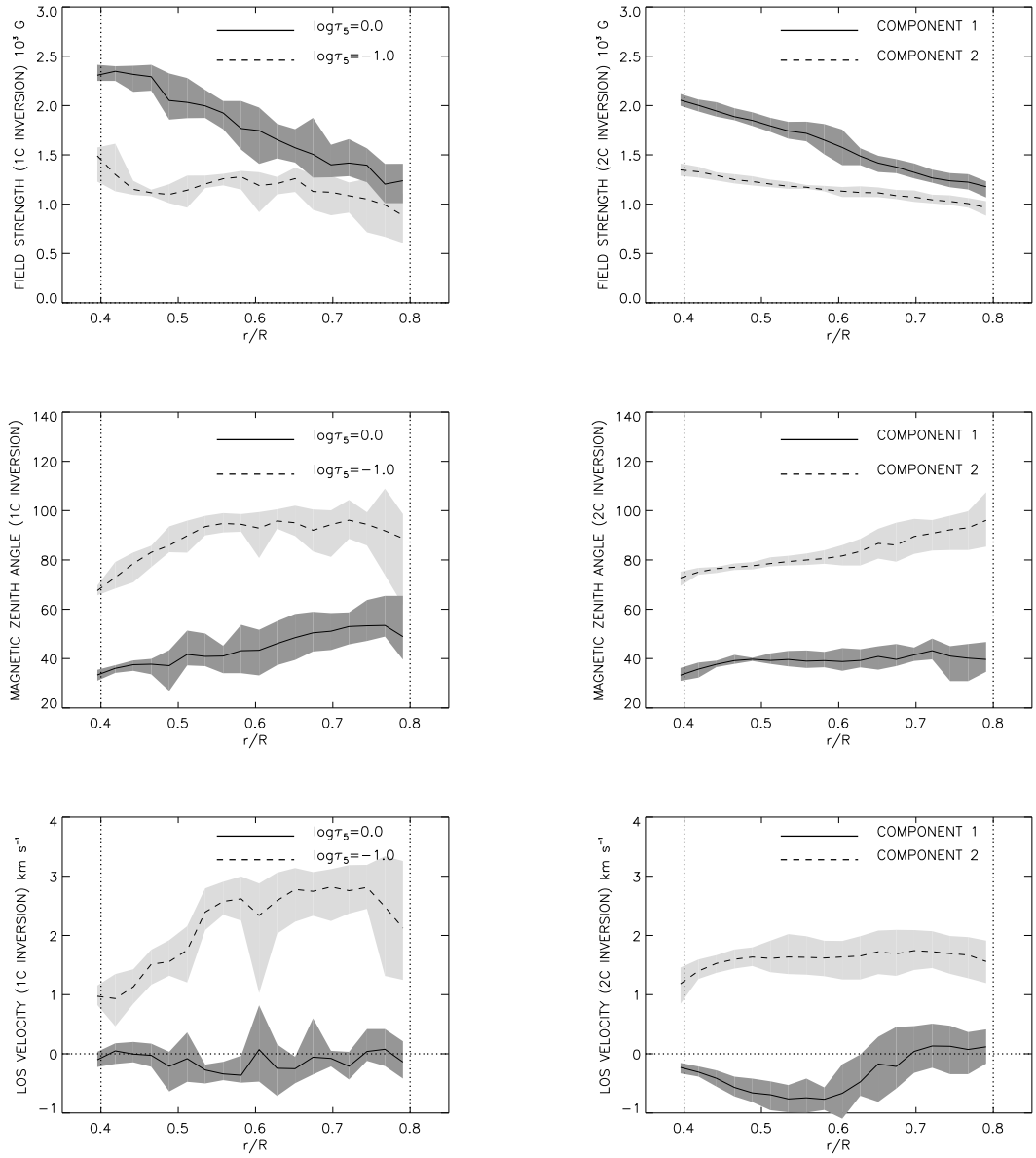

FIGURE 3.4: Radial variation of the inferred physical quantities. Top panels: magnetic field strength. Middle panels: magnetic zenith angle. Bottom panels: line-of-sight velocity. The results of the 1C inversions are shown in the left panels. For these inversions we extract the values at $\log\tau_5 = 0$ (solid lines) and $\log\tau_5 = -1$ (dashed lines). The 2C results are plotted in the right panels. Component #1 (the background) is represented by solid lines, whereas dashed lines correspond to component #2 (flux–tube atmosphere). Solid and dashed lines are averages over all the points at the same radial distance, while the shaded areas correspond to the maximum individual deviations. The 1C results have been corrected (for $r/R \gtrsim 0.75$) by interchanging the values at $\log\tau_5 = -1$ and $\log\tau_5 = 0$ where necessary (see text for details).

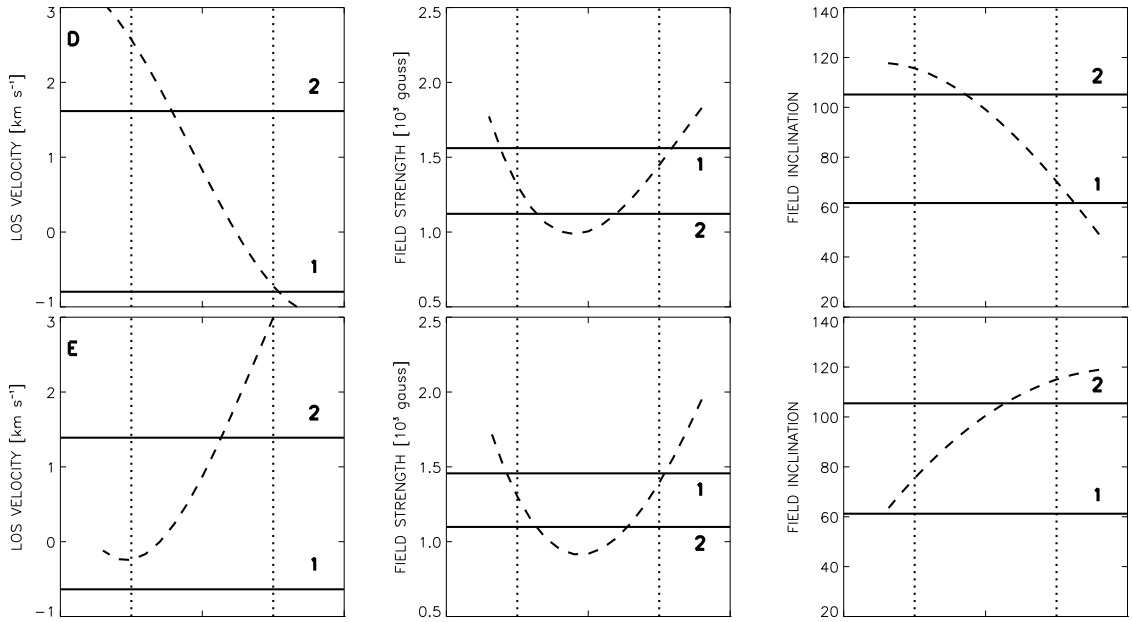

FIGURE 3.5: Atmospheric stratifications derived from the 1C inversion (dashed lines) and 2C inversion (solid lines) of two consecutive radial points referred to as D and E in Figure 3.1. Note the sudden change in the gradient of the LOS velocity and field inclination from point D to E.

and to shift the flux tube to $\log\tau_5 = 0$, where the horizontal Evershed flow would now be located. All considered radial cuts show this tendency in the outer penumbra. We have corrected for this shift in Fig. 3.4 by simply interchanging the values of the atmospheric parameters at $\log\tau_5 = 0$ and $\log\tau_5 = -1$ where necessary. One may speculate that the shift is due to the flux tubes sinking back into the photosphere at large radial distances, so that they should be observed in deeper layers as the outer penumbral boundary is approached. Such an explanation is consistent with the retrieved zenith angles which, for the flux tubes, increase radially and finally become larger than 90°. We note here that Mathew et al. (2003) found a similar behavior. They detected large LOS velocities in high layers and small velocities in the deep photosphere for the inner penumbra, but the opposite behavior in the outer penumbra. The uncombed-like inversions of Bellot Rubio (2003) (see footnote 4 in pag 83) also suggest that the flux tubes are located at increasingly lower layers in the outer penumbra (from $r/R \sim 0.75$ outwards), although this tendency is not well marked.

Before discussing the results and their implications in the next sections, we need to address why the results presented in Fig. 3.4 are based on the inversion of a region restricted to the limb-side penumbra. The reason for this is the greater coherence and reliability of the results obtained from the profiles observed in this region when compared with those at the center side. A possible explanation for the smaller reliability of the 2C inversion results in the center side could be that, in this region, the magnetic field vector in both flux tubes and magnetic background has the same polarity with respect to the line of sight ($\gamma < 90°$), so that both atmospheres give a similar signature and the resulting Stokes V profiles are two lobed. The information carried

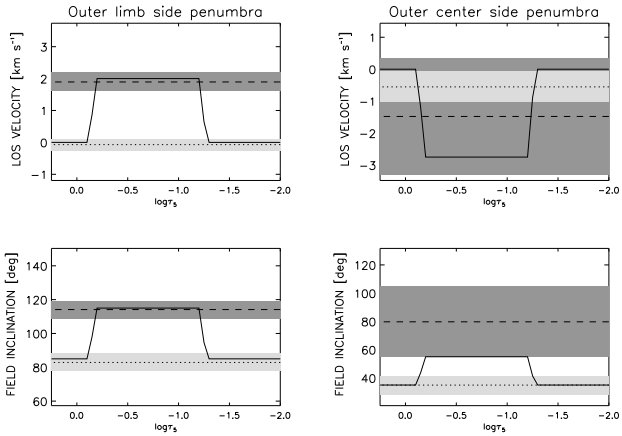

FIGURE 3.6: Stratifications of LOS velocity (upper panels) and magnetic field inclination (lower panel) for two hypothetical points in the outer ($r/R > 0.7$) limb side (left panels) and center side (right panels) of the penumbra. Dotted and dashed lines are the results obtained by applying a 2C inversion to the profiles synthesized with the uncombed model (solid lines; see also Table 3.2). The shaded areas represent the standard deviations corresponding to 10 random initializations.

by the two different components in the circular polarization is then mixed together, making its separate inference more difficult.

To test this idea we have created synthetic data and inverted them for different positions in a hypothetical sunspot. The model underlying the calculation of the synthetic profiles is basically the uncombed model of Solanki & Montavon (1993; see also Borrero et al. 2003b), with the parameters indicated in Table 3.2. These profiles are then inverted using 10 random initial 2C models (as described in Sec. 3.4) whose results are presented in Figure 3.6. In the limb side we have mixed polarities: flux tube with $\gamma > 90^\circ$ (dashed lines) and background with $\gamma < 90^\circ$ (dotted lines). The 2C inversion recovers both structures almost perfectly in this case. However, in the center side the polarities are the same ($\gamma < 90^\circ$) and the 2C inversion recovers the original stratifications with larger uncertainties. This supports the explanation proposed above. Note that this conclusion is based on the behavior showed by the circular polarization profiles in different regions of the spot. It could well be that, under the appropriate viewing angles, the different signature of the two components in the center-side penumbra appear mostly in the linear polarization (Stokes Q and U) profiles. For example, if a sunspot is observed near the limb ($\theta \simeq 40^\circ$), the background magnetic field in the center side of the penumbra would be aligned with the observer ($\gamma_B = 0^\circ$) and would not produce any linear polarization signal; thus, allowing for a better distinction of the different components when inverted with a 2C model. This idea must be confirmed by inverting a wider sample of sunspots at different heliocentric angles (see also Sect. 2.2.2; unresolved structure).

TABLE 3.2: Physical parameters of the uncombed field model used for the numerical test. Index **T** refers to a flux tube which is embedded in a background (index **B**). B and γ are the strength and inclination of the magnetic field vector (with respect to the observer) respectively. $V_{\rm LOS}$ is the line of sight velocity. $\alpha_{\rm T}$ and $\alpha_{\rm Q}$ have the same meaning as in Eq. 3.1. $R_{\rm T}$ is the flux tube's radius and z_0 is its central position. The uncombed model is basically a modified 2C model where the **B** component is a pure penumbral background field with no height variation is the physical parameters. The component **T** has the same stratifications than the latter except between $z_0 - R_{\rm T}$ and $z_0 + R_{\rm T}$ where the tube is located and where physical parameter suffer a jump (from index **B** to **T**, e.g., solid line in Fig. 3.6). . In the local reference frame $\zeta_{\rm B} = 60^\circ$ and $\zeta_{\rm T} = 90^\circ$ are chosen. However in the observer's frame we have $\gamma = \zeta + \theta$ on the limb side or $\gamma = \zeta - \theta$ on the center side, where $\theta = 25^\circ$ as in our observations.

Parameter	Units	Outer Center Side	Outer Limb Side
$B_{\rm B}$	Gauss	1000	1000
$\gamma_{\rm B}$	deg	35	85
$V_{\rm LOS,B}$	kms^{-1}	0	0
$B_{\rm T}$	Gauss	1000	1000
$\gamma_{\rm T}$	deg	55	115
$V_{\rm LOS,T}$	kms^{-1}	-2.75	2.00
$\alpha_{\rm T}$		0.65	0.65
$R_{\rm T}$	km	150	150
z_0	km	100	100
$\alpha_{\rm Q}$		0.15	0.15

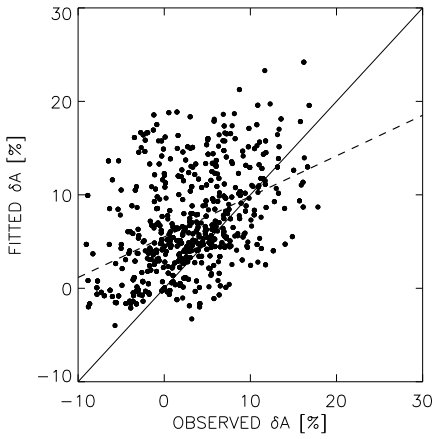

FIGURE 3.7: Area asymmetry, δA, of the best-fit Stokes V profiles vs. the observed δA. The mean δA is around 3% and 7% for the observed and best-fit profiles, respectively. The solid line represents the expectation value, while the dashed line is a linear fit to the points.

3.6 Stokes V area asymmetry

A potentially powerful diagnostic of the penumbral fine structure that has not been considered in the previous section is the Stokes V area asymmetry, δA (see Sect. 1.4.1 and 2.2.2). Observations show thatδA, defined as

$$\delta A = \frac{\int V(\lambda)\,\mathrm{d}\lambda}{\int |V(\lambda)|\,\mathrm{d}\lambda}, \tag{3.2}$$

is non-zero in the penumbra for both visible and infrared spectral lines (Illing et al. 1974a, 1974b; Makita 1986; Sánchez Almeida & Lites 1992; Schlichenmaier & Collados 2002; Schlichenmaier et al. 2002; Müller et al. 2002). While the 2C model used here possesses height independent quantities (e.g., B, γ, $V_{\rm LOS}$) , so that it is unable to produce asymmetric profiles, the 1C model incorporates such height variations (i.e. gradients). To test how well the 1C inversion reproduces the observed area asymmetries we plot in Figure 3.7 the Stokes V area asymmetry of the best-fit Fe I 15648 and 15652 Å profiles resulting from the 1C inversion versus the observed values. Figure 3.7 shows that the observed δA is small, with values never exceeding 20% [2] , in contrast to the visible lines at 6300 Å where larger values are quite common (Westendorp Plaza et al. 2001a). This figure also shows that the 1C model tends to overestimate the observed area asymmetry (see linear fit). The reason for the large scatter is basically the small sensitivity of these infrared lines to line-of-sight gradients in the atmospheric parameters together with the oversimplified picture of the real penumbral structure represented by the 1C model. To demonstrate this we construct a magnetic atmosphere similar to those obtained from the 1C inversion (see Fig. 3.3) but where the gradients are substituted by a step–like jump in the stratifications of the physical parameters at a

[2] We estimate that a noise level of $5\times10^{-4}I_C$ in the observed circular polarization can introduce a maximum bias of ±1% in the observed δA, so that this cannot be the cause of the relatively poor correspondence.

prescribed level τ_0. This jump is similar to the one present at the lower boundary of a horizontal flux tube carrying the Evershed flow (see Fig. 3.8a). A constant magnetic field with $B = 1500$ G, $\gamma = 70^\circ$, $\phi = 0^\circ$ and no flows are assumed below τ_0 to simulate a background with properties similar to those in Fig. 3.3. For the flux tube (layers above τ_0) we adopt the following values: $B = 1000$ G, $\gamma = 115^\circ$, $\phi = 0^\circ$ and $V_{\rm LOS} = 1.75$ km s^{-1}. The temperature stratification is taken from the penumbral model by del Toro Iniesta et al. (1994). Stokes V profiles and δA values are computed for the two analyzed infrared lines 15648 and 15652 Å as well as the widely used pair of lines Fe I 6301 and 6302 Å . This is done for τ_0 values ranging between 10^{-5} and 10. Obviously, for a line formed in the height range $\tau = [\tau_{\rm u}, \tau_\ell]$, a non-zero δA will be obtained only when the discontinuity τ_0 is located between $\tau_{\rm u}$ and τ_ℓ (see Fig. 3.8a). The results are presented in Figure 3.8b. The δA of the visible lines is much more sensitive to discontinuities along the line of sight than that of the infrared lines. Indeed, the lines used in this work are almost insensitive to such discontinuities, exhibiting some area asymmetry ($\delta A_{max} \sim 10\%$) only in a very narrow range of optical depths (from $\log\tau_5 \sim -1$ to $\log\tau_5 \sim 0$, with a maximum around $\log\tau_5 \sim -0.2$). As explained by Landolfi & Landi degl'Innocenti (1996) and Grossmann-Doerth et al. (1989) this results follows directly from the properties of the lines (Landé factors, saturation). From these results we draw the following conclusions:

- The formation of the Fe I 15648 and 15652 Å lines is dominated by the presence of two opposite polarities in the resolution element. Successful fits can be achieved with the help of the 2C model because the lines are only slightly influenced by discontinuities.[3].
- The visible Fe I 6301 and 6302 Å lines are strongly influenced by discontinuities, which gives rise to large δA values. Successful fits to those kind of profiles can only be achieved by means of models including gradients (e.g. our 1C model), or discontinuities.
- The stratifications inferred from the 1C inversions, the observed Stokes V area asymmetry of the iron lines at 1.56 μm, and the results from the numerical experiment suggest that at least in the inner penumbra these lines detect the lower boundary of the horizontal flux tube. This needs to be confirmed by inversions with a more realistic model.
- The wider formation height range of visible lines may allow to detect both tube's boundaries if its width does not exceed 250–300 km and if it lies entirely above $\tau_5 = 1$ in the photosphere.

3.7 Magnetic flux tubes and the Evershed flow

One of the most interesting result of our analysis concerns the radial variation of the magnetic field strength (top panels in Fig. 3.4). Whereas the strength in the more vertical component (component #1 in the 2C inversion or $\log\tau_5 = 0$ level in the 1C inversion) drops rapidly from the

[3]As pointed out by Müller et al. (2002) and Schlichenmaier et al. (2002), δA for Fe I 1.56 μm lines is dominated by the jump in azimuths between the flux tube and background. Assuming $\Delta\phi = 0$ is justified as long as our studied region is near the line of symmetry of the sunspot (see Sect. 2.2.2). We have checked that, as expected, δA for the infrared lines changes when $\Delta\phi \neq 0$, but remains smaller than in the visible lines.

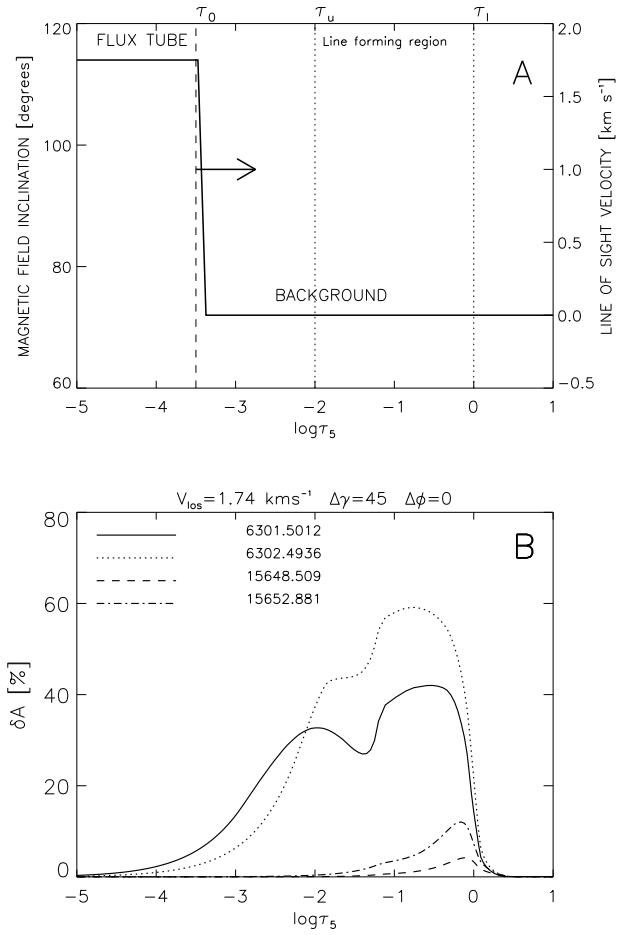

FIGURE 3.8: **A**: illustration of the method employed to determine the sensitivity of the Stokes V area asymmetry to discontinuities of the physical parameters along the line of sight. The thick solid line corresponds to a possible stratification including a flux tube. The vertical dashed line marks the position of the boundary τ_0 which is displaced following the arrow. The vertical dotted lines limit the formation region for a generic spectral line. **B**: Stokes V area asymmetries resulting from the calculations of two visible and two infrared neutral iron lines. For the infrared lines, $\delta A_{\max} \simeq 10\%$ and the range of sensitivity is $\log\tau \in [0,-1]$. Visible lines are much more affected by the discontinuity in a wider optical depth range. The maximum area asymmetry of the visible lines occurs when the discontinuity is placed at higher layers than in the case of the infrared lines.

inner to the outer penumbra, the field strength of the flux tube component decreases very slowly (component #2 of the 2C model or $\log\tau_5 = -1.0$ level in the 1C model). Roughly speaking, B changes only from $\sim$ 1300 G in the inner penumbra (where upflows are present) to $\sim$ 1000 G in the outer penumbra (where downflows dominate; $\zeta > 90^\circ$). A small radial decrease of the field strength in the flux tube was also obtained by Bellot Rubio (2003) from both 2C inversions and uncombed-like inversions of another spot [4]. However, this effect has passed unnoticed in previous 1C analyses.

To understand why, it is important to recall the limitations of the empirical models typically employed to analyze sunspot spectropolarimetric data. Generally only one atmosphere is assumed to be present in the resolution element and all atmospheric parameters are taken to be constant with height. Such models provide a horizontal and vertical average (over the resolution element and the height range of formation of the lines, respectively) of the magnetic and kinematic properties of the different penumbral structures. Thus, deduced field strengths generally drop from $\sim$ 2000 G in the inner penumbra to $\sim$ 1000 G at the outer penumbral boundary (Lites & Skumanich 1990; Solanki et al. 1992; McPherson et al. 1992; Lites et al. 1993; Keppens & Martínez Pillet 1996; cf. Solanki & Schmidt 1993).

This large decrease of the magnetic field strength has long been considered to present a major difficulty for explaining the Evershed effect in terms of a siphon flow whose downflowing footpoint lies within the penumbra (see Sect. 2.3). In the last decade it has become clear that most of the mass carried by the Evershed flow emerges first in the inner part of the penumbra and returns below the solar surface at the outer penumbral boundary (Solanki et al. 1994,1999; Westendorp Plaza et al. 1997).

Siphon flow models, according to which the Evershed flow is driven by the gas pressure difference between the two footpoints (Meyer & Schmidt 1968; Degenhardt 1989; Thomas 1988; Thomas & Montesinos 1990, 1991; Montesinos & Thomas 1993, 1997) , require the opposite behavior, that is, larger magnetic fields in the (outer) downflowing footpoint than in the (inner) upflowing footpoint. In fully dynamic models a similar behavior is found (Schlichenmaier 2002; c.f. Schlichenmaier et al. 1998a,1998b) if mass return is to be present within the penumbra. Montesinos & Thomas (1997) have argued that differences in the geometrical height at which the magnetic field is measured in the inner and outer penumbra can make the observed field in the downflowing footpoint appear smaller, while in reality it is larger. This hypothesis remains to be proven for realistic sunspot models (Solanki 2003).

In agreement with the results obtained from Ti I 2.2 μm lines by Rüedi et al. (1998,1999), our inversions show a slowly decreasing (almost constant) field strength inside the (almost) horizontal magnetic component carrying the Evershed flow (flux tube). This result removes one of the main hurdles facing the siphon flow mechanism and reduces the need to invoke changes in the height of the observed layers within the penumbra (Montesinos & Thomas 1997). Thus, most of the magnetic flux in the penumbra exhibits the strong reduction in field strength with radial distance required to attain a magnetohydrostatic equilibrium. The small part of the magnetic flux supporting the Evershed flow is almost independent of radial distance, however. An investigation

[4] The term uncombed-like inversions refer to a two component model where a Gaussian function is used to represent the discontinuities along the line of sight in the physical quantities. This mimics the step function used in Fig. 3.6. The central position and width of the Gaussian would be equivalent to the central position Z_0 and radius R_T of the penumbral flux tubes as in the uncombed model from Solanki & Montavon (1993) in Table 3.2.

involving a more realistic geometry of the penumbral magnetic field, including constraints on the pressure gradients within the flux tubes will be carried out in Chapters 4-5.

3.8 A picture of the penumbral fine structure

In Sect. 3.5 we have seen that the atmospheric parameters resulting from the 1C and 2C inversion show essentially the same behavior: a weaker, more horizontal field supporting the Evershed flow (flux tubes) coexists with a stronger, more vertical field containing gas that is essentially at rest (background). From a geometrical point of view, however, the two models are significantly different. In the 1C model the flux tube lies on top of the background, while in the 2C model, both structures coexist next to each other, without any vertical interlacing. It is not straight forward to decide, on the basis of the present data, which model comes closer to reality. On the one hand, the 1C model is able to provide slightly better fits to the observed profiles while the inversions based on the 2C model show smoother radial variations (see Fig. 3.4). However, it is important to recall that, for comparison purposes, we have defined two (somewhat arbitrary) fixed optical depths in the 1C model to extract the atmospheric parameters. It is likely that a different or more dynamic selection of these two points produces smoother radial variations for the 1C model. On the other hand, an advantage of the 2C inversions is that the physical meaning of the two components is very intuitive, whereas in the 1C inversions the two structures are described by the same atmosphere. In addition, the 1C model presents large gradients in the magnetic field inclination with height which are likely to produce unrealistically large magnetic curvature forces (Solanki et al. 1993). However, these gradients are an essential ingredient of the model, needed to produce asymmetric Stokes V profiles. Nevertheless, the observed Stokes V area asymmetry of the 1.56 μm lines is so small that it does not by itself completely rule out the 2C model.

Westendorp Plaza et al. (2001a, 2001b) used a 1C model applied to visible 630 nm Fe I lines and found LOS velocities and magnetic field inclinations decreasing with height, but field strengths increasing with height. From the application of a similar 1C inversion, but applied to the infrared 1.56 μm Fe I lines, we have obtained (see also Bellot Rubio et al. 2002 and Mathew et al. 2003) field strengths that decrease and velocities and magnetic field inclination angles that increase with height As discussed in Mathew et al. (2003) all these results are consistent if visible lines are assumed to sample the upper boundary of the penumbral flux tubes (arrow labeled 1C-VISIBLE in Fig. 3.9) while infrared lines, more sensitive to deep layers, sample the lower boundary (arrow 1C-INFRARED in Fig. 3.9). In addition, the results returned by the 2C model in this work (see also del Toro Iniesta et al. 2001, Bellot Rubio 2003, and Bellot Rubio et al. 2003) provide information on the flux tubes and the background fields (2C-no.1 and 2C-no.2 arrows). Note, however, that this picture needs to be tested using a more realistic model incorporating a magnetic flux tube.

Another very remarkable result from the 2C model concerns the difference in the azimuthal angle of the magnetic field vector for the flux tube and the magnetic surrounding. After carrying out a 2C inversion for the whole penumbral region (not restricted now to the selected region in Fig. 3.1) we can plot this azimuth difference $\varphi_t - \varphi_s$ as a function of the position in the penumbra. This result is presented in Fig. 3.10 (cf Fig.2.14). As we can see, this difference is positive of the left side of the line of symmetry but negative on the right side. This behaviour was already pre-

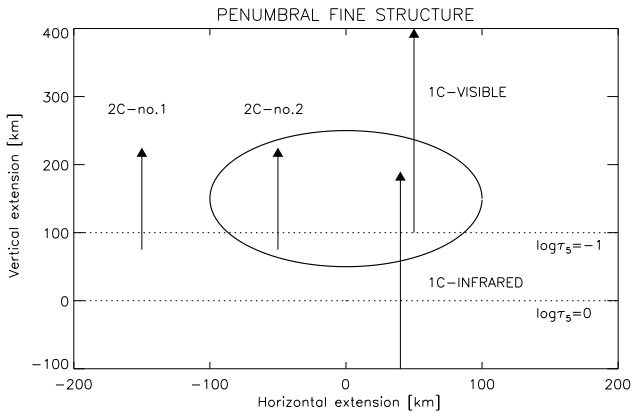

FIGURE 3.9: Sketch of the fine structure of the penumbra. A vertical slice through the penumbra in a direction perpendicular to the fibrils is shown. The oval structure is a cross-section of the flux tube (its shape is of no consequence for the present discussion). The different arrows mark the structures and layers to which the results of 1C inversions with gradients of the atmospheric parameters (right arrows) and 2C inversions without gradients (left arrows) of visible and infrared lines should be ascribed. See text for details.

dicted by Müller et al. (2002) and Schlichenmaier et al. (2002) from the NCP shown by the 1.56 μm lines (see Sect. 2.2.2). Note however, that our 2C model is unable to produce any Net Circular Polarization (Eq. 3.2), and therefore we must conclude that the information on the azimuthal angles comes mainly from the linear polarization profiles (Stokes Q and U). This result provides strong evidence supporting the picture of a flux tube and magnetic background atmosphere that, in the local reference frame, have the same azimuthal angle. This result, althought with a much smaller correlation and only for some radial distances, is also seen in the 1C inversion.

3.9 Summary

We have studied the structure of sunspot penumbrae by means of spectral line inversions considering two different geometries. The first model assumes a one-component atmosphere where all physical parameters are allowed to change with height, while the second model consists of two independent, horizontally interlaced magnetic components whose velocities and magnetic vectors are constant with height. We have shown that both models provide very similar results featuring an almost horizontal magnetic field with a strength of about 1200 G which remains almost constant with radial distance and carries the Evershed flow. This field is inclined slightly upwards in the inner penumbra, is horizontal in the middle penumbra and is inclined downwards at large radial distances. This relatively weak field neighbours a strong (up to $\simeq 2000$ G) and more vertical one (zenith angle, $\zeta \simeq 40^\circ$). The strength of the stronger field decreases rapidly with radial distance, becoming almost identical to that of the weaker field in the outer penumbra.

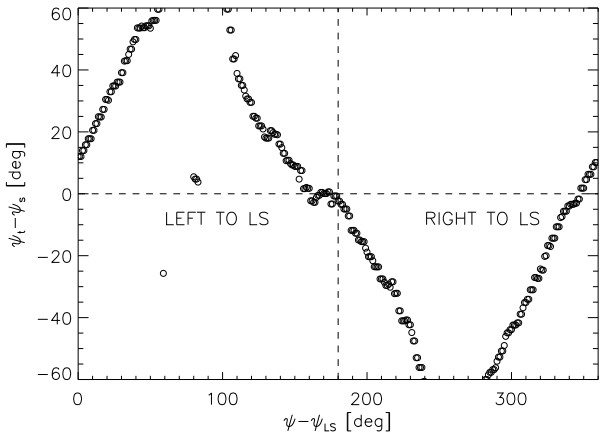

FIGURE 3.10: Difference in the azimuthal angle between component 2 and component 1 retrieved from the 2C inversion as a function of the position around the spot for a radial position at $r/R = 0.65$. Compare with Figure 2.14. Good correlations are also obtained at small-intermediate radial distances from the sunspot center. For the 1C inversion this correlation is also found in $\varphi(-1) - \varphi(0)$, where the number in brackets indicate the optical depth points from where the azimuthal is taken.

No clear signature of the Evershed flow is found in this stronger, more vertical field. The small radial decrease of the magnetic field strength in the component carrying the Evershed flow significantly reduces a major hurdle facing the siphon flow mechanism as the driver of the Evershed effect.

Although the two models lead to the same basic results, they are significantly different from a geometrical point of view. While in the 1C model the weaker field overlies the stronger one, in the 2C model they lie side by side. Consequently, the 1C model includes gradients along the line of sight. In the second model, no gradients are present because the two components do not interlace vertically. Such gradients or discontinuities along the line of sight are needed to reproduce the area asymmetry observed in the circular polarization profiles. In order to understand why both assumed geometries lead to similar properties for the penumbral fine structure, we have studied the sensitivity of the area asymmetry of selected spectral lines to discontinuities along the line of sight. The infrared lines used in this paper turn out to be almost insensitive to such gradients. This explains why the two-component model is able to provide a good fit to the observations and why inversions based on it reveal a very similar penumbral structure as the one-component model with gradients. The same sensitivity analysis carried out for visible lines commonly used in spectropolarimetry (Fe I 6301 and 6302 Å) indicates that the corresponding Stokes V profiles are much more asymmetric than their infrared counterparts. Therefore, it is very likely that models including gradients/discontinuities will be necessary to reproduce these lines (see Chapter 5).

We also point out that the results obtained from both assumed geometries can be naturally interpreted in terms of nearly horizontal flux tubes with a lower field strength containing outflowing gas that are embedded in a more vertical, stronger field in which gas is essentially at rest. This picture is in line with that proposed by Solanki & Montavon (1993) and Martínez Pillet (2000). The obvious next step is to carry out an inversion based on such a model (see Chapter 4).

The current work cannot contribute to the intense debate over the last years about the width of the flux tubes, in particular whether they are optically thick or thin (Sánchez Almeida 1998, 2001; Martínez Pillet 2000, 2001; Sütterlin 2001; Scharmer et al. 2002). The same observable effects would result from either one single thick tube (such as depicted in Fig. 3.9) or a bundle of smaller flux tubes of similar total optical thickness concentrated around $z \simeq 150$ km above the continuum layers. Recent observations of the penumbra at very high spatial resolution (Scharmer et al. 2002) show individual filaments 100–200 km thick (depending on whether only the inner dark core is considered to be a flux tube or the lateral bright features are also included). This strongly suggests that at our spatial resolution we deal with a situation where more than one fibril is present in the resolution element.

Chapter 4

The nature of the Evershed flow

The next step in the modelling of the penumbral fine structure will be to employ a model such as that sketched in Sect 3.8. This model allows for a flux tube embedded in a magnetic background, and requires horizontal pressure balance between the two magnetic components. We apply our model to spectropolarimetric observations of two neutral iron lines at 1.56 μm and invert several radial cuts in the penumbra of the same sunspot at two different heliocentric angles. In the inner part of the penumbra we find hot flux tubes that are somewhat inclined to the horizontal. They become gradually more horizontal and cooler with increasing radial distance. This is accompanied by an increase in the velocity of the plasma and a decrease of the gas pressure difference between flux tube and background components. At large radial distances the flow speed seems to experiment a super-subcritical transition leading to a possible formation of a shock front. These results are in good agreement with simulations of the penumbral fine structure and so far provide the strongest evidence supporting the siphon flow as the physical mechanism driving the Evershed Flow.[†]

4.1 Introduction

The picture of the fine structure of the penumbra has strongly evolved over the last decade (e.g., Degenhardt & Wiehr 1991; Title et al. 1993; Solanki & Montavon 1993; Westendorp Plaza et al. 1997; Schlichenmaier et al. 1998a; Scharmer et al. 2002; see Solanki 2003 and Bellot Rubio 2003 for an overview). Consequently it is now accepted that the penumbral magnetic field is *uncombed*, i.e. inclined at least in two different directions on a small scale. There is also considerable evidence that the more horizontal component must be in the form of flux tubes, but the diameter of these flux tubes is still a matter of debate (Sánchez Almeida 1998,2001; Martínez Pillet 2000,2001). These flux tubes carry the Evershed flow (Evershed 1909; Title et al. 1993; Westendorp Plaza et al. 2001a,2001b; Bellot Rubio et al. 2003; Borrero et al. 2004; see also Chapter 3). Many of the tubes return to the solar interior within the penumbra (Westendorp Plaza

[†]This chapter has been submitted for publication to Astronomy & Astrophysics: Borrero, J.M., Solanki, S.K., Lagg, A. & Collados, M. A&A (submitted)

et al. 1997; del Toro Iniesta et al. 2001; Mathew et al. 2003; Borrero et al. 2004) and along with the magnetic flux a large fraction of the mass flux carried by the Evershed flow returns also to the solar interior within the penumbra or just outside it (Börner & Kneer 1992; Solanki et al. 1994,1999).

The combination of these results raises questions regarding the commonly considered physical mechanism for driving the Evershed flow. Since the wave hypothesis is ruled out (Bünte & Solanki 1995) and episodic Evershed flow produced when a flux tube *falls* and drains (Wentzel 1992) faces difficulties due to the relative immutability of the penumbral magnetic pattern (Solanki & Rüedi 2003), the most widely accepted mechanism is that the flow is caused by a gas pressure gradient between the upflowing and the downflowing footpoints (Meyer & Schmidt 1968). Commonly, this pressure gradient is thought to be produced by a difference in the field strength between the footpoints, which, due to horizontal pressure balance leads to a gas pressure difference (e.g. Degenhardt 1991; Montesinos & Thomas 1993,1997). All else being equal, the gas flows from the footpoint with lower field strength to the footpoint with the higher field strength. However, if most of the gas flows only within the penumbra, then due to the roughly factor of 2 larger magnetic field strength at the inner boundary of the penumbra than at the outer edge, one would mainly expect the gas to flow inwards, contradicting observations. Montesinos & Thomas (1997) have argued that this radial decrease of the field strength is only apparent, being caused by different $\tau = 1$ levels at the footpoints. However, the global magnetic structure of a sunspot is close to potential, which implies a field strength decreasing towards the edges of the sunspot at a given geometrical height.

A possible resolution of this dilema was noticed by Borrero et al (2004; see Chapter 3), who found that whereas the strength of the inclined magnetic component indeed drops very rapidly in the radial direction, the horizontal component carrying the Evershed flow shows far less variation (cf. Rüedi et al. 1998,1999). The analysis of Borrero et al. was incomplete in the sense that the two components were independent of each other. Here we overcome this shortcoming and take into account the flux-tube structure of the field. We apply a powerful inversion technique (described in Section 4.2) to spectropolarimetric observations of infrared Zeeman sensitive spectral lines (Section 4.3). General results are presented and discussed in Section 4.4. In Section 4.5 we discuss the generation of Net Circular Polarization by the uncombed model and the implications for the typical size of the penumbral flux tubes. Section 4.6 is entirely devoted to explain our results in the frame of the theoretical models employed to explain the Evershed effect in terms of gas pressure differences. Our main findings and conclusions are summarized in Section 4.7.

4.2 Description of the employed model and inversion process

The analysis of spectropolarimetric observations of the sunspot penumbra by means of Stokes profile inversion has, so far, either considered 2 distinct components (assuming the physical quantities to be constant with depth: Bellot Rubio et al. 2003) or 1 component (allowing gradients to be present; Westendorp Plaza et al. 1997a, 2001a, 2001b; Bellot Rubio et al. 2002; Mathew et al. 2003). In Chapter 3 we have suggested that the *uncombed* penumbral model described by Solanki & Montavon (1993) provides a picture for the penumbral fine structure that is able to embrace the results of these investigations. This conclusion was based on the application of

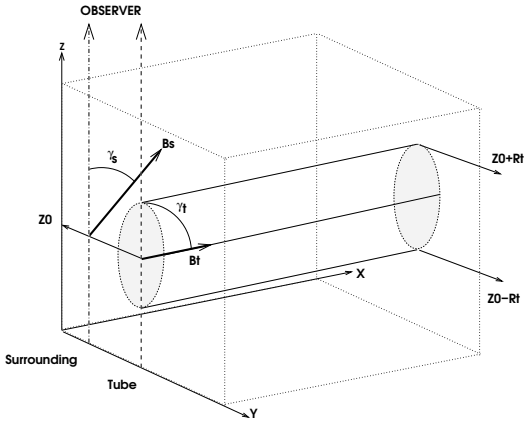

FIGURE 4.1: Example of the geometrical scheme used in the inversion. The radiative transfer equation is solved along the 2 rays (dashed and dot-dashed lines) representing the flux tube and surrounding atmospheres respectively. γ_s and γ_t refer to the inclination of the magnetic field vector with respect to the observer. In this picture for simplicity the heliocentric angle is $\theta = 0$ and $\gamma_t = 90$.

a Stokes profiles inversion technique assuming the two different geometries mentioned above, together with considerations on how the area asymmetry of the circular polarization profiles is influenced by gradients in the magnetic and kinematic stratifications.

In this chapter we carry out Stokes profile inversions based on the uncombed model. This basically consists of a flux tube embedded in magnetic surroundings. Although restricted to Stokes V, the foward modelling has already been addressed in the past (see e.g. Degenhardt & Kneer 1992) The basic geometry is illustrated in Figure 4.1. The simplest representation of the uncombed model is in terms of two rays: the first ray passes along the surrounding atmosphere (vertical dot-dashed line pointing towards the observer) and rays cutting both surrounding atmosphere and the flux tube (vertical dashed line). Let us denote with χ_s any of the magnetic and kinematic physical quantities for the surrounding atmosphere[1]. For the flux tube component we adopt the following form for $\chi_t(z)$:

$$\chi_t(z) = \begin{cases} \chi_t & \text{if } \; z \in [z_0 - R_t, z_0 + R_t] \\ \chi_s & \text{otherwise} \end{cases} \tag{4.1}$$

where χ_t on the right hand side of Eq. 1 is height independent, z_0 is the height where the axis of the flux tube is located and R_t is its radius. Note that Eq. 4.1 implies that physical stratifications along the flux tube atmosphere (vertical dot-dashed line in Fig. 4.1) are the same as in the surrounding atmosphere above and beneath the flux tube: $z < z_o - R_t$ and $z > z_o + R_t$. At the flux tube lower and upper boundaries ($z^* = z_0 \pm R_t$) the physical quantities suffer a jump whose magnitude is $\Delta_\chi = \chi_t - \chi_s$. These jumps/gradients are the essential ingredients to explain the NCP observed in the sunspot penumbra (Solanki & Montavon 1993; cf. Martínez Pillet 2000; see also Sect. 2.2.2).

The inversions based on this geometry have been carried out using the inversion code SPINOR (see Frutiger 1999; Frutiger et al. 2000; see also Sect. 1.5.6). The code performs spectral line syn-

[1] χ_s is assumed to be height independent.

thesis in Local Thermodynamic Equilibrium (LTE) and employs a Levenberg-Marquart nonlinear least-squares algorithm (Press et al. 1986) whereby derivatives are calculated through numerical response functions (RF's; see Ruiz Cobo & del Toro Iniesta 1992; see also Sect. 1.5.3). The free parameters allowed in the inversion are, for the surrounding atmosphere: $V_{\rm LOS,s}$ (line of sight velocity), $B_{\rm s}$ (magnetic field strength), $\gamma_{\rm s}$ (magnetic field inclination with respect to the observer), $\phi_{\rm s}$ (magnetic field azimuth) and $T_{\rm s}(\tau_5 = 1)$ for temperature. The height dependence of $T_{\rm s}(\tau)$ is taken from the penumbral model by del Toro Iniesta et al. 1994). For the flux tube: $V_{\rm LOS,t}$, $B_{\rm t}$, $\gamma_{\rm t}$, $\phi_{\rm t}$, macro and microturbulent velocities, $v_{\rm mac,t}$ and $v_{\rm mic,t}$, and $T_{\rm t}(\tau_5 = 1)$ (where again $T_{\rm t}(\tau)$ is taken from the mean penumbra model of del Toro Iniesta et al.). In addition z_0, $R_{\rm t}$ and $\alpha_{\rm t}$ (fractional area covered by the flux tube component with respect to the total area) are also allowed to change. Finally we employ a stray light correction to model the contribution of light from the neighbouring granulation that enters into the spectrograph's slit. To this end we have used the two component model for the quiet sun from Borrero & Bellot Rubio (2002) to produce synthetic intensity profiles, $I_{\rm q}$ of the observed spectral lines (see Sect. 4.3) and combined it with the emergent spectrum of the pure penumbral profiles using a filling factor $\alpha_{\rm q}$ which is also retrieved from the inversion. This results in a total of 16 free parameters. Note that inversions carried out in chapter 3 used a total number of 23 and 18 free parameters for the 1 component and 2 component inversions respectively.

The radiative transfer equation is integrated using the Hermitian Approach (see Bellot Rubio et al. 1998) for each ray separately. The Stokes profiles from quiet sun, flux tube and surrouding atmosphere are finally combined using the filling factors $\alpha_{\rm t}$ and $\alpha_{\rm q}$:

$$\boldsymbol{S}(\lambda) \;\; = \;\; \alpha_{\rm q}\boldsymbol{S}_{\rm q}(\lambda) + (1-\alpha_{\rm q})[(1-\alpha_{\rm t})\boldsymbol{S}_{\rm s}(\lambda) + \alpha_{\rm t}\boldsymbol{S}_{\rm t}(\lambda)] \;\; , \tag{4.2}$$

where $\boldsymbol{S}$ represents Stokes vector (I,Q,U,V) as calculated along the surrounding atmosphere (dashed ray in Fig. 1) $\boldsymbol{S}_{\rm s}$, the ray cutting the flux tube (dot dashed ray in Fig. 1) $\boldsymbol{S}_{\rm t}$ as well as the quiet sun contribution $\boldsymbol{S}_{\rm q} = (I_{\rm q}, 0, 0, 0)$ which is a non polarized contribution and only affects the total intensity profiles. These synthetic profiles are now compared with the observations and the free parameters are changed according to the RF's until the minimum is reached. A detailed study of the numerical performance of this procedure as well as the uniqueness of the retrieved atmosphere under different levels of noise in the observations is presented by Borrero et al. (2003b).

The radiative transfer is always performed in optical depth scale, but the flux tube and its force balance with its surroundings are more naturally described in geometrical depth scale. This interplay requires a sufficiently complex procedure that we deem it neccesary to detail. First, a geometrical height scale is assigned to the surrounding atmosphere following the strategy outlined in Gray (1992) and integrating the hydrostatic equilibrium equation (assuming a force free situation $\nabla \times \mathbf{B} \parallel \mathbf{B}$)).

$$\frac{\partial P_{g,s}}{\partial \tau_s} = \frac{g}{\kappa_{c,s}} \tag{4.3}$$

where g is the solar surface gravitational acceleration and τ is the optical depth computed using the continuum opacity at 5000 Å: κ_c. This requires an estimate of the the gas pressure at the

top of the tabulated atmosphere: $P_{g,s}(\tau_{s,max})$. With this, the gas pressure stratification $P_{g,s}(\tau_s)$ is obtained in the surrounding atmosphere, and since the temperature had been obtained from the inversion, the equation of state (ideal gas law including a variable mean molecular weight to account for the ionization of the different species) provides us the density: $\rho_s(\tau_s)$. The relation $d\tau_s = -\rho_s \kappa_{c,s} dz$ is now integrated setting $z = 0$ at $\log \tau_5 = 0$ and thus defining the geometrical height scale.

The gas pressure in the tube component is obtained under the assumption of total pressure balance with the surroundings at the height of the axis of the flux tube.

$$P_{\mathrm{g,t}}(z) = \begin{cases} P_{\mathrm{g,s}}(z) + \frac{B_s^2 - B_t^2}{8\pi} & \text{if} \quad z \in [z_0 - R_\mathrm{t}, z_0 + R_\mathrm{t}] \\ P_{\mathrm{g,s}}(z) & \text{otherwise} \end{cases} \tag{4.4}$$

This assumption is valid as long as the magnetic field of the external atmosphere does not penetrate into the flux tube and vice versa (Kippenhahn & Möllenhof 1975, Chap.3). Since $P_{g,t}(z)$ is now known and $T_t(z)$ was obtained from the inversion, the density $\rho_t(z)$ can be evaluated, and thus a new optical depth scale for the atmosphere containing the flux tube can be obtained through the relation: $d\tau_t = -\rho_t \kappa_{c,t} dz$. For the integration of this last equation a boundary condition which implies that for $z > z_0 + R_\mathrm{t}$ the surrounding and flux tube components must have the same z values: $z(\tau_t) = z(\tau_s)$

4.3 Observations and data reduction

The active region NOAA AR 8706 was observed in Sep 21st, 1999 and Sep 27th, 1999 at two different positions on the solar disk: $\mu = 0.51$ and $\mu = 0.91$ respectively, using TIP (Tenerife Infrared Polarimeter, Martínez Pillet et al. 1999) attached to the spectrograph of the 70cm German VTT of the Observatorio del Teide. The recorded spectral region contains the full polarization profiles of the pair of lines Fe I ($g_{eff} = 3$) 15648.5 Å and Fe I ($g_{eff} = 1.53$) 15652.8 Å. The wavelength sampling is about 29 mÅ. The diagnostic properties of these lines have been discussed by Solanki et al. (1992b). They are formed in the deep photosphere as a result of their high excitation potentials and the low continuum opacity at this wavelength. These lines sample a relatively narrow layer not wider than $\log \tau_5 = [0.5, -2]$ (see Bellot Rubio et al. 2000; Mathew et al. 2003), where τ_5 is the optical depth at a reference wavelength of 5000 Å. The second neutral iron line is heavily blended by two molecular OH lines in the umbra (15651.9 and 15653.5 Å). These lines belong to the Meinel system (3,1; see Berdyugina & Solanki 2002 for details). Their equivalent widths greatly decreases towards the penumbra, however they can still be seen clearly at umbra-penumbra boundary. The atomic parameters for the observed Fe I lines were taken from Borrero et al. (2003a), while for the OH lines the values given by Abrams et al. (1994) and Mies (1974) were used (see Table 4.1).

The usual data reduction procedures for TIP were in general followed; we proceeded carefully at several points, however. Firstly the neutral iron line, Fe I 15648.5, appears to be blended by a telluric line in its red wing. This complication was overcome by fitting the average quiet Sun profile of the second line with an appropriate model atmosphere. This model was then used to synthetize the first iron line. The ratio between the average observed and computed line allowed us to recover the shape of the telluric blend, which was subsequently eliminated from the rest of

TABLE 4.1: Atomic and molecular parameters of the observed spectral lines. λ_0 represents the laboratory central wavelength, χ_l the excitation potential of the lower energy level, and $\log gf$ the logarithm of the oscillator strength times the multiplicity of the level. The parameters α and σ (in units of Bohr's radius, a_0) are used to calculate the broadening of the lines by collisions with neutral hydrogen atoms as resulting from the ABO theory (Barklem & O'Mara 1997). The last column gives the effective Landé factor of the transition, $g_{\rm eff}$. For the molecular lines $I_{\rm U}$, $I_{\rm L}$, $V_{\rm U}$ and $V_{\rm L}$ represent the upper/low multiplets sublevels and vibrational levels respectively. $J_{\rm L}$ stands for the rotational number of the lower level. Finally, the oscillator strength is given.

Atom	λ_0 (Å)	χ_l (eV)	log gf (dex)	α	σ (a_0^2)	$g_{\rm eff}$
Fe I	15648.515	5.426	-0.675	0.229	977	3.00
Fe I	15652.874	6.246	-0.043	0.330	1444	1.53
Molecule	λ_0	Branch	$I_{\rm U}$-$I_{\rm L}$	$V_{\rm U}$-$V_{\rm L}$	$J_{\rm L}$	f
OH	15651.895	P	1-1	3-1	6.5	0.8×10^{-6}
OH	15653.478	P	1-1	3-1	6.5	0.8×10^{-6}

the profiles. This procedure, although not perfect, does not introduce modifications to the original profile (equivalent width and line core intensity) larger than $\sim$3 %.

Secondly, the continuum correction posed a considerable problem. The four quadrants configuration of TIP's camera produce small gradients in the continuum intensity that remain after applying the flat field correction. To account for this we compared our spatially averaged flat field with the infrared FTS atlas from Livingston & Wallace (1991) and define several wavelength positions where the continuum should be reached. A smooth second order polynomial is interpolated over those selected points and used to bring the continuum in the flat field image to the same level as the FTS continuum. Thirdly, the polarization signals were corrected for residual cross talk using the statistical approach described in Collados 2001 (see also Schlichenmaier & Collados 2002). Finally, the wavelength was calibrated by assigning the laboratory wavelengths to the cores of the Fe I lines in the average quiet Sun profiles. To account for the effects of the granulation we shifted this wavelength scale by -400 m s^{-1}, which is the approximate value for the convective blueshift as deduced from the quiet sun model of Borrero & Bellot Rubio (2002).

The seeing conditions were rather good during the observations, with the granulation being clearly discernible in the reconstructed continuum images (see Figure 4.2; left panels). By calculating the power spectrum of the continuum intensity in the neighbouring quiet Sun we estimate the spatial resolution to be about 1 arc sec. In Fig. 4.2 (right panels) the maps of the total circular polarization are also shown. Due to projection effects the polarity inversion line (region in the limb side of the penumbra where the Stokes V signal changes its sign, i.e.: where the average magnetic field is perpendicular to the observer) appears in the outer penumbra when the sunspot is observed near disk center ($\mu = 0.91$) but approaches the umbra as the spot moves towards the limb ($\mu = 0.51$). Part of this data set has been analyzed earlier by Mathew et al. (2003) and Borrero et al. (2004).

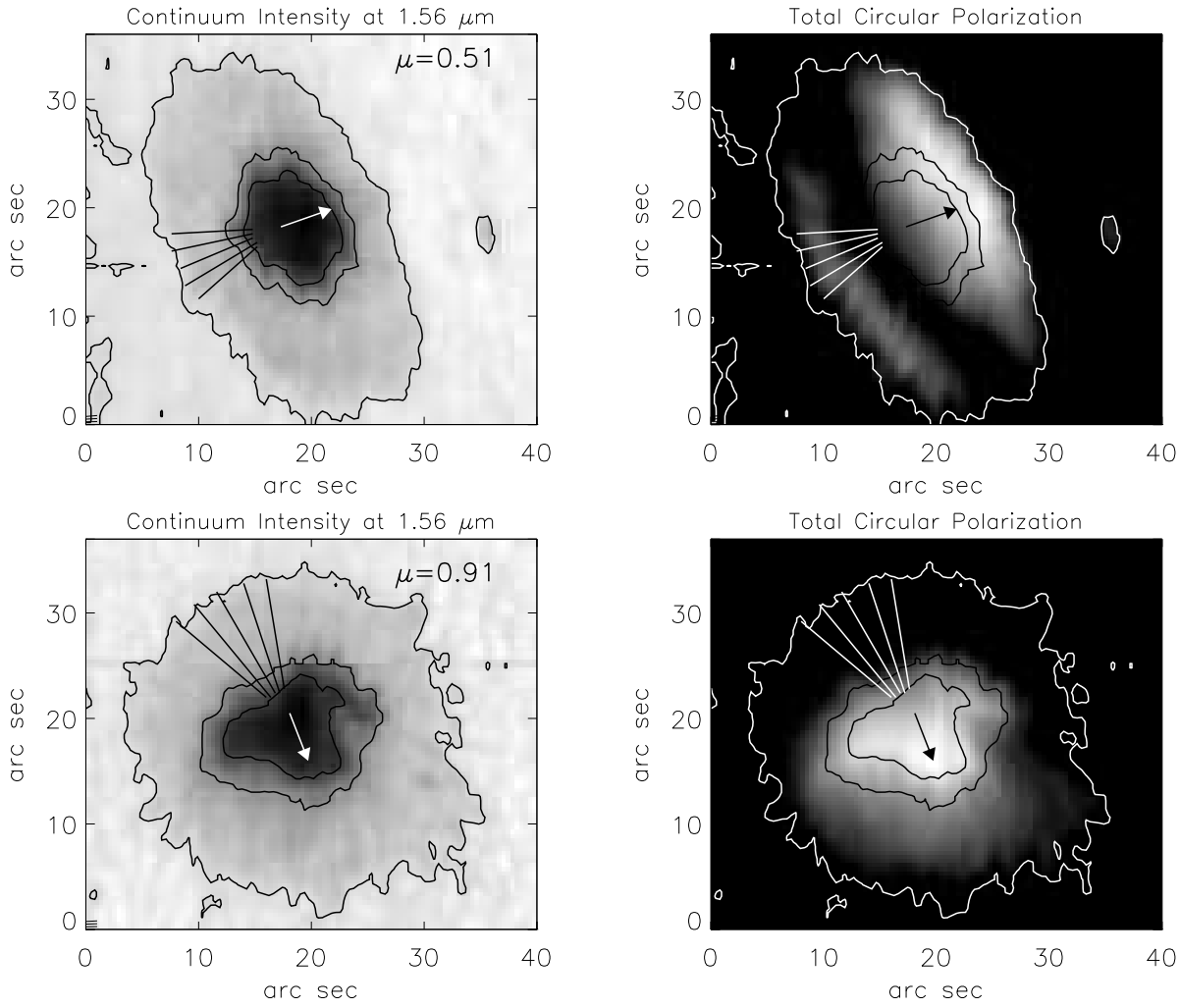

FIGURE 4.2: Top panels: NOAA 8706 observed in 21 September 1999 at a heliocentric angle $\mu = 0.51$ (left: continuum intensity map at 1.56 μm; right: total circular polarization map for Fe I 15648.5 Å). Bottom panels: NOAA 8706 observed in 27 September 1999 at a heliocentric angle μ=0.91 (left: continuum intensity map at 1.56 μm; right: total circular polarization map for Fe I 15648.5 Å). The arrows point towards the direction of the solar disk center. The two inner-most contours enclose between them the umbral-penumbral boundary. The external contour defines the sunspot radius $r = R$, at each position angle. These three contours have been defined as $0.45I_c$,$0.65I_c$ and $0.85I_c$, where I_c represents the average continuum intensity of the quiet Sun. The radial cuts selected for our analisys are also shown.

4.4 Results and discussion

We have inverted individually all the pixels along the radial cuts shown in Fig. 4.2 (5 for each heliocentric angle). Each cut contains approximatively 20 pixels and ranges roughly from $r/R = 0.4$ to $r/R = 0.9$ (where R is the penumbral radius, indicated by the external contour in Fig. 4.2). As in chapter 3 we have chosen the cuts such that they all lie on the limbward side of the penumbra and near the line of symmetry (i.e. the line connecting the sunspot's center and the center of the solar disk), since this is where the the flux tubes leave the most distinctive fingerprints on the observed profiles, thus allowing for a reliable determination of their properties.

4.4.1 Example

In Fig. 4.3 we present an example of the observed (filled circles) and fitted (solid lines) circular polarization profiles for a penumbral point. These multi-lobed profiles can be successfully fitted by means of two different Stokes V profiles. The profile from the flux tube surroundings, V_s, is produced by a positive polarity magnetic field ($\gamma < 90^\circ$; dot-dashed line) with zero line-of-sight velocity (zero crossing is at λ_0), and the Stokes V profile from the flux tube itself, V_t, which is produced by a negative polarity magnetic field ($\gamma > 90^\circ$; dashed line) carrying a flow directed away from the observer (zero crossing is red shifted with respect to λ_0). The filling factor of the flux tube atmosphere α_t and of the stray light contribution α_q are applied to V_s and V_t to obtain the final emergent profile (solid line) according to Eq. 4.2.

In Fig. 4.4 we present the atmospheric stratifications resulting from the inversion of the profiles shown in Fig. 4.3 using the uncombed model. The surrounding atmosphere (dot-dashed lines) possesses height independent parameters (except for the temperature), while the flux tube atmosphere (dashed) has the same stratifications except between $z_0 \in [z_0 - R_t, z_0 + R_t]$ where the line of sight crosses the tube and therefore the physical parameters suffer a jump. Outside the flux tube the magnetic field strength is about 2000 Gauss and is inclined with respect to the observer by about 75°. Inside the flux tube the magnetic field is weaker ($\simeq$ 1300 Gauss) and is more inclined $\gamma \simeq 100^\circ$. While the surrounding atmosphere is basically at rest, $V_{\mathrm{LOS,s}} \simeq 0.2$ km s^{-1}, inside the flux tube we detect red shifts of $V_{\mathrm{LOS,t}} \simeq 1.1$ km s^{-1}. In addition, the results from the inversion indicate that the flux tube is hotter, by roughly 500 K, than the surrounding atmosphere. The presence of the discontinuity along the flux tube atmosphere produces the area asymmetry in Stokes V, δA_{FIT}, as shown in Fig. 4.3.

4.4.2 General properties

We have taken the individual results for the inversions of the considered radial cuts (separately for each heliocentric angle) at the geometrical height $z = z_0$ (i.e. at the location of the tube axis), and calculated the averages at each radial position in the sunspot. This is done individually for the flux tube component and the surrounding magnetic field. The results are presented for the temperature (Fig. 4.5; top panels), line-of-sight velocity (Fig. 4.5; middle panels), the flux tube's filling factor α_t (Fig. 4.5; bottom panels), magnetic field zenith angle (Fig. 4.6; top panels) and magnetic field strength (Fig. 4.6; bottom panels). For the temperature we plot the difference between the flux tube and the surrounding atmosphere at $z = z_0$. In order to compare the magnetic

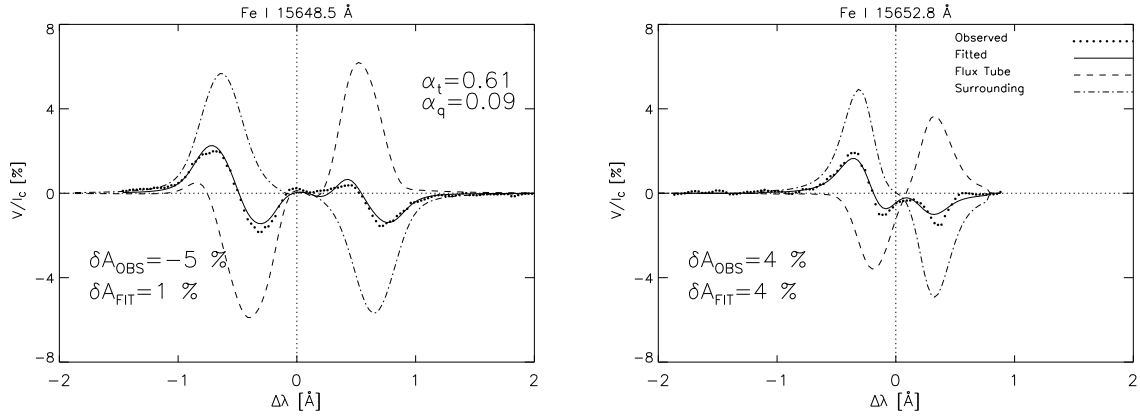

FIGURE 4.3: Example of the observed (filled circles) and fitted (solid lines) Stokes V profiles (left: 15648.5 Å; right: 15652.5 Å) for a penumbral point. The fitted profile is obtained after a linear combination of the profile emerging from the surrounding component (dot-dashed line; see also Fig. 4.1) and the profile emerging from the ray piercing the flux tube (dashed line; see also Fig. 4.1). The used filling factors α_t and α_q, as well as the area asymmetry of the observed and fitted profiles are also shown.

field inclination deduced for sunspots located at different heliocentric positions we have converted from the observer's reference frame, γ, to the local reference frame. Therefore, we plot now the zenith angle, ζ (Fig. 4.5; top panels). A zenith angle smaller than, equal to or larger than 90 degrees indicates that the magnetic field is inclined upwards, lies parallel to or is inclined downwards with respect to the solar surface. All in all, the results for the two sets of observations are remarkably similar in spite of the different viewing angles.

In the inner penumbra, we detect nearly, but not completely horizontal flux tubes ($\zeta_t \simeq 70-80^\circ$) that are hotter than their surroundings by about 500-1000 K. These flux tubes carry almost the whole fraction Evershed flow, with LOS velocities in the inner penumbra ranging between 0.5 and 3 km s^{-1}. The magnetic field strength in the flux tubes is around 1500 Gauss. The atmosphere surrounding these flux tubes possesses a more vertical $\zeta_s \simeq 20-40^\circ$ and stronger magnetic field $B \simeq$ 2300-2500. No signatures of the Eveshed flow are detected here.

As the radial distance increases, the flux tubes cool down to temperatures similar to those of the surroundings. At large radial distances $r/R \geq 0.7$ the temperature in the flux tube component decreases even below the surrounding temperature, although only slightly ($\simeq$ 200-300 K). At the same time the tubes become more horizontal, reaching $\zeta_t \simeq 90^\circ$, and points slightly downwards with respect to the solar surface, $\zeta_t \simeq 95-100^\circ$, near the outer edge of the penumbra, i.e. at $r/R \geq 0.8$. In addition, their magnetic field strength decreases slowly to 800-1000 Gauss at $r/R = 0.9$ while the LOS velocity increases monotonically in both spots, although for $\mu = 0.51$ it suffers sudden drop near the outer penumbral boundary. The filling factor of the flux tubes (Fig. 4.5; bottom panels) increases continuously from very small values at the inner penumbra $\alpha_t \simeq 0.2-0.3$ until they cover almost all the resolution element at the outer boundary $\alpha_t \simeq 0.9$. This can be interpretated either as an increase in the horizontal cross section of the flux tubes or as an increase in the number of flux tubes per resolution element.

The surrounding atmosphere exhibits quite a different behaviour. The magnetic field strength

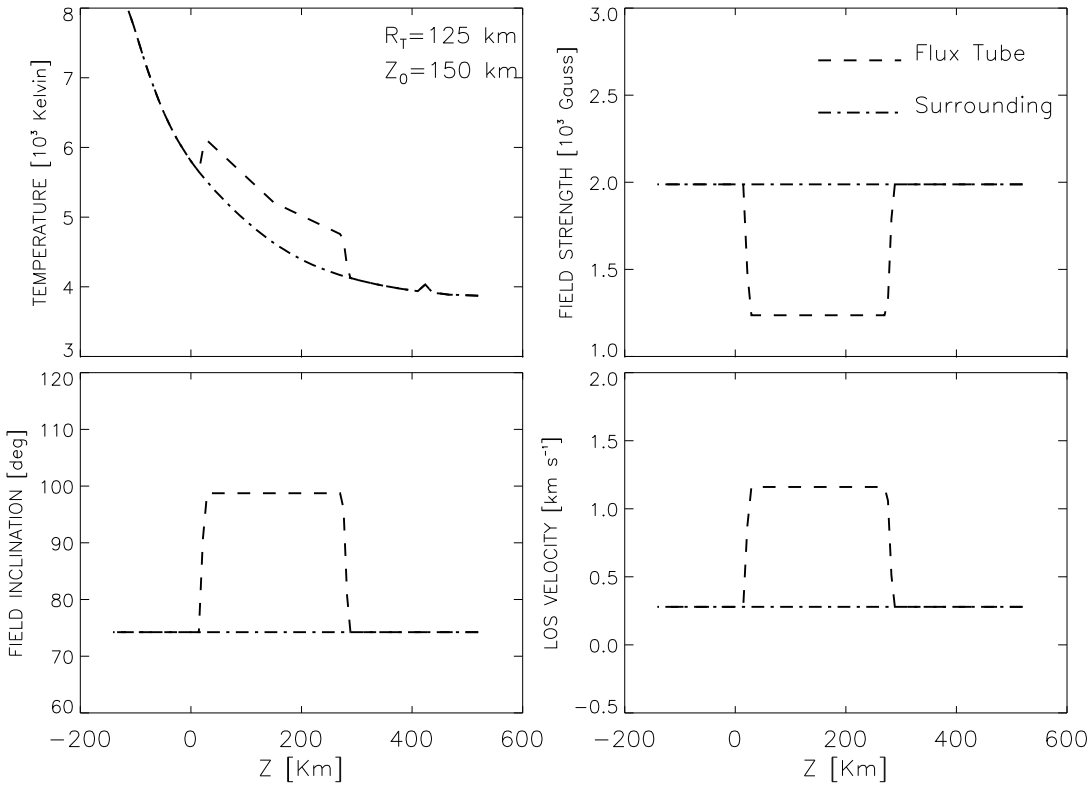

FIGURE 4.4: Temperature (top-left panel), magnetic field strength (top-right panel), magnetic field inclination (bottom-left) and line-of-sight velocity (bottom-right) for the flux tube atmosphere (dashed lines) and its surroundings (dashed-dotted lines) as a function of the geometrical depth, obtained from the inversion of the profiles in Fig. 3. The flux tube's radius is 125 km and its central position is $z_0 = 150$ km.

decreases very rapidly towards the outer penumbra, reaching similar values to those of the flux tube's magnetic field strength ($\simeq$ 800-1000 Gauss). The inclination of the magnetic field increases slightly with radial distance up to $\zeta_s \simeq 40-50^\circ$. The LOS velocities remain small throughout the penumbra.

Before discussing in more detail the individual results there are several points which need to be clarified. First of all, we want to stress that the results obtained from the inversions of the radial cuts when the spot is near the disk center (Figs. 4.5 and 4.6; left panels) are more reliable at intermediate to large radial distances, while results inferred from the sunspot at large heliocentric angles (Figs. 4.5 and 4.6; right panels) are more reliable in the inner penumbra. The reason for this is that the magnetic neutral line is located in the outer penumbral for sunspots near the disk center, $\mu = 0.91$, but it shifts towards the umbra as the sunspot is located closer to the limb ($\mu = 0.51$). The magnetic neutral line is where multi-lobed Stokes V profiles are commonly observed (Sánchez & Lites 1992; Schlichenmaier & Collados 2002). As already mentioned in Chapter 3 inferred parameters from the inversion are more reliable for exactly such complex profiles, since the signature of the two unresolved components (flux tubes and magnetic surrounding) can be better distinguished there (e.g. Fig. 4.3), allowing for a more reliable inference of their properties. In general, however, larger and more accurate line-of-sight velocities are obtained from the sunspot near the limb are to be given more confidence (at all radial distances) since the Evershed flow is here more aligned with the line of sight, giving rise to larger and more accurate line-of-sight velocities.

We note that if we take into account that the possible size of the flux tubes is much smaller than our spatial resolution of 1 arc sec (Sütterlin 2001; Scharmer et al. 2002; Van der Oort et al. 2004) the deduced properties are unlikely to correspond to one single flux tube but rather to some average over all the possible penumbral fibrils contained in the resolution element. However, as one can see from Fig. 4.5 and 4.6, the inferred properties are similar to those expected for a single flux tube which crosses the penumbra from its inner to the outer boundary.

4.5 Size of the penumbral filaments and area asymmetry

The area asymmetry, δA, of the circular polarization is defined as:

$$\delta A = \frac{\int V(\lambda)\,\mathrm{d}\lambda}{\int |V(\lambda)|\,\mathrm{d}\lambda}, \tag{4.5}$$

It is different from zero whenever gradients along the line-of-sight of the magnetic field vector and LOS velocity are present (Landolfi & Landi degl'Innocenti 1996). Solanki & Montavon (1993) realized that the huge gradients needed to reproduce the area asymmetry observed in the sunspot penumbra with the visible Fe I lines at 6301.5 and 6302.5 Å (Sánchez Almeida & Lites 1992) could be interpretated as a horizonal flux tube embedded in a more vertical background. As the line of sight crosses the tube's boundaries the physical stratifications describing the atmosphere suffer a jump that is directly responsible for the generation of the area asymmetry in Stokes V. Schlichenmaier at al. (2002) and Müller et al. (2002) further investigated this issue and pointed out that the area asymmetry observed in the visible Fe I 6301 Å lines is dominated by jumps in the magnetic field inclination, while the area asymmetry observed in the infrared 1.56 μm lines

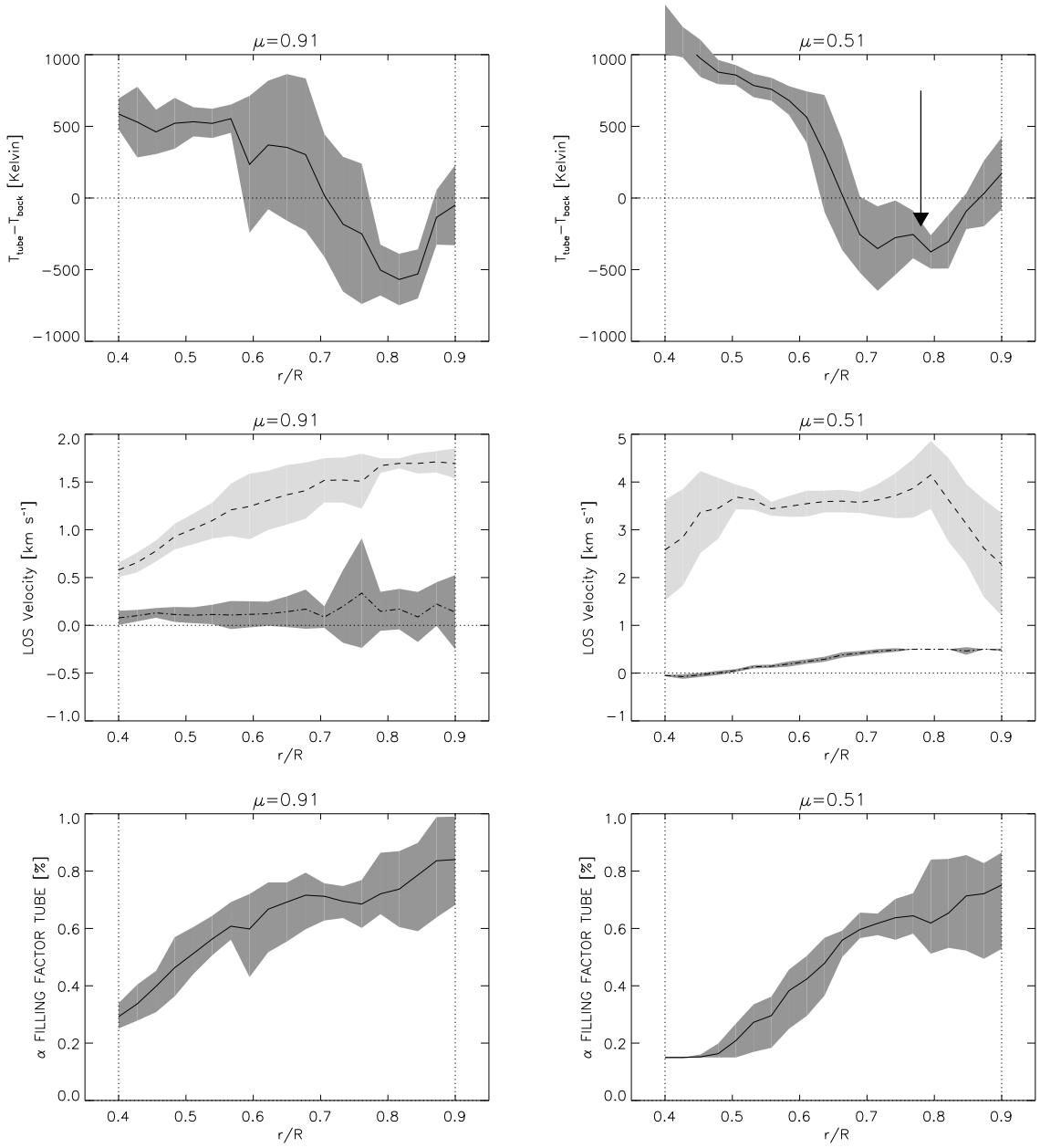

FIGURE 4.5: Top panels: temperature difference between the flux tube atmosphere and its surroundings as a function of radial distance from the spot center. Middle panels: radial variation of the line-of-sight velocities inside the flux tubes (dashed lines) and outside them (dashed-dotted lines). Bottom panels: radial variation of the flux tube's filling factor, α_t. Left panels: sunspot at $\mu = 0.91$. Right Panels: sunspot at $\mu = 0.51$. All quantities refer to the central position of the tube, $z = z_0$. Shaded areas denote the maximum deviations from the average at each radial position, obtained from the individual inversions of all the radial cuts. The arrow indicates the appoximate radial position where the flux tube experiments a final temperature enhacement (see Sect. 4.6.4).

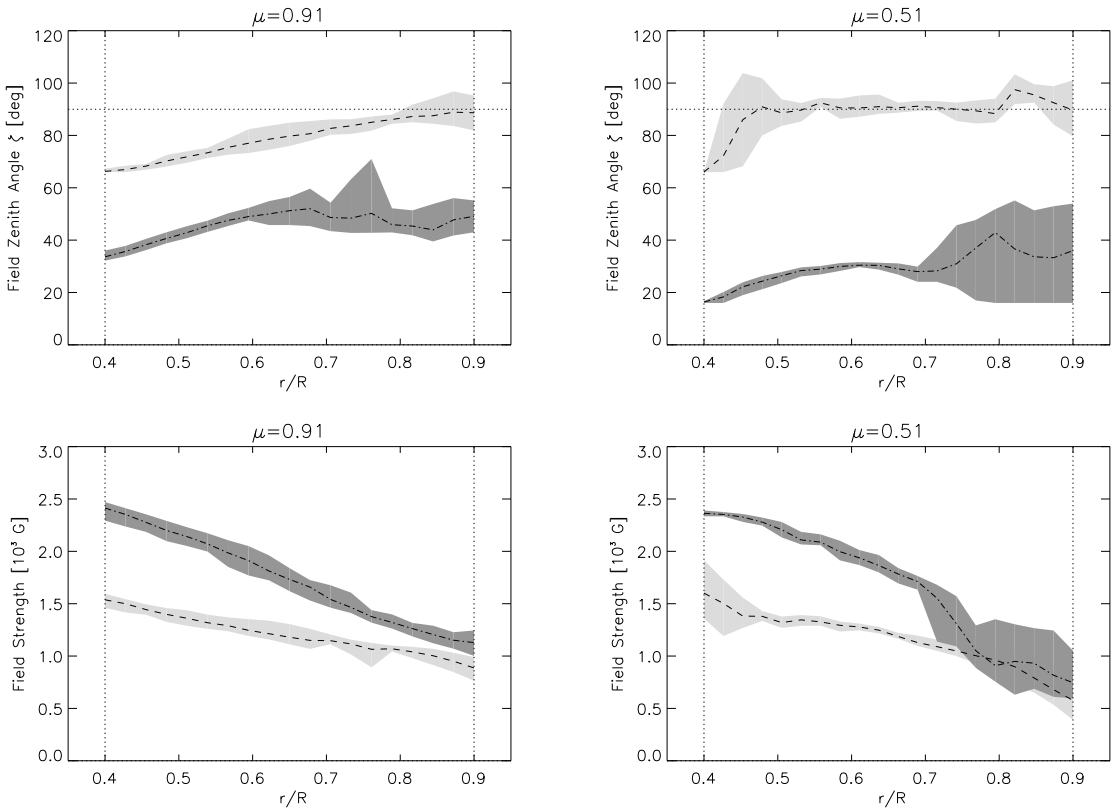

FIGURE 4.6: Top panels: radial variation of the magnetic zenith angle. Bottom panels: radial variation of the magnetic field strength. Left panels: sunspot at $\mu = 0.91$. Right Panels: sunspot at$\mu = 0.51$. Dashed lines correspond to the flux tube atmosphere and dashed-dotted to its surroundings. All magnitudes have been taken from the atmospheric stratifications at a height which corresponds to the central position of the tube, $z = z_0$. Shaded areas are as in Fig. 4.5.

can be explained in terms of jumps in the magnetic field azimuth. Both cases are compatible with the uncombed penumbra proposed by Solanki & Montavon (1993; see also Sect. 2.2.2).

As already described in Sect. 4.2, in the uncombed model, the discontinuities needed to produce asymmetric circular polarization profiles are located at the tube's boundaries: $z^* = z_0 \pm R_t$, with R_t and z_0 (the tube's radius and central position) being free parameters of the inversion. The radius we obtain from the inversion of all the pixels contained in the 10 radial cuts in Fig. 1 in the same sunspot at two different heliocentric angles is, consistently, 125 Kilometres, which is precisely the maximum value we allow for R_t[2]. This means that the inversion tries to make the flux tube as thick as possible. The area asymmetry of the synthetic profiles, $\delta A_{\rm FIT}$ only poorly reproduces the observed one: $\delta A_{\rm OBS}$ (see Fig. 4.7; top panels). In most cases the uncombed model produces an area asymmetry which is very little or almost zero, and varies over a smaller range than $\delta A_{\rm OBS}$.

The small observed area asymmetries (average of $\delta A_{\rm OBS} \sim 3$ %) clearly indicate that δA is a parameter which plays a minor role in the inversion since the shape of the circular polarization profiles can be successfully fitted by means of profiles showing little or no area asymmetry at all (as the 2C model in Fig. 3.2 in Chapter 3). Even extremely strange profiles, such as those presented in Fig. 4.3 can be reasonably fitted. This is because the circular polarization profiles of the spectral lines used in this work are mainly affected by the presence of two different polarities in the resolution element (background with $\gamma < 90^\circ$ and flux tube with $\gamma > 90^\circ$) rather by discontinuities along the line of sight in the physical parameters. Note that Borrero et al. (2004) also reached the same conclusion and suggested that using the visible iron lines at Fe I 6301 Å , whose area asymmetry is far more sensitive to such discontinuities, might help to further constrain the size of the penumbral filaments. For the case of the infrared Fe I lines at 1.56 μm they constrained a small region where the area asymmetry of these lines is sensitive to gradients along the line of sight: $\log \tau_5 \in [0, -0.5]$.

In Fig. 4.7 (middle panels) the position (in the optical depth scale) of the tube's lower boundary is plotted as a function of r/R. At $r/R < 0.7$ the lower boundary is located at $\log \tau_5 > 0$. At the outer penumbra, however, the lower boundary shifts to higher layers: $\log \tau_5 \sim -0.25$, where the discontinuity is effective in generating area asymmetry (see Chapter 3). For comparison we plot in Fig. 4.7 (bottom panel) the observed, $\delta A_{\rm OBS}$ (solid line), and fitted (dashed line), $\delta A_{\rm FIT}$, area asymmetry for all the considered radial cuts versus r/R. $\delta A_{\rm OBS}$ increases radially in the penumbra, from small negative values (~ -2 %) up to larger positive ones: ~ 7 % . Interestingly the fitted area asymmetry displays a similar behaviour, specially in the outer penumbra, where observed and fitted values become similar.

The combination of these results lead us to conclude that, in the inner-intermediate penumbra, where the observed area asymmetry in the circular polarization profiles of the Fe I 1.56 μm lines is small, discontinuities are not important to reproduce the profiles and therefore the tube radius is a parameter which is not well constrained from the inversion. However, in the outer penumbra, the observed area asymmetry becomes large enough, so that it turns out to be an important ingredient if the circular polarization profiles are to be successfully fitted. In these regions, the lower boundary of the flux tube is located at heights where it is effective in generating area asymmetry.

[2]This maximum value is set in the inversion code so that the upper boundary of the flux tube lies below the top of the tabulated atmosphere. This ensures that the condition $z(\tau_t) = z(\tau_s)$ for $z > z_0 + R_t$ (see Sect. 4.2) can be applied.

As the upper boundary remains unseen we still cannot draw any reliable conclusion on the actual size of the penumbral filaments.

At this point it is important to note that, given the fact that Fe I lines at 1.56 μm do not see much of the tube's boundaries, our uncombed model could be, in principle simplified into a two component model where all physical quantities are constant with height (e.g., making the tube's radius infinite in Fig. 4.4). Such models have been previously used to study the fine structure of the penumbra (Bellot Rubio et al. 2003; Borrero et al. 2004; see also Chapter 3). However a feature, which is included in the uncombed model but has been neglected by previous two component models, remains. The use of the total pressure balance between the fux tube and its surroudings. As we shall discuss in Sect. 4.6.2, this has important consequences.

4.6 Nature of the Evershed Flow

4.6.1 General considerations

The physical mechanism that drives the Evershed flow is still poorly understood. In the last decades many attempts have been made using falling flux tubes (Wentzel 1992), wave models (Erikson & Maltby 1967; Maltby & Erikson 1967; Bünte et al. 1993), buoyant flux tubes (Schlichenmaier et al. 1998a,1998b), siphon flows (Meyer & Schmidt 1968; Montesinos & Thomas 1993,1997; Degenhardt 1989,1991). In general, none of them is able to provide a fully consistent scenario where all observational features are reproduced satisfactorily. However, among the most successful models we shall cite stationary siphon flow models (Thomas & Montesinos 1993, Montesinos & Thomas 1997) and time-dependent simulations of a thin flux tube embedded in the penumbra (Schlichenmaier et al. 1998a,1998b; cf. Schlichenmaier 2002). Regardless of their differences, in both models the plasma is accelerated outwards due to a larger gas pressure in the inner footpoint as compared to the outer footpoint of an arched loop that crosses the penumbra. If the two footpoints are at the same geometrical height the total pressure (gas + magnetic) must be equal in both footpoints. Being the gas pressure larger at the inner one this readly implies that the magnetic field must be smaller here as compared to the outer footpoint.

However, observationally such a pressure gradient or increasing magnetic field strength with increasing radial distance has never been found. Previous observational analysis has not considered the fact that in our resolution element we have mixed signals coming from the flux tubes and the magnetic surroundings. They obtained that the magnetic field strength showed a strong radial decrease from $B_{\rm inner} \simeq 2500$ G to $B_{\rm outer} \simeq 1000$ G (Beckers & Schröter 1969; Wittmann 1974; Lites & Skumanich 1990; McPherson et al. 1992; Lites et al. 1993; Keppens & Martínez Pillet 1996; Stanchfield et al. 1997). This implies that the magnetic field is larger at the inner footpoint than in the outer one, contradicting theoretical predictions based on gas pressure differences.

If the fine structure of the penumbra is taken into account (Rüedi et al. 1998,1999, Borrero et al. 2004) a more favourable situation appears: an inclined magnetic field whose strength rapidly decreases with radial distance and an almost horizontal magnetic field carrying the Evershed flow with a far smaller radial drop in field strength are inferred. The small decrease in the field strength for the component carrying the Evershed flow still implies a stronger inner magnetic field, but now the difference is significantly reduced to $\simeq 300 - 500$ G. Although this finding on its own

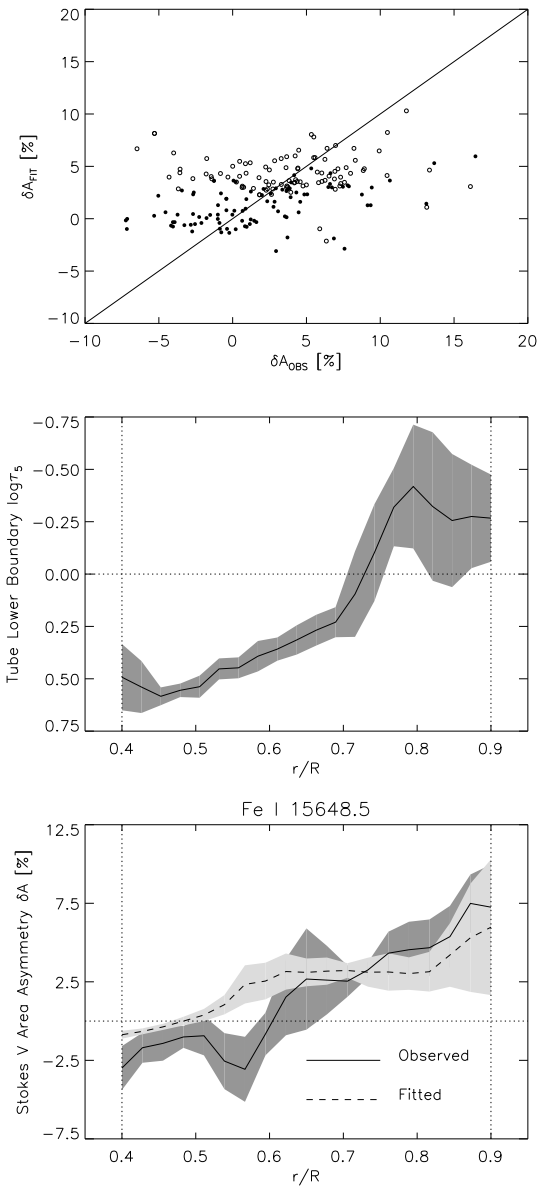

FIGURE 4.7: Top panel: area asymmetry from the best-fit Stokes V profiles, $\delta A_{\rm FIT}$, versus area asymmetry of the observed Stokes V for both Fe I lines for the case $\mu = 0.91$. For $\mu = 0.51$ (not shown) the result is very similar. Filled circles are for Fe I 15648.5 Å and open circles for 15652.8 Å . Middle panel: average position, in the optical depth scale, of the lower boundary of the flux tube (solid line). Maximum and minimum individual deviations of the 10 radial cuts considered are indicated by the shaded area. Bottom panel: radial variation of the fitted (dashed line) and observed area asymmetry (solid line) of Fe I 15648.5 Å .

is unsufficient to produce an outwards accelerated flow it certainly represents a much favourable situation, specially if we take into account that, as noticed by Montesinos & Thomas (1997) the inner and outer footpoints, as measured by observations, are not necessarily at exactly the same height.

In this work, by considering a flux tube embedded in a magnetic surrounding we obtain a very similar picture (see Fig. 4.5 middle panels and Fig. 4.6 bottom panels). Dot-dashed lines in those figures show an atmosphere (that we have identified with magnetic surroundings) carrying no velocities, with a magnetic field inclined (with respect to the vertical) by about 45° and where the strength decreases from $B_{\rm s}(r/R=0.4)=2500$ G to $B_{\rm s}(r/R=0.9)=1000$ G. The other atmosphere (flux tubes) has a magnetic field almost horizontal at all radial distances (although small upflows and downflows are present at the inner and outer penumbra respectively), carries large redshifted velocities (Evershed flow) and the magnetic field strength decreases radially much more slowly from $B_{\rm t}(r/R=0.4)=1500$ G to $B_{\rm t}(r/R=0.9)=1000$ G.

4.6.2 Gas pressure gradient

Note that in Chapter 3 we have reached this same conclusion from the application of two different geometrical models to spectropolarimetric data. In particular the model referred to by those authors as the 2C model contains many of the features of our flux tube model. The main difference is due to the inclusion of the line of sight gradients needed to produce area asymmetry in the observed circular polarization (see Sect. 4.5). There, we have already pointed out (see Sect. 5) that the infrared lines we have used in this work do not see the flux tube's boundaries in most of the penumbra, therefore our model becomes very similar to the 2C model in Chapter 3 (see also Bellot Rubio et al. 2003). However a major difference still exists. This has to do with the horizontal force balance between the flux tube and its surroundings. While in previous works this point has been neglected, we explicitely make use of it.

According to Fig. 4.6 (bottom panels) the magnetic field strength of the flux tubes is much smaller than that of the surrounding atmosphere in the inner penumbra at a geometrical height $z=z_0$ (central position of the tube). By requiring total pressure balance between the flux tube interior and the external atmosphere, Eq. 4.4, one can easily deduce that $P_{\rm gas,t}(z_0) \gg P_{\rm gas,s}(z_0)$. At large radial distances the situation is such that the magnetic field strength in the flux tube and its surrounding atmosphere becomes very similar and therefore: $P_{\rm gas,t}(z_0) \simeq P_{\rm gas,s}(z_0)$. In Fig. 4.8 we plot the actual $\Delta P_{\rm gas} = P_{\rm gas,t}(z_0) - P_{\rm gas,s}(z_0)$ as a function of radial distance in the penumbra (top panel for $\mu=0.91$ and bottom panel for $\mu=0.51$). As can be seen the difference almost linearly with r/R, reaching values close to zero near the outer penumbral boundary.

Unfortunately, this effect does not imply a radial decrease in the gas pressure inside the flux tube, because of the unknown radial behaviour of external pressure $P_{\rm gas,s}(z_0)$. In particular, its calculation is ill-posed by the boundary condition described in Sect. 4.2, where a value of the gas pressure at the highest photospheric layers is prescribed for the surrounding atmosphere. This is done for all pixels independently of its position on the spot: $P_{\rm gas,s}(\tau_{\rm max})=P_0$. Consequently, the geometrical height scale $z_{\rm s}(\tau_{\rm s})$ in the surrounding atmosphere does not to take into account pixel to pixel variations of the absolute geometrical height scale (Wilson depression). Nevertheless the radial variation of the difference in gas pressure between the flux tube and the surrounding atmosphere is a robust result. It only depends on the difference in the magnetic field strength be-

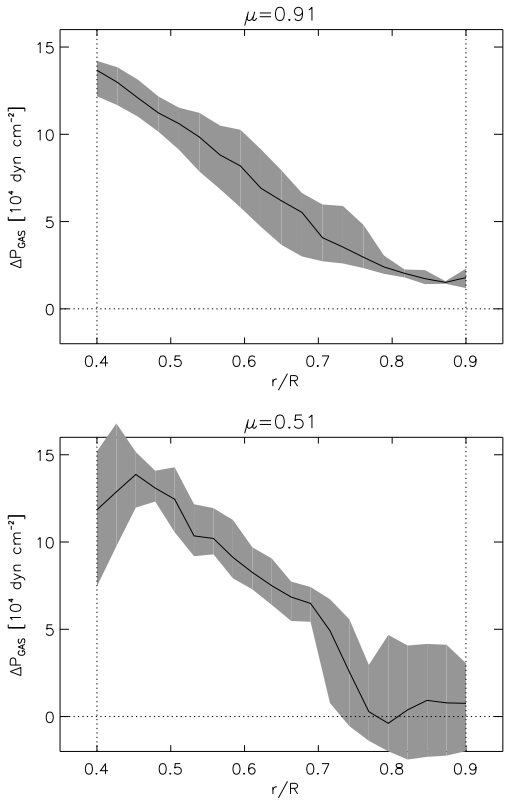

FIGURE 4.8: Radial variation of the gas pressure difference, $\Delta P_{\rm gas}$, between the flux tube and its surrounding atmosphere at $z = z_0$. Top panel: for NOAA 8706 at an heliocentric angle of $\mu = 0.91$. Bottom panel: the same for μ =0.51.

tween them and it is calculated under the condition of total pressure balance (magnetohydrostatic constraint). Although it can not directly prove that there is a radial decrease in the gas pressure along the flux tube axis, it does provide a strong indication that this is indeed the case. This is to our knowledge one of the strongest piece of evidence in favour of the siphon flow model as a driver of the Evershed effect.

4.6.3 Cooling flux tubes

Our results show that in the inner penumbra the atmosphere describing the flux tubes is hotter (by roughly 500-1000 K) than its surroundings. As we move to larger radial distances the temperature becomes very similar inside and outside the flux tube. This is in very good agreement with the theoretical predictions of the moving flux tube model (Schlichenmaier et al. 1998a, 1998b). The result that at a given point, $r/R \simeq 0.7$, the flux tube becomes cooler than its surroundings can be explained if we assume that the flow becomes adiabatic due to a less efficient radiative exchange in the higher parts of the anchored flux tube (Montesinos & Thomas 1997). The heating seen at larger radial distances is explained in terms of a shock front (see Sect. 4.6.4).

In order to clarify this result we shall describe in some detail how the spectral lines are formed in the inner penumbra. To this end we have selected a point located at a short radial distance, $r/R \simeq 0.45$ in the spot at $\mu = 0.51$. The total intensity and circular polarization profiles, Stokes I and V, respectively, are plotted in Fig. 4.9 (left panels) for the observed profiles (filled circles), along with the fitted profile (solid line). In the middle panels the fitted profile is again shown in solid lines but now we plot it together with the contribution from the flux tube (dashed line) and the surrounding atmosphere (dot-dashed line). In the right panels we do the same but now the profiles have been weightened with their corresponding filling factors. This example will allow us to deduce qualitatively that the flux tubes are hotter than the surrounding atmosphere in the inner penumbra.

Observed Stokes I for the Fe I 15625 Å line shows the two σ and the π components of the Zeeman pattern and therefore it is mainly produced by a magnetic field inclination which is close to 90 deg. In addition the total intensity profiles show no signature of the Evershed flow, neither in the OH line nor in the neutral iron line: the central positions of the lines are at the laboratory wavelengths (indicated by the vertical dotted lines). This features suggest that the Stokes I profiles are mainly affected by the atmosphere surrounding the flux tubes: no velocities seem to be present and they are almost horizontal in the observer's reference frame, $\gamma_s \simeq 80^\circ$ (almost vertical in the local reference frame, $\zeta_s \simeq 20^\circ$). This conclusion can also be made by comparing the observed or fitted Stokes I profiles (Fig. 4.9; left panels) with those produced by the surrounding atmosphere (Fig. 4.9; dot-dashed lines in middle and right panels). In addition, the surrounding atmosphere must be sufficiently cold for the OH line to appear clearly in the spectrum. The fact that the flux tube does not affect the formation of the total intensity profiles is explained by its small filling factor, $\alpha_t \simeq 0.15$. This is clear when one looks at Stokes I produced by the flux tube before (dashed line in middle panel of Fig. 4.9) and after (dashed line in right panel of Fig. 4.9) multiplying by its filling factor.

On the other hand, the observed circular polarization profiles, Stokes V, show for the Fe I line, the common multi-lobed shape produced by the coexistence of two different polarities in the resolution element: surrounding field with $\gamma_s < 90^\circ$ (dot-dashed line in middle bottom panel of Fig. 4.9) and flux tube with $\gamma_t > 90^\circ$ (dashed line in middle bottom panel of Fig. 4.9) , the flux tube signal being displaced towards the red due to the Evershed effect. The fact that the flux tube signal contributes significantly to Stokes V, regardless of its small filling factor, is because the surrounding field has an inclination close to 90 deg and therefore producing a very weak Stokes V signal (see dashed dotted lines in middle and right bottom panels in Fig. 4.9). This, together with the large inclination of the flux tube's magnetic field ($\gamma_t \simeq 150^\circ$), produces strong Stokes V profiles that after being weighted with the filling factor, becomes comparable to the circular polarization signal from the surroundings (see dashed lines in middle and right bottom panels of Fig. 4.9).

Interestingly, the circular polarization signal in the molecular line shows a common, positive polarity shape, whose zero crossing is almost at the laboratory wavelength. This indicates that its signal comes from a cold component carrying no velocities (the surrounding). The flux tube must be therefore hotter than its surroundings, otherwise it would produce a significant signal in the observed circular polarization of the OH line that we do not observe (as happens in the Fe I line). This combination of effects allows us to distinguish with great accuracy between the properties of the flux tube and the surrounding magnetic field, specially in the inner penumbra of the sunspot

at large heliocentric angles, where the neutral line is located near the umbra and the molecular lines are still clearly observed[3].

The molecular lines therefore trace a cold and vertical (in the local reference frame but highly inclined in the observer's reference frame) magnetic field that carries no velocities. This closely resembles a pure umbral atmosphere. At the umbral-penumbral boundary, a first set of hot flux tubes (small ones or a small number of them according to the tiny filling factor inferred) carrying high velocities is mixed with this umbral field producing multi-lobed Stokes V profiles in the Fe I lines, but not affecting the formation of the molecular lines which are dissociated at large temperatures. Remarkably, these flux tubes that have just emerged already carry strong velocities, perhaps as an indication that most parf of the plasma acceleration has already occurred. Again this is in very good agreement with the moving flux tube simulations (see Schlichenmaier et al. 1998a,1998b) where the acceleration takes place in the inner penumbra, where hot flux tubes carrying plasma at about 8000-10000 K rapidly cool down. The opacity in such extremely hot tubes would be too large to make them observable; therefore what we see is perhaps, the latest stages of this cooling process. Needless to say, hotter flux tubes in the inner penumbra were already expected considering that at small radial distances, the magnetic field strength in the flux tubes is much smaller than in the surrounding atmosphere, and therefore, in order to keep horizontal total pressure balance between these two atmosphere the gas pressure in the flux tube component has to increase.

4.6.4 Shock front

Another point of special interest concerns the magnitude of the Evershed flow. Theoretical models predict different values for the speed of the flow inside penumbral flux tubes. Stationary siphon flow models (Thomas & Montesinos 1993; Montesinos & Thomas 1997) distinguish between subcritical and supercritical velocities with respect to the characteristic critical tube's speed (Ferriz Mas 1988). Transitions between both regimes can be present within the flux tube, leading to shock fronts. Time dependent simulations of thin flux tubes in the penumbra predict supercritical flows in most of the penumbra regardless of whether the flux tubes remains horizontal beyond the visible limit of the sunspot (Schlichenmaier et al. 1998a,1998b) or bend back within the penumbra (Schlichenmaier 2002).

Observationally all kinds of velocities have been observed. Interestingly, when the fine structure of the penumbra is taken into account large velocities, > 4 km s^{-1}, are favoured (Wiehr 1995, del Toro Iniesta et al. 2001; Bellot Rubio et al. 2003; Bellot Rubio et al. 2004b). Most of these values have been obtained under the assumption that the magnetic field and the velocity vectors are mutually parallel.

According to Bellot Rubio et al. (2003) it is justified to assume also that the magnetic field is parallel to the velocity vector inside the flux tube, so the absolute flux tube velocity is: $v_t =$

[3]The fact that we see molecular lines in the inner penumbra can not be explained in terms of scattered light from the umbra. Although this possibility seems pausible, specially in the infrared, where the brightness contrast between umbra and penumbra is smaller than in the visible range, it is ruled out because in this case Stokes V would also be affected. As we do not observe a strong signal for the OH lines in the circular polarization profiles, we deem this effect neligible and we therefore conclude that the OH lines do appear becuase the temperature in the atmosphere that surrounds the flux tubes in the penumbra is sufficiently cold.

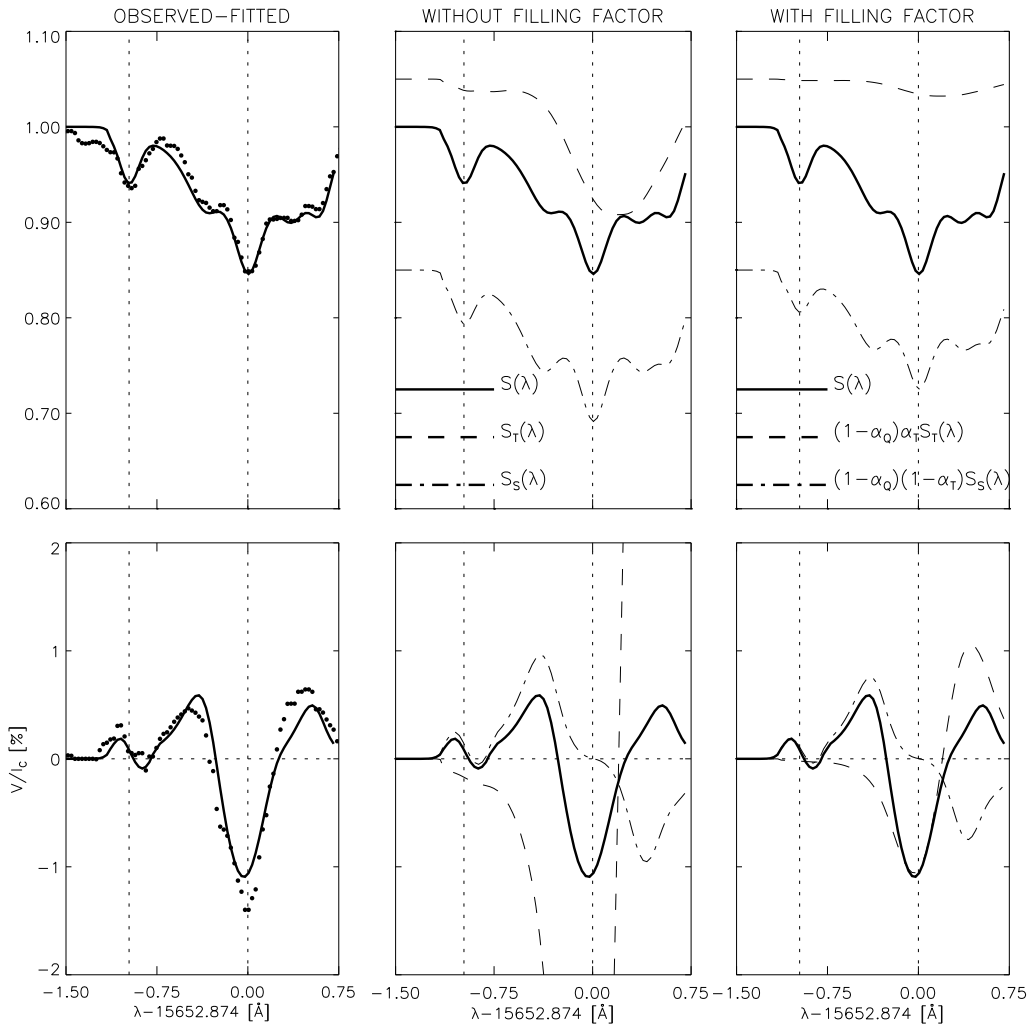

FIGURE 4.9: Top panels: Stokes I for a point in the inner penumbra in the sunspot at $\mu = 0.51$. Bottom panels: the same for Stokes V. Left panels: observed profile (filled circles) and fitted profiles (solid line). Middle panels: spectrum emerging from the flux tube component alone $S_{\rm T}$ (dashed line) and spectrum from the surrounding atmosphere only $S_{\rm S}$ (dashed dotted lines). Right panels: the same but considering the filling factors of each component (different areas covered by each atmosphere in the resolution element) . In all panels solid line represents the total emergent profile produced by the inferred atmosphere (fitted profile). Vertical dotted lines indicate the laboratory (unshifted) wavelength for one of the OH lines: $\lambda_0 = 15651.895$ Å and for one of the Fe I lines: $\lambda_0 = 15652.874$ Å . Fitted profiles are produced by an atmosphere with the following parameters: $\gamma_{\rm s} = 86^\circ$, $v_{\rm los,s} = 0.14$ km s^{-1} (surrounding), $\gamma_{\rm t} = 146^\circ$, $v_{\rm los,t} = 3.81$ km s^{-1}, $\alpha_{\rm t} = 0.14$. The contribution from stray light is $\alpha_{\rm q} = 0.09$. Note that inclination angles are given with respect to the observer. In the local reference frame (with the vertical axis being perpendicular to the solar surface) the inclinations would be: $\zeta_{\rm t} \simeq 87^\circ$ and $\zeta_{\rm s} \simeq 27^\circ$ for the flux tube and the surrounding atmosphere respectively. For a better visualization, the intensity profiles emerging from the flux tube and the surrounding atmosphere have been shifted vertically by an arbitrary amount.

$v_{\rm los,t}/\cos\gamma_{\rm t}$, where $\gamma_{\rm t}$ is the inclination of the tube's magnetic field vector with respect to the observer (both $v_{\rm los,t}$ and $\gamma_{\rm t}$ are obtained from the inversion). $v_{\rm t}$ is plotted in Fig. 4.10 (top left panel) for the sunspot at an heliocentric angle of $\mu = 0.51$[4]. Also plotted are the local sound speed $c_{\rm s} \sim T^{1/2}$ and the tube's critical speed $c_{\rm t} = c_{\rm s}c_{\rm a}/\sqrt{c_{\rm s}^2 + c_{\rm a}^2}$, with $c_{\rm a} \sim B\rho^{-1/2}$ being the Alvén speed. The velocity in the flux tube always remains subsonic, although we cannot rule out the possibility for supersonic values (del Toro Iniesta et al. 2001; Penn et al. 2003) in the penumbra given the limited amount of radial cuts we are considering.

At almost all radial distances, $v_{\rm t} < c_{\rm t}$ as well, except for a few regions in the inner ($r/R \simeq 0.4$), and the outer penumbra ($r/R \simeq 0.78$). Given the error bars, we do not deem the first case to be reliable. However, for large radial distances (arrow in Fig. 4.10; top left panel) it seems plausible that the velocity becomes supercritical. Remarkably, after this happens, the velocity suddenly drops again to subcritical values at larger distances: $r/R > 0.85$ by roughly 2 km s^{-1}. This is accompained by an increase in the flux tube temperature of about 300-400 K at these locations (see arrow in Fig. 4.5; top right panel). Indeed, this is the behaviour expected from a transition between supercritical to subcritical velocities in penumbral flux tubes (Montesinos & Thomas 1997) produced by a shock front that dissipates kinetic energy and heats the gas. The presence of shocks in the siphon flows has been predicted by numerous authors (Meyer & Schmidt 1968; Degenhardt 1989,1992; Thomas & Montesinos 1993; Montesinos & Thomas 1997; Schlichenmaier et al. 1998a, 1998b; Schlichenmaier 2002), but this is the first time such a shock front is observed.

Shock fronts, if present, are likely to produce an enhancement both in the line width (e.g. FWHM) and in the equivalent width (see Degenhardt et al. 1993; Solanki et al. 1996). In the penumbra, the radial variation of the line width is dominated by the Zeeman splitting (magnetic field). However, the magnetic field affects the equivalent widths of the comparatively weak (i.e. unsaturated) lines considered here only very slightly. In Fig 4.10 (top right panels) we plot the radial variation of the equivalent width for Fe I 15648.5 Å . It clearly shows an enhancement ($\simeq 10\%$) at roughly the same radial distance as the flow speed becomes supercritical (see vertical arrow). Three different radial positions, corresponding to locations before, during and after the shock have been marked with open circles. Intensity profiles for Fe I 15648.5 Å at those locations has been extracted and plotted together in Fig. 10 (bottom left panel). Intensity profile before the shock (dashed line) shows an enhancement in the red wing which is produced by the strongly red shifted flux tube contribution (i.e. satellite line; see Stellmacher & Wiehr 1980; Wiehr et al. 1984; Wiehr 1995,1997). During the shock (solid line) the equivalent width of the redshifted component is enhanced. This broadening is likely to be produced by a new structure in our resolution element that out model does not account for. Therefore, the only way that the inversion code has to make the profile broader (within the constraints of the chosen model) is to increase the micro and macroturbulent velocities. In Fig. 4.10 (bottom right panel) the tube's broadening velocity, defined as: $v_{\rm broad} = \sqrt{v_{\rm mic,t}^2 + v_{\rm mac,t}^2}$ is plotted. It shows a peak exactly at the radial positions at which the flow speed becomes supercritical. This provides a strong indication that this spectral signature really corresponds to a shock front in the flux tube at large radial distances in the penumbra.

[4]Results for $\mu = 0.91$ are not considered as dividing by cosine of the small heliocentric angle enhances any error in line-of-sight velocities

In our observations the shock seems to occupy up to three consecutive radial pixels, corresponding to roughly 1.2-1.6 arc sec. The fact that we do not observe a jump over a smaller radial range can be due to smearing effects introduced by seeing.

Finally, it is important to recall that this result is based on some assumptions that must be considered carefully. In particular the density inside the flux tube, ρ_t, is obtained through the gas pressure and temperature by applying the ideal gas equation (see Sect. 4.2). Note that this density does not necessarily imply that vertical hydrostatic equilibrium is satisfied inside the tube. The Alven speed, and therefore, the tube's critical speed are affected by this uncertainty, making this an important shortcoming for our results.

4.7 Summary and conclusions

We have presented the first full inversions of infrared penumbral spectropolarimetric data with a model that accounts for the vertical and horizontal inhomoneities of the penumbral fine structure. This model is a slightly modified version of the uncombed model of Solanki & Montavon (1993; cf Martínez Pillet 2000) and allows for the presence of a randomly orientated flux tube embedded in a magnetic surrounding atmosphere. The main advantages of this model, as compared with those used in Chapter 3 (see also Borrero et al. 2004) are: **a** -it contains two different atmospheres in the direction perpendicular to the observer (flux tube and magnetic surrounding) that allows the observed multilobed Stokes V profiles to be easily reproduced; **b** -these two atmospheres are also present in the direction parallel to the observer line-of-sight and therefore the model includes gradients along the line of sight (in the form of sharp jumps in the physical quantities at the flux tube's boundaries) needed to produce asymmetric Stokes V profiles ($\delta A \neq 0$); **c** -flux tubes and their magnetic surroundings are coupled to each other using total pressure balance at every height.

Feature **b** is suitable to investigate the vertical size of the penumbral filaments, since the radius of the flux tube R_t, which is ultimately linked to the amount of area asymmetry generated, is also obtained from the inversion. The small amount of δA shown by the Fe I lines at 1.56 μm is not enough to constrain the position of the flux tubes' upper and lower boundaries, except at the outer penumbra where δA is sufficiently large, allowing us to set a rather accurate position for the lower flux tube's boundary at around $\log\tau_5 \in [-0.5, 0]$, while the upper boundary remains undetected. Although for individual profiles the produced area asymmetry by the uncombed model fails to reproduce the observed one, general trends, such as the radial behaviour are fairly reproduced. In agreement with Chapter 3 (see Sect. 3.6) the use of visible lines, that show in general much larger δA should help in this matter (see Chapter 5).

Feature **c** has allowed us to detect, for the first time, a strong radial decrease in the pressure difference between the flux tube and its surroudings, that is likely to induce an outward directed flow. This is to our mind the strongest evidence so far supporting siphon flows (Montesinos & Thomas 1993,1997) as the physical mechanism driving of the Evershed effect.

In addition, we have seen that the Evershed flow already carries velocities as large as $v \sim 4$ km s^{-1} in the inner penumbra. This has passed unnoticed in previous works (see Schmidt & Schlichenmaier 2000; Tritschler et al. 2004) where only Stokes I was considered. A possible explanation is found in the small filling factor and inclinations, larger than 90 deg with respect to the observer, of the magnetic field vector in the flow channels at the inner penumbra, that produces

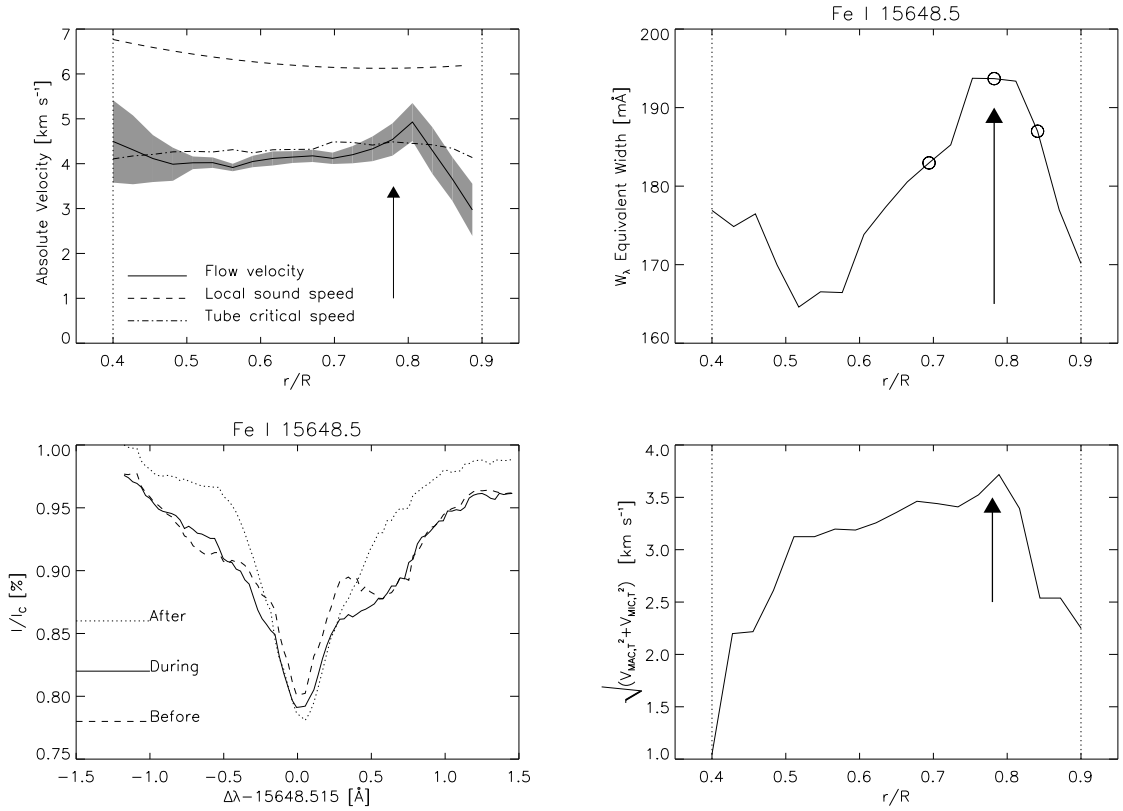

FIGURE 4.10: Top left panel: Radial variation of the absolute plasma velocity inside the flux tube or flow velocity (solid line). Local sound speed and tube's critical speed are also plotted (dashed and dashed-dotted lines respectively). The vertical arrow marks the position where the flow speed becomes supercritical, $r/R \simeq 0.78$. Top right panel: radial variation of the equivalent width for Fe I 15648.5 Å line. The open circles are three selected radial positions before, during and after the shock occurs. Bottom left panels: Intensity profiles corresponding to the 3 selected radial positions (top right panel in this Figure) before (dashed line), during (solid line) and after the shock (dotted line). Bottom right panels: radial variation of $\sqrt{v_{\rm mic,t}^2 + v_{\rm mac,t}^2}$.

small line asymmetries in Stokes *I* but large Stokes *V* zero crossing shifts. At the inner penumbra these fast flows are also associated with hot gas and flux tubes that are somewhat inclined with respect to the horizontal, in agreement with Schmidt & Schlichenmaier (2000). These results are in close agreement with the dynamical simulations of penumbral flux tubes by Schlichenmaier et al. (1998a,1998b) and Schlichenmaier (2002). The tubes reach the same temperature as theirs surroundings very rapidly in the radial direction, and at the same time the flow speed increases smoothly (up to $v \sim 5$ km s^{-1}) as the pressure drops (Montesinos & Thomas 1993, 1997).

At large radial distances the flow speed suffers a sudden decrease that is associated with positions where the tubes return back to the solar interior (Westendorp Plaza et al. 1997). In addition to this well estabished result, we have also detected a possible transition between critical and subcritical velocities (as predicted by Montesinos & Thomas) that is co-spatial with a rise in temperature and equivalent width at the outer penumbra, and seems to indicate that part of the kinetic energy is being dissipated into thermal energy. Therefore, part of the sudden drop in the velocity at the outer penumbra could be adscribed to the development of shock fronts.

Chapter 5

Size of the penumbral flaments

In this Chapter we study the fine structure of the penumbra as inferred from the uncombed model when applied to penumbral spectropolarimetric data for the neutral iron lines at 6300 Å. The inversion deduces very similar radial dependences in the physical quantities (LOS velocity, magnetic field strength etc) as those obtained from the inversion of the Fe I 1.56 μm lines (see Chapter 4). In addition, the large Stokes V area asymmetry exhibited by the visible lines helps to constrain the size of the penumbral flux tubes. As we will demonstrate, the uncombed model is able to reproduce the area asymmetry with striking accuracy, returning flux tubes as thick as 100-200 kilometres in the vertical direction, in good agreement with previous investigations.

5.1 Introduction

In Chapter 4 we attempted, without success, to infer the thickness of the penumbral flux tubes by inverting penumbral spectropolarimetry data of the Fe I lines at 1.56 μm. The small Stokes V area asymmetry present in those lines led us to conclude that the discontinuities along the line of sight in the velocity and magnetic field vector play a minor role in the line formation and therefore the flux tube's diameter, which is ultimately responsible of those discontinuities, could not be constrained. Already in Chapter 3 (see Sect. 3.6) we pointed out that the visible Fe I lines at 6300 Å are far more sensitive to such discontinuities and therefore they might be a useful tool to infer the typical sizes of the penumbral flux tubes. In this Chapter we shall investigate in more detail this conjecture by inverting penumbral spectropolarimetric data of the aforementioned lines. Sect. 5.2 briefly describes the observations ; Sect. 5.3 presents the radial behaviour of the inferred physical parameters; in Sect. 5.4 the inferred size of the penumbral flux tubes and its implications are discussed. Finally, in Sect. 5.5 we study whether the uncombed model satisfies the null divergence condition for the magnetic field vector.

TABLE 5.1: Atomic parameters of the observed lines. λ_0 represents the laboratory central wavelength, χ_l the excitation potential of the lower energy level, and $\log gf$ the logarithm of the oscillator strength times the multiplicity of the level. The parameters α and σ (in units of Bohr's radius, a_0) are used to calculate the broadening of the lines by collisions with neutral hydrogen atoms as resulting from the ABO theory. The seventh column gives the effective Landé factor of the transition, g_{eff}. The values of the relatives weights given in the inversion w_j are indicated, for each Stokes parameters, in the last four columns.

Species	λ_0 (Å)	χ_l (eV)	log gf (dex)	α	σ (a_0^2)	g_{eff}	w_I	w_V	w_Q	w_U
Fe I	6301.5012	3.654	−0.718	0.243	832	1.67	20	100	35	35
Fe I	6302.4916	3.686	−1.235	0.240	847	2.50	20	100	35	35
Fe I	6303.4600	4.320	−2.550	0.276	712	1.50	1	1	1	1
Ti I	6303.7560	1.443	−1.611	0.236	357	0.92	50	1	1	1

5.2 Observations

The active region NOAA 8545 was observed in May 21st, 1999 at an heliocentric angle of $\mu = \cos\theta = 0.79$ using the ASP (Advance Stokes Polarimeter; Elmore et al. 1992) instrument. The recorded spectral region ranges about 3.2 Å with a wavelength sampling of 12.8 mÅ. It contains the full Stokes vector of 4 Zeeman sensitive spectral lines: Fe I (g_{eff}=1.67) 6301.5 Å , Fe I (g_{eff}=2.5) 6302.5 Å , Fe I (g_{eff}=1.5) 6303.4 Å and Ti I (g_{eff}=0.92) 6303.7 Å. Note that the first two neutral iron lines are blended by two telluric H_20 lines in the red wing of Stokes I.

The data reduction was performed by usual means (see Skumanich et al. 1996). As always, special care was taken in the wavelength calibration, for which we first proceeded to assume that the average umbral profile of 6301.5 and 6302.5 Å is at rest (i.e. the core positions in Stokes I correspond to the central laboratory wavelengths) and later a minor correction was done at each pixel using the telluric lines. The laboratory wavelength for the Ti I line, as well as the oscillator strengths of Fe I 6303.4 Å and Ti I 6303.7 Å are very inaccurate, and therefore we recalculated them using the two component model for the quiet Sun by Borrero & Bellot (2002) using the procedure described in Borrero et al. (2003a). The relevant atomic parameters for the four lines are presented in Table 5.1. Fig. 5.1 shows the active region as seen in the continuum intensity, total circular polarization and Stokes V area asymmetry.

Although these lines are less sensitive to the magnetic field than their infrared counterparts (see Chapter 3 and 4), they present a number of advantages that makes them very suitable for our purposes. The visible lines provide a better height coverage, as they are formed over a wider range of optical depth layers in the solar photosphere: $\log\tau_5 \in [-4, 0]$. In addition, as already pointed out in Sect. 3.6 the visible Fe I lines are far more sensitive to gradients along the line of sight in the physical quantities. Finally, the visible lines are in principle more affected by changes in the temperature stratification than the Fe I lines at 1.56 μm, but if we take into account the OH lines that blend the Fe I 15652 Å line, this situation is compensated, at least in the inner penumbra.

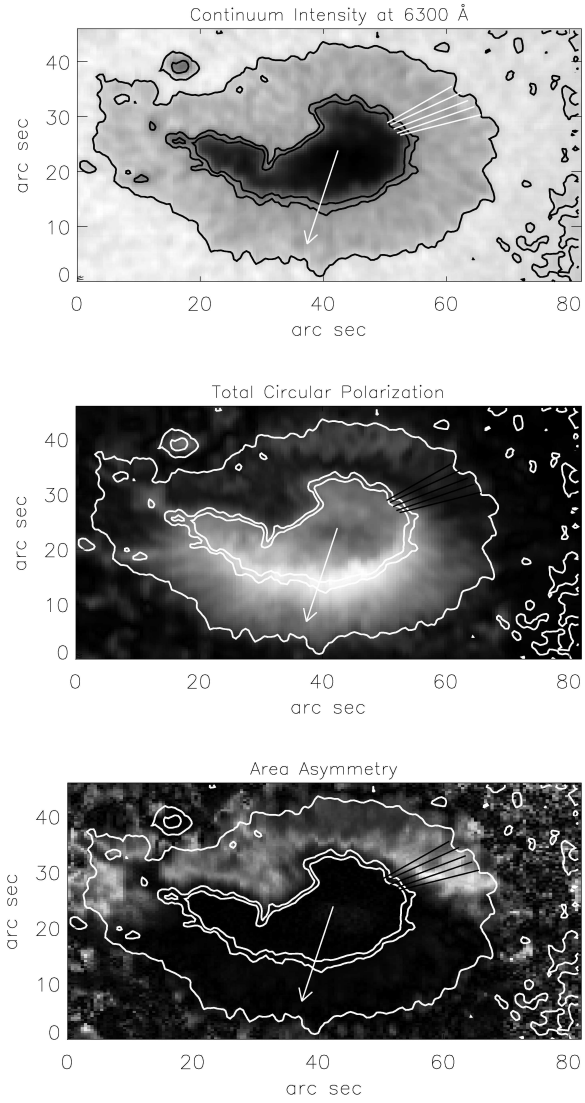

FIGURE 5.1: Continuum intensity map of NOAA 8545 (top panel). Total circular polarization map (middle panel) and area asymmetry map (bottom panel). The contours correspond to the levels 0.45, 0.6 and 0.85 in units of the quiet sun intensity I_C. The outermost boundary defines the sunspot radius $r = R$. The arrow points towards the direction of the disk center. The 5 radial cuts indicated by the white lines lie on the limb side of the penumbra, somewhat out of the line of symmetry of the sunspot, where the area asymmetry reaches the largest values. A map of the Net Circular polarization for the Fe I 6302.5 Å line can be found in Fig. 2.12 (left panel).

5.3 Inversion results

We have selected for the inversion the five radial cuts shown in Fig. 5.1. They lie on the limb side of the penumbra at around 30 degrees clockwise from the line of symmetry of the spot. This region was selected, because, as can be seen in Fig. 5.1 (bottom panel), there is a maximum in the area asymmetry of the circular polarization profiles, and hence it seems very suitable to test whether we can obtain accurate values for the flux tube radius. Each radial cut contains approximately 25 pixels ranging from $r/R \simeq 0.4$ up to $r/R \simeq 0.9$. As in Chapter 4, the uncombed model (Sect. 2.2.2-4.2) was used to describe the fine structure of the penumbra. Since the spectral lines we are using now are sensitive to a much wider range of heights than those used in Chapter 4 (see also Sect. 3.6) we fix a maximum value for the thickness of the penumbral flux tube D_t of 500 kilometres (cf. Sect. 4.5). The number of free parameters, physical quantities and their stratifications with optical depth are the same as in Chapter 4 (Sect. 4.2).

During the inversion process all pixels were inverted individually giving more relative weight to the polarization profiles (V, Q and U) of Fe I 6301.5 Å and Fe I 6302.5 Å than to Stokes I. The other two lines, Fe I 6303.5 Å and Ti I 6303.8 Å are comparatively weaker. Therefore they are of minor importance in the inversion, except for Stokes I of the Ti I line, whose weight was similar to the weights in Stokes V,Q and U in the first two iron lines in Table 5.1. The reason is that the combination of the very small excitation energy of this line and the relatively low ionization energy of Titanium, makes it quite sensitive to variations in the temperature stratification. In fact, the Ti I line behaves similarly to the OH lines that blend the Fe I 15652.5 Å line (see Chapter 4). Its equivalent width, being rather large in the umbra and inner penumbra, is significantly reduced towards the middle and outer penumbra. More details about the employed weights are given in Table 5.1.

5.3.1 Fitting examples

In Fig. 5.2 we present some examples of the observed and fitted Stokes V profiles for three pixels located at increasing distance from the sunspot center. The fits to the observational data are reasonably successful, with differences always below 1% of the continuum intensity. Even Stokes V profiles, with typical shapes of Stokes Q and U (see Sánchez Almeida & Lites 1992), are almost perfectly reproduced (Fig. 5.2; middle panels). Furthermore, single-lobed Stokes V profiles (Fig. 5.2; bottom panels) are also nicely fitted. Note that, in contrast to the Fe I lines at 1.56 μm, these fits can not be achieved by simple 2C models as in Chapter 3, because if gradients along the line-of-sight in the velocity and magnetic field vector are neglected the produced area asymmetry will be zero, giving rise to Stokes V profiles that, although they may have several lobes (cross-over effect), will have equal positive and negative areas in strong contrast to the observed profiles.

5.3.2 Radial dependences

From the retrieved stratifications with geometrical height, both for the ray crossing the surrounding atmosphere only and the ray crossing through the surrounding and the flux tube atmosphere (see Fig. 4.1 and Fig. 4.4), we have extracted, for all inverted pixels, the values of the physical

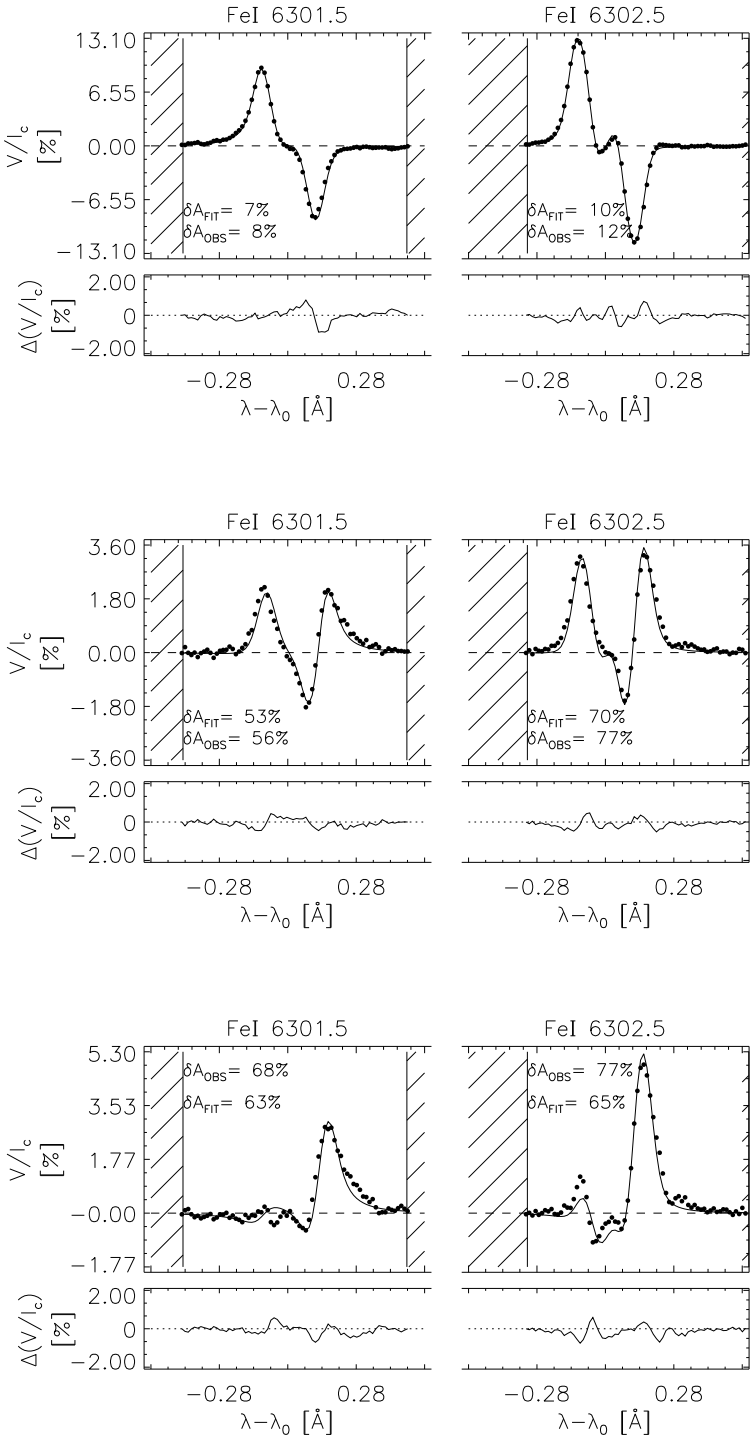

FIGURE 5.2: Three examples of observed (filled circles) and fitted (solid lines) Stokes V profiles for Fe I 6301.5 (left panels) and Fe I 6302.5 Å (right panels) lines. These profiles have been taken from the same radial cut in Fig. 5.1 at three locations with increasing radial distance: $r/R = 0.45, 0.65, 0.85$, such that the upper panel corresponds to the inner penumbra and the bottom panel lies at the outer boundary of the sunspot. The observed and fitted Stokes V area asymmetry, δA are also indicated.

parameters (temperature, LOS velocity, magnetic field strength and inclination, gas pressure etc.) at $z = z_0$ and plotted them, as a function of the radial distance in the penumbra, in Fig. 5.3. For the temperature and gas pressure we plot, instead of the separate values for the flux tube and the surrounding atmosphere, the difference between them. The filling factor of the flux tube component, α_t (Fig. 5.1; bottom left panel) corresponds, obviously to the flux tube alone, with being $1-\alpha_t$ the area covered by the surrounding atmosphere (Eq. 4.2). As in previous chapters, we have transformed the magnetic field inclination, that is always obtained in the observer's reference frame from the inversion, into the local reference frame. Therefore in the following we discuss about zenith angles ζ instead of γ, $\zeta = 0^\circ$ meaning that the magnetic field is perpendicular to the solar surface.

A comparison of the results obtained with the Fe I 1.56 μm lines by means of the uncombed model (see Fig. 4.5, 4.6 and 4.8) shows that very similar radial trends are obtained when the uncombed model is applied to a set of spectral lines with very different atomic and thermodynamic properties. In particular, the flux tubes also appear hotter than the surrounding atmosphere in the inner penumbra, supporting our arguments in Sect. 4.6.3. In addition, the flux tube magnetic field strength remains fairly constant with radial distance, while the external magnetic field strength drops rapidly towards the outer penumbra. This, together with the radial decrease in the gas pressure difference between the flux tube and the surrounding atmosphere, provides additional evidence supporting siphon flows as the physical mechanism responsible for the Evershed flow (see Sect. 3.7 and Sect. 4.6.2).

An obvious difference to the results from the infrared lines is, however, worth mentioning. The values of the flux tube filling factor at small radial distances from the inversion of the infrared lines were $\alpha_t \sim 0.2$ in the inner penumbra, whereas the visible lines show $\alpha_t \sim 0.5$. We believe this effect is due to the lack of information that the visible profiles carry about the flux tube atmosphere in the inner penumbra. In fact, the filling factor here partially loses its significance, as the inferred properties, like the magnetic field zenith angle (middle left panel) and LOS velocity (top right panel) are very similar for the flux tube and its surroundings [1]. A qualitative example can be found in Fig. 4.9 and Fig. 3.2 (top panel) where the contribution from the flux tube component to the Stokes V profiles of the Fe I 1.56 μm lines at the inner penumbra is clearly visible. In contrast, this contribution is not evident at all in the visible lines (e.g. Fig. 5.2; top panels). This can also explain the fact that the errors bars in the flux tube component are not only much larger than those in the surrounding atmosphere (except perhaps for the outer penumbra, $r/R > 0.8$), but also much larger than in the case of the 1.56 μm lines. This indicates that it would be highly desirable to use simultaneous observations in both spectral windows, using the infrared lines to characterize the horizontal properties of the penumbral fine structure and the diagnostic capabilities of the visible lines to infer the vertical stratification (i.e. gradients along the line-of-sight).

5.4 Size of the Penumbral Flux tubes

In order to produce a non vanishing Net Circular Polarization an atmospheric model must include gradients along the line-of-sight in the velocity and magnetic field vector (Landolfi & Landi Degl'Innocenti 1996). In the case of the penumbra of sunspots, the Net Circular Polarization is

[1] Note that this is not the case for the magnetic field strength (middle right panel in Fig. 5.3).

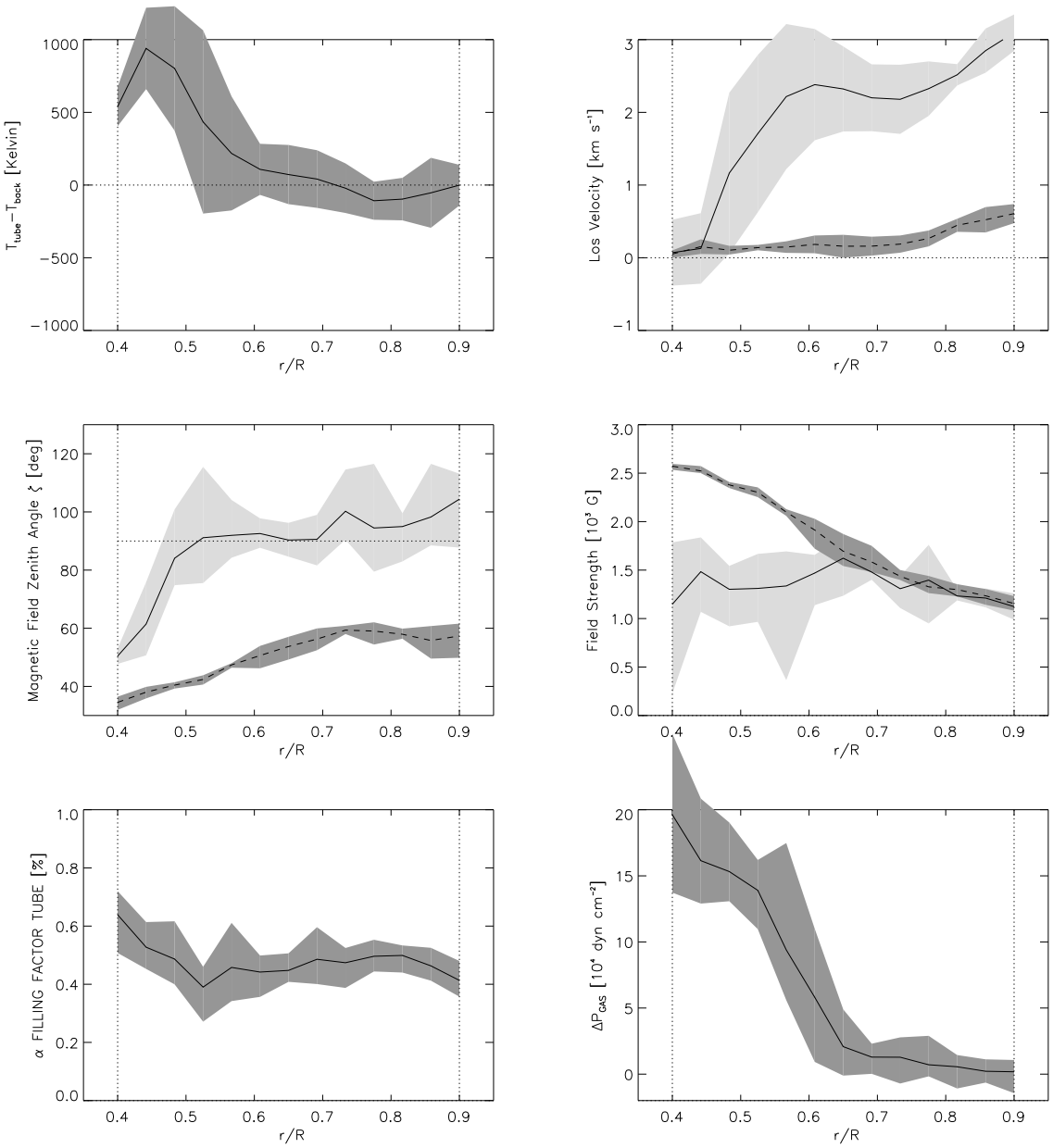

FIGURE 5.3: Radial variation of properties of the magnetic surrounding (dashed lines) and the penumbral flux tube (solid lines). Shaded areas represent the scatter around the mean obtained from the inversion of each of the 5 radial cuts considered. From left to right and top to bottom: temperature difference between the flux tube and its surroundings, LOS velocity, magnetic zenith angle ζ, magnetic field strength B, flux tube filling factor α, and gas pressure difference between the flux tube and its surroundings. All quantities have been taken at a geometrical depth that corresponds to the central position of the flux tube: $z = z_0$.

of the Fe I lines at 6300 Å is so large that gradients in the inclination of the magnetic field and in the line-of-sight velocity as large as $\Delta\gamma \simeq 45^\circ$ and $\Delta v_{los} \simeq 1.5$ km s^{-1} must be introduced (Sánchez Almeida & Lites 1992). Such gradients would certainly produce large curvature forces and electric currents that are difficult to match with the idea of a sunspot in hydrostatic equilibrium (Solanki et al. 1993). A way out of this problem was proposed by Solanki & Montavon (1993) who realized that including a three layered atmospheric model (see Sect. 2.2.2) where the middle one would have larger velocities and a more horizontal magnetic field could reproduce the observed NCP without invoking to net (i.e. large scale) gradients along the line of sight, but rather strong gradients on a small scale that are compensated as the line-of-sight crosses the three atmospheric layers. This is the basic idea of the *uncombed model*. In Sect. 2.2.2 we had already identified the intermediate layer as a horizontal flux tube (carrying the Evershed flow) which is embedded in a magnetic surrounding where the magnetic field is more vertical and essentially at rest. Except for the addition of a pure surrounding atmosphere (Sect. 4.2; see also Martínez Pillet 2000) , the model for the fine structure of the penumbra that we have used in Chapters 4 and 5 of this thesis, is essentially the uncombed model as proposed by Solanki & Montavon (1993).

This model has been applied in Chapter 4 to penumbral spectropolarimetric data observed in the Fe I lines at 1.56 μm. This allowed us to characterize the horizontal inhomogeneities of the penumbral fine structure, but we were not able to model the vertical inhomogeneities. The reason given was that the used spectral lines showed only some NCP (with typical values for the area asymmetry of $\delta A \sim 3-5$ %) and therefore the positions of the boundary layers, where the gradients along the line of sight are produced, and thus the thickness of the inner layer or penumbral flux tube, were not constrained in the inversion process. The result was that the uncombed model tends to retrieve flux tubes of infinite thickness, because in those lines the horizonal fine structure of the magnetic field plays a more important role than the vertical one (see Sect. 1.5.7; *unresolved structure*).

A different situation appears when the uncombed model is applied to the Fe I lines at 6300 Å. The area asymmetry in these lines is so large that the vertical structure (i.e. discontinuities along the line-of-sight produced at the flux tube boundaries) of the magnetic field and velocity vectors play now the leading role. Fig. 5.4 (top panels) demonstrates that the uncombed model now reproduces almost perfectly the observed area asymmetry of the visible Fe I lines (cf. Fig. 4.7; top panel). As a function of the radial distance (Fig. 5.4; middle and bottom panels) we see that the observed area asymmetry (solid lines) increases radially up to $\delta A \sim 60$ % in the middle penumbra ($r/R \sim 0.6$) and remains fairly constant hereafter. The fitted area asymmetry (dashed lines) presents an almost identical behaviour, although for the Fe I 6302.5 Å line it seems to slightly underestimate the observed values. Note that the small δA observed in the inner penumbra ($r/R < 0.5$) can either indicate that the flux tube is very thick here (so that its boundaries will fall out of the region where these lines are formed) or that the properties of the flux tube and its magnetic surrounding are very similar (so that there is no jump is the physical quantities along the line of sight). In fact we see indications of both effects. On the one hand, as already mentioned, in the inner penumbra flux tube and magnetic surrounding atmosphere have very similar zenith angles and LOS velocities (see Fig. 5.3) which obviously means that little NCP will be produced. On the other hand, the magnetic field in the flux tube is much smaller than in the external atmosphere at small radial distances. This, through total pressure balance considerations as shown in Fig. 5.3 (bottom right panel), implies that the gas pressure in the flux tube must be

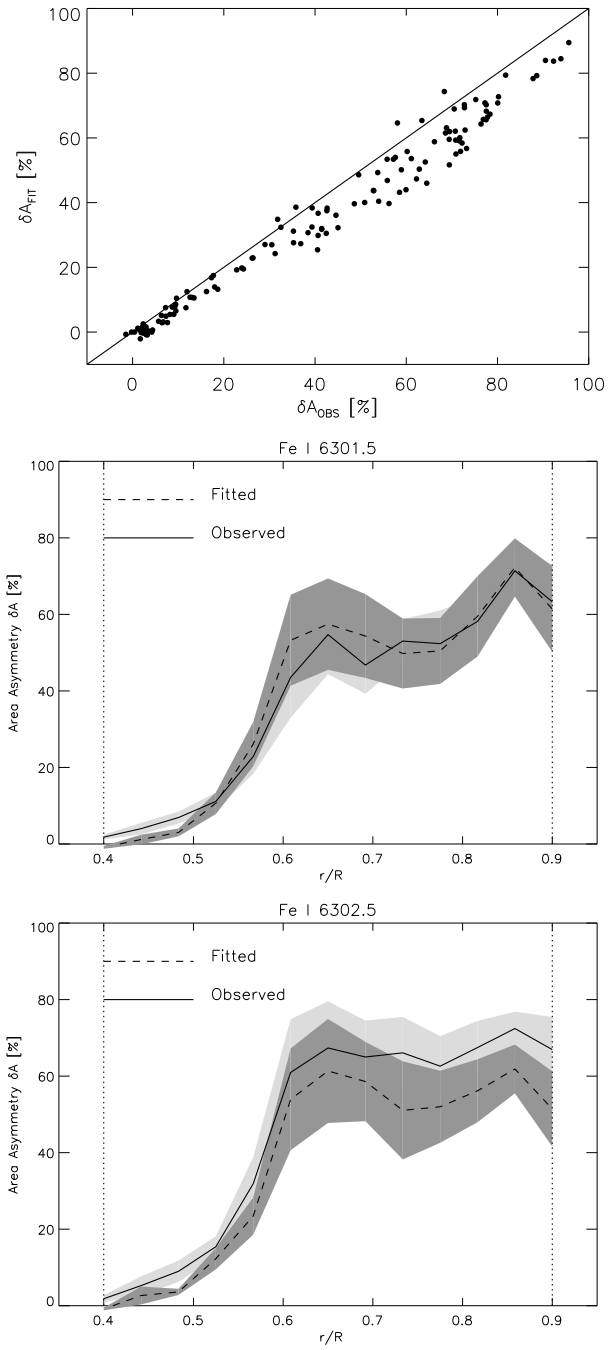

FIGURE 5.4: Top panel: fitted Stokes V area asymmetry versus observed one. Straight line indicates the expectation values. Middle panel: radial variation of the observed (solid line) and fitted (dashed line) area asymmetry of Fe I 6301.5 Å. Shaded areas corresponds to the maximum and minimum deviations for the five radial cuts considered. Bottom panel: same but for Fe I 6302.5 Å.

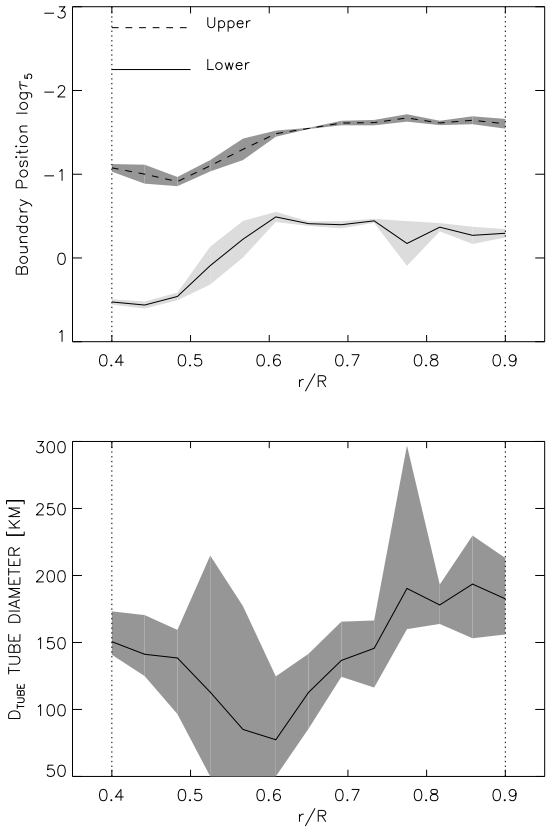

FIGURE 5.5: Top panel: locations, in the optical depth scale, of the lower (solid line) and upper (dashed line) boundaries of the flux tube as a function of the radial distance in the penumbra. Bottom panel: inferred flux tube diameter as a function of r/R.

much larger: $\Delta P_g \sim \Delta B^2$. In addition, the higher temperature in the flux tubes also increases the opacity. As a consequence the flux tube is very opaque in the inner penumbra and the continuum level, $\log\tau_5 = 0$, is formed within the tube, making its lower discontinuity invisible (see Fig. 5.5; top panel). Again, the simultaneous inversion of the visible and infrared lines will allow for a better distinction between these two possibilities in the inner penumbra.

For the rest of the penumbra, $r/R > 0.5$, the lower and upper flux tube boundaries are consistently located at $\log\tau_5 \sim 0.2$ and $\log\tau_5 \sim -1.7$ respectively (see Fig. 5.5; top panel), right in the region where the discontinuities are more effective in generating NCP (see Fig. 3.8). This corresponds to a thickness of roughly 100-200 Km (see Fig. 5.5; bottom panel). This is in agreement with previous investigations based on the Net Circular Polarization (Solanki & Montavon 1993; Martínez Pillet 2000,2001).

5.5 Discussion

Flux tubes of 100-200 km diameter have been also inferred from continuum images at very high spatial resolution (Sütterlin 2001; Scharmer et al. 2002; Sütterlin et al. 2004; cf. van der Oort et al. 2004; see also Fig.2.2). However, any comparison with our results must be made carefully as we must bear in mind that our definition of flux tubes refers to the different magnetic field inclinations and velocities found within the resolution element, whereas the other authors consider the brightness structuring. Therefore measurements of the full Stokes vector at resolutions of 0.1 arc sec would be desirable to study the magnetic and kinematic fine structure of the dark core penumbral filaments seen by Scharmer et al. (2002).

Another point of special interest concerns the null divergence condition of the magnetic field vector. Sánchez Almeida (1998, 2001) have argued that any penumbral model, compatible with the $\nabla\mathbf{B}=0$ condition and able to fit the Stokes V area asymmetry must be based in flux tubes with typical diameters of only several kilometres. As we have demonstrated the uncombed model is able to reproduce, with striking accuracy, the area asymmetry in the circular polarization profiles. It is therefore also necessary to check whether the model also satisfies $\nabla\mathbf{B}=0$. Taking cylindrical coordinates where the vectors $\mathbf{e_z}$ and $\mathbf{e_r}$ point perpendicular to the solar surface and radially outwards in the sunspot respectively,

$$\nabla\mathbf{B}=\frac{1}{r}\frac{\partial}{\partial r}\left(rB_r\right)+\frac{1}{r}\frac{\cancelto{0}{\partial B_\phi}}{\partial\phi}+\frac{\cancelto{0}{\partial B_z}}{\partial z} \tag{5.1}$$

Note that the derivatives with respect to ϕ and z vanish as a consequence of the model construction [2] (see Sect. 4.2 and Fig. 4.4 and footnote in page 93). Therefore it is sufficient to use

$$\nabla\mathbf{B}=\frac{1}{r}\frac{\partial}{\partial r}\left(rB_r\right) \tag{5.2}$$

From our results in Fig. 5.3 (middle panels) we have interpolate third order polynomials in order to obtain analytical expressions for $B(r)$ and $\zeta(r)$. Taking into account that $B_r(r)=B(r)\sin\zeta(r)$ we can easily compute Eq. 5.2 as a function of the radial distance in the penumbra. The result is presented in Fig. 5.6. The magnetic field configuration for the penumbral fine structure, as deduced from the application of the uncombed model, clearly verifies, with an error of half a Gauss per kilometre in the inner penumbra, the null divergence condition of the magnetic field vector for both the external and flux tube magnetic field, showing that optically thin flux tubes are not necessary to verify the afore mentioned conditions (see Martínez Pillet 2001, Sánchez Almeida 2004; cf. Sánchez Almeida 2001).

[2] Although we have not checked it, we are assuming that the magnetic field vector (in the local reference frame) is oriented radially in the penumbra and therefore it has no azimuthal component. This has been demonstrated in Sect. 3.8 for the 2C model.

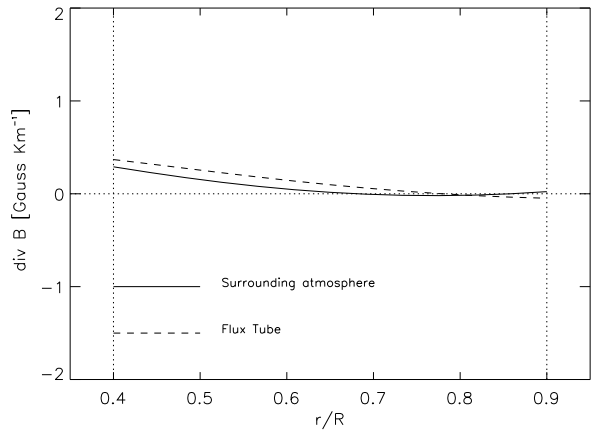

FIGURE 5.6: $\nabla \mathbf{B}$ as a function of the radial distance in the penumbra, for the external magnetic field (solid line) and the flux tube magnetic field (dashed line).

5.6 Conclusions

The uncombed model is able to satisfactorily reproduce the polarization signals emerging from the sunspot penumbra both for the Fe I lines at 6300 Åand at 1.56 μm. The area asymmetry in the circular polarization profiles, Stokes V, as well as its behaviour with radial distance in the penumbra are also reproduced. The deduced magnetic topology verifies very consistently the null divergence condition for the magnetic field vector.

It is important to note that the inferred vertical sizes for the penumbral flux tubes (around 100-200 km) have been obtained from the interpretation of the polarized spectrum, and in particular, of the net circular polarization, within the assumptions on the geometry of the penumbral fine structure included in the uncombed model. Therefore we can not rule out other models, that offering a consistent explanation of the observed profiles, consider flux tubes with smaller sizes.

Thick flux tubes would imply that simulations of penumbral flux tubes embedded in the penumbra (e.g Montesinos & Thomas 1997, Schlichenmaier et al. 1998a,1998b) would need to be revisited, since they all rely on the thin flux tube approximation and therefore they neglect any variation in the physical quantities in the plane perpendicular to the tube's axis. In Chapter 6 we will address this point in some more detail.

Chapter 6

MHS equilibrium of thick penumbral filaments

In this chapter we study in some detail the magnetohydrostatic equilibrium of penumbral flux tubes. We will show that for typical penumbral conditions the magnetic field vector can not be completely aligned with the axis of the flux tube, but rather there must exist a non-vanishing component on the plane perpendicular to it.

6.1 Introduction

The equilibrium configuration of penumbral fibrils has been usually studied under the thin-flux tube approximation (Thomas & Montesinos 1993; Montesinos & Thomas 1997). This approximation has the advantage that the equations governing the dynamical evolution of the flux tube become a set of spatially one-dimensional equations, allowing for a fast and less complicated integration. However, the thin-flux tube approximation can be questioned in the solar photosphere, where the radius of the penumbral fibrils becomes comparable to the pressure scale height. The flux tubes are then said to be *thick*. In this case the flow must be considered two dimensional due to the fact that there will be a velocity, pressure, density and temperature distribution in its interior.
In this chapter we will present a equilibrium configuration for thick penumbral fibrils, trying to keep as much as possible of the features of the sunspot penumbra we have determined in the previous chapters. Our aim is to set up a basic formulation of the problem that might allow for a more general treatment.

6.2 Basic equations and boundary conditions

Let us consider the case of a horizontal flux tube that carries the Evershed flow and is embedded in a static plasma with and inclined magnetic field. The flux tube's radius is denoted as R and its central position in the vertical direction will be for simplicity at $z = 0$. The stationary momentum equation can be written in *cgs* units as (see Priest 1971)

$$\rho\mathbf{v}(\nabla\mathbf{v}) = -\nabla p + \frac{1}{c}\mathbf{j}\times\mathbf{B} + \rho\mathbf{g} \tag{6.1}$$

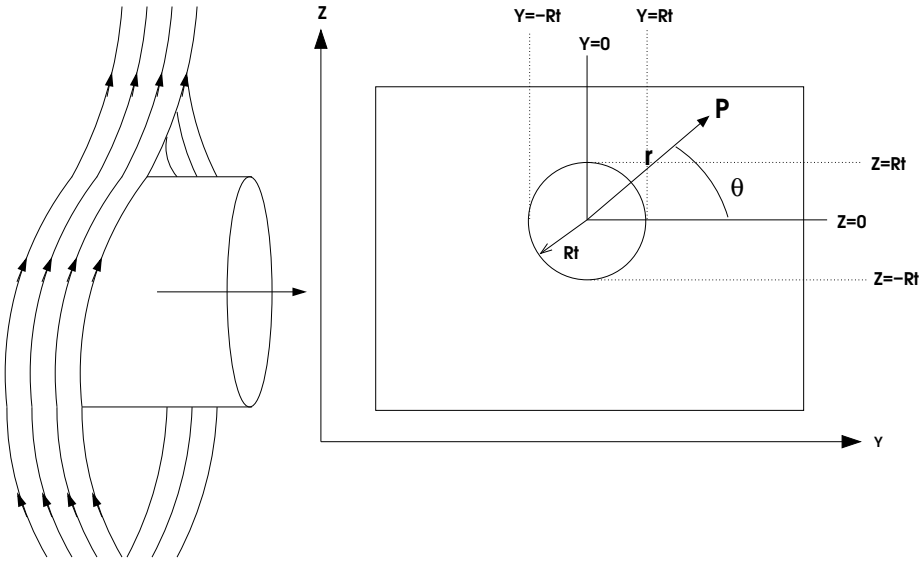

FIGURE 6.1: Left panel: scheme of a horizontal penumbral filament embedded in a magnetic atmosphere with a more vertical magnetic field. Right panel: coordinate system in the plane perpendicular to the tube's axis (X-axis).

This equation describes the force balance between the inertial force, the pressure gradient, the Lorentz force and the gravity force. We set up a reference and coordinate system in order to project this vector equation. We shall use cylindrical coordinates, where the axis of symmetry will be along the tube's axis (see Fig. 6.1). We have already seen in Chapter 3 and 4, that the properties of the flux tubes and the background atmosphere change rather smoothly radially in the penumbra, being quantitatively smaller than the variations in the plane perpendicular to the tube axis, where large gradients can be present at very small scales. We will therefore neglect any variation of all quantities along the tube's axis (X-coordinate, Fig. 6.1). This simplifies our problem to a large extent, since now we can restrict ourselves to consider only polar coordinates in the selected plane. We can therefore write, separately for the flux tube interior (index 't', tube) and exterior (index 's', surroundings)

$$\mathbf{B} = \begin{cases} \mathbf{B_s} = B_{rs}(r,\theta)\mathbf{e_r} + B_{\theta s}(r,\theta)\mathbf{e}_\theta + B_{xs}(r,\theta)\mathbf{e_x} & r > R \\ \mathbf{B_t} = B_{rt}(r,\theta)\mathbf{e_r} + B_{\theta t}(r,\theta)\mathbf{e}_\theta + B_{xt}(r,\theta)\mathbf{e_x} & r < R \end{cases} \tag{6.2}$$

$$\mathbf{v} = \begin{cases} \mathbf{v_s} = 0 & r > R \\ \mathbf{v_t} = v_{t0}\mathbf{e_x} & r < R \quad \rightarrow \text{Evershed flow} \end{cases} \tag{6.3}$$

The normal component of the external and the internal magnetic field are assumed to vanish at the tube's boundary $r = R$. This is important in order to keep a clear distinction between the flux tube and the surrounding atmosphere:

$$B_{rs}(R,\theta) = B_{rt}(R,\theta) = 0 \tag{6.4}$$

This boundary condition satisfies the continuity of the normal component of the magnetic field vector across the interface. The jump in the azimuthal component will lead to an azimuthal surface current. We can now project our generic magnetic and velocity fields (Eq. 6.2 and 6.3) in order to obtain

$$\begin{cases} \mathbf{e_r} : 0 = -\frac{\partial p}{\partial r} + \frac{1}{c}(j_\theta B_x - j_x B_\theta) - \rho g \sin\theta \\ \\ \mathbf{e}_\theta : 0 = -\frac{1}{r}\frac{\partial p}{\partial \theta} + \frac{1}{c}(j_x B_r - j_r B_x) - \rho g \cos\theta \end{cases} \tag{6.5}$$

These equations that are valid for both the exterior and for the flux tube interior. In addition we can make use of the relation $\nabla \times \mathbf{B} = \frac{4\pi}{c}\mathbf{j}$, in order to obtain

$$\frac{1}{r}\frac{\partial B_x}{\partial \theta} = \frac{4\pi}{c} j_r \tag{6.6}$$

6.3 Pressure and density balance

The fact that both the radial component of external and internal magnetic field vanishes in the vicinity of the flux tube's boundary (Eq. 6.4) leads to continuity of the normal stress across the interface (Kippenhahn & Möllenhoff 1975). Therefore, by integrating the Maxwell stress tensor across the interface we find total pressure balance (thermal plus magnetic) between the flux tube's interior and its surroundings:

$$P_{gs}(R,\theta) + \frac{B_s^2(R,\theta)}{8\pi} = P_{gt}(R,\theta) + \frac{B_t^2(R,\theta)}{8\pi} \tag{6.7}$$

Taking derivatives with respect to θ and regrouping, we obtain: terms,

$$\underbrace{\frac{\partial P_{gs}(R,\theta)}{\partial \theta}}_{1} - \underbrace{\frac{\partial P_{gt}(R,\theta)}{\partial \theta}}_{2} = \frac{1}{8\pi}\frac{\partial}{\partial \theta}\left\{ B_{\theta t}^2(R,\theta) + B_{xt}^2(R,\theta) + \cancelto{0}{B_{rt}^2(R,\theta)} - B_{\theta s}^2(R,\theta) - B_{xs}^2(R,\theta) - \cancelto{0}{B_{rs}^2(R,\theta)} \right\} \tag{6.8}$$

Both terms labelled as 1 or 2 in Eq. 6.8 can be written as a function of the density using Eq. 6.5 and 6.6,

$$\frac{\partial P_g(R,\theta)}{\partial \theta} = \frac{R}{c}\left\{ \cancelto{0}{j_x B_r(R,\theta)} - j_r(R,\theta) B_x(R,\theta) \right\} - \rho(R,\theta) R g \cos\theta \tag{6.9}$$

$$\frac{\partial P_g(R,\theta)}{\partial \theta} = -\rho(R,\theta) R g \cos\theta - \frac{1}{8\pi}\frac{\partial B_x^2(R,\theta)}{\partial \theta} \tag{6.10}$$

Now, by plugging Eq. 6.10 into 6.8 one obtains

$$\rho_t(R,\theta) - \rho_s(R,\theta) = \frac{1}{8\pi R g \cos\theta} \frac{\partial}{\partial \theta} \left\{ B_{\theta t}^2(R,\theta) - B_{\theta s}^2(R,\theta) \right\} \tag{6.11}$$

Note that Eq. 6.7 and 6.11 link the gas pressure and density of the flux tube and the surrounding atmosphere across the interface. They have been obtained with a number of assumptions: the radial component of the flux tube and surrounding magnetic field has to vanish at the boundary $r = R$, velocity and magnetic field vectors are constant along the tube's axis and the velocity fields are given by Eq. 6.3. Indeed, Eq. 6.11 is valid whatever the external or internal magnetic field configuration is, as long as the boundary conditions, given by Eq. 6.4, are satisfied.

6.4 Potential external field

We shall now consider a very simple case that will permit an analytical treatment of the equilibrium equations and, at the same time, will highlight the difficulties to find a MHS equilibrium for the penumbral flux tubes. The simplest configuration we can choose for the external magnetic field is a potential field: $\nabla^2 \Phi_s = 0$, with $\mathbf{B_s} = -\nabla \Phi_s$. This problem can be solved by variable separation. In addition, boundary conditions given by Eq. 6.4 must be satisfied

$$B_{sr}(R,\theta) = 0 \tag{6.12}$$

We also know (see Chapters 3-4-5) that the external atmosphere it is at rest, and possesses a magnetic field that it is somewhat inclined with respect to the vertical axis. We therefore, assume that $\mathbf{B_s}$ has the following form far away form the tube

$$\begin{aligned} \lim_{r\to\infty} \mathbf{B_s} = & \quad B_0 \cos\gamma_0 \mathbf{e_z} + B_0 \sin\gamma_0 \mathbf{e_x} \\ = & \quad B_0 \cos\gamma_0 \sin\theta \mathbf{e_r} + B_0 \cos\gamma_0 \cos\theta \mathbf{e}_\theta + B_0 \sin\gamma_0 \mathbf{e_x} \end{aligned} \tag{6.13}$$

This yields the following solution for $\mathbf{B_s}(R,\theta)$

$$\mathbf{B_s} = B_0 \sin\gamma_0 \mathbf{e_x} + B_0 \sin\theta \cos\gamma_0 (1 - \frac{R^2}{r^2}) \mathbf{e_r} + B_0 \cos\theta \cos\gamma_0 (1 + \frac{R^2}{r^2}) \mathbf{e}_\theta \tag{6.14}$$

For the flux tube we will assume that both the magnetic field and Evershed flow are constant and parallel to its axis: $\mathbf{B_t} = B_{t0} \mathbf{e_x}$ and $\mathbf{v_t} = v_{t0} \mathbf{e_x}$. We now insert the magnetic fields into Eq. 6.11 and thus, we obtain a relation between the external and internal densities required for the flux tube to be in force equilibrium

$$\rho_t(R,\theta) - \rho_s(R,\theta) = \frac{B_0^2 \sin\theta \cos^2\gamma_0}{\pi R g} \tag{6.15}$$

The physical significance of this equation is clear from the point of view that, in the middle half above the tube (i.e. $\theta \in [0,\pi]$) the external magnetic field lines close around the flux tube,

resulting in a net tension force that pushes up the tube. In order to stay stationary the internal density of in such layers has to be larger than the surrounding so it will compensate this force. Opposite situation happens in the middle half beneath the tube, where the external magnetic field lines are opening around the tube, pushing it down. To compensate this effect the tube's density has to become larger as compared to the surrounding, so the flux tube will become buoyant.

Typical values, obtained from spectropolarimetric analysis (see Chapter 3-4) indicate: $B_0 \simeq$ 1500 G, $\gamma_0 \simeq 45^\circ$, $R \simeq 100$ km. Taking also $g = 2.74 \times 10^4$ cm s^2, we can estimate an order of magnitude for the density difference

$$\rho_t(R,\theta) - \rho_s(R,\theta) \sim 2 \times 10^{-6} \sin\theta \quad \mathrm{gcm}^{-3} \tag{6.16}$$

Typical photospheric densities, at a height slightly above the continuum layers, are of the order of $\rho_s \sim 2 - 3 \times 10^{-7}$ g cm^{-3}. This means that at a given point, the modulation factor (right hand side in Eq. 6.16) becomes larger than the external density itself, resulting in negative densities inside the middle bottom part of the tube. The presence of the flux tube acts as an obstacle for the external magnetic field (Eq. 6.4), and forces it around tube. Thus, a smaller area is available, and in order to keep a constant flux, the strength of the magnetic field has to increase in the neighbourhood of the flux tube. This local enhancement of the external magnetic field makes the azimuthal component of the external magnetic field, $B_{\theta s}$, to change dramatically along the tube's boundary: from $B_{\theta s} = 0$ at $(r = R, \theta = -\pi/2)$ to $B_{\theta s} = 2B_0$ at $(r = R, \theta = 0)$.

It is not clear whether the presence of electric currents in the external atmosphere can produce Ohmic dissipation large enough to avoid such an enormous enhancement of the magnetic field. Indeed, there will be always field amplification to some extent, as it is a direct consequence of the null divergence of the magnetic field vector.

6.5 Non-uniform flux tube field

Inspection of Eq. 6.11 reveals that if the flux tube magnetic field possesses an azimuthal component such that

$$B_{\theta t}(R,\theta) = \sqrt{\alpha \mathcal{F}(\theta) + B_{\theta s}^2(R,\theta)} = \sqrt{\alpha \mathcal{F}(\theta) + 4B_0^2 \cos^2\theta \cos^2\gamma_0} \tag{6.17}$$

the density difference that follows from Eq. 6.11 is

$$\rho_s(R,\theta) - \rho_t(R,\theta) = \frac{\alpha}{8\pi R g} \frac{1}{\cos\theta} \frac{\mathrm{d}\mathcal{F}(\theta)}{\mathrm{d}\theta} \tag{6.18}$$

so that we have freedom to choose α and $\mathcal{F}(\theta)$ in such a way that the right hand side term of Eq. 6.18 is very small, ensuring with this that the flux tube density will not become negative. For instance: $\alpha \ll 8\pi R g \rho_s(R,\theta) \sim 1 \times 10^6$ and $\mathcal{F}(\theta) = \sin\theta$.

Considering now $\nabla \mathbf{B_t} = 0$ we can write

$$\frac{\partial(rB_{rt})}{\partial r} = -\frac{\partial B_{\theta t}}{\partial \theta} \tag{6.19}$$

Assuming again separation of variables in the following form

$$B_{rt}(r,\theta) = \mathcal{H}(\theta)\mathcal{M}(r) \tag{6.20}$$
$$B_{\theta t}(r,\theta) = \mathcal{G}(\theta)\mathcal{N}(r) \tag{6.21}$$

with the following boundary conditions, that are used in order to satisfy Eq. 6.18 and Eq. 6.4

$$\mathcal{M}(0) = 0 \qquad \mathcal{M}(R) = 0 \qquad \mathcal{N}(0) = 0 \tag{6.22}$$
$$\mathcal{N}(R) = 1 \qquad \mathcal{G}(\theta) = \sqrt{\alpha\mathcal{F}(\theta) + B_{\theta s}^2(R,\theta)} \tag{6.23}$$

Using Eq. 6.20 and after some algebra, it can be shown that a possible magnetic field configuration is given by

$$B_{rt}(\theta,r) = \frac{r}{2R^2}(R-r)\frac{1}{\sqrt{\alpha\mathcal{F}(\theta) + B_{\theta s}^2(R,\theta)}}\left[\alpha\frac{\mathrm{d}\mathcal{F}(\theta)}{\mathrm{d}\theta} + 2B_{\theta s}(R,\theta)\frac{\mathrm{dB_{\theta s}(R,\theta)}}{\mathrm{d}\theta}\right] \tag{6.24}$$

$$B_{\theta t}(\theta,r) = \frac{r}{R^2}(3r-2R)\sqrt{\alpha\mathcal{F}(\theta) + B_{\theta s}^2(R,\theta)} \tag{6.25}$$

For illustrate purposes we have chosen an example that we will describe in some detail, $\alpha = 0$. This situation implies that the azimuthal component of the flux tube at $r = R$ is equal, for all angles, to the azimuthal component of the external magnetic field at the tube's boundary (which is taken from the potential field, Sect. 6.4). Hence this make $\rho_s(R,\theta) = \rho_t(R,\theta)$. With this, the components of the magnetic field are as follows

$$B_{rt}(\theta,r) = -\frac{2r}{R^2}(R-r)B_0\sin\theta\cos\gamma_0 \tag{6.26}$$
$$B_{\theta t}(\theta,r) = \frac{2r}{R^2}(3r-2R)B_0\cos\theta\cos\gamma_0 \tag{6.27}$$

Fig. 6.2 shows the 2 dimensional distribution inside the flux tube of the radial component of the magnetic field strength (top panel), azimuthal component (middle panel), as well as the total perpendicular component ($(B_\theta^2 + B_r^2)^{1/2}$). Note that we have also included the potential solution for the external field, $B_s(R,\theta)$, as given by Eq. 6.15. Looking at the magnitude and distribution of the flux tube magnetic field two important questions arise. Firstly, we have learnt, from the inversion of spectropolarimetric data, that the magnetic field inside the flux tube is mainly parallel to its axis and possesses a strength of about 1200 Gauss: $B_{xt} \simeq 1200$ Gauss. However, we can not rule out the existence of a small, but non-vanishing, component of the magnetic field perpendicular to the tube's axis: $B_{rt}, B_{\theta t} \ll B_{xt}$. The perpendicular magnetic field,

$(B_\theta^2 + B_r^2)^{1/2}$, inside the flux tube reaches, except for it outermost part, values smaller that $\simeq 400$ Gauss (see Fig. 6.2), which can be considered to be within the mentioned limits. This means that the total magnetic field vector, once the X-component is added, is still mainly parallel to the tube's axis, in agreement with observations.

Secondly, we must acknowledge that the magnetic configuration for the flux tube interior described here, that leads to an equilibrium configuration, is unlikely to be present in the flux tubes as soon as they appear in the penumbra, but rather it should be a consequence of a dynamical behaviour. Moreover, this study, although it is beyond the scope of this work, should be accompanied by an stability analysis in order to check whether this is a stable equilibrium.

Finally we shall remark that, although in the external atmosphere there are no currents (obviously because $\mathbf{B_s}$ is potential), they can exist at the interface layer: $\mathbf{j} = \mathbf{e_r} \times [\mathbf{B_s}(R,\theta) - \mathbf{B_t}(R,\theta)] \neq 0$ as well as inside the flux tube, $\mathbf{j} = \frac{c}{4\pi}\nabla \times \mathbf{B_t}$. The presence of these currents will transform the energy stored in the magnetic field into thermal energy, that will be ultimately, via ohmic dissipation, radiated away.

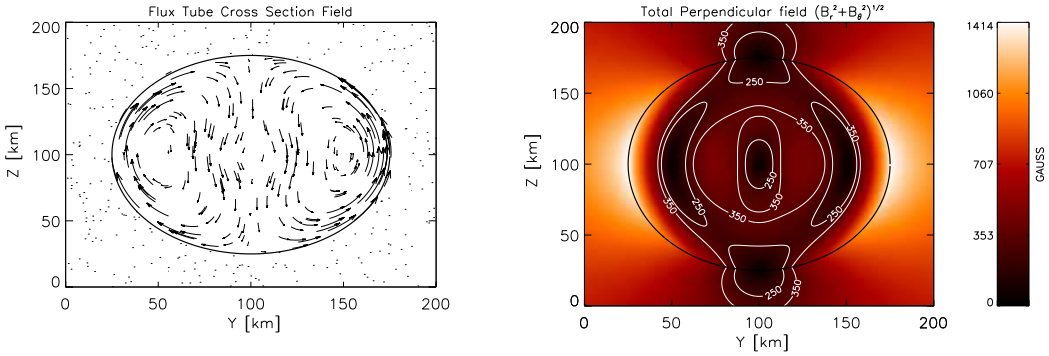

FIGURE 6.2: Left panel: vector field representation of the flux tube magnetic field given by Eq. 6.26-6.27. Right panel: color plot of perpendicular component $(B_\theta^2(r,\theta) + B_r^2(r,\theta))^{1/2}$ of the magnetic field. Now an external field as in Eq. 6.14, is also included. In this example we have used $B_0 = 1000$ Gauss and $\gamma_0 = 45°$. Note everywhere there is a component of the magnetic field parallel to the tube's axis: $B_{xs} = B_0 \sin\gamma_0 \simeq 700$ Gauss and $B_{xt} \simeq 1000$ Gauss.

Conclusions

In this thesis we have presented a picture of the fine structure of the penumbra that explains, in a natural way, the polarization signals emerging from the sunspot penumbra and embraces many of the different, sometimes contradictory, results obtained from the application of different geometrical models to interpret the Stokes profiles observed in different spectral lines.

This picture consists in magnetic flux tubes that carry the Evershed flow and are embedded in a surrounding magnetic atmosphere. From the application of such a model to interpret the polarization signals of several sunspots observed with different viewing angles (i.e. heliocentric angles) at different spectral regions we have been able to characterize the properties of the penumbral fine structure:

1. The magnetic field vector in the flux tubes is almost horizontal with respect to the vertical direction in the solar surface, being slightly inclined upwards in the inner penumbra but downwards in its outer boundary. The surrounding atmosphere possesses a magnetic field which is less inclined (with respect to the vertical) than that in the flux tubes.

2. The strength (modulus) of the magnetic field vector in the flux tube remains fairly constant radially in the penumbra $B \sim 1200$ Gauss, whereas the strength in the surrounding atmosphere decreases very rapidly towards the outer penumbra: from $B \sim 2500$ to $B \sim 1200$ Gauss.

3. In the local reference frame, the azimuthal angle of the magnetic field vector is the same for the flux tubes and their magnetic surroundings, being both of them almost perfectly aligned with the radial direction. However it turns out to be different in the observer's reference frame. In this case, the difference between the azimuthal angle in the flux tubes and their surroundings has opposite signs on the regions divided by the line of symmetry of the sunspot.

4. While the plasma in the surrounding is essentially at rest, rapid flows with velocities up to 4 km s^{-1} are detected in the flux tubes at the inner penumbra. The speed increases radially slightly up to 5 km s^{-1}, corresponding to almost supercritical velocities. Sometimes it is seen to suffer a sudden drop at the outer penumbra that could be explained through a shock front or due to the fact that the flux tubes are returning back into the solar interior (see item 1)

5. Flux tubes are hotter than their surroundings in the inner penumbra, but they rapidly reach similar temperatures. This, together with items 1 and 4 indicates the presence of fast hot

upflows in the inner penumbra.

6. The gas pressure inside the flux tubes is likely to decrease radially, leading to larger gas pressures in the inner footpoints than in the outer ones, as required by the siphon flow mechanism to explain the Evershed effect.

7. The excess of gas pressure in the flux tubes, as compared with their surroundings, in the inner penumbra leads to an enhanced opacity that prevents the observer to detect the flux tubes boundaries and therefore no Net Circular Polarization is observed in Stokes V (i.e. there are no discontinuities along the line of sight in the physical parameters). At intermediate-large radial distances the flux tubes become optically thinner because the temperature and gas pressure decreases. This makes the flux tubes boundaries visible. From the amount of NCP generated at the flux tubes' boundaries we have been able to study their vertical extension, finding diameters of about 100-200 kilometres. Nevertheless we can not rule out the possibility of smaller flux tubes because these values have been obtained within the constraints imposed by our model of the penumbra.

There is much yet to be done to fully understand the penumbral dynamics and magnetic and thermal structure. In science, the fact that a model is able to consistently explain what we observe, is no proof of its validity. There are other scenarios, far less investigated, that might also give a consistent explanation of the observations. In order to be able to distinguish among them, further developments in the instruments and analysis techniques are mandatory. In the case of the penumbra, the combination of simultaneous observations in the Fe I lines at 6300 Åand 1.56 μm will certainly allow for a better characterization of the vertical and horizontal penumbral structure. In addition, the improvement in the spatial resolution of the observations will be most useful to distinguish between the different scenarios. In fact this is already possible with the new instrumental set up of the infrared (TIP) and visible (POLIS) polarimeters and adaptive optic system (KAOS) installed in the German Vacuum Tower Telescope located at the Spanish observatory of Izaña. In the near future we hope to have access to such instruments in order to further investigate this challenging and exciting feature of the solar magnetism.

Another point of special interest concerns the fate of the penumbral flux tubes that submerge into the deep layers of the solar photosphere at the outer boundary of the penumbra. They are believed to reappear again further away of the visible limit of the spot, as bright features seen in the G-band (moving magnetic features; MMF), that move away from the spot with similar velocities to that of the moat flow. These MMFs are seen sometimes to merge with magnetic flux concentrations at the edge of the moat, leading to emission peaks in the core of the Ca II K line, which is formed in the chromosphere. These features seem to indicate the possibility of flux cancellation due to magnetic reconnection of magnetic fluxes of opposite polarity in the photosphere. If so, these processes would be extremely relevant, not only to explain the decay of active regions, but also to understand the coupling between the different layers of the solar atmosphere.

Bibliography

Abrams, M. C., Davis, S. P., Rao, M. L. P., Engleman, R., Jr., & Brault, J. W., 1994 ApJS, 93, 351

Alissandrakis, C.E., Dialetis, D., Mein, P., Schmieder, B. & Simon, G., 1988, A&A, 201, 339

Auer, L.H., 1976, JQSRT, 16, 931

Barklem, P.S., O'Mara, B.J., 1997, MNRAS, 290, 102

Barklem, P.S., O'Mara, B.J. & Ross, J.E., 1998, MNRAS, 296, 1057

Beckers, J.M., 1969a, SoPh., 9, 372

Beckers, J.M., 1969b, SoPh., 10, 262

Beckers, J.M. & Scröter, E.H., 1969, SoPh., 7, 22

Bellot Rubio, L.R., Ruiz Cobo, B. & Collados, M., 1998, ApJ, 506, 805

Bellot Rubio, L.R., Collados, M., Ruiz Cobo, B. & Rodríguez Hidalgo, I., 2000, ApJ, 534, 989

Bellot Rubio, L.R., Collados, M., Ruiz Cobo, B. & Rodríguez Hidalgo, I., 2002, Il Nuovo Cimento, 25C, 543

Bellot Rubio, L.R., Balthasar, H., Collados, M. & Schlichenmaier, R., 2003, A&A, 403, L47

Bellot Rubio, L.R., 2003 in Solar Polarization Workshop, eds. J. Trujillo Bueno & Sánchez Almeida, (ASP Conf. Ser. Vol. 307), 301

Bellot Rubio, L.R., Schlichenmaier, R. & Tritschler, A., 2004b, A&A (submitted)

Bellot Rubio, L.R., Balthasar, H. & Collados, M., 2004b, A&A (in press)

Berdyugina, S.V. & Solanki, S.K., 2002, A&A, 385, 701

Berdyugina, S.V., Solanki, S.K. & Frutiger, C., 2003, A&A, 412, 513

Börner, P. & Kneer, F., 1992, A&A, 259, 307

Borrero, J.M. & Bellot Rubio, L.R., 2002, A&A, 385, 1056

Borrero, J.M., Bellot Rubio, L.R., Barklem, P.S. & del Toro Iniesta, J.C., 2003a, A&A, 404, 749

Borrero, J.M., Lagg, A., Solanki, S.K., Frutiger, C., Collados, M. & Bellot Rubio, L.R., 2003b in High Resolution Solar Observations: preparing for ATST, eds. A. Pestov & H. Uitenbroek, (ASP Conf. Ser. 286), 235

Borrero, J.M., Solanki, S.K., Bellot Rubio, L.R., Lagg, A. & Mathew, S.K., 2004, A&A (in press)

Bünte, M., Darconza, G. & Solanki, S.K., 1993, A&A, 274, 478

Bünte, M. & Solanki, S.K., 1995, A&A, 297, 861

Carroll, T.A. & Staude, J., 2001, A&A, 378, 316

Collados, M., Martínez Pillet, V., Ruiz Cobo, B., del Toro Iniesta, J.C. & Vázquez, M., 1994, A&A, 291, 622

Collados, M., 2001 in Advanced Solar Polarimetry: Theory, Observations and Instrumentation, ed. M. Sigwarth, (ASP Conf. Ser. 236), 255

Crawford, F.H., 1934, Rev. Mod. Phys., 6, 90

Degenhardt, D., 1989, A&A, 222, 297

Degenhardt, D., 1991, A&A, 248, 637

Degenhardt, D. & Wiehr, E., 1991, A&A, 252, 821

Degenhardt, D. & Kneer, F., 1992, A&A, 260, 411

Degenhardt, D., Solanki, S.K., Montesinons, B. & Thomas, J.H., 1993, A&A, 279, L29

Dere, K.P., Schmieder, B. & Alissandrakis, C.E., 1990, A&A, 233, 207

Dialetis, D., Mein, P. & Alissandrakis, C.E., 1985, A&A, 147, 93

Elmore, D.F., Lites, B.W., Tomczyk, S. et al., 1992, Proc. SPIE, 1746, 22

Eriksen, G. & Maltby, P., 1967, Astrophys. J., 148, 833

Evershed, J., 1909, MNRAS, 69, 454

Feautrier, P., 1964, C. R. Acad. Sci. Paris, 258, 3189

Ferriz-Mas, A., 1988, PhFl., 31, 2583

Frutiger, C., Solanki, S.K., Fligge, M. & Bruls, J.H.M.J., 1999 in Solar Polarization workshop, eds. K.N. Nagendra and J.O. Stenflo (Astrophysiscs and Space Science library vol 243), 281

Frutiger, C., 2000, PhD Thesis, Institute of Astronomy, ETH, Zürich, No. 13896

Gray, D.F., 1992, The observations and analysis of stellar photospheres, (Cambridge: Cambridge University Press)

Grossmann-Doerth, U., Schüssler, M. & Solanki, S.K., 1989, A&A, 221, 338

Gustafsson, B., 1973, Upps. Astron. Obs. Ann., 5

Hale„ G.E., 1908, Astrophys. J., 28, 100

Henson, G.D. & Kemp, J.C., 1984, SoPh., 93, 289

Hill, E.L., 1929, Phys. Rev., 34, 1507

Hirzberger, J. & Kneer, F., 2001, A&A, 378, 1078

Illing, R.M., Landmann, D.A. & Mickey, D.L., 1974a, A&A, 35, 327

Illing, R.M., Landmann, D.A. & Mickey, D.L., 1974b, A&A, 37, 97

Kemp, J.C. & Henson, G.D., 1983, ApJ, 266, L69

Keppens, R. & Martínez Pillet, V., 1996, A&A, 316, 229

Kinman, T.D., 1952, MNRAS, 112, 425

Kippenhahn, R. & Möllenhoff, C., 1975, Elementare Plasmaphysik (Zürich, Wissenschaftsverlag)

Kronig, R. de L., 1928, Phys. Rev., 31, 195

Küveler, G. & Wiehr, E., 1995, A&A, 142, 205

Lagg, A., Woch, J., Krupp, N. & Solanki, S.K., 2004, A&A, 414, 1109

Landi degl'Innocenti, E., 1983, SoPh., 85, 3

Landi degl'Innocenti, E., 1992 in Solar Observations: techniques and interpretation, eds. F. Sánchez, M. Collados & M. Vázquez (Cambridge: Cambridge University Press), 84

Landolfi, M. & Landi degl'Innocenti, E., 1982, SoPh., 78, 355

Landolfi, M., 1987, SoPh., 109, 287

Landolfi, M. & Landi degl'Innocenti, E., 1996, SoPh., 164, 191

Leka, K.D., Socas-Navarro, H., 2000, Bulletin of the American Astronomical Society, 32, 804

Lites, B.W. & Skumanich, A., 1990, ApJ, 348, 747

Lites, B.W., Skumanich, A. & Scharmer, G. B., 1990, ApJ, 355, 329

Lites, B.W., Elmore, D.F., Seagraves, P. & Skumanich, A.P., 1993, ApJ, 418, 928

Lites, B., Socas-Navarro, H., Skumanich, A. & Shimizu, T., 2002, ApJ, 575, 1131

Livingston, W., & Wallace, L., 1991, An Atlas of the Solar Spectrum in the infrared from 1.1 to 5.4 microns, NSO Technical Rep. 91-101

Makita, M., 1986, SoPh., 106, 269

Makita, M. & Ohki, Y., 1986, Annals of Tokyo Astronomical Observatory, 21, 1

Maltby, P., 1964, Astrophys. Norvegica, 8, 205

Maltby, P. & Eriksen, G., 1967, SoPh., 2, 249

Martínez Pillet, V., 1997 in Advances in Physics of Sunspots, eds. B. Schmieder, J.C. del Toro Iniesta, & M. Vázquez, (ASP Conf. Ser. Vol. 118), 212

Martínez Pillet, V., Collados, M., Bellot Rubio, L.R., Rodríguez Hidalgo, I., Ruiz Cobo, B. & Soltau, D., 1999, AGM, 15, P05

Martínez Pillet, V., 2000, A&A, 361, 764

Martínez Pillet, V., 2000, A&A, 369, 644

Mathew, S.K., Lagg, A., Solanki, S.K., Collados, M., Borrero, J.M., Berdyugina, S., Krupp, N., Woch, J. & Frutiger, C., 2003, A&A, 410, 695

Mathew, S.K., Lagg, A., Solanki, S.K., Collados, M., Borrero, J.M., Berdyugina, S., 2004, A&A, 422, 703

McPherson, M.R., Lin, H. & Kuhn, K.R., 1992, SoPh., 139, 255

Meyer, F. & Schmidt, H.U., 1968, Z. Ang. Math. Mech, 48, T218

Mies, F. H., 1974, J. Molec. Spec., 53, 150

Mihalas, D., 1978, Stellar atmospheres, (San Francisco: W.H Freeman and Company)

Montesinos, B. & Thomas, J., 1989, ApJ, 337, 977

Montesinos, B. & Thomas, J., 1997, Nature, 390, 485

Müller, D.A.N., Schlichenmaier, R., Steiner, O. & Stix, M., 2002, A&A, 393, 305

Penn, M.J., Cao, W.D., Walton, S.R., Chapman, G.A & Livingston, W., 2003, ApJ, 590, L119

Press, W.H., Flannery, B.P., Teukolsky, S.A. & Vetterling, W.T., 1986 Numerical Recipes (Cambridge: Cambridge University Press) Priest, E.R., 1984 in Solar magneto-hydrodynamics (Dordrecht: Geophysics and Astrophysics Monographs)

Rachkovsky, D.N., 1962a, Izv. Krymsk. Astrofiz. Obs., 27, 148

Rachkovsky, D.N., 1962b, Izv. Krymsk. Astrofiz. Obs., 28, 259

Rees, D.E., Durrant, C.J. & Murphy, G.A., 1989, ApJ, 339, 1093

Rees, D.E., López Ariste, A., Thatcher, J. & Semel, M., 2000, A&A, 355, 759

Rimmele, T.R., 1995, A&A, 298, 260

Rouppe van der Voort, L., 2002, A&A, 389, 1020

Rouppe van der Voort, L., Löfdahl, M.G., Kiselman, D. & Scharmer, G.B., 2004, A&A, 414, 717

Rüedi, I., Solanki, S.K., Keller, C.U. & Frutiger, C., 1998, A&A, 338, 1089

Rüedi, I., Solanki, S.K. & Keller, C.U., 1999, A&A, 348, L37

Ruiz Cobo, B. & Del Toro Iniesta, J.C. 1992, ApJ, 398, 375

Ruiz Cobo, B. & Del Toro Iniesta, J.C. 1994, A&A, 283, 129

Ruiz Cobo, B., 1998, Ap&SS, 263, 331

Sánchez Almeida, J., Collados, M. & del Toro Iniesta, J.C., 1989, A&A, 222, 311

Sánchez Almeida, J. & Lites, B.W., 1992, ApJ, 398, 359

Sánchez Almeida, J. & Landi degl'Innocenti, E., 1996, SoPh., 164, 203

Sánchez Almeida, J., Ruiz Cobo, B. & del Toro Iniesta, J.C., 1996, A&A, 314, 295

Sánchez Almeida, J., 1998, ApJ, 497, 967

Sánchez Almeida, J., 2001, A&A, 369, 643

Sánchez Almeida, J., 2004, ApJ (submitted)

Schadee, A., 1978, JQSRT, 19, 517

Scharmer, G.B., Gudiksen, B.V., Kiselman, D., Löfdahl, M.G. & Rouppe van der Voort, L., 2002, Nature, 420, 151

Schlichenmaier, R., Jahn, K. & Schmidt, H.U., 1998a, ApJ, 483, L121

Schlichenmaier, R., Jahn, K. & Schmidt, H.U., 1998b, A&A, 337, 897

Schlichenmaier, R., Bruls, J.H. & Schüssler, M., 1999, A&A 349, 961

Schlichenmaier, R. & Schmidt, W., 2000, A&A, 358, 1122

Schlichenmaier, R. & Collados, M., 2002, A&A, 381, 668

Schlichenmaier, R., Müller, D.A.N., Steiner, O. & Stix, M., 2002, A&A, 381, L77

Schlichenmaier, R., 2002, AN, 323, 303

Schlichenmaier, R. & Solanki, S.K., 2003, A&A, 411, 257

Schmidt, W., Hofmann, A., Balthasar, H., Tarbell, T.D. & Frank, Z.A., 1992, A&A, 264, L27

Schmidt, W. & Schlichenmaier, R., 2000, A&A, 364, 829

Schüssler, M., 2002, AN, 323, 377

Schröter, E.H., 1965, Z. Astrophys., 62, 228

Skumanich, A. & Lites, B.W., 1987, ApJ, 322, 473

Skumanich, A., Lites, B.W., Martínez Pillet, V. & Seagraves, P., 1996, ApJS, 110, 357

Skumanich, A. & López Ariste, A., 2002, ApJ, 570, 379

Sobotka, M., Brandt, P.N. & Simon, G.W., 1999, A&A, 348, 621

Sobotka, M. & Sütterlin, P., 2001, A&A, 380, 714

Socas-Navarro, H., López Ariste, A. & Lites, B.W., 2001, ApJ, 553, 949

Socas-Navarro, H., 2001 in Advanced Solar Polarimetry: Theory, Observations and Instrumentation, ed. M. Sigwarth, (ASP Conf. Ser. 236), 487

Socas-Navarro, H. & Sánchez Almeida, J., 2002, ApJ, 565, 1323

Solanki, S.K. & Pahlke, K.D., 1988, A&A, 201, 143

Solanki, S.K., Rüedi, I. & Livingston, W., 1992a, A&A, 263, 339

Solanki, S.K., Rüedi, I. & Livingston, W., 1992b, A&A, 263, 312

Solanki, S.K. & Montavon, C.A.P., 1993, A&A, 275, 283

Solanki, S.K., Walther, U. & Livingston, W., 1993, A&A, 277, 639

Solanki, S.K., Schmidt, H.U., 1993, A&A, 267, 287

Solanki, S.K., Montavon, C.A.P. & Livingston, W., 1994, A&A, 283, 221

Solanki, S.K., Rüedi, I., Bianda, M. & Steffen, M., 1996, A&A, 308, 623

Solanki, S.K., Finsterle, W., Rüedi, I. & Livingston, W., 1999, A&A, 347, L27

Solanki, S.K. & Rüedi, I., 2003, A&A, 411, 249

Solanki, S.K., 2003, A&ARv, 11, 153

Stanchfield, D.C.H., Thomas, J.H. & Lites, B.W., 1997, ApJ, 477, 485

Stellmacher, G. & Wiehr, E., 1980, A&A, 82, 157

Sütterlin, P., 2001, A&A, 374, L21

Sütterlin, P., Bellot Rubio, L.R. & Schlichenmaier, R., 2004, A&A (in press)

Thomas, J., 1988, ApJ, 333, 407

Thomas, J. & Montesinos, B., 1990, ApJ, 359, 550

Thomas, J. & Montesinos, B., 1991, ApJ, 375, 404

Thomas, J. & Montesinos, B., 1993, ApJ, 407, 398

Title, A.M., Frank, Z.A., Shine, R.A., Tarbell, T.D., Topka, K., Scharmer, G. & Schmidt, W., 1993, ApJ, 403, 780

del Toro Iniesta, J.C., Tarbell, T.D. & Ruiz Cobo, B., 1994, ApJ, 436, 400

del Toro Iniesta, Bellot Rubio, L.R. & Collados, M., 2001, ApJ, 548, L139

del Toro Iniesta, J.C., 2003 in Introduction to Spectropolarimetry (Cambridge: Cambridge University Press)

del Toro Iniesta, J.C., 2003, AN, 324, 387

del Toro Iniesta, J.C. & Ruiz Cobo, B., 1996 in La polarimétrie, outil pour l'étude de l'activité magnétique solaire et stellaire, eds. N. Mein & S. Sahal-Bréchot (Obs. de Paris, Paris), 126

del Toro Iniesta, J.C. & Ruiz Cobo, B., 1997 in Science with THEMIS, eds. N. Mein & S. Sahal-Bréchot (Obs. de Paris, Paris), 93

Tritschler, A., Schlichenmaier, R., Bellot Rubio, L.R. & KAOS Team, 2004, A&A, 415, 717

Unno, W., 1956, PASJ, 8, 108

Unsöld, A., 1955, Physik der Sternatmospharen, (Berlin: Springer)

Wentzel, D.G., 1992, ApJ, 388, 211

Westendorp Plaza, C., del Toro Iniesta, J.C., Ruiz Cobo, B., Martínez Pillet, V., Lites, B.W. & Skumanich, A., 1997, Nature, 389, 47

Westendorp Plaza, C., del Toro Iniesta, J.C., Ruiz Cobo, B., Martínez Pillet, V., Lites, B.W. & Skumanich, A., 1998, ApJ, 494, 453

Westendorp Plaza, C., del Toro Iniesta, J.C., Ruiz Cobo, B., Martínez Pillet, V., Lites, B.W. & Skumanich, A., 2001a, 547, 1130

Westendorp Plaza, C., del Toro Iniesta, J.C., Ruiz Cobo, B. & Martínez Pillet, V., 2001b, ApJ, 547, 1148

Wiehr, E., Stellmacher, G., Knölker, M., Grosser, H., 1986, A&A, 155, 402

Wiehr, E., Koch, A., Knölker, M., Küveler, G. & Stellmacher, G., 1984, A&A, 140, 352

Wiehr, E. & Stellmacher, G., 1989, A&A, 225, 528

Wiehr, E. & Degenhardt, D., 1992, A&A, 259, 313

Wiehr, E., 1995, A&A, 298, L17

Wiehr, E., 1997 in Advances in Physics of Sunspots, eds. B. Schmieder, J.C. del Toro Iniesta, & M. Vázquez, (ASP Conf. Ser. Vol. 118), 175

Wittmann, A., 1974, SoPh, 35, 11

Acknowledgements

There are many people who have contributed to the completion of this thesis and little the available space to acknowledge all of them as they would deserve. My first words are dedicated to my father and mother who have always encouraged and supported me to do what I thought it was worthy doing, regardless the final results.

Sami Solanki, my supervisor at the Max Planck Institut, will always have my infinite gratitude for believing in me when I was still an undergraduate student at La Laguna. He gave me the chance to come to work to Lindau's just born Solar Physics group, making available for me, not only the huge amount of resources provided by the Max Planck, but also his precious time and his deep knowledge about Solar Physics. Whatever good I might have as a researcher should be ascribed to him.

Franz Kneer, my supervisor at the University of Göttingen, has also played a significant role in my formation as a scientist. His sharp and, sometimes also, naughty questions during the Wednesday Seminars at Göttingen Observatory have been most useful to learn, not only how to be prepared for the worst, but also how to look at the problem from different points of view.

Very special thanks to my friends and colleagues from the IAC, KIS and MPAe: Luis Bellot, Manolo Collados, Basilio Ruiz, Manfred Schüssler, Valentín Martínez, Jorge Sánchez for being always interested in my work, criticising it when needed and encouraging me to follow *that* path whenever it seemed interesting and promising.

Wherever I am in the future, it will be impossible to forget Andreas Lagg and ShibuDa *Master* Mathew, the other members of Lindau's inversion committee, as well as the VTT table tennis team.

My friends at the Max Planck Institute have helped me enormously to make my life normal regardless the obvious limitations of a 1000 inhabitants town. Together with the southamerican group: Francisco Frutos (now in Costa Rica), Santo Salinas (now in Singapore), Gerónimo Villanueva, Luciano Rodríguez and Hebe Cremades, everything was possible. There was always something to do together: beers, BQB, watching football, going shopping, pool , or whatever it might help to disconnect from the endless working hours. With the football gang: Nour-Eddine, Santo, Gero, Durgesh, Zou, Redouane, Yevgen, Mark, Aziz, Lim Fu, David one always had the chance to stare at the German rain waiting for the moment when it will stop and be able to play.

If there are two persons whom I should thank for giving me the needed push up whenever I was in trouble, they are Anna and Rubén. Anna has shown to me that there is something much more beautiful and important in this world than science.

Rubén, I will not express you my gratitude here because wherever you are now, you do not need to read these lines. I will let you know the day God allows us to meet again. This is also your thesis my friend.

Scientific contributions

Conference Contributions :

[1] Borrero, J.M., Lagg, A., Solanki, S.K., Frutiger, C., Collados, M. & Bellot Rubio, L.R. *Modeling the sunspot penumbra through the inversion of Stokes profiles*. High resolution solar observations: preparing for ATST. (Sunspot, New Mexico 2003). ASP Conference Series vol 286. Eds:

[2] Borrero, J.M., Bellot Rubio, L.R. *Two component modeling of convective motions in the solar photosphere and determination of atomic parameters*. Modeling stelalr atmospheres. (Uppsala, Sweden 2004). IAU Symposium 210. Eds: N.Piskunov, W.Weiss and D.F.Gray.

Refereed Publications :

[1] Borrero, J.M. & Bellot Rubio, L.R. *A two component model for the solar photosphere from the inversion of spectral lines*. Astron. and Astrophys. 2002, vol 385, 1056.

[2] Bellot Rubio, L.R. & **Borrero, J.M.** *Iron abundance in the solar photosphere. Application of a two component model*. Astron. and Astrophys. 2003, vol 391, 331.

[3] Borrero, J.M., Bellot Ruibio, L.R., Barklem, P.S. & del Toro Iniesta, J.C. *Accurate atomic paramters for near-infrared spectral lines*. Astron. and Astrophys. 2003, vol 404, 749.

[4] Mathew, S.K., Lagg, A., Solanki, S.K., Collados, M., **Borrero, J.M.**, Berdyugina, S., Krupp, N., Woch, N. & Frutiger, C. *Three dimensional structure of a regular sunspot from the inversion of IR Stokes profiles*. Astron. and Astrophys. 2003, vol 410, 695.

[5] Mathew, S.K., Solanki, S.K., Lagg, A., Collados, M., **Borrero, J.M.** & Berdyugina, S. *Thermal-magnetic relation in a sunspot and a map of its Wilson depression*. Astron. and Astrophys. 2004, vol 422, 693.

[6] Borrero, J.M., Solanki, S.K., Bellot Rubio, L.R., Lagg, A. & Mathew, S.K. *On the fine*

structure of the sunspot penumbrae. I. A quantitative comparison of two semiempirical models with implications for the Evershed effect. Astron. and Astrophys. (in press)

[7] Borrero, J.M., Lagg, S.K., Solanki, S.K. & Collados, M. *On the fine structure of the sunspot penumbrae. II. On the nature of the Evershed flow*. Astron. and Astrophys. (submitted)

Lebenslauf

Persönliche Daten

Name	Juan Manuel Borrero Santiago
Geburtstag	07.10.1977
Geburtsort	Algeciras (Cádiz, Spanien)
Familienstand	verheiratet
Staatsangehörigkeit	Spanisch

Schulbildung

1982 - 1987	Colegio Público Santa María de Jesús (Algeciras, Spanien)
1988 - 1989	Colegio Público Valdés Leal (Sevilla, Spanien)
1990 - 1994	I.B. Miguel de Mañara (La Rinconada, Sevilla, Spanien)

Studium

1995 - 1999	Physik an der Universidad de Sevilla (Spanien)
2000 - 2001	Astrophysik an der Universidad de La Laguna (Tenerife,Spanien)

Promotion

09.2001 - 08.2004	Promotion an der Universitäts Göttingen
.	Stipendium des Max Planck Instituts für Aeronomie